SPECIAL ISSUE

ANNUAL REPORT

of

THE INSTITUTE OF PHYSICS ACADEMIA SINICA

VOLUME 16 SEPTEMBER 1986

IN HONOR OF PROFESSOR TA-YOU WU ON THE OCCASION OF HIS 80TH BIRTHDAY

THE INSTITUTE OF PHYSICS, ACADEMIA SINICA
TAIPEI, TAIWAN, REPUBLIC OF CHINA

SPECIAL ISSUE

ANNUAL REPORT
of
THE INSTITUTE OF PHYSICS
ACADEMIA SINICA

VOLUME 16 SEPTEMBER 1986

IN HONOR OF PROFESSOR TA-YOU WU
ON THE OCCASION OF HIS 80TH BIRTHDAY

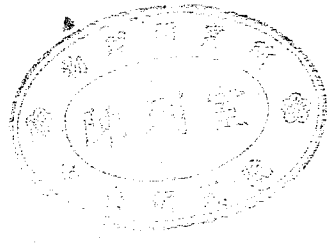

THE INSTITUTE OF PHYSICS, ACADEMIA SINICA
TAIPEI, TAIWAN, REPUBLIC OF CHINA

中央究研院物理研究所集刊

發 行 人 (Publisher)
林 爾 康 (E. K. Lin)

執行編輯 (Executive Editor)
黃 榮 鑑 (R. R. Hwang)

The Annual Report is published annually by the Institute of Physics, Acadmia Sinica, Taipei Taiwan, 115, Republic of China.

PREFACE

It is with great enthusiasm and pleasure that colleagues of the Institute of Physics of Academia Sinica have decided to honor their long-time academic advisor and former director of this Institute, Professor Ta-You Wu, on the occasion of his eightieth birthday with the articles published in this issue of the Annual Report of the Institute of Physics, Academia Sinica.

Professor Wu began his teaching of physics at Peking University, after his return to China from Ann Arbor, Michigan, where he received his Ph. D. at University of Michigan in 1933. Between 1946 and 1978, he taught and engaged in research abroad at the University of Michigan, Columbia University, Polytechnic Institute of Brooklyn, and Princeton Institute of Advanced Studies, and headed the Theoretical Physics Division of the National Research Council of Canada (1949-63) and the Department of Physics and Astronomy of the State University of New York at Buffalo (1966-69).

In the five decades that have passed since Professor Wu wrote his dissertation, he has published about 120 scientific papers. He is also the author of 13 monographs and books. It is not easy to summarize his contributions, since they encompass such a great variety of subjects, covering the fields of atomic physics, molecular physics, nuclear structure, scattering theory, plasmas and gases, satistical physics, astro-and atmospheric physics, relativity theory and many other fields. His first book, Vibrational Spectra and Structure of Polyatomic Molecules, Prentice Hall (1939); 2nd Ed. Edward Bros. (1945), has been one of the earliest and best reading book on the subject. Another book "Quantum Theory of Scattering" (co-author, T. Ohmura), Prentice Hall (1962), well known to the physicists in the western world, was translated into Russian in 1968. In recent years, he was devoted to writing books in Chinese for university students here in Taiwan, ROC. A series of books on theoretical physics have been published (7 volumes, Lien-Kiang Publ.) since 1977.

Professor Wu has made tremendous contribution to the invigoration of science education and development in Taiwan, ROC. He was appointed Director of the Institute of Physics of Academia Sinica in 1962, which led to the reinauguration of this Institute here in Taiwan. He has organized the Committee for Long-Range Development of Science and served as Chairman of the Committee for Science Development, National Security Council for many years. From 1967 to 1973 he concurrently chaired the National Science Council. His wealth of thought and

leadership in science development have earned him highest admiration of this country. Among the many honors and awards that Professor Wu has received in the past years, the recent one is the 1984 Ramon Magsaysay Award in the Philippine in recognition of "his contribution in designing this country moving toward the fore-front of science in education and practice."

At present, Professor Wu is the President of Academia Sinica. We sincerely hope that we shall be able continuing to work with him for many years to come. His eightieth birthday gives us an opportunity to express our warmest thanks to him for all that we have learned from him.

Finally, we wish to express our sincere thanks to contributors from abroad for their generous support to the publication of this Issue.

September 1986

E. K. Lin

中央研究院物理研究所集刊

第十六卷

中央研究院物理研究所印行

CONTENTS 目 錄

HIGH INTENSITY LASER INTERACTIONS WITH MICROMETER SIZE DYE DROPLETS

Wen-Feng Hsien, Huey-Ming Tzeng, and Richard K. Chang*

Yale University
Section of Applied Physics and Center for Laser Diagnostics
New Haven, Connecticut 06520, USA

Abstract

In this paper, we will review the emission characteristics of a single ethanol droplet containing Rhodamine 590 dye when the incident laser intensity is greatly increased above the threshold for lasing and SRS. The nonlinear optical mechanisms which occur when high incident intensity is directed on the dye droplets will also be discussed.

Introduction

When the radius (a) of a liquid droplet is larger than the incident laser wavelength (λ_i), the spherical liquid air interface significantly alters the intensity distribution of the incident plane wave illuminating the droplet. The intensity distribution inside the droplet is concentrated primarily in an area within the exit face of the droplet, to a lesser extent in an area within the entrance face. When either a or λ_i is tuned to a morphology-dependent resonance (MDR), the intensities in these two areas as well as in a shell within the interface are further enhanced. whether or not the input MDR condition is reached, the effect of the interface is to increase the internal intensity, i.e., to enhance the pumping for stimulated processes such as lasing and stimulated Raman scattering (SRS).

The emission characteristics of diploes radiating at a shifted wavelength (λ_s) are also greatly influenced by the droplet interface. The effect of the interface on the induced dipole within the droplet is to trap the fluorescence or Raman radiation at specific wavelengths which correspond to MDR's. Since the linewidth of the fluorescence or spontaneous Raman emission from molecules within the droplet is generally broader than the wavelength separations between the MDR's, some

*Present address: IBM Almaden Research center, san Jose, California 95120, USA.

Special Issue of Annual Report of the Institute of Physics, Academia Sinica, Vol. 16, 1986
In Honor of Prof. Ta-You Wu on the Occasion of his 80th Birthday

portions of the broad inelastic radiation are bound to satisfy numerous conditions for MDR's. At these wavelengths within the line-widths of the inelastic radiation, the droplet interface serves as an optical cavity with specific Q-factors.

The Q-factor associated with each MDR is dependent on the mode number and mode order. The density of MDR's has recently been calculated[3]. Specifically, for a droplet $\sim$ 50 μm in radius and wavelengths in the visible range, numerous MRD's with different Q-factors[3] can theoretically exist within a $10cm^{-1}$ interval. Threshold conditions for stimulated emission, such as lasing or SRS, can be reached whenever the gain within the droplet (provided by the incident radiation at several concentrated areas within the droplet) exceeds the absorption losses within or leakage from the droplet. Wavelengths corresponding to MDR's with the highest Q-factor will undoubtedly reach threshold condition first since, for these modes, the radiation leakage is less than for modes with lower Q-factors, analogous to a laser cavity consisting of external mirrors with different amounts of reflectivity.

In this paper, we will review the emission characteristics of a single ethanol droplet containing Rhodamine 590 dye when the incident laser intensity is greatly increased above the threshold for lasing and SRS. This topic is of particular interest to experimentalists who wish to use lasing droplets as bright tracers or markers which emit at wavelengths different from the incident wavelength. The nonlinear optical mechanisms which occur when high incident intensity is directed on the dye droplets will also be discussed.

Experimental Apparatus

The incident radiation is provided by the second harmonic (λ_i = 532 nm) of a Q-switched Nd: YAG laser (pulse duration $\sim$15 ns), and the highly monodispersed droplets are produced in a linear stream by a Berglund-Liu vibrating orifice generator The incident beam is aligned at 90° relative to the vertically flowing droplets, while the lasing radiation from the droplets is collected by lenses placed at 90° relative to both the incident beam and the droplet flow direction. The collection optics magnify and rotate by 90° (via a dove prism) the image of the droplet onto the slit of a spectrograph, which has a two-dimensional vidicon camera (SIT) placed at the exit plane. This combination of a spectrograph and a vidicon camera [commonly referred to as an optical multichannel analyzer (OMA)] permits spectral dispersion from numerous sample volumes along one dimension. Consequently, it is possible to detect simultaneously the emission spectra from regions in front of the illuminated face of the droplet, encompassing it, and behind the shadow face of it. Should

plumes be ejected from the droplet as a result of the intense laser pumping, the OMA can detect the emission spectra within the plumes (either in front of or behind the droplet) and from resolved portions encompassing the droplet. No time resolution was attempted with the present OMA system, since to date we have not electronically gated the vidicon.

Experimental Results

At incident intensities near the threshold for droplet lasing, the emission spectra consist of peaks separated by nearly equally spaced wavelengths, corresponding to a series of MDR'S with the same mode or derbut with different mode number.[4,5] Lasing with Rhodamine 590 in ethanol droplets[4] has been observed with cw pumping from an argon laser at input intensities as low as 500 mW/cm^2. The entire lasing spectrum, consisting of discrete peaks, is relatively narrow and is centered at the longer wave-length side of the dye fluorescence maximum in order to avoid the tail of the dye absorption.

Lasing has also been observed with the second-harmonic output of a Q-switched Nd: YAG laser at intensities in the 1-100 MW/cm^2 range.[4,5] The entrie lasing spectrum is considerably broader and shifted to shorter wavelengths than observed with cw pumping. Such observations are consitient with the fact that the gain provided by the Q-switched pulse is considerably greater than that observed with the cw pump. The threshold condition can therefore be reached, even in a shorted wave-length region which experiences more dye absorption. However, under bigher intensity pumping, the lasing spectra usually consist of several sets of peaks separated by nearly equally spaced wavelengths, implying that several mode orders (each with its series of different mode numbers) are providing sufficient optical feedback for the droplet to achieve or exceed the lasing threshold.

As the pumping intensities progressively increase beyond 100 MW/cm^2, the lasing spectra become broad and are nearly devoid of distinct peaks associated with MRD'S. The observed broad lasing profile is consistent with the fact that the lasing peaks with the high Q-factor MDR peaks have saturated while those with lower Q-factor MDR peaks have achieved the lasing threshold.[6] With high pumping intensities, the numerous lasing peaks associated with MRD's of different mode orders and mode numbers are no longer spectrally resolvable and the broad profile consequently results. Power broadening of each lasing peak can also result because of the intensity-dependent index of refraction of the host liquid,[7] i. e., the lasing intensity inside the droplet induces a time-dependent phase change as the laser radiation circumvents within the droplet interface.

At input intensities above 500 MW/cm^2, the high intensity regions within the droplet at λ_i ands the feedback provided by the MDR's (within the Raman linewidth) can cause SRS. The SRS of the host liquid can deplete the input pump radiation and thus compete with the lasing process. The advantage of using water as the solvent has been reported,[5] i. e., the SRS threshold of ethanol is much lower than that of water. However, at high dye concentration (e. g., Rhodamine 590 at 2.5 x 10^{-3} M). the dye absorption at the SRS wavelength (e. g., at $\sim$630 nm for ethanol) is large enough to suppress SRS which is pumped by the 532 nm incident beam.[6]

Figure 1 shows the spatially resolved spectra at several different wavelength segments with input intensities in the 6 GW/cm^2 range. The spatial resolution is determined by the magnification of the collèction optics which image (with 90° rotation) the regions in front of the droplet, encompassing it, and behind it onto the vertical slit of the spectrograph. The latter preserves the spatial integrity of this image on the vidicon camera at the exit plane of the spectrograph. The wavelength segment is dictated by the linear dispersion of the spectrograph and the diameter of the vidicon detector.

Figure 1(a) shows the broad lasing, fluorescence, and continuum profiles emerging from ethanol droplets contatining 2.5 x 10^{-4} M Rhodamine 590. The lasing profile is devoid of discrete peaks at 6 GW/cm^2. Note that in Fig. 1(a) the lasing, fluorescence, and continuum spectra within the droplets ($\sim$70 μm in diameter) are spatially resolved into four OMA tracks. The fluorescence and a continuum appear to emerge from an area behind the illuminated side of the droplet (spatially resikved bt tge OMA into ten tracks), implying a backward plume at least 175 μm long. No fluorescence or continuum radiation is apparent in front of the shadow side of the droplet, i. e., no forward plume exists.

Figure 1(b) shows the spatially resolved spectra at a longer wavelength segment. The broad lasing spectra merge into the SRS emission of ethanol. The wavelength of this SRS peak corresponds to the C-H stretching mode of ethanol (2932 cm^{-1}) pumped by the 532 nm incident laser beam. Both the SRS emission and the lasing emission are spatially confined within the droplet, which is resolved by the OMA into four tracks (corresponding to $\sim$70 μm in diameter). However, both the continuum emission and the discrete emission behind the illuminated side of the droplet are clearly resolved by the ten OMA tracks (corresponding to a backward plume at least 175 μm long). The discrete emission (at 656 nm) corresponds to the H_a line of atomic hydrogen.[8] The continuum emission is recombination radiation associated with the laser-produced plasmas which were transported from the droplet

to the region behind the illuminated face.[8]

At an even longer wavelength segment, broad asymmetrical profiles and a continuum are evident [see Fig. 1(c)] and are noted to be confined within the four resolved OMA tracks associated with the droplet. The asymmetrical profiles correspond to the Raman active C-H stretching mode of ethanol which is optically pumped by the lasing radiation trapped within the droplet. Thus, SRS can be generated not only by the input pump beam at 532 nm but also by the internal lasing radiation of Rhodamine 590 which was initially pumped by the 532 input radiation. The SRS emission pumped from the broad lasing emission is expected to be much broader than that pumped by the monochromatic input radiation. Again note, in Fig. 1(c), that the continuum emission is clearly resolved by ten OMA tracks, implying a plume $\sim$ 175 μm long behind the illuminated side of the droplet. Also note that this continuum increases toward shorter wavelengths. No emission was detected in the region in front of the shadow side of the droplet.

In a shorter wavelength segment [see Fig. 1(d)], no emission was detected from OMA tracks corresponding to the region in front of the shadow side of the droplet. However, a continuum emission was observable in four and ten OMA tracks corresponding to regions encompassing the droplet and behind the illuminated face, respectively. This continuum appears to continue to rise toward even shorter wavelengths, indicating that the continuum maximum must occur at even shorter wavelengths than can be detected by the OMA. The discrete peaks which are superimon the continuum spectrum have been identified as atomic emission[8] from singly lonized nitrogen [N(II) at 500.5nm], singly ionized oxygen [0(II) at 470 nm] and the H_β line at 486 nm.

The various sources of emission in the plume behind the illuminated face of the droplet need to be investigated further.[8] The transformation of neutral liquid to hot plasma involves the following stages:[9] (1) the creation of free electrons via multiphoton absorption; (2) the growth of the number of electrons via cascade collisonal processes; (3) the development of a plasma accompanied by shock wave generation and its propagation in the surrounding air; and (4) the extinction of the plasma via recombination radiation, attachments, and conduction of thermal energy to the surrounding gas.

The fluorescence appearing in the region behind the illuminated side of the droplet [see Fig. 1(a)] is most likely from the vapor containing dye or from the aerosol plume which is optically excited by the continuum radiation (known to persist for 100 ns). Optical excitation of the vapor containing dye or of the aerosol plume by the incident laser beam is also possible but less likely as it lasts for only

30 ns. The continuum radiation, which was observed in regions within and behind the illuminated face, is associated with recombination and radiative energy losses of electrons, ionized atoms, and molecules which were created initially by the high intensity beam within the droplet (via multiphoton absorption and cascade collisional ionization processes) and subsequently transported outward into the backward plume.

The presence of the neutral H_α and H_β peaks [see Figs. 1(b) and 1(d) and the ionized N(II) and 0(II) peaks [see Fig. 1(d)] clearly indicates that multiphoton absorption and ionization have taken place. The excited atomic hydrogen emission (H_α and H_β) is from the laser-induced decomposition of ethanol liquid. It is likely that the multiphoton absorption leading to molecular decomposition first took place within the ethanol droplet and that a subsequent shock wave transported these excited H atoms outward into the backward plume. The N(II) and O(II) emission is from the laser-induced breakdown of N_2 and O_2 from the surrounding air. The optical excitaion of N(II) and O(II) is most likely from cascade collisional ionization by the electrons which were transported from the droplet via a shock w wave. The existence of a shock wave is consistent with an acoustic "snap" accompanying the detection of the continuum within a droplet and in the plume behind the illuminated side.

Conclusions

For input intensities near the lasing threshold of dyed droplets with $a \geqslant \lambda_i$, the lasing spectrum consists of a set of distinct peaks which are nearly equally spaced in wavelength and can be assigned to MDR's of a given mode order but with diggerent mode numbers with high Q-factors. As the input intensity exceeds the lasing threshold, the original set of peaks saturates and a different set (or sets) of distinct peaks appears in the lasing spectrum, consistent with the fact that MDR's with lower Q-factors (belonging to different mode orders and mode numbers) can also achieve threshold. The density of the lasing peaks continues to grow as the input intensity is raised and the peaks eventually merge. Power broadening of each lasing peak is also possible and can contribute to the coalescing of the numerous lasing peaks into one broad featureless profile. At input powers beyond - 500 MW/cm^2, the input intensity is sufficient to cause SRS of the host liquid which, like lasing, also has a remarkably low threshold. This is because of the enhancement of the incident intensities at specific locations within the droplet and because of the optical feedback provided by the MDR's at various wavelengths within the spontaneous Raman profile. Because of the dye absorption at the SRS wavelength, the SRS

threshold is higher than that of liquid without dye. At still higher incident intensities even the internal lasing intensity is sufficient to pump SRS of the host liquid.

Finally, at input intensities in the 6 GW/cm^2 range, a continuum radiation is produced within the droplet as well as in a backward plume (several droplet diameters in length) behind the illuminated face of the droplet. The continuum radiation caused by the recombination and radiative energy losses of electrons, ionized atoms, and excited state molecules is thought to be produced initially by multiphoton absorption and cascade collisional ionization within the droplet. Discrete atomic emission peaks of H_α, H_β, O(II), and N(II), associated with laser-induced decomposition of ethanol [for H_α, H_β, and O(II)] and air [for N(II) and O(II)], are noted to be superimposed on the continuum spectrum. The electrons, ionized atoms, and excited state molecules in the backward plume are initiated within the droplet and are then transported from the droplet toward the direction of the laser beam (e. g., by a shock wave or an optically driven detonation wave), facilitating the subsequent air breakdown behind the illuminated side of the droplet.

Acknowledgments

Studies on tne interactions of an intense laser beam in the visible and UV range with micrometer-size liquid droplets containing fluorescent dye molecules require detailed knowlegde of electrodynamics, nonlinear optics, fluid mechanics, plasma physics, and atomic spectroscopy. These are all areas to which Professor Ta-You Wu has contributed significantly and profoundly in his research, taught with inspiration to his countless students, and supported vigorously through the National Science Council of the Republic of China. We dedicate this article to him in celebration of his 80th birthday with the realization that the science discussed in this paper would have been much richer had we had the pleasure of discussing our results with him beforehand.

We thank Boa-Teh Chu, Johannes Eickmans, and Carol Wood for several helpful discussions and gratefully acknowledge the partial support of this work by the Air Force Office of Scientific Research (Contract No. F49620-85-K-0002) and the National Science Foundation (Grant No. CBT-8401441).

References

1. J. F. Owen, R. K. Chang, and P. W. Barber, Opt. Lett. 6, 540 (1981).
2. P. Chylek, J. D. Pendleton, and R. G. Pinnick, Apple. Opt. 24, 3941 (1985).
3. S. C. Hill and R. E. Benner, "Morphology-Dependent Resonances Associated

with Stimulated Processes in Microspheres," to be published in J. Opt. Soc. Am. B.

4. H. –M. Tzeng, K. F. Wall, M. B. Long, and R. K. Chang, Opt. Lett. 9, 499 (1984).
5. H. –B. Lin, A. L. Huston, B. L. Justus, and A. J. Campillo, "Some Characteristics of a Droplet Whispering Gallery Mode Laser," to be published in Opt. Lett.
6. W. –F. Hsieh, C. F. Wood, and R. K. Chang, "Emission Spectra of Lasing Droplets under High Intensity Pumping," submitted to Opt. Lett.
7. S. –X. Qian and R. K. Chang, Opt. Lett. Lett. 11, 371(1986).
8. J. H. Eickmans, W. –F. Hsieh, and R. K. Chang, "Laser-Induced Explosion of H_2O Droplets: Spatially Resolved Spectra," submitted to Opt. Lett.
9. C. G. Morgan, Rep. Prog. Phys. 38, 621(1975).

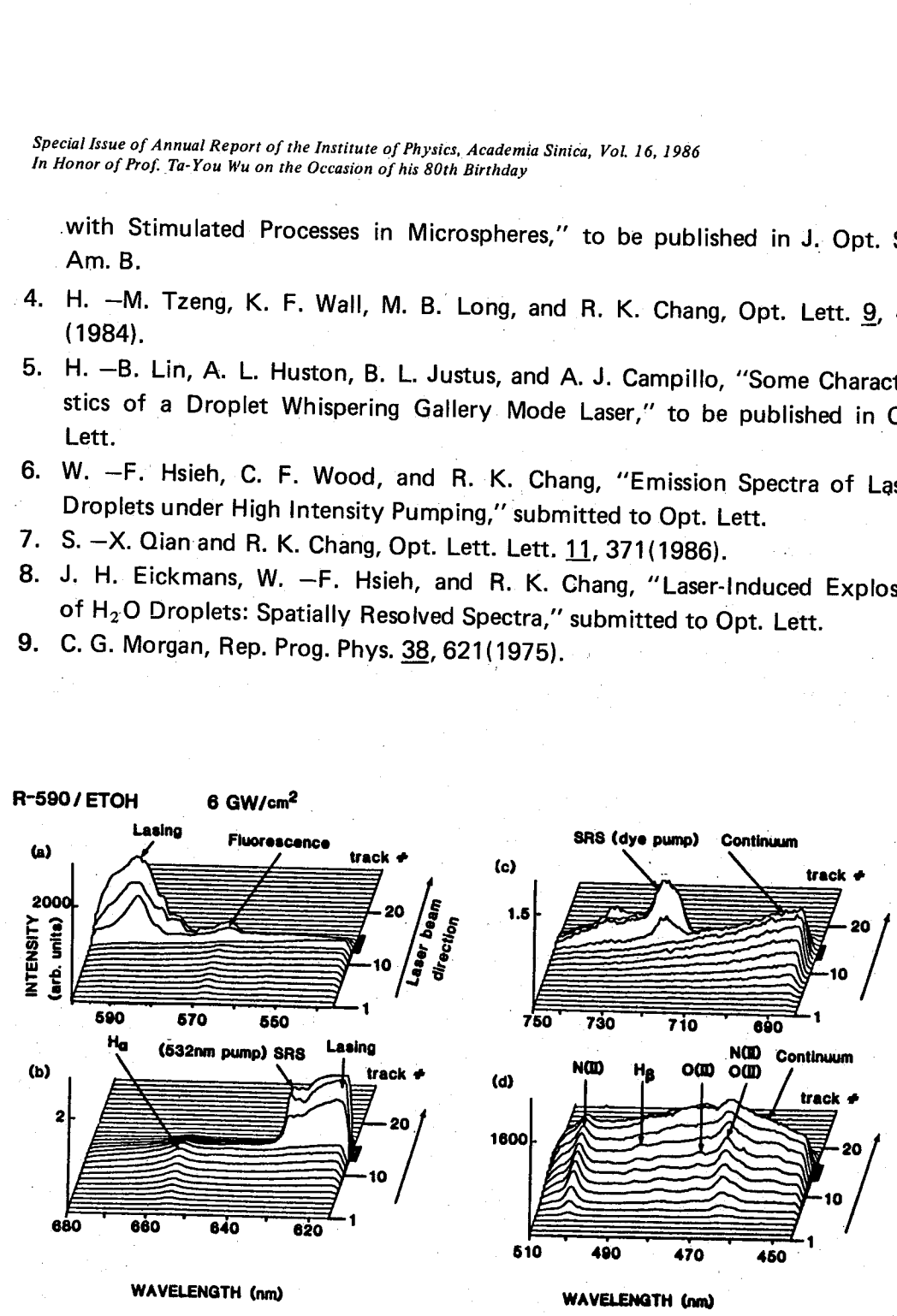

Fig. 1

CURIE TEMPERATURE OF A SEMI-INFINITE HEISENBERG FERROMAGNET

D. L. Lin

Department of Physics and Astronomy
State University of New York at Buffalo
Amherst, New York 14260

Abstract

The technique of equations of motion for the retarded Green's function is employed to investigate the transition temperature of a semi-infinite Heisenberg ferromagnet. It is shown that at temperatures higher than the bulk transition temperature, quasi-two-dimensional long range order can occur near the surface when the surface anisotropy energy is taken into account. Assuming a simple cubic lattice structure with S = 1, relations between the microscopic parameters and between the surface transition temperature and these parameters are investigated.

I. Introduction

Surface effects on the magnetic phase transition has been of much interest in recent years. It was first discovered by Mills[1], on the Landau theory of mean field, that when the ratio between the surface exchange energy J_s and the bulk exchange J_b is greater than certain critical value or when $\Delta = J_s/J_b > \Delta_c$, the surface orders before the bulk does. More reliable methods such as scaling method based on cluster model, high temperature series expansion and mean field approximation of Ising model, Monte Carlo calculation of classical Heisenberg model and spherical model, were employed by Binder and Hohenberg[2] and others[3-8] to study this problem. Qualitatively they all agree and quantitatively Δ_c may differ only in numerical value. Thus it has been established within the framework of either mean field theory or Ising model that magnetization can occur near the surface even at a temperature higher than the bulk transition temperature $T_c^{(b)}$.

There exist in the literature considerable amount of work about the properties of Heisenberg ferromagnet near the transition temperature. However, relatively

few are concerned with the surface effect on physical properties of the magnet, especially near the transition temperature. Binder and Hohenberg[2] discussed the surface magnetization of a Heisenberg magnet by mears of Monte Carlo method. More recently, Cottam and Kontos have investigated Heisenberg magnet in semi-infinite and slab geometry[9-12]. Their method, however can not be applied to discuss properties near the transition temperature.

Heisenberg model distinguishes itself from the Landau mean field theory and Ising model in that the two-dimensional Heisenberg ferromagnet does not possess long range order at finite temperature as has been proved rigorously by Mermin and Wagner[13]. They also show that it is the long range fluctuation that suppresses the formation of ordered phase. On the other hand, the exact solution of a two-dimensional Ising model[14] shows that it can have long range order at finite temperature. That the existence of long range order at finite temperature in the two-dimensional Landau theory is obvious.

It has been demonstrated that[15] with isotropic interaction of Heisenberg type, a ferromagnetic slab of finite thickness can not have phase transition. They have also shown that by introducing a term of surface anisotropy in the interaction, finite transition temperature results for any finite thickness. We attempt, in this paper, to investigate the surface magnetization of a semi-infinite Heisenberg ferromagnet. Using the technique of equation of motion for the retarded Green's function[16], we find that there exists quasi-two-dimensional long range order near the surface at temperatures higher than the bulk transition temperature $T_c^{(b)}$ as long as the ratio $\Delta = J_s/J_b > \Delta_c$ of course, the value of Δ_c can not be the same as any of those found in different models. The dependence of the transition temperature for such guasi-two-dimensional long range order on the microscopic parameter is investigated.

II. Equations of motion

Consider a semi-infinite Heisenberg ferromagnet with simple cubic lattice structure of lattice constant a. Assuming nearest neighbor interaction, we write the Hamiltonian

$$H = -J_s \sum_{\langle i,j\rangle}^{surf} \vec{s}_i \cdot \vec{s}_j - J_b \sum_{\langle i,j\rangle}^{\Sigma'} \vec{s}_i \cdot \vec{s}_j - D' \sum_i^{surf} (s_i^z)^2 \qquad (1)$$

where $\sum_{\langle i,j\rangle}^{surf}$ indicates that all pairs i and j to be summed are on the surface, $\sum_{\langle i,j\rangle}^{\Sigma'}$

means that at least one of the pair i and j is in the bulk and $\sum_i^{surf}$ sums over all the lattice sites on the surface. The last term in (1) is introduced to represent the surface anisotropy energy due to the fact that the magnetic ions on the surface see only axial symmetry in positive z-direction. We choose the coordinate frame such that the surface is (0, 0, 1) of the crystal and coincides with the xy-plane. In the following we shall take J_b as the unit of energy and define

$$\Delta = J_s/J_b, \qquad D = D'/J_b \qquad (2)$$

For definiteness, we limit our discussion to S = 1. There is no essential difficulty to generalize the theory to arbitrary S value.

It can be shown that the equations of motion of the retarded Greens function for the present problem are

$$E\,[g_{\vec{k}}(E)]_{mn} = \delta_{mn} + 2\langle s_m^z\rangle \alpha(\vec{k})\,[g_{\vec{k}}(E)]_{mn} - 2\langle s_m^z\rangle \Sigma_{\pm}[g_{\vec{k}}(E)]_{m\pm1,n} + 2\,\Sigma_{\pm}\langle {}^{z}_{m\pm1}\rangle [g_{\vec{k}}(E)]_{mn}, \quad m \geqslant 1 \qquad (3a)$$

$$E\,[g_{\vec{k}}(E)]_{On} = \delta_{On} + 2\langle S_o\rangle \Delta\alpha(k)\,[g_{\vec{k}}(E)]_{On} - 2\langle S_o^z\rangle [g_{\vec{k}}(E)]_{1n} + 2\langle S_l^z\rangle [g_{\vec{k}}(E)]_{On} + D\langle S_o^z\rangle [g_{\vec{k}}(E)]_{On} \qquad (3b)$$

where the indices m and n label the magnetic ion layer of the crystal, and we have set m = 0 for the surface layer. The function $\alpha(\vec{k})$ is defined by

$$\alpha(\vec{k}) = z_2\,[1 - \gamma_2(\vec{k})] \qquad (4a)$$

with the coordination number $z_2 = 4$ and

$$\gamma_2(\vec{k}) = \frac{1}{2}\,(\cos k_x a + \cos k_y a). \qquad (4b)$$

For convenience, we can rewrite the mean value $\langle S_m{}^z \rangle$ as

$$\langle S_m{}^z \rangle = S_b + \sigma_m \tag{4c}$$

where S_b stands for the bulk value, namely, $\langle S_m{}^z \rangle \xrightarrow{m\to\infty} S_b$, and σ_m represents change due to the influence of the surface. Thus, we have $\sigma_m \xrightarrow{m\to\infty} 0$. Eqs. (3) represent a set of infinite coupled equations with infinite number of variables, and can be not solved exactly. We shall develope a perturbation method through iteration to handle the problem.

Imagine that our semi-infinite system is a cleavage of an infinite pertect crystal splitted between the layers of m = 0 and m = − 1.
Since our Hamiltonian stands only for the nearest neighbor interactions, there is no more connection whatsoever between the magnetic ions on the opposite sides of the cleavage plane. In the following we shall take a to be the unit for length.

Let us introduce the system of equations

$$E\,[g_{\vec{k}}(E)]_{mn} = \delta_{mn} + 2(S_b+\sigma_m)\,\alpha(\vec{k})\,[g_{\vec{k}}(E)]_{mn} - 2(S_b+\sigma_m)\sum_{\pm}[g_{\vec{k}}(E)]_{m\pm1,n}$$
$$+2\sum_{\pm}(S_b+\sigma_{m\pm1})\,[g_{\vec{k}}(E)]_{mn},\quad m\geqslant 1 \tag{5a}$$

$$E\,[g_{\vec{k}}(E)]_{On} = \delta_{On} + 2(S_b+\sigma_o)\,\Delta\alpha(\vec{k})\,[g_{\vec{k}}(E)]_{On} - 2(S_b+\sigma_o)\,[g_{\overleftarrow{k}}(E)]_{1n}$$
$$+2(S_b+\sigma_1)\,[g_{\overleftarrow{k}}(E)]_{On} + D(S_b+\sigma_o)\,[g_{\vec{k}}(E)]_{On}$$
$$+2S_b\alpha(k)\,[g_{\vec{k}}(E)]_{On} - 2S_b\alpha(\vec{k})\,[g_{\overleftarrow{k}}(E)]_{On}$$
$$-2S_b\,[g_{\vec{k}}(E)]_{-1,n} + 2S_b\,[g_{\vec{k}}(E)]_{On} - 2S_b\,[g_{\vec{k}}(E)] \tag{5b}$$

$$E\,[g_{\vec{k}}(E)]_{-1,n} = \delta_{-1,n} + 2S_b\alpha(\vec{k})\,[g_{\vec{k}}(E)]_{-1,n} - 2S_b\,\{[g_{\vec{k}}(E)]_{On}$$
$$+[g_{\vec{k}}(E)]_{-2,n}\} + 4S\,[g_{\vec{k}}(E)]_{-1,n} + 2S_b[g_{\vec{k}}(E)]_{On} \tag{5c}$$

$$E\,[g_{\vec{k}}(E)]_{mn} = \delta_{mn} + 2S_b\alpha(k)\,[g_{\vec{k}}(E)]_{mn} - 2S_b\sum_{\pm}[g_{\vec{k}}(E)]_{m\pm1,n}$$
$$+4S_b\,[g_{\vec{k}}(E)]_{mn} \qquad m\leqslant -2 \tag{5d}$$

where $n \geqslant 0$. It is clear that the inhomogeneous term in the last two equations vanish because $n \geqslant 0$. Consequently, $[g_{\vec{k}}(E)]_{mn} = 0$ for $m \leqslant -1$ and $n \geqslant 0$, and the first two equations of (5) become (3). Multiplying these two equations by e^{-iqm} and summing over m, we find

$$E\,[g_{\vec{k}}(E)]_{qn} = e^{-iqn} + 2S_b\,[\alpha(\vec{k}) + 2 - 2\cos q]\;[g_{\vec{k}}(E)]_{qn}$$
$$+2\alpha(\vec{k})\sum_{m=1}e^{-iqm}\,\sigma_m\,[g_{\vec{k}}(E)]_{mn} - 2\sum_{m=1}e^{-iqu}\sigma_m\,\{[g_{\vec{k}}(E)]_{m+1,n}$$
$$+[g_{\vec{k}}(E)]_{m-1,n}\} + 2\sum_{m=1}e^{-iqm}\,(\sigma_{m+1}+\sigma_{m-1})\,[g_{\vec{k}}(E)]_{mn}$$
$$+[2S_b\,(\Delta-1)\alpha(\vec{k}) + 2\sigma_o\Delta\alpha(\vec{k})]\;[g_{\vec{k}}(E)]_{On}$$
$$-2\sigma_o[g_{\vec{k}}(E)]_{1n} + 2\sigma_1\,[g_{\vec{k}}(E)]_{On} + D(S_b+\sigma_o)\,[g_{\vec{k}}(E)]_{On}$$
$$-2S_b\,[g_{\vec{k}}(E)]_{On} + 2S_b\,e^{iq}\,[g_{\vec{k}}(E)]_{On} \tag{6a}$$

$$[g_{\vec{k}}(E)]_{qn} = \sum_{m=-\infty}^{\infty}e^{-iqm}\,[g_{\vec{k}}(E)]_{mn} \tag{6b}$$

In Eq. (6a) we first move the second term to the left hand side, divide the equation by $E - 2S_b\,[\alpha(\vec{k}) + 2 - 2\cos q]$, then multiply it by $e^{iq\ell}$, and sum over q. The result is

$$[g_{\vec{k}}(E)]_{\ell n} = [g^b_{\vec{k}}(E)]_{\ell n} + [2S_b\,(\Delta-1)\alpha(\vec{k}) - 2S_b + D\,S_b]$$
$$[g^b_{\vec{k}}(E)]_{\ell n}\,[g_{\vec{k}}(E)]_{On} + 2S_b\,[g^b_{\vec{k}}(E)]_{\ell+1,n}\,[g_{\vec{k}}(E)]_{On}$$
$$+[2\sigma_o\Delta\alpha(\vec{k}) + 2\sigma_1$$
$$+D\sigma_o]\;[g^b_{\vec{k}}(E)]_{\ell o}\,[g_{\vec{k}}(E)]_{On} - 2\sigma_o[g^b_{\vec{k}}(E)]_{\ell o}\,[g_{\vec{k}}(E)]_{1n}$$
$$+2\alpha(\vec{k})\sum_{m=1}[g^b_{\vec{k}}(E)]_{\ell m}\,\sigma_m\,[g_{\vec{k}}(E)]_{mn}$$
$$-2\sum_{m=1}[g^b_{\vec{k}}(E)]_{\ell m}\,\sigma_m\,\{[g_{\vec{k}}(E)]_{m+1,n} + [g_{\vec{k}}(E)]_{m-1,n}\}$$
$$+2\sum_{m=1}[g^b_{\vec{k}}(E)]_{\ell m}\,[\sigma_{m+1}+\sigma_{m-1}]\;[g_{\vec{k}}(E)]_{mn} \tag{7a}$$

$$[g^{b}_{\vec{k}}(E)]_{\ell n} = \frac{1}{N_z} \sum_{q} \{ e^{iq(\ell-n)} / [E - 2S_b(\alpha(\vec{k}) + 2 - 2\cos q)] \} \tag{7b}$$

We shall solve (7a) by means of the iteration procedure. The idea is that the change in magnetization σ_m ($m \geqslant 0$) due to the introduction of the cleavage plane is a small quantity as compared to S_b. Hence we can neglect σ_m in the zeroth order approximation for all $m \geqslant 0$. Thus (7a) becomes

$$[g^{(0)}_{\vec{k}}(E)]_{mn} = [g^{b}_{\vec{k}}(E)]_{mn} + 2S_b [g^{b}_{\vec{k}}(E)]_{m+1} [g^{(0)}_{\vec{k}}(E)]_{On} + [2S_b(\Delta-1)\alpha(\vec{k}) - 2S_b + DS_b] [g^{b}_{\vec{k}}(E)]_{m} [g^{(0)}_{\vec{k}}(E)]_{On} \tag{8}$$

which yields the solution

$$[g^{(0)}_{\vec{k}}(E)]_{mn} = \frac{[g^{b}_{\vec{k}}(E)]_{mn} + \{2S_b [g^{b}_{\vec{k}}(E)]_{m+1} + [2S_b(\Delta-1)\alpha(\vec{k}) - 2S_b + DS_b] [g^{b}_{\vec{k}}(E)]_{m}\} [g^{b}_{\vec{k}}(E)]_{o}}{1 - 2S_b [g^{b}_{\vec{k}}(E)]_{1} - [2S_b(\Delta-1)\alpha(\vec{k}) - 2S_b + DS_b] [g^{b}_{\vec{k}}(E)]_{o}} \tag{9}$$

The first order correction $\sigma^{(1)}_m$ can be found[15] from the fluctuation-dissipation theorem, that is,

$$\sigma^{(1)}_m = \langle S^z_m \rangle - S_b = \{ (1 + 2\phi^{(0)}_m) / [1 + 3\phi^{(0)}_m + 3(\phi^{(0)}_m)^2] \} - S_b \tag{10}$$

where

$$\phi^{(0)}_m = i \int_{-\infty}^{\infty} dE \frac{1}{2\pi N_{11}} \sum_{\vec{k}} [g^{(0)}_{\vec{k}}(E + i o^+)]_{mm} - g^{(0)}_{\vec{k}}(E - i o^+)_{mm} / (e^{\beta E} - 1) \tag{11}$$

The solution $[g^{(1)}_{\vec{k}}(E)]_{mn}$ corrected to the first order can be obtained bu substituting (10) and (11) in (7a). The procedure, in principle, can be applied repeatedly to any order of accuracy. In practice, however, it depends on how complex one is willing

to handle in the actual calcualtion.

what is more interesting to us is that we can find S_b in the above iteration procedure. It is seen from $S_b = \langle S_m{}^z \rangle - \sigma_m$ that S_b is equal to that part of $\langle S_m{}^z \rangle$ that is independent of m. Since $[g^{b}_{\vec{k}}(E)]_{mm}$ does not depend on m, as can be seen from (9), we find from (9), (10) and (11) that

$$S_b = (1 + 2\phi^{b}_m) / [1 + 3\phi^{b}_m + 3(\phi^{b}_m)^2] \tag{12}$$

where

$$\phi^{b}_m = i \int_{-\infty}^{\infty} dE \frac{1}{2\pi N_{11}} (e^{-\beta E} - 1)^{-1} \sum_{\vec{k}} \{ [g^{b}_{\vec{k}}(E + i o^+)]_{mm} - [g^{b}_{\vec{k}}(E - i o^+)_{mm} \} \tag{13}$$

It is then standard[16,18] to determine the Curie temperature for a bulk sample from (12) and (13). That is

$$T^{(b)}_c = \frac{4}{3} \{ \frac{1}{N_{11} N_z} \sum_{\vec{k},q} [1/(\alpha(\vec{k}) + 2 - \cos q)] \}^{-1} \tag{14}$$

Since $\sigma_m \to 0$ as m increases indefinitely, $\langle S_m{}^z \rangle = S_b$ for large m. This character remains unchanged in the iteration process. Because the ratio of the number of ions N_{11} in the surface layer to the total number of ions $N_{11} N_z$ is $1/N_z$ which is exceedingly small, the existence of surface does not influence the Curie temperature of a bulk sample.

It must be emphasized, however, that the above iteration is based on the assumption that σ_m / S_b is a small quantity for all $m \geqslant 0$. This is not necessarily true, especially when $T > T^{(b)}_c$, because σ_m is not necessarily zero for $m \geqslant 0$ even though $S_b = 0$ at temperatures higher than T_c. We shall discuss such cases in the following.

III. Phase transition near the surface

Under the condition that $S_b = 0$, we first define the surface magnetic phase transition temperature to be the temperature at which the surface order parameter σ_0 vanishes. Since $S_b = 0$, a vanishing σ_0 implies both $\langle S_0{}^z \rangle = 0$ and $\langle S_\infty{}^z \rangle = 0$. To our semi-infinite ferromagnet, there is no reason to expect $\langle S_m{}^z \rangle \neq 0$ for any finite m. In the neighborhood of transition temperature σ_m can again be determined by the fluctuation-dissipation theorem,

$$\sigma_m = \frac{4}{3}\{1+2\phi_m + O(\phi_m^{-1})\}^{-1} \tag{15}$$

$$\phi_m = i\int_{-\infty}^{\infty} dE \frac{1}{2\pi N_{11}} (e^{-\beta E}-1)^{-1} \sum_{\vec{k}} \{[g_{\vec{k}}(E+i\,o^+)]_{mn} - [g_{\vec{k}}(E-i\,o^+)]_{mn}\} \tag{16}$$

The equations of motion (3), when $S_b = 0$, become

$$E(g_{\vec{k}}(E)]_{mn} = \delta_{mn} + 2\sigma_m \alpha(\vec{k})\,[g_{\vec{k}}(E)]_{mn} - 2\sigma_m \sum_{\pm}[g_{\vec{k}}(E)]_{m\pm1,n} + 2\sum_{\pm}\sigma_{m\pm1}\,[g_{\vec{k}}(E)]_{mn} \qquad m \geqslant 1 \tag{17a}$$

$$E[g_{\vec{k}}(E)]_{On} = \delta_{On} + 2\sigma_o \Delta\alpha(\vec{k})\,[g_{\vec{k}}(E)]_{On} - 2\sigma_o[g_{\vec{k}}(E)]_{1n} + 2\sigma_1\,[g_{\vec{k}}(E)]_{On} + D\,\sigma_o[g_{\vec{k}}(E)]_{On} \tag{17b}$$

and it can be shown that[15] the solution takes the form

$$[g_{\vec{k}}(E)]_{mm} = \sum_i \delta_i^m/(E-\theta_i), \tag{18}$$

with

$$\Sigma_i \delta_i^m = 1 \tag{18a}$$

Since there are infinite number of atomic layers in an semi-infinite ferromagnet, the summation in (18) runs over infinite number of terms. Substituting (18) in (16) we find

$$\phi_m = \frac{1}{N_{11}} \Sigma_{\vec{k}} \sum_i \delta_i^m/[\exp(\beta\theta_i) - 1] \tag{19}$$

It is not difficult to see from (17) that the eigenvalues $\theta_i \to 0$ as $\sigma_m \to 0$. This implies that we can set

$$1 + 2\phi_m = \frac{1}{N_{11}} \Sigma_{\vec{k}} \Sigma_i\ \delta_i^m \coth\frac{\beta\theta_i}{2} \cong \frac{1}{N_{11}} \Sigma_{\vec{k}}\ \Sigma_i\ \delta_i^m\ \frac{2}{\beta\theta_i} \tag{20}$$

Thus, the surface Curie temperature $T_c^{(s)}$ is determined by the expression[15,16]

$$\frac{1}{\sigma_m} = \frac{3}{2}\,T_c^{(s)}\,\frac{1}{N_{11}}\Sigma_{\vec{k}}\sum_i \delta_i^m/\theta_i \tag{21}$$

The question is then to find the sum in (21). Comparing (21) with (19) we find

$$\frac{1}{N_{11}}\ \Sigma_{\vec{k}}\Sigma_i \delta_i^m/\theta_i = \frac{1}{N_{11}}\Sigma_{\vec{k}}\{-[g_{\vec{k}}(E=0)]_{mm}\} \tag{22}$$

Therefore the Curie temperature follows directly if we can solve (17). for $[g_k(E=0)]_{mn}$. In other words, we have to solve the euqations

$$2\sigma_m\alpha(\vec{k})\,[g_{\vec{k}}(O)]_{mn} - 2\sigma_m\Sigma_{\pm}[g_{\vec{k}}(O)]_{m\pm1,n} + 2\ \Sigma_{\pm}\sigma_{m\pm1}\,[g_{\vec{k}}(O)]_{mn} = -\delta_{mn}, \qquad m \geqslant 1 \tag{23a}$$

$$2\sigma_o\Delta\alpha(\vec{k})\,[g_{\vec{k}}(O)]_{On} - 2\sigma_o[g_{\vec{k}}(O)]_{1n} + 2\sigma_1\,[g_{\vec{k}}(O)]_{On} + D\sigma_o[g_{\vec{k}}(O)]_{On} = -\delta_{On} \tag{23b}$$

We look for the long range order parameter of the following form in the neighborhood of surface

$$\sigma_m = \sigma_o e^{-\gamma m}, \qquad m \geqslant 0 \tag{24}$$

where $\gamma > 0$ is a quantity to be determined. Substituting (24) in (23), we have

$$\alpha(\vec{k})\,[g_{\vec{k}}(O)]_{mn} - \Sigma\,[g_{\vec{k}}(O)]_{m\pm1,n} + 2\cosh\gamma\,[g_{\vec{k}}(O)]_{mn} = -\frac{\delta_{mn}}{2\sigma_m}, \quad m \geqslant 1 \tag{25a}$$

$$\Delta\alpha(k)\,[g_{\vec{k}}(O)]_{On} - [g_{\vec{k}}(O)_{1n} + e^{\gamma}\,[g_{\vec{k}}(O)]_{On} + \frac{D}{2}\,[g_{\vec{k}}(O)]_{On} = -\frac{\delta_{On}}{2\sigma_o}. \tag{25b}$$

This set of equations can be solved in the same fashion as that in which the solution (7a) is obtained for Eqs. (3), the result is

$$-[g_{\rightarrow}(O)]_{mm} = \frac{1}{2\sigma_m}\{f_{\vec{k}}(O) - \frac{[(\Delta-1)\alpha(\vec{k}) - e^{\gamma} + \frac{D}{2}]\,f_{\vec{k}}(O) + f_{\vec{k}}(1)}{1 + [(\Delta-1)\alpha(\vec{k}) - e^{\gamma} + \frac{D}{2}]\,f_{\vec{k}}(O) + f_{\vec{k}}(1)} f_{\vec{k}}(2m)\} \tag{26}$$

$$f_{\vec{k}}(n) = \frac{1}{N_z} \sum_q \frac{e^{iqn}}{\alpha(\vec{k}) + 2\cosh\gamma - \cos q}$$

$$= \frac{\{[\frac{1}{2}\alpha(\vec{k}) + \cosh\gamma] - [[\frac{1}{2}\alpha(\vec{k}) + \cosh\gamma]^2 - 1]^{1/2}\}^{|n|}}{2[(\frac{1}{2}\alpha(\vec{k}) + \cosh\gamma)^2 - 1]^{1/2}} \quad (27)$$

With the solution (26), the surface Curie temperature is determined by

$$1 = \frac{3}{4} T_c^{(s)} \frac{1}{N_{11}} \Sigma_{\vec{k}} \{ f_{\vec{k}}(0) - \frac{[(\Delta-1)\alpha(\vec{k}) - e^{\gamma} + \frac{D}{2}] f_{\vec{k}}(0) + f_{\vec{k}}(1)}{1 + [(\Delta-1)\alpha(\vec{k}) - e^{\gamma} + \frac{D}{2}] f_{\vec{k}}(0) + f_{\vec{k}}(1)} f_{\vec{k}}(2m) \} \quad (28)$$

Since $[\frac{1}{2}\alpha(\vec{k}) + \cosh\gamma] - \{[\frac{1}{2}\alpha(\vec{k}) + \cosh\gamma]^2 - 1\} < 1$, Eq. (27) implies that $f_{\vec{k}}(2m) \to 0$ when $m \to \infty$. But the Curie temperature $T_c^{(s)}$ must not depend on the index m, therefore we require that in (28), the second term in the parenthesis must vanish as m = 0. That is

$$\frac{1}{N_{11}} \Sigma_{\vec{k}} \frac{[(\Delta-1)\alpha(\vec{k}) - e^{\gamma} + \frac{D}{2}] f_{\vec{k}}(0) + f_{\vec{k}}(1)}{1 + [(\Delta-1)\alpha(\vec{k}) - e^{\gamma} + \frac{D}{2}] f_{\vec{k}}(0) + f_{\vec{k}}(1)} f_{\vec{k}}(0) = 0 \quad (29)$$

which can be solved for γ. The surface transition temperature $T_c^{(s)}$ is then obtained from the equation

$$1 = \frac{3}{4} T_c^{(s)} \frac{1}{N_{11}} \Sigma_{\vec{k}} f_{\vec{k}}(0) \quad (30)$$

Setting n = 0 and 1 in (27) and substituting the results in (29), we find

$$\frac{1}{N_{11}} \Sigma_{\vec{k}} \frac{(\Delta - \frac{1}{2})\alpha(\vec{k}) - \sinh\gamma + \frac{D}{2} - \{[\frac{1}{2}\alpha(\vec{k}) + \cosh\gamma]^2 - 1\}^{1/2}}{(\Delta - \frac{1}{2})\alpha(\vec{k}) - \sinh\gamma + \frac{D}{2} + \{[\frac{1}{2}\alpha(\vec{k}) + \cosh\gamma]^2 - 1\}^{1/2}}$$

$$\times \frac{1}{2\{[\frac{1}{2}\alpha(\vec{k}) + \cosh\gamma]^2 - 1\}^{1/2}}$$

$$= \frac{1}{N_{11}} \Sigma_{\vec{k}} \frac{\Delta(\Delta-1)\alpha^2(\vec{k}) - [\cosh\gamma + (2\Delta-1)\sinh\gamma - D(\Delta - \frac{1}{2})]\alpha(\vec{k}) - D\sinh\gamma + D^2/4}{(\Delta - \frac{1}{2})\alpha(\vec{k}) - \sinh\gamma + \frac{D}{2} + \{[\frac{1}{2}\alpha(\vec{k}) + \cosh\gamma]^2 - 1\}^{1/2} \{2[\frac{1}{2}\alpha(\vec{k}) + \cosh\gamma)^2 - 1]^{1/2}\}}$$

$$= 0 \quad (31)$$

Equation (31) has solution for γ only when Δ is greater than some critical value Δ_c for any given D, which is usually a small number. In other words, only if the ratio between J_s, the ion exchange interaction coefficient on the surface, and J_b, the coefficient in the bulk, is larger than Δ_c, there can exist the long range order of the form $\sigma_m = \sigma_o e^{-\gamma m}$ localized near the surface.

It may be pointed out at this point that (31) diverges if D = 0 and $\gamma > 0$. This can be seen as follows. In the small k limit, $\alpha(\vec{k}) = k^2$ and (31) can be approximately expressed in integral form as

$$\frac{1}{2\pi}\int_0^{k_c} 2\pi k dk \frac{\frac{D}{2} - 2\sinh\gamma + (\Delta - \frac{1}{2} - \frac{1}{2}\coth\gamma)k^2}{\frac{D}{2} + (\Delta - \frac{1}{2} - \frac{1}{2}\coth\gamma)k^2} \frac{1}{2\sinh\gamma + k^2\coth\gamma} \quad (32)$$

When D = 0, the first denominator of the integrand behaves like k^2. Hence the integral diverges logarithmically at the lower limit of integration. This is the well-known infrared divergence which requires $T_c = 0$ according to (28). Physically it

Special Issue of Annual Report of the Institute of Physics, Academia Sinica, Vol. 16, 1986
In Honor of Prof. Ta-You Wu on the Occasion of his 80th Birthday

means that the large scale long range fluctuation suppresses the occurance of the ordered phase, and the logarithmic infrared divergence is characteristic to the Heisenberg ferromagnet. Therefore, the quasi-two-dimensional long range order can not occur near the surface if D = 0. However, D ≠ 0 on the surface of ferromagnets of transition or rare earth elements because of the local environment.

IV. Results and discussions

We solve Eq. (31) numerically on a personal computer. We first compute the critical value Δ_c for a given D, and then find the relation between γ and Δ. For each γ value, we compute $f_{\vec{k}}(O)$ from (27) and $T_c^{(s)}$ from (30).

In Fig. 1, we plot the critical value Δ_c as a function of D, the strengh of the surface anisotropic energy. That Δ_c decreases with increasing D is easy to understand. The formation of quasi-two-dimensional long range order does not need a much stronger surface exchange force than the bulk exchange force if the surface anisotropy is large enough.

Fig. 2 shows the parameter γ as a function of Δ for two different D values, and the surface Curie temperature is plotted in Fig. 3 as a function of γ. From the relations shown in these figures, we find the dependence of the surface transition temperature $T_c^{(s)}$ on Δ. The results are given in Fig. 4. It is observed that as Δ increases, so does the transition temperature for quasi-two-dimensional long range order. This is expected physically because larger Δ means stronger surface exchange force strength and hence higher $T_c^{(s)}$.

We have shown that for a semi-infinite Heisenberg ferromagnet, there can be quasi-two-dimensional long range order near the surface even at temperatures higher than the Curie temperature $T_c^{(b)}$ of the bulk sample. The existence of such quasi-two-dimensional ordered phase may be explored by experimental techniques such as LEED. We have attempted in this paper to calculate $\langle S_m^z \rangle$ for temperatures below $T_c^{(b)}$ by means of an iteration procedure. The technique, however, does not work as the temperature approaches $T_c^{(b)}$, because σ_m can not be treated as a small quantity at $T_c^{(b)}$ as $S_b = 0$. It would be of great interest ot investigate the critical behavior of Heisenberg ferromagnets at temperatures around the critical point.

We have limited our discussions to simple cubic crystal with (0,0,1) surface. Different crystal structure or different crystal plane will certainly yield different quantitative results, but there should not be qualitiative difference.

The author wishes to express his deepest gratitude to Professor Ta-You Wu from whom he has received education as a physicist and as a person as well throughout the years. He is also indebted to Dr. H. Zheng for his generous help in the present work.

References

1. D. L. Mills, Phys. Rev. B *3,* 3887 (1971); ibid., B *8,* 4424 (1973).
2. K. Binder and P. C. Hohenberg, Phys. Rev. B *6,* 3461 (1972); ibid., B *9,* 2194 (1974).
3. T. C. Lubensky and M. H. Rubin, Phys. Rev. B *12,* 3995 (1975).
4. R. Pandit and M. Wortis, Phys. Rev. B *25,* 3226 (1982).
5. R. Lipowski and W. Speth, Phys. Rev. B *28,* 3983 (1983).
6. T. Kaneyoshi, I. Tamura and E. F. Sarmento, Phys. Rev. B 28, 6491 (1983).
7. K. Binder, in *Phase Transition and Critical Phenomena,* ed. C. Domb and J. B. Libowitz, Academic Press, New York (1983), Vol. 8.
8. K. Binder and D. P. Landau, Surf. Sci. *61,* 577 (1976).
9. M. G. Cottam, J. Phys. C *9,* 2121 (1976).
10. M. G. Cottam and D. E. Kontos, J. Phys. C *13,* 2945 (1980).
11. R. C. Moul and M. G. Cottam, J. Phys. C *16,* 1307 (1985).
12. D. E. Kontos, Phys. Stat. Sol. (b) *127,* 147 (1985).
13. N. D. Mermin and H. Wagner, Phys. Rev. Letters *17,* 1133 (1966).
14. L. Onsagar, Phys. Rev. *65,* 117 (1944).
15. H. Zheng and D. L. Lin, (unpublished).
16. R. A. Takir-Kheli, in *Phase Transitions and Critical Phenomens,* Vol. 5B, Ed. C. Domb and M. S. Green, Academic Press, New York (1976).
17. D. Kalkstein and P. Socen, Surf. Sci. *26,* 85 (1971).
18. R. Tahir-Kheli and D. ter Haar, Phys. Rev. *127,* 99 (1962).

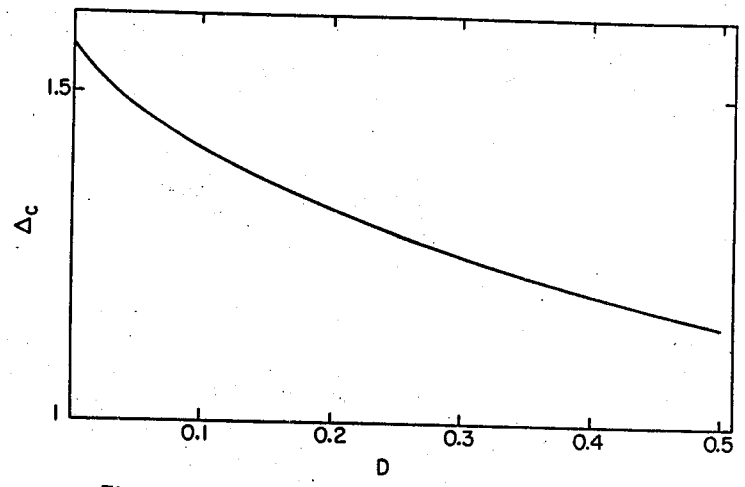

Fig. 1. The critical value Δ_c as a function of D.

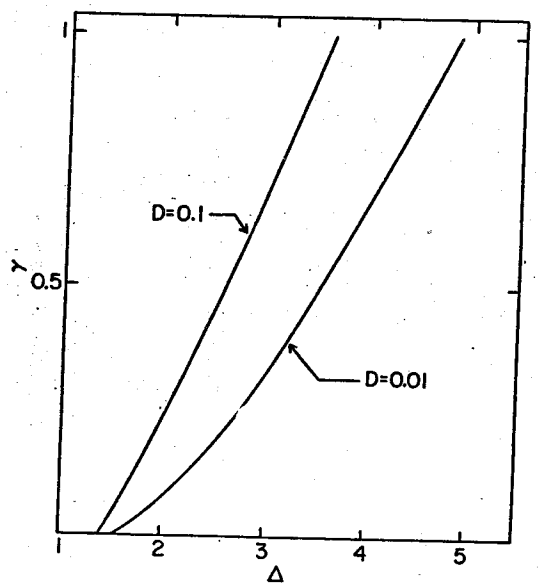

Fig. 2. The parameter γ as a function of Δ for D = 0.1 and D = 0.01.

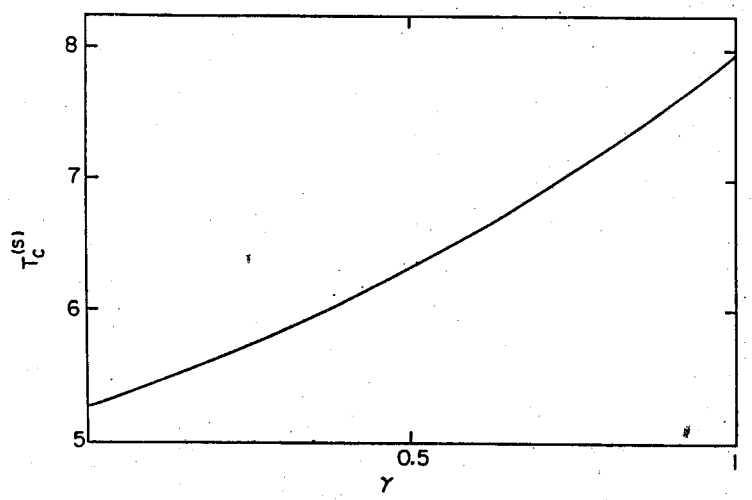

Fig. 3. The surface Curie temperature as a function of γ.

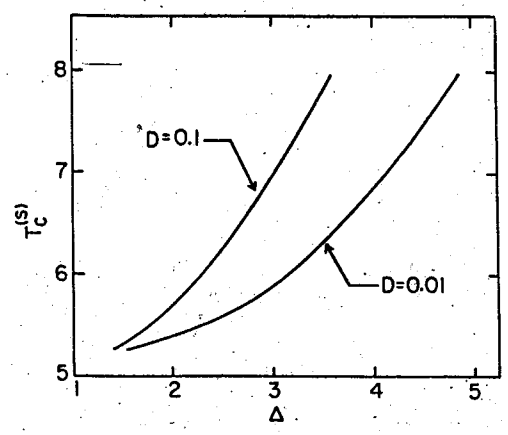

Fig. 4. The dependence of the surface transition temperature $T_c^{(s)}$ on Δ.

THERMODYNAMICS OF PARTICLE IN A BOX*

F. Y. Wu

Department of Physics
Northeastern University
Boston, Massachusetts 02115
U.S.A.

Abstract

The statistical mechanics of a quantum oscillator whose energy levels are given by the Turschner expression is exactly analyzed in the limit that the potential becomes an infinite square well. We show that the partition function in this limit is expressible in terms of a complete elliptic integral, leading to simple, closed-form expressions for the energy and the specific heat.

The quantum oscillator described by the Hamiltonian of the form

$$H = \frac{1}{2m}\left[P^2 + a^{1+\nu/2}|x|^{\nu}\right], \qquad a,\nu > 0 \tag{1}$$

has been of interest for many years.[1] Except in the case of $\nu = 2$ for which the energy spectrum and thermodynamics of the system are well-known, studies for other values of ν have always been numerical or approximate.[2] Several years ago Turschner[3] obtained an energy spectrum for the oscillator (1). While it has since been shown[4] that Turschner's result is actually a semiclassical approximation which is exact only for $\nu = 2$, the Turschner closed-form expression for the energy eigenvalues nevertheless serves as a basis for further developments. For example, it has been shown that the Turschner formula yields a lower bound to the ground energy.[5] More recently, Maris and Tsallis have computed the specific heat of the oscillator using the Turschner spectrum.[6]

In this paper we show that the thermodynamics of a system described the Turschner energy spectrum for $\nu = \infty$ can be exactly analyzed, and is given in terms

*Work supported in part by NSF Grant DMR-8219254.

of complete elliptical integrals. Since in the $\nu = \infty$ limit the Turschner energy spectrum is essentially that of a particle in a box, we thus establish a connection of the statistical mechanics of a quantum ideal gas with the mathematics of complete elliptical integrals, a curious relationship which appears to have escaped heretofore attention.[7]

In the limit of $\nu \to \infty$, the potential in (1) becomes that of an infinite square well of width $2\sqrt{a}$ and for which the Turschner's energy spectrum becomes[4]

$$E_n = (n^2 + n + \tfrac{1}{2})\,\epsilon, \qquad n = 0, 1, 2, \ldots \tag{2}$$

where

$$\epsilon = \pi^2 \hbar^2 a/8m. \tag{3}$$

Our analysis is then based on the observation that the partition function

$$Z = \sum_{n=0}^{\infty} e^{-\beta E_n} \tag{4}$$

where $\beta = 1/k_B T$, is expressible in terms of a complete elliptic integral. Indeed, the use of a standard identity[11] gives rise to the following expression for the partition function:

$$Z = e^{-\beta\epsilon/4} \sqrt{kK(k)/2\pi} \tag{5}$$

where $K(k)$ is the complete elliptic integral of the first kind whose modulus k is determined from

$$\pi K(\sqrt{1-k^2}) = \beta\epsilon K(k). \tag{6}$$

Investigation of the thermodynamic properties of the oscillator is facilitated by using the infinite-product representation of the elliptic moduli and integrals. Thus we are led to[12]

$$Z = q^{1/2} \prod_{n=1}^{\infty} \left(\frac{1-q^{4n}}{1-q^{4n-2}} \right) \tag{7}$$

where

$$q = e^{-\beta\epsilon}. \tag{8}$$

The expression (7) is rapidly converging at low temperatures. We may obtain an equivalent expression which converges rapidly at high temperatures. By using (6) to interchange roles of k and $k' = \sqrt{1-k^2}$, we obtain[13]

$$Z = e^{-\pi^2/8\lambda} \left(\frac{\lambda}{2\pi}\right)^{1/2} \prod_{n=1}^{\infty} \tanh(n\lambda) \tag{9}$$

where

$$\lambda = \pi^2 k_B T/2\epsilon. \tag{10}$$

It should be pointed out that expressions (7) and (9) are related by the well known Jacobi transformation of theta-functions:[14]

$$\sum_{n=-\infty}^{\infty} e^{-\alpha\pi n^2 + 2niz} = \frac{1}{\sqrt{\alpha}} \sum_{n=-\infty}^{\infty} e^{-(z-n\pi)^2/\alpha} \tag{11}$$

which has been "rediscovered" by other authors from time to time.[15]

It is now straightforward to compute the energy E and the specific heat C by taking the logarithmic derivatives of (7) and (9). We find

$$\frac{E}{\epsilon} = \frac{1}{2} + \sum_{n=1}^{\infty} (-1)^{n+1} \frac{n e^{-n\beta\epsilon}}{\sinh(n\beta\epsilon)}$$

$$= \frac{\lambda}{n^2} + \frac{1}{4} + \left(\frac{2\lambda}{\pi}\right)^2 \sum_{n=1}^{\infty} \frac{n}{\sinh(2n\lambda)}$$

$$= \frac{\lambda}{\pi^2} + \frac{1}{4} + \frac{4\lambda^2}{\pi^4} K(K-E) \tag{12}$$

where E is the complete elliptical integral of the second kind with modulus k, and

$$\frac{C}{K_B} = (\beta\epsilon)^2 \sum_{n=1}^{\infty} (-1)^{n+1} \left[\frac{n}{\sinh(n\beta\epsilon)} \right]^2$$

$$= \frac{1}{4} + 4 \sum_{n=1}^{\infty} \frac{n\lambda}{\sinh(2n\lambda)} [1 - n\lambda \coth(2n\lambda)] . \qquad (13)$$

These lead to the following expressions in the low and high temperature limits:

$$E \cong \frac{1}{2}\epsilon + 2\epsilon e^{-2\beta\epsilon}, \qquad T \to 0$$

$$\cong \frac{1}{2} k_B T + \frac{1}{4}\epsilon, \qquad T \to \infty \qquad (14)$$

$$C \cong k_B (2\beta\epsilon)^2 e^{-2\beta\epsilon}, \qquad T \to 0$$

$$\cong k_B \left(\frac{1}{2} - 8\lambda^2 e^{-2\lambda} \right). \qquad T \to \infty \qquad (15)$$

Expressions (12) and (13) permit numerical evaluations of the energy and specific heat to arbitrary degree of accuracy.

Finally, we remark that the exact energy levels of a particle in a box are $E_n = (n+1)^2 \epsilon$, n = 0, 1, 2, . . . The thermodynamics associated with this spectrum can also be analyzed in a similar fashion. These considerations can be extended to higher dimensions as well as to many-particle systems.[7]

I wish to thank Professor C. Tsallis for his interest in this work, and Professor M.L. Glasser for providing the last expression in (12).

References

1. F.T. Hioe and E.W. Montroll, J. Math. Phys. *16,* 1945 (1975).
2. See, e.g., R.A.T. Lima and C. Tsallis, Phys. Rev. B*2,* 458 (1980), and Refs. cited therein.
3. H. Turshner, J. Phys. A*12,* 451 (1979).
4. B.J.B. Crowley and T.F. Hill, J. Phys. A*12,* L223 (1979).
5. M.S. Ashbaugh and J.D. Morgan, J. Phys. A*14,* 809 (1981).
6. A.M. Mariz and C. Tsallis, Phys. Rev. A*29,* 2871 (1984).
7. The statistical mechanics of an ideal gas in a finite box has been studied by

Osbourne (Ref. 8), Pathria (Ref. 9) and coworkers (see, e.g., Ref; 10 and references therein) without explicitly making references to complete elliptical integrals.
8. M.F.M. Osbourne, Phys. Rev. *76,* 396 (1979).
9. R.K. Pathria, Phys. Rev. A*5,* 1451 (1972).
10. S. Singh and R.K. Pathria, Phys. Rev. A*30,* 442 (1984).
11. See, E.g., Eq. (8.197.2) in *Tables of Integrals, Series and Product,* I.S Gradshteyn and I.M. Ryzhik, Academic Press (N.Y.) 1965.
12. Use, e.g., (8.197.3) and (8.197.5), Gradshteyn and Ryzhilk, ibid.
13. Use, e.g., (8.197.4) and (8.197.6), Gradshteyn and Ryzhilk, ibid.
14. See, e.g., E.T. Whittaker and G.N. Watson, Modern Analysis (Cambridge University Press, London, 1958) p. 476.
15. See, e.g., G. Greenspoon and R.K. Pathria, Phys. Rev. A*9,* 2103 (1974), for a derivation of the case z=0 using the Poisson's summation formula.

CALCULATION OF THE EFFECTIVE COUPLING CONSTANT AT FINITE TEMPERATURE USING AN IMPROVED ONE-LOOP APPROXIMATION

Swee-Ping Chia

Physics Department, University of Malaya
59100 Kuala Lumpur, Malaysia

Abstract

The $\lambda\phi^4$ theory with negative μ^2 is analysed at $T \neq 0$ using an *improved* one-loop approximation in which each of the *bare* propagators in the one-loop diagram is replaced by a *dressed* propagator to take into account of the higher-loop effects. The mass of the dressed propagator is temperature-dependent and is determined by a self-consistency relation. It is explicitly shown that realistic physics is obtained with this improved approximation. The effective mass and the effective coupling constant are explicitly calculated and are shown to be real at temperatures both above and below the critical temperature T_c. Furthermore, the effective coupling constant is found to exhibit the striking behaviour that it approaches a nonzero constant value as $T \to \infty$, rather than droopping to zero.

I. Introduction

One-loop approximation has been widely employed at finite temperatures in the calculation of the effective potential and in the discussion of spontaneous symmetry breaking and symmetry restoration[1]. Recently, however, it has come to realise that the one-loop approximation is not adequate[2)-4)]. In a typical calculation in the one-loop approximation at high T, one usually makes expansion in inverse powers of T, with the expansion containing a T^2 term in the leading order, a linear-T term, a ℓnT term, and followed by a constant term, then a T^{-2} term, a T^{-4} term, etc[1]. The T^2 term controls the dominant behaviours, whereas the linear-T term gives the fine tuning. It is this linear-T term that makes the *simple* one-loop approximation inadequate. This is most clearly demonstrated in a system which exhinits spontaneous symmetry breaking (SSB) at T = 0, such as the $\lambda\phi^4$ theory with negative μ^2. The T^2 term, in this case, determines the critical temperature at

which the broken symmetry is restored. It also gives the dominant behaviour of the temperature dependent effective mass. But the effective potential and the effective mass also contain the linear-T term. This linear-T term always involves the linear power of μ. Since $\mu^2 < 0$, we run into imaginary quantities, and the effective potential and the effective mass are complex[2)-3)]. Worst of all, the effective coupling constant has its temperature dependence determined predominatly by this linear-T term. The effective coupling constant is thus also complex[2)-4)]. Physics therefore is not realistic when this linear-T contribution is included. Fortunately, it is also known that the same linear-T contributions in the effective mass and in the effective coupling constant are strongly modified by contributions from higher-loop diagrams[1),5)]. It is therefore hoped that by including the effects of these higher-loop contributions, the ills of the one-loop approximation can be cured.

In this paper, we shall present a scheme of calculation which we shall call, for convenience, the *improved one-loop approximation,*[2)-4)] in which the effects of higher-loop contributions are taken into account, by using dressed propagators in the one-loop diagram. The mass of the dressed propagator is temperature-dependent and is determined by a self-consistency condition.[2)-4)] Our discussions shall be confined specifically to the $\lambda\phi^4$ theory. We shall demonstrate explicitly that the linear-T term is indeed strongly modified in the improved one-loop approximation, so much so as to make this linear-T term real. The difficulties faced by the simple one-loop result are thus overcome.

In the next section, we shall review the simple one-loop approximation at $T \neq 0$, revealing its inadequacy. The improved one-loop approximation is formulated in Section III together with calculation of the temperature-dependent effective mass. The calculation of the effective coupling constant is presented in Section IV, followed by our conclusion in Section V.

II. The simple one-loop approximation

The Lagrangian for the $\lambda\phi^4$ theory is

$$\mathcal{L} = \frac{1}{2}\,\partial_\mu\phi\,\partial^\mu\phi - \frac{1}{2}\,\mu^2\phi^2 - \frac{\lambda}{4!}\,\phi^4 . \tag{1}$$

Unless otherwise stated, we shall take μ^2 to be negative so that SSB occurs at $T = 0$. In the simple one-loop approximation, the effective potential at $T \neq 0$ is easily calculated, and is given by

$$V_{\text{eff}}^{(T)} = \frac{1}{2}\,\mu^2\phi^2 + \frac{\lambda}{4!}\,\phi^4 + \frac{1}{2}\,B\phi^2 + \frac{C}{4!}\,\phi^4 + V_1^{(T)} \tag{2}$$

where ϕ here is understood to be the classical field, B and C are renormalisation costants, and $V_1^{(T)}$ is the one-loop contribution at temperature T to $V_{\text{eff}}^{(T)}$,

$$V^{(T)} = -\frac{1}{2}\,i\int_k \ell n\,(k^2 - \mu^2 - \frac{1}{2}\,\lambda\phi^2). \tag{3}$$

Here the integral sign denotes

$$\int_k = iT \sum_n \int \frac{d^3k}{(2\pi)^3} \tag{4}$$

with the summation extending over $n = 0, \pm1, \pm2, \ldots$, and the zero-component of k^μ in the integrand is to be equated with $i2\pi nT$. Renormalization is performed at $T = 0$ with the following conditions:

$$\left.\frac{\partial^2 V_{\text{eff}}^{(0)}}{\partial\phi^2}\right|_{\phi=0} = \mu^2 , \qquad \left.\frac{\partial^4 V_{\text{eff}}^{(0)}}{\partial\phi^4}\right|_{\phi=0} = \lambda . \tag{5}$$

These conditions fix the constants B and C at $T = 0$ to be

$$B = -\frac{1}{2}\,\lambda\int \frac{d^4k}{(2\pi)^4}\,\frac{i}{k^2 - \mu^2 + i\epsilon} \tag{6}$$

$$C = \frac{3}{2}\,i\lambda^2 \int \frac{d^4k}{(2\pi)^4}\,\left(\frac{i}{k^2 - \mu^2 + i\epsilon}\right)^2 . \tag{7}$$

To demonstrate the inadequacy of the simple one-loop approximation, we expand the integral in Eq. (3) in inverse powers of T. The resultant expression for $V_{\text{eff}}^{(T)}$, after renormalization, is[1)]

$$V_{eff}^{(T)} = \frac{1}{2}(\mu^2 + \frac{\lambda}{24}T^2)\phi^2 + \frac{\lambda}{4!}\phi^4 - \frac{1}{12\pi}(\mu^2 + \frac{1}{2}\lambda\phi^2)^{3/2}T + \ldots \quad (8)$$

In Eq. (8), we have displayed, for clarity, only the leading T^2 term and the trouble-causing linear-T term. First, let us retain only the T^2 term in order to determine the critical temperature at which the broken symmetry is restored. The thermal average of ϕ is given by

$$\begin{aligned} <\phi>_T^2 = v^2 &= -\frac{6\mu^2}{\lambda} - \frac{1}{4}T^2, \quad T < T_c \\ &= 0, \quad T \geqslant T_c \end{aligned} \quad (9)$$

where T_c is given by

$$T_c = (-24\mu^2/\lambda)^{1/2}. \quad (10)$$

With the value of ϕ given by Eq. (9), it is simple to see that the expression $\mu^2 + \frac{1}{2}\lambda\phi^2$ is negative for $T > (-16\mu^2/\lambda)^{1/2}$. Thus the effective potential is complex in this range of T.

We shall now demonstrate that the effective mass m_T is complex when computed up to the linear-T term. For simplicity, we shall calculate it for $T > T_c$. The temperature-dependence of m_T is given by the diagram of Fig. 1, and we obtain[1)]

$$m_T^2 = \mu^2 + \frac{\lambda}{24}T^2 - \frac{\lambda}{8\pi}T\mu, \quad (11)$$

which is complex because μ is purely imaginary. The effective coupling constant $\lambda(T)$ for $T > T_c$ is calculated from Fig. 2. In the simple one-loop approximation, it is given by[2)-4),6)]

$$\lambda(T) = \lambda - \frac{3\lambda^2}{16\pi}\left(\frac{T}{\mu} - \frac{1}{\pi}\ell n\frac{T}{\mu}\right), \quad (12)$$

which is again clearly imaginary. In Eq. (12), we have kept up to the ℓnT term for later comparison.

III. The improved one-loop approximation

We have remarked in Section I that the linear-T term in the simple one-loop approximation is strongly modified by contributions from higher-loop diagrams. To see this clearly, we consider the series of diagrams as shown in Fig. 3. These diagrams are obtained by attaching bubbles to the one-loop diagram of Fig. 1. The contributions of these diagrams to the self-energy are

$$\Sigma_T = \frac{1}{2}\lambda\bar{J}_1(\mu^2,T) - i\frac{\lambda^2}{4}\bar{J}_2(\mu^2,T)\bar{J}_1(\mu^2,T) - \frac{\lambda^3}{8}\bar{J}_3(\mu^2,T)\{\bar{J}_1(\mu^2,T)\}^2 + i\frac{\lambda}{16}\bar{J}_4(\mu^2,T)\{\bar{J}_1(\mu^2,T)\}^3 + \frac{\lambda^5}{32}\bar{J}_5(\mu^2,T)\{\bar{J}_1(\mu^2,T)\}^4 + \ldots \quad (13)$$

In Eq. (13), we have introduced the notation $\bar{J}_n(\mu^2, T)$ which is defined by

$$\bar{J}_n(\mu^2,T) = \left[\int_k - \int\frac{d^4k}{(2\pi)^4}\right]\left(\frac{i}{k^2 - \mu^2 + i\epsilon}\right)^n \quad (14)$$

It is easy to see that

$$\bar{J}_n(\mu^2,T) = \frac{i^{n-1}}{(n-1)}\left(\frac{\partial}{\partial\mu^2}\right)^{n-1}\bar{J}_1(\mu^2,T). \quad (15)$$

Making use of Eq. (15), we find that Eq. (13) becomes

$$\Sigma_T = \frac{1}{2}\lambda\bar{J}_1(\mu^2 + \frac{1}{2}\lambda J_1(\mu^2,T),T). \quad (16)$$

The integral $J_1(\mu^2, T)$ has been evaluated at high T, and it is given by

$$\bar{J}_1(\mu^2,T) = \frac{T^2}{12} - \frac{\mu T}{4\pi} + \frac{\mu^2}{8\pi^2}\ell n\frac{T}{\mu} + \ldots \quad (17)$$

Substitution of Eq. (17) into Eq. (16), we obtain the following expression for the effective mass:

$$m^2 = \mu^2 + \frac{\lambda}{24} T^2 - \frac{\lambda}{8\pi} T(\mu^2 + \frac{\lambda}{24} T^2)^{1/2} + \dots \quad . \tag{18}$$

Comparison of Eq. (18) with the one-loop result, Eq. (11), makes it clear that the linear-T term is indeed strongly modified by higher-loop contributions.

We can continue the process further by adding bubbles to the bubbles in Fig. 3, and obtain what are known as the "superdaisy" diagrams[1]. Instead of doing that, we shall describe here a self-consistent method of including higher-loop effects, which we shall refer to as the *imporved one-loop approximation*[2)-4)]. We replace each of the internal *bare* propagators in the simple one-loop approximation by the corresponding *dressed* propagator, with the mass of the dressed propagator, μ_T, determined by a self-consistency condition as depicted in Fig. 4. Summing the series in Fig. 4, we are led to the following gap equation for μ_T[1)]:

$$\mu_T^2 = \mu^2 + B + \frac{1}{2}\lambda \int_k \frac{i}{k^2 - \mu_T^2 + i\epsilon} \tag{19}$$

where B is the mass renomalization constant to be determined.

We shall now examine what renormalization conditions are needed in the *improved* one-loop approximation. The effective potential at $T \neq 0$ is given by an expression similar to Eq. (2), but with different expression for $V_1^{(T)}$. The renormalization constants will therefore be different. The improved one-loop contribution to the effective potential is

$$V_1^{(T)} = -\frac{1}{2} i \int_k \ell n\,(k^2 - \mu_T^2 - \frac{1}{2}\lambda\phi^2) \,, \tag{20}$$

where μ_T is the mass of the dressed propagator. Since μ_T is, in general, temperature-dependent, $(\partial^2/\partial\phi^2)\, V_1^{(T)}|_{\phi=0}$ will contain a divergent term that is proportional to μ_T^2. This implies the renormalization constant B has to be temperature-dependent. This is also obvious from Eq. (19). This may come as a surprise, but it is not unreasonable. We are dealing here with the summation of an infinite series of diagrams. For the $\lambda\phi^4$ theory, once the renormalization is performed at $T = 0$, no additional renormalization is required at $T \neq 0$ when calculation is carried out to any finite order in the perturbation expansion. However, when we sum over a series involving an infinite order in perturbation, there is no such guarantee. In fact, what we see here is a case where temperature-dependent renormalization is required. The renormalization conditions are chosen to be

$$B = -\frac{1}{2}\lambda \int \frac{d^4k}{(2\pi)^4} \frac{i}{k^2 - \mu_T^2 + i\epsilon} \,, \tag{21}$$

$$C = \frac{3}{2} i\lambda^2 \int \frac{d^4k}{(2\pi)^4} \left(\frac{i}{k^2 - \mu_T^2 + i\epsilon} \right)^2 . \tag{22}$$

With B as given in Eq. (21), the gap equation, Eq. (19), becomes[2)-4)]

$$\mu_T^2 = \mu^2 + \frac{\lambda}{24} T^2 - \frac{\lambda}{8\pi} T\mu_T + \frac{\lambda}{16\pi^2}\mu_T^2 \ell n \frac{T}{\mu_T} \,, \tag{23}$$

after making use of Eq. (17).

The effective potential is straightforwardly computed, and is given by[2)-3)]

$$V_{eff}^{(T)} = \frac{1}{2}(\mu^2 + \frac{\lambda}{24} T^2)\phi^2 + \frac{\lambda}{4!}\phi^4 - \frac{1}{12\pi}(\mu^2 + \frac{1}{2}\lambda\phi^2)^{3/2} T$$

$$+ \frac{1}{32\pi^2}(\lambda\mu_T^2\phi^2 + \frac{1}{4}\lambda^2\phi^4) \ell n \frac{T}{\mu_T} + \dots \quad . \tag{24}$$

The effective potential is now real because $\mu_T^2 + \frac{1}{2}\lambda\phi^2$ is positive around the solution $\phi = <\phi>_T = v$. To see this, let us compute $v = <\phi>_T$ from the following condition

$$\left. \frac{\partial V_{eff}^{(T)}}{\partial\phi} \right|_{\phi=v} = 0 \,, \tag{25}$$

which yields, using Eq. (24),[2),3)]

$$v \{ \mu^2 + \frac{\lambda}{24} T^2 + \frac{\lambda}{6} v^2 - \frac{\lambda}{8\pi}(\mu_T^2 + \frac{1}{2}\lambda v^2)^{1/2} T$$

$$+ \frac{\lambda}{16\pi^2}(\mu_T^2 + \frac{1}{2}\lambda v^2) \ell n \frac{T}{\mu_T} + \dots \} = 0 \,. \tag{26}$$

Since μ_T^2 enters Eq. (26) only in the linear-T term, it suffices for us to obtain μ_T^2 up to the leading T^2 term. From Eq. (23), we have

$$\mu_T^2 = \mu^2 + \frac{\lambda}{24} T^2 . \tag{27}$$

Eq. (26) then has a nontrivial solution for $T < T_c$, with T_c given by Eq. (10). This nontrivial solution is

$$v^2 = \frac{1}{4} (T_c^2 - T^2) + \frac{(3\lambda)^{1/2}}{8\pi} T(T_c^2 - T^2)^{1/2}, \qquad T < T_c . \tag{28}$$

For $T > T_c$, v takes on only the trivial solution

$$v = 0, \qquad T > T_c . \tag{29}$$

It is straightforward to show that $\mu_T^2 + \frac{1}{2}\lambda v^2$ is always positive for both T below and above T_c, and is zero at T_c. Thus $V_{eff}^{(T)}$ is always real.

Next, we shall calculate the effective mass, and demonstrate that it is real up to the next-to-leading linear-T term. To compute the effective mass above T_c, the self-energy diagram of Fig. 5 is considered, where the dressed propagator is used in the loop. The self-energy is given by[2),3)]

$$\Sigma_T = \frac{1}{2} \lambda \bar{J}_1 (\mu_T^2, T) . \tag{30}$$

The effective mass m_T above T_c is therefore given by[2),3)]

$$m_T^2 = \mu^2 + \frac{1}{2} \lambda \bar{J}_1 (\mu_T^2, T) . \tag{31}$$

Comparing Eq. (31) with Eq. (19), we see that m_T is equal to μ_T for $T > T_c$. Using Eq. (23), we find that

$$m_T^2 \simeq \frac{\lambda}{24} (T^2 - T_c^2) - \frac{\lambda^{3/2}}{16\sqrt{6\pi}} T(T^2 - T_c^2)^{1/2}, \quad \text{for } T - T_c \gg \frac{\lambda}{24} T_c ,$$

$$m_T \simeq \frac{2\pi}{3} (T - T_c) - \frac{32\pi^2}{9} \frac{(T-T_c)^2}{\lambda T_c} \qquad \text{for } T - T_c \ll \frac{\lambda}{24} T_c . \tag{32}$$

For the case when $T < T_c$, the computation of the effective mass is more involved. We shall first shift the ϕ field to the physical field ϕ' by[2),3)]

$$\phi = \phi' + v , \tag{33}$$

where v is as given by Eq. (28). In terms of the new field ϕ', the Lagrangian becomes

$$\mathcal{L} = \frac{1}{2} \partial_\mu \phi' \partial^\mu \phi' - v(\mu^2 + \frac{1}{6}\lambda v^2)\phi' - \frac{1}{2} (\mu^2 + \frac{1}{2} \lambda v^2)\phi'^2 - \frac{1}{6} \lambda v \phi'^3 - \frac{\lambda}{4!} \phi'^4 . \tag{34}$$

The tree-level mass-square is $\mu^2 + \frac{1}{2}\lambda v^2$. In the spirit of the improved one-loop approximation, we would replace μ^2 by μ_T^2. The mass-square to be used in the dressed propagators, for $T < T_c$, is therefore

$$m^2 = \mu_T^2 + \frac{1}{2} \lambda v^2 \tag{35}$$

Because the Lagrangian in Eq. (34) also contains a ϕ'^3 term, there is an additional self-energy diagram as shown in Fig. 6 besides that of Fig. 5. Using $\bar{m}^2$ in the dressed propagators in both Feynmann diagrams, we obtain[3)]

$$\Sigma_T = \frac{1}{2} \lambda \bar{J}_1 (\bar{m}^2, T) - \frac{1}{2} i\lambda^2 v^2 \bar{J}_2 (\bar{m}^2, T) , \tag{36}$$

where J_1 and J_2 are as defined in Eq. (14). At high T, J_1 is given by Eq. (17), and J_2 is given by

$$\bar{J}_2 (m^2, T) = -\frac{i}{8\pi} \left(\frac{T}{m} - \frac{1}{\pi} \ell n \frac{T}{m} \right) . \tag{37}$$

The effective mass of ϕ' at $T < T_c$ is therefore

$$m_T^2 = \mu^2 + \frac{1}{2}\lambda v^2 + \frac{\lambda}{24}T^2 - \frac{\lambda}{8\pi}\bar{m}T - \frac{\lambda^2}{16\pi}\frac{v^2 T}{\bar{m}} . \tag{38}$$

Putting in the expressions for v^2 and $\bar{m}$, we obtain

$$m_T^2 = \frac{\lambda}{12}(T_c^2 - T^2) + \frac{\lambda^{3/2}}{32\sqrt{3\pi}}T(T_c^2 - T^2)^{1/2} , \qquad T < T_c . \tag{39}$$

From Eqs. (32) and (39), it is obvious that the effective mass as calculated in the improved one-loop approximation is always real at all T.

IV. The effective coupling constant

The effective coupling constant at $T \neq 0$ receives a dominant contribution from the linear-T term in the high T expansion. As a consequence it is most susceptible to the higher-loop effects. We therefore expect the *improved* one-loop approximation to strongly modify the simple one-loop result for the effective coupling constant.

First let us compute the effective coupling constant $\lambda(T)$ at $T > T_c$[2)-4)]. The correction to the coupling constant in the improved one-loop approximation is from the Feynman diagram as shown in Fig. 7, where the dressed propagators have mass μ_T. The calculation is straightforward, and we obtain[2)-4)]

$$\lambda(T) = \lambda - \frac{3i}{2}\lambda^2 \bar{J}_2(\mu_T^2, T) , \qquad T > T_c . \tag{40}$$

Using Eq. (37), we find that

$$\lambda(T) = \lambda - \frac{3\lambda^2}{16\pi}\left(\frac{T}{\mu_T} - \frac{1}{\pi}\ln\frac{T}{\mu_T}\right) . \tag{41}$$

From Eq. (23), μ_T is given approximately, for T not too close to T_c, by

$$\mu_T^2 = \frac{\lambda}{24}(T^2 - T_c^2) . \tag{42}$$

We see tht as T becomes very large.

$$\frac{T^2}{\mu_T^2} \to \frac{24}{\lambda} , \tag{43}$$

which is a constant. Thus the effective coupling constant approaches a constant value as $T \to \infty$.[4)]

$$\lambda(T) \to \lambda - \frac{3\lambda^2}{16\pi}\left[\left(\frac{24}{\lambda}\right)^{1/2} + \frac{1}{2\pi}\ell n\frac{\lambda}{24}\right] . \tag{44}$$

This rather surprising asymptotic behaviour of $\lambda(T)$ was first noted by Chia and Chiang[2),3)], and was confirmed by an independent calculation employing the Dyson-Schwinger equation[7)]. When $T \to T_c$, $\mu_T \to 0$ according to[3),4)]

$$\mu_T \simeq \frac{2\pi}{3}(T - T_c) . \tag{45}$$

The effective coupling constant as given by Eq. (41) becomes indefinite. To overcome this problem, we note that Eq. (41) for $\lambda(T)$ can further by improved. Iterating the *improved* one-loop diagram of Fig. 7 yields a series of diagrams as depicted in Fig. 8.[4)] The series is easily summed (for small λ) to yield[4)]

$$\lambda(T) = \lambda\left\{1 + \frac{3\lambda}{16\pi}\left(\frac{T}{\mu_T} - \frac{1}{\pi}\ln\frac{T}{\mu_T}\right)\right\}^{-1} \tag{46}$$

It is to be noted that this same expression can be obtained by the method of renormalization group equation[7)]. Eq. (46) gives a constant asymptotic value for $\lambda(T)$ as $T \to \infty$, with a value which is only slightly different (for small λ) from that given by Eq. (44). The expression in Eq. (46) gives a good description of $\lambda(T)$ when T is very close to T_c. Using the value of μ_T from Eq. (45), we find that, for $T \gtrsim T_c$,[4)]

$$\lambda(T) \simeq \frac{32\pi^2}{9}\frac{T - T_c}{T_c} , \tag{47}$$

which approaches zero as $T \to T_c$, indicating that the system becomes non-interating at T_c.

For $T < T_c$, the computation of $\lambda(T)$ is more involved. We have two more diagrams, Fig. 9, to calculate in addition to that in Fig. 7. In all the three diagrams, the dressed propagators have mass m as given by Eq. (35). Adding the contributions of these three diagrams together, we find that[3)]

$$\lambda(T) = \lambda - \frac{3}{2} i\lambda^2 \bar{J}_2(\bar{m}^2, T) - 6\lambda^3 v^2 \bar{J}_3(\bar{m}^2, T) + 3i\lambda^4 v^4 \bar{J}_4(\bar{m}^2, T). \quad (48)$$

J_2 is as given by Eq. (37), and J_3 and J_4 are, at high T, given by

$$J_3^s(m^2, T) = -\frac{T}{32\pi m^3}, \quad (49)$$

$$J_4(m^2, T) = \frac{iT}{64\pi m^5}. \quad (50)$$

Substituting into Eq. (48), and using Eqs. (28) and (35) for v^2 and $\bar{m}^2$, we obtain the following expression for $\lambda(T)$ at $T < T_c$,

$$\lambda(T) = \lambda - \frac{3\lambda^2}{64\pi}\frac{T}{m} + \frac{3\lambda^2}{16\pi^2}\ln\frac{T}{m}$$

$$= \lambda\left\{1 - \frac{3\sqrt{3}}{32\pi}\frac{\lambda^{1/2}T}{(T_c^2 - T^2)^{1/2}} + \frac{3\lambda}{16\pi^2}\ln\left[\frac{2\sqrt{3}}{\lambda^{1/2}}\frac{T}{(T_c^2 - T^2)^{1/2}}\right]\right\} \quad (51)$$

The result as given in Eq. (51) is valid only when T is not too close to T_c. For $T \lesssim T_c$, we cannot iterate the result of Eq. (51) in a simple way. The calculation of $\lambda(T)$ for $T \lesssim T_c$ will entail a detailed analysis which is beyond the scope of this paper.

V. Conclusion

We have described here a way to improve on the one-loop approximation which is known to be inadequate at finite temperature. The linear-T term, which is

the next-to-leading term in the high T expansion of the effective potential, is unreliably given by the one-loop approximation. For a system with spontaneous symmetry breaking, this linear-T term is imaginary, making the effective potential complex, and hence also for the physical effective mass and the effective coupling constant at finite T.

It has been shown that the linear-T term in the one-loop approximation is strongly modified by the higher-loop effects. In the *improved* one-loop approximation, these higher-loop effects are effectively taken into account by replacing each of the *bare* propagators in the one-loop approximation by a *dressed* propagator. The mass of the *dressed* propagator is determined by a self-consistency condition. It is straightforward to show that, upon iteration, this self-consistency relation yields a summation of all higher-loop diagrams with non-overlapping bubbles.

The $\lambda\phi^4$ theory with negative μ^2 is described in detailed in the *improved* one-loop approximation. It is found that the linear-T term is indeed strongly modified, so much so as to make it real. Realistic physics is therefore obtained, both above and below the critical temperature. The effective potential turns out to be real, so are the effective mass and the effective coupling constant.

Whereas the effective mass m_T is given predominantly by the T^2 term which is unchanged, the effective coupling constant $\lambda(T)$ is dominated by the linear-T term. The modification to the linear-T term introduced by the improved one-loop approximation is therefore most strongly felt in the result for $\lambda(T)$. Apart from making it real, the improved one-loop approximation gives a totally different behaviour for $\lambda(T)$ as $T \to \infty$. It is found that $\lambda(T)$ approaches a constant value as $T \to \infty$, rather than dropping to zero.

The crucial ingredient of the improved one-loop approximation is the effective inclusion of higher-loop effects. It is clear from our procedure that the higher-loop diagrams included are those with non-overlapping bubbles attached to the simple one-loop diagram. It is indeed remarkable that the inclusion of contributions from these diagrams would yield such a strong modification to the one-loop result, so much so as to alter the asymptotic high T behaviour of $\lambda(T)$. It is unlikely that inclusion of *other* higher-loop diagrams, such as those with overlapping loops, would be able to change our conclusion on the asymptotic behaviour of $\lambda(T)$. The reason is quite simple. These other higher-loop diagrams may change the expression only slightly. But the dominant T^2 term in μ_T is virtually unchanged, leaving the fact that $\mu_T^2 \propto T^2$ as $T \to \infty$ unchanged. The behaviour that T/μ_T approaches a constant value as $T \to \infty$ is still valid, giving rise to the same conclusion on the asymptotic behaviour of $\lambda(T)$.

We have also calculated the effective mass and the coupling constant at temperatures below T_c. We are, however, unable to extend our analysis to cover the range of temperature below T_c but very close to it.

The improved one-loop approximation is formulated to take into account the higher-loop effects. It is therefore also applicable when $\mu^2 > 0$. Thus the fact that the higher-loop effects strongly modify the linear-T contribution in $\lambda(T)$ is equally valid here. We therefore conclude that $\lambda(T)$ approaches a constant nonzero value as $T \to \infty$, irrespective of whether spontaneous symmetry breaking occurs at $T = 0$ or not.

References

1. L. Dolan and R. Jackiw, Phys. Rev. D *9,* 3320 (1974).
2. S.P. Chia and C.C. Chiang, in *Proceedings of the First Asia-Pacific Physics Conference, Singapore 1983,* Ed. A. Arima et. al. (World Scientific, Singapore, 1984), pp. 830-840.
3. S.P. Chia and C.C. Chiang, Academia Simica, Taipei report 1983 (unpublished).
4. S.P. Chia, University of Malaya report UMKL-86-1 (1986).
5. D.A. Kirzhnits and A.D. Linde, Ann. Phys. (N.Y.) *101,* 195 (1976).
6. K.B. Joseph, V.C. Kuriakose and M. Sabir, Phys. Lett. *115B,* 120 (1982).
7. O.J.P. Eboli and G.C. Marques, Phys. Lett. *162B,* 189 (1985).

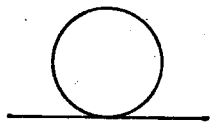

Fig. 1

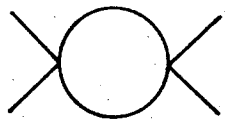

Fig. 2

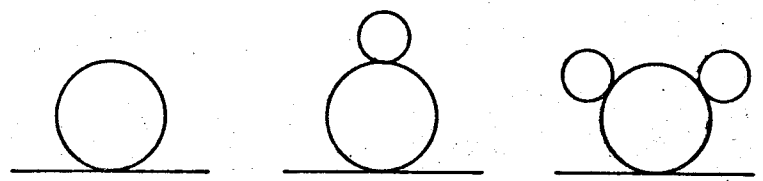

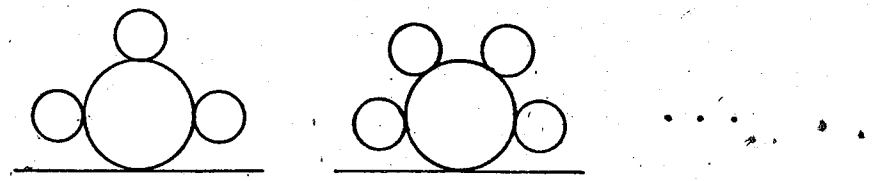

Fig. 3

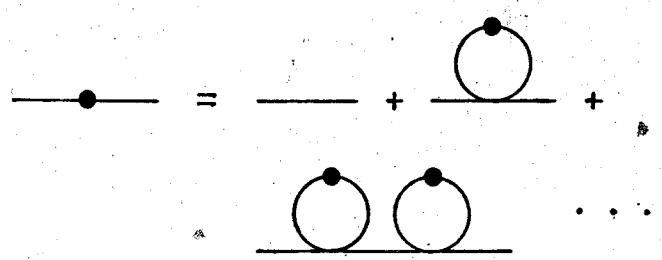

Fig. 4

Special Issue of Annual Report of the Institute of Physics, Academia Sinica, Vol. 16, 1986
In Honor of Prof. Ta-You Wu on the Occasion of his 80th Birthday

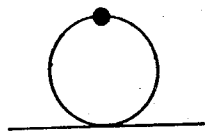

Fig. 5

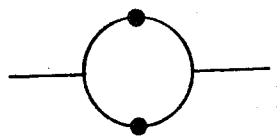

Fig. 6

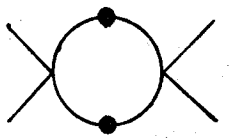

Fig. 7

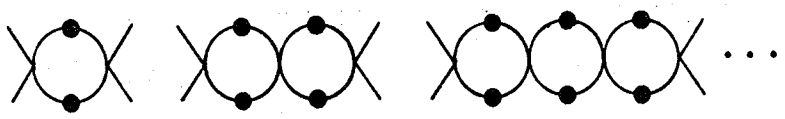

Fig. 8

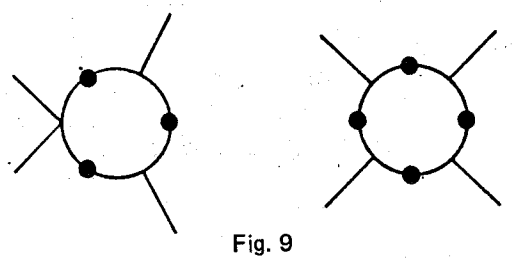

Fig. 9

HOW UNIVERSAL IS UNIVERSALITY?

Bambi Hu

Department of Physics.
University of Houston-University Park
Houston, TX 77004

Abstract

Fundamental problems concerning universality in phase transitions on inhomogeneous structures such as hierarchical and fractal lattices are discussed. As yet universality is only an extrapolated hypothesis for which conclusive evidence, theoretical or experimental, is still lacking. The critical exponents depend on so many details of the lattice that it seems unlikely that a finite complete set of universality criteria exists. It is proposed that a distinction be made between a "strong statement of universality" and a "weak statement of universality." New ways of defining universality may also have to be introduced.

Universality is one of the most remarkable and important features of phase transitions. On regular (Bravais) lattices, universality had under-gone extensive theoretical and experimental scrutiny before its validity was established. The renormalization group then provided a first-principle explanation of universality.

In recent years, there has been considerable interest in the study of phase transitions on inhomogeneous structures such as hierarchical[1,2] and fractal[3] lattices. These lattices are iteratively constructed to be exactly self-similar. They possess scale, but not translational invariance. Because of the highly inhomogeneous nature of such lattices, there is hope that they may serve as models to gain understanding of such low-symmetry systems as random magnets, polymers, and percolation clusters, etc.

Just as on regular lattices, second-order phase transitions exist for spin systems on hierarchical and fractal lattices. A seemingly superflous question[4] to ask is: Is

universality valid on such lattices? Despite its deceptively superfluous appearance, the question is difficult yet important, and it leads to the deep question of what the necessary and sufficient conditions for universality are.

Universality depends on a number of factors, and physical systems can be classified accordingly. On regular lattices, the universality criteria are dimensionality and symmetry. On hierarchical and fractal lattices, it is obvious that one would need more than two criteria. Geometric factors such as the order of ramification, fractal dimension, connectivity, and lacunarity may play a useful role in the characterization of hierarchical[5] and fractal lattices; however, it is entirely unclear whether they can serve as universality criteria. Hence, the crucial question is not that of whether a few more criteria are needed, but that of whether a finite complete set of universality criteria exists. [Of course, if the set is finite but very large, there is also the concomitant question of how useful these criteria are in practice.]

Non-rigorous notwithstanding, there are simple reasons to believe that it is unlikely that a finite complete set of universality criteria exists. There is virtually unlimited freedom in the construction of hierarchical and fractal lattices. Since these lattices are exactly self-similar, any minute change in their construction will persist to all length scales. For example, consider the following two slightly different hierarchical lattices shown in Fig. 1.

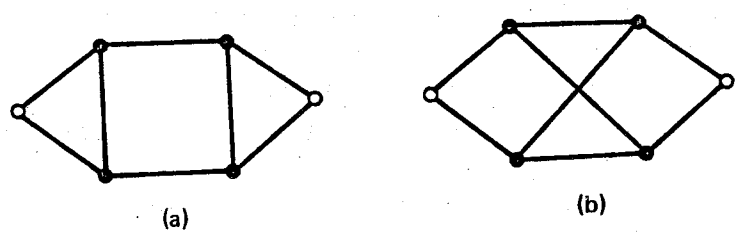

Fig. 1

They not only have the same order of ramification, intrinsic dimension D=1nA/1nb, and connectivity Q=1nC/1nb, but also the same aggregation number A, minimum cut C, and the lattice rescaling factor b. However, an exact analytical calculation of the Ising model shows that their thermal eigenvalues λ_t are different [Table 1].

Table 1. Thermal eigenvalues λ_t of the Ising model on the two hierarchical lattices shown in Fig. 1. They have identical A=8, C=2, b=3, and D=3(1n2/1n3), Q=1n2/1n3. x* denotes the fixed point (x=exp K); analytical results are enclosed in curly brackets.

Fig. 1	x*	λ_t
(a)	3.87513 $\{[\frac{1}{3}[4+(73+6\sqrt{87})^{1/3}+(73-6\sqrt{87})^{1/3}]\}$	2.07364
(b)	3.25426 $\frac{1}{4}[3+\sqrt{17}+(\sqrt{10}+6\sqrt{17})^{1/2}]$	2.15767

Of course, one point of view, taking universality for granted, is to say that another universality criteria (e.g., planarity) has to be introduced to distinguish these two lattices. However, a different point of view, not taking universality for granted, is to simply regard the source of difference as dependence on the detailed structure of the lattice.

There are many peculiar features of phase transitions on hierarchical and fractal lattices. For example, consider these two distinct hierarchical lattices shown in Fig. 2.

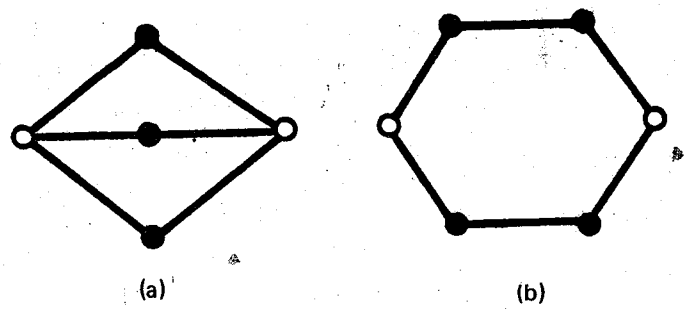

Fig. 2

They have the same thermal eigenvalue λ_t but different magnetic eigenvalue λ_h [Table 2].

Table 2. Two hierarchical lattices, illustrated in Fig. 2, that have the same thermal eigenvalue λ_t, but different magnetic eigenvalue λ_h.

Fig. 2	λ_t	λ_h
(a)	1.85410	4.85410
(b)	1.85410	5. 8011

Moreover, this example is by no means a singular case. One can, by design, construct reducible hierarchical lattices from their irreducible components such that, although their renormalization-group recursion relations would give the same thermal exponent, their geometry is however different to produce different magnetic exponents. Such examples render an extended universality principle untenable[4].

There are many other peculiar features, such as critical amplitude oscillation[6], which has no experimental evidence, that should caution people that conventional wisdom of phase transitions should not be taken for granted. One should re-examine all the premises and conclusions of conventional phase transitions before one extrapolates their validity to hierarchical or fractal lattices.

In any attempt to rescue universality on hierarchical or fractal lattices, it is logically more appropriate to first identify the factors which critical properties are independent of. In other words, one should repeat the careful work done on regular lattices before universality was established. In the case of hierarchical lattices, one such factor identified is spin. By studying[4] the spin-1 Blume-Emery-Griffiths model[7] on a family of generalized diamond hierarchical lattices with N rungs shown in Fig. 3,

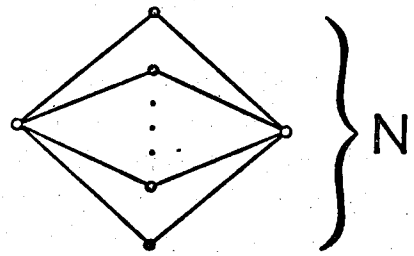

Fig. 3

we found both the thermal and magnetic eigenvalues at the Ising fixed point are the same as those of the spin-½ Ising model.

Table 3. Thermal eigenvalues of the spin-½ Ising model and the Spin-1 Blume-Emery-Griffiths model on a family of generalized diamond lattices with N rungs shown in Fig. 3.

N	Spin-1/2	Spin-1
2	1.67857	1.67857
3	1.85410	1.85410
4	1.91737	1.91737
5	1.94695	1.94695
6	1.96310	1.96310
7	1.97286	1.97286
8	1.97921	1.97921
9	1.98357	1.98357
10	1.98668	1.98668

Therefore it seems that the spin independent aspect of universality is retained.

Recently, Hu[4] proposed that a distinction be made between a "weak statement of universality" and a "strong statement of universality." In making a "weak statement of universality," one states what factors critical properties are *independent* of; whereas in making a "strong statement of universality," one states

what factors critical properties are *only dependent* on. It is always safer to start with a weak statement and be wary of the pitfalls in making the transition to a strong statement.

In a broader context, the fundamental question is that of what the necessary and sufficient conditions for universality are. Translational invariance does seem to play an essential role. Universality as an exact principle may however be valid only for a certain class of "high symmetry" systems under appropriate conditions. It is not inconceivable, especially for "low-symmetry" or inhomogeneous systems, that universality is only approximate, restricted, or even invalid. One may also have to introduce new ways of defining universality to begin with. Recently, Halsley *et al*[8] proposed that a more complete characterization of the global universal scaling features of fractals is provided by a spectrum of exponents and their densities. Perhaps the same is true of the study of phase transitions on fractals. Any progress made in the understanding of the necessary and sufficient conditions for universality will undoubtedly be a great contribution to theoretical physics.

References

1. A.N. Berker and S. Ostlund, J. Phys. C 12, 4961 (1979).
2. R.B. Griffiths and M.Kaufman, Phys. Rev. B 26, 5022 (1982), and reference therein.
3. Y. Gefen, A.Aharony, and B.B. Mandelbrot, J. Phys. A 17, 1277 (1984), and references therein; A. Aharony, "Fractals in Statistical Physics," paper presented at the International Conference on Collective Phenomena, Tel Aviv University (May 1984).
4. B. Hu, Phys. Rev. Lett. 55, 2311 (1986); B. Hu, Phys. Rev. B 33, 6503 (1986); Y. Wu and B. Hu, "Comments on Phase Transitions on Fractals," University of Houston preprint (1986).
5. J.R. Melrose, J. Phys. A 16, 1041, 3077 (1983).
6. B. Derrida, C. Itzykson, and J.M. Luck, Commun. Math. Phys. 94, 115 (1984).
7. M. Blume, V.J. Emery, and R.B. Griffiths, Phys. Rev. A 4, 1071 (1971).
8. M. H. Jensen, L.P. Kadanoff, A. Libchaber, I. Procaccia, and J. Stavans, Phys. Rev. Lett. 55, 2798 (1985); T.C. Halsey, M.H. Jensen, L.P. Kadanoff, I. Procaccia and B.I. Shraiman, Phys. Rev. A 33, 1141 (1986).

THEORETICAL ANALYSIS OF OPEN-CELL CONDUCTIVITY PROBES

S. C. Ling and H. P. Pao**

General Technology, Inc.
12903 Autumn Drive
Silver Spring, Mary land 20904

I. Introduction

In the past years we have conducted a search for an optimum conductivity sensor suitable for the measurement of the micro structure in oceans. This work has resulted in an open-cell four-electrode probe design, as shown in Fig. 1. The probe has two hemispherical current electrodes, C_1 and C_2, mounted in opposition on two parallel insulating probe supports, as shown. Coaxial to the two current electrodes are two equipotential ring-electrodes V_1 and V_2, respectivly. Fluid, whose conductivity is to be measured, flows between the electrodes. The probe mount is designed, as shown, to be free from fouling by sea weeds and other biological matters in the ocean. Preliminary sea trial has proven the validity of the design concept. Our present task is to give the probe a detailed theoretical analysis, so that a more refined optimization and characterization of the probe can be achieved. This report investigates the basic electrical field of the sensor.

In operation, an alternating current I is developed by the application of a 10 KHz low potential of 0.2 volt rms across the current electrodes C_1 and C_2. The potential field established in the fluid medium is sensed by the two equipotential ring-electrodes V_1 and V_2. The in-phase potential across these two electrodes is maintained constant at exactly 0.100 volt rms by regulating the current I through a feedback control circuit. The resulting current I between C_1 and C_2 is then linearly proportional to the conductivity σ of the fluid; i.e.,

$$\sigma = KI, \tag{1}$$

* Permanent Address: Departments of Mechanical Engineering, and Civil Engineering, respectively, the Catholic University of America, Washington, D.C. 20064, U.S.A.

where K is the gage constant of the sensor. The value of K is analytically derivable.

II. Theoretical Analysis

The electric field created by the current electrodes can be simulated by an infinite sets of current sources +q and sinks −q distributed along the x-axis containing the centers of the current electrodes C_1 and C_2. The width of the sensor W is the distance between the centers of C_1 and C_2. We shall normalize all linear dimensions by W, hence C_1 and C_2 are located at the normalized positions X = x/W = 0.5 and −0.5, respectively, see Fig. 2. A current source +q is placed along the X-axis at each of the following locations: X = 0.5, 2.5, 4.5, ... , and −1.5, −3.5 −5.5, ... ; similarly a current sink −q is located at X = −0.5, −2.5, −4.5, ... , and 1.5, 3.5, 5.5, ... The potential field produced by these fluxes will provide the required electric field between the two current electrodes of the sensor. The distribution of pairs of sources and sinks at X>0.5 and X<−0.5 is necessary to produce the required boundary condition of zero current flux across the insulating surfaces of the probe mounts; i.e.,

$$\left.\frac{d\phi}{dX}\right|_{X=\pm 0.5} = 0,$$

where ϕ is the potential. The resulting potential field contributed by the distributed sources and sinks is axially symmetrical about the X-axis. Hence, the field in the meridianal XY-plane, see Fig. 2, will represent the three-dimensional field. In this plane, the potential of the flow field can be expressed as, Smythe (1950),

$$\phi = \sum_{n=1}^{\infty} \frac{q}{4\pi\sigma W}\left(\frac{1}{\sqrt{(X-n+0.5)^2+Y^2}} - \frac{1}{\sqrt{(X+n-0.5)^2+Y^2}}\right)^{(-1)^n}, \quad (2)$$

where σ is the conductivity of the fluid, and Y = y/W. In general, summing n up to 80 will give result more than sufficient for this application.

For the present probe design, we choose to make the current electrodes with a normalized radius $\bar{r}_c = r_c/W = 0.10$. Hence, with X = 0.40 and Y = 0 in Eq. 2, the

potential ϕ_{c1} at the surface of electrode C_1 is found to be

$$\phi_{c1} = 8.595 \frac{q}{4\pi\sigma W} \quad (3)$$

Normalizing Eq. 2 by Eq. 3, we have

$$\Phi = \frac{\phi}{\Phi_{c1}} \frac{1}{8.595} \sum_{n=1}^{\infty} \left(\frac{1}{\sqrt{(X-n+0.5)^2+Y^2}} - \frac{1}{\sqrt{(X+n-0.5)^2+Y^2}}\right)^{(-1)^n}, \quad (4)$$

The solutions to Eq. 4 for different constant Φ are shown in Fig. 2. Note that the normalized potentials Φ at C_1 and C_2 are by definition equal to 1.0 and −1.0, respectively; and $\Phi = 0$ at X = 0. The equipotential electrodes V_1 and V_2 are circular rings with normalized radius $r_v = r_v/W = 0.177$ and concentric to C_1 and C_2, respectively. From Fig. 2, the corresponding Φ_{v1} and Φ_{v2} are 0.50 and −0.50, respectively. Thus, with $\bar{r}_v/\bar{r}_c = 1.77$, we have $\Phi_v/\Phi_c = 0.50$.

Similarly, one may solve for the stream lines or lines of force. By Gauss's electric flux theorem, Smythe (1950), the stream line ψ can be expressed as

$$\psi = \sum_{n=1}^{\infty} q \left(\frac{X-n+0.5}{\sqrt{(X-n+0.5)^2+Y^2}} - \frac{X+n-0.5}{\sqrt{(X+n-0.5)^2+Y^2}}\right)^{(-1)^n} \quad (5)$$

The stream function is further normalized by q as

$$\Psi = \frac{\psi}{q} = \sum_{n=1}^{\infty} \left(\frac{X-n+0.5}{\sqrt{(X-n+0.5)^2+Y^2}} - \frac{X+n-0.5}{\sqrt{(X+n-0.5)^2+Y^2}}\right)^{(-1)^n} \quad (6)$$

Normalized stream lines or stream surfaces for different constant Ψ are shown in Fig. 2. The stream line along the X-axis has a value of $\Psi = 0$. The stream surface along the surfaces of the insulating probe mounts has a value of $\Psi = 1$. Theoretically, $\Psi = 1$ is infinitely long, hence no significant amount of current flows along this surface. This provides an ideal characteristic for the sensor; i.e., the probe will be

Special Issue of Annual Report of the Institute of Physics, Academia Sinica, Vol. 16, 1986
In Honor of Prof. Ta-You Wu on the Occasion of his 80th Birthday

insensitive to surface contamination.

The distribution of Ψ along the central plane of symmetry (X = 0, Y) is shown in Fig. 3. Here, the function of Ψ is plotted with respect to Y. Note, that by definition, Ψ represents the integral value of current flux. The flux between $\Psi = 0$ and $\Psi = 1$ stream tubes contains all the fluxes q from electrode C_1. It should be noted that only q/2 flows within the sensor volume, see Fig. 2. The other symmetrical half flows to the right hand side of C_1, not shown in Fig. 2. Stream tubes Ψ = 0, 0.2, 0.4, 0.6 and 0.8 are plotted in Fig. 2. Thus, each of these tube intervals carries 1/5 of the net current flux q/2 flowing in the sensor. From Fig. 3, one notes that a majority of the fluxes, $\Psi = 0.86$ or 86%, is conducted within Y = 1.0, and 99% up to Y = 2.0. Hence, the effective sensing length of the detector can be approximately taken as 2W. This represents the spatial resolution limit of the probe. The effective volume of the fluid being measured can be assumed to be confined between the equipotential surfaces of $\Phi_{v1} = 0.5$ and $\Phi_{v2} = -0.5$, and the stream tube $\Psi \simeq 0.8$. Note that no part of this fluid volume is in contact with the current electrodes or any solid walls, hence the sensor is uniquely free from surface contamination and polarization effects. Most of all, it is free from the slow diffusion effect of the boundary layer flow near the surfaces of the electrodes. Therefore, for the intended application, the sensor has almost unlimited spatial and time resolving capability.

It should also be noted that the hemispherical form of current electrodes provides not only uniform surface flux, but uniform minimum potential gradient achievable over any electrodes. Furthermore, the ring potential-electrodes are precisely aligned with the equipotential field of the fluid; they should be relatively free from surface contamination effect. Thus, optimal operating stability for the sensor is assured.

III. Gage Constant

Having solved the electrical field problem, one can easily obtain the gage constant for a given sensor design. By definition, the resistance of the gage R is equal to the potential across V_1 and V_2 divided by the current flux,

$$R = \frac{\phi_{v1} - \phi_{v2}}{q/2} = \frac{4\phi_{v1}}{q} = \frac{2\phi_{c1}}{q} \quad . \tag{7}$$

With Eq. 3 in Eq. 7, we have

$$R = \frac{8.595}{2\pi\sigma W} = \frac{1.368}{\sigma W} \tag{8}$$

If we consider a minimum spatial resolution of 2 cm is required for detecting the microstructure of the ocean, a gage with a width of W = 1 cm will be a practical size to make and to use. Thus, with standard sea-water conductivity $\sigma = 5.3 \times 10^{-2}$ $(\text{ohm-cm})^{-1}$ or 53 mmho and W = 1.00 cm, the gage will have a typical resistance of R = 25.8 ohms. This is varified by experiment. Hence, the preceeding theoretical analysis is correct.

For the present sensor design, the conductivity of fluid can be expressed through Eq. 8 as

$$\sigma = \frac{1.368}{WE_v} \; I \, , \tag{9}$$

where E_v is the potential difference between V_1 and V_2. In operation, E_v is precisely regulated at a constant value of 0.100 volt. Hence, the gage constant K is by Eq. 9

$$K = \frac{1.368}{1.00 \times 0.100} = 13.68, \; (\text{ohm-cm-amp})^{-1} \, ,$$

and Eq. 1 can be expressed as

$$\sigma = 13.68 \; I, \; (\text{ohm-cm})^{-1} \, , \tag{10}$$

where I is the current of the gage in amp.

IV. Conclusion

We believe, that if the new open-cell sensor is constructed with high dimensional precision, it can serve as a standard-cell for direct determination of fluid conductivities. Technically, the new probe is in every respect superior to the four-

electrode U-tube (Bradshaw and Schleicher, 1980) and T-tube (Neil Brown) conductivity cells, which are now in common use; i.e., there is no physical reason why fluid medium should be confined within a tube in order to have its conductivity measured. Perhaps, the reason for using confining tubes is to simplify the handling of the electrical field problem. However, this apparent simplicity introduces more uncertainties due to tube wall contamination, electrodes, and boundary layer problems. In conclusion, this analyitical study demonstrates the superiority of open-cell conductivity measurements.

References

1. Bradshaw, A. L., and Schleicher, K. E. (1980), J. of Oceanic Engineering, IEEE, Vol. OE-5, No. 1, p. 51-61.
2. Neil Brown Instrument System, Inc., Cataumet, Massachusetts.
3. Smythe, W. R. (1950), Static and Dynamic Electricity, McGraw-Hill, N. Y., p. 1-13.

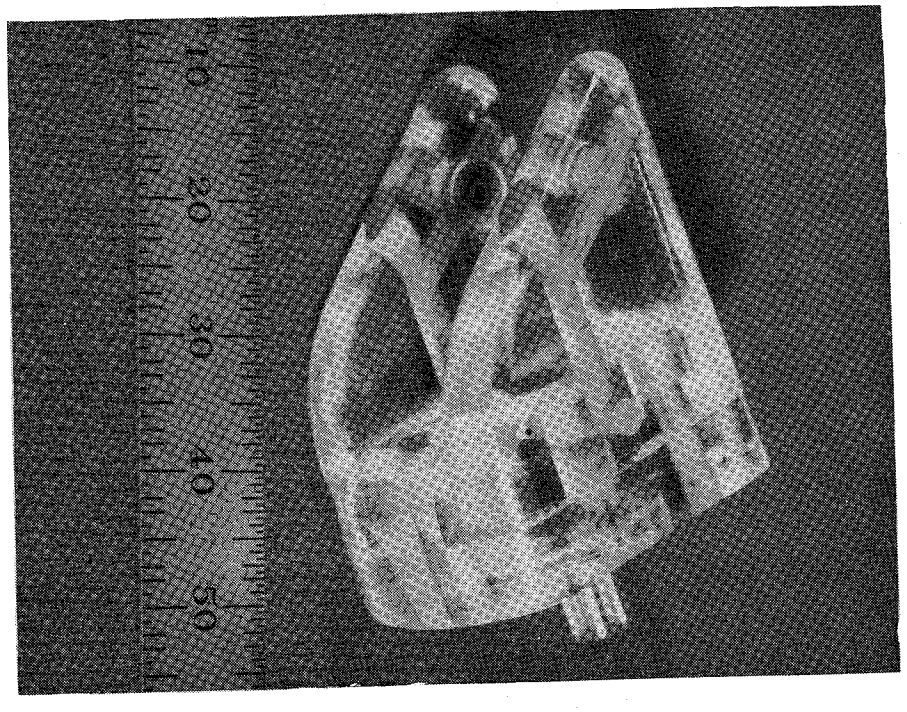

Fig. 1. Photo of an open-cell conductivity probe. *Flow is from left to right. On the left is a centimeter scale.

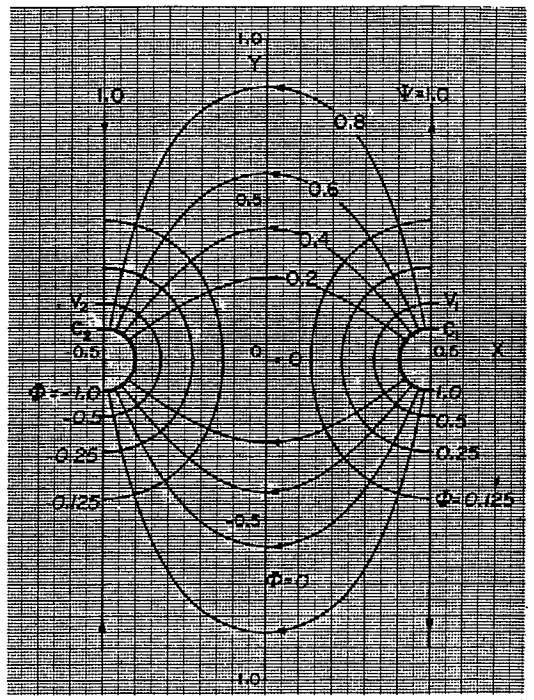

Fig. 2. The electric field of open-cell conductivity probe.

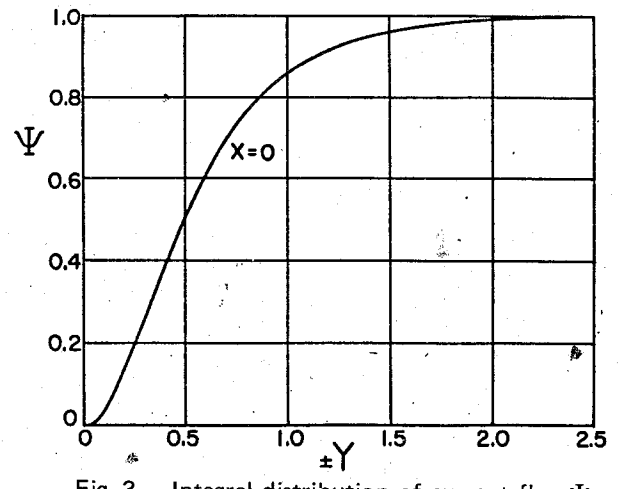

Fig. 3. Integral distribution of current flux Ψ at the central plane of conductivity probe, X=0, as function of distance Y from the X-axis.

*A patent application has been filed with the U.S. Patent Office.

APPLICATION OF FIELD THEORY TO CRITICAL PHENOMENA

*Tung-Mow Yan**

Laboratory of Nuclear Studies
Cornell University
Ithaca, N.Y. 14853
U.S.A.

&

Department of Physics
National Taiwan University
Taipei, Taiwan
R.O.C.

and

Simon Chengchien Lin+
Institute of Physics
Academia Sinica
Taipei, Taiwan 11529
R.O.C.

Abstract

We begin with an introduction to the basic concepts of critical phenomena: critical points, order parameter and critical exponents. Properties of critical exponents will be mentioned. The importance of critical exponents will be pointed out. Kadanoff's idea of block spin will be introduced and K. G. Wilson's generalisation will then be discussed. We then turn to relativistic field theory. Relativistic invariance and locality naturally lead to a simplest field theory of a scalar field with a Lagrangian similar in structure to the Hamiltonian for the spin system discussed above. Finally, we apply the technology developed for field theory to the problem of critical phenomena. The physics at the critical temperature is equivalent to a massless field theory, and therefore the renormalisation group is particularly useful. We use the Callan-Symanzik equation to discuss the two-point correlation function as an example. The analogy between critical phenomena and field theory, and its implications will be stressed throughout.

---

* This paper is based on a talk I gave at the 1986 Workshop on Statistical Mechanics, Taipei. I have learned a lot about the subject from Dr. S.C. Lin who is also responsible for translating the talk given originally in Chinese into English. Dr. Lin's contribution to the physics content of this paper is crucial, and without his efforts this article will never come into being. It is only appropriate that he and I publish this paper together. We would like to dedicate it to President Ta-You Wu, of Academia Sinica, for the occasion of his 80th birthday. — — — — — — T.M.Y.

+ This is a condensed version of Prof. Yan's talk. Due to the time constraint and my inefficiency, I was not able to send the manuscript to Prof. Yan for proofreading. Therefore, I am responsible for any mistake, misprint, or inaccuracy that might appear in this article. — — — S.C.L.

Special Issue of Annual Report of the Institute of Physics, Academia Sinica, Vol. 16, 1986
In Honor of Prof. Ta-You Wu on the Occasion of his 80th Birthday

I. Introduction

I am here to advocate the idea that the classical statistical mechanics is very closely connected with the quantum field theory. In fact, I shall prove to you that these two subjects are mathematically equivalent to each other with the only difference that one is in three dimensions, the other in four dimensions. Why am I driven by this close connection to give you a talk which I know very little? The reason is that I would like to take this opportunity to introduce the possible applications of the field theory to the critical phenomena and I also like to encourage the communication between the statistical physicists and field theorists. In a country with small community of theoretical physicists as in Taiwan, this may help to promote the morale of theoretical physicists in both fields. What are the advantages of the similarity between statistical mechanics and field theory to physics? We know that decades of efforts have been put into the research of field theory, we have gathered very much experience and insight. Firstly, the possible applications of these intuitive ideas may help statistical physicists to save a lot of energy and time. Secondly, the understanding of a new problem is possible usually only when one can find the connection with the old goodies one has already known. Therefore, if one can manage to translate the problems in statistical mechanics to field theory, by the experience and understanding in field theory, one may acquire new understanding in statistical mechanics. Thirdly, this may inspire communication between different subjects as we have already mentioned. I regard this aspect as a very important issue in the community of theoretical physicists.

Let me give a few examples about the interaction between different fields in physics now. The techniques developed in field theory, for example, Green's functions, second quantisation and Feynman diagrams, have been applied to many-body physics since the end of Second World War. On the other hand, the study of phase transitions in statistical physics helps field theorist to understand the mechanism of spontaneous symmetry breaking in gauge theories. As a matter of fact, one can find a great deal of field theorists, nowadays, who know phase transition and critical phenomena very well. The reason is, of course, they have been influenced greatly by the statistical physics. There are also many opportunities for statistical physicists and field theorists to communicate with each other. Consequently, the interface between two fields is becoming fuzzier and fuzzier. In many occasions, the researches into both field theory and statistical mechanics are virtually of the same nature and one cannot differentiate physicists from these two fields. One may recall that this is a particularly familiar phenomenon appeared

in many recent conferences. I, therefore, sincerely hope that the same phenomenon would happen here in Taiwan.

Let me now outline today's talk in the following. In the first part of my talk, the basics of critical phenomena and statistical mechanics will be introduced briefly, block spin picture and Wilson's formulation of critical phenomena will also follow. The second part is about quantum field theory. One of the simplest ways to construct quantum field theory is via Feynman's path integral formalism. One would discover immediately that field theory and statistical mechanics are of the same problem. The connection lies in the equivalence of the vacuum-to-vacuum transitional amplitude in field theory to the partition function in statistical mechanics. The last section is about the application of renormalisation group in field theory to critical phenomena. One of the consequences of this translation from field theory to critical phenomena, for example, is the use of Callan-Symanzik equation from field theory, which would explain the concept of scaling, fixed point, etc. The concept of fixed point will, in turn, give the idea of universality. I shall also explain that critical exponents in critical phenomena correspond to anomalous dimensions in field theory. We now turn to the introduction of critical phenomena.

II. Critical Phenomena

Although the word, critical phenomena, sounds very academic, it is actually very closely related to what happens in our daily life. These phenomena existed in many forms, as Chinese put them, of the Five Elements (or the Five States of Change), metal, wood, water, fire, and earth. Let us take the example of fluid for illustration (see Figure 1). This pressure-temperature diagram (Figure 1) is a very familiar one from thermodynamics. It is the liquid phase above the liquid-gas line in Figure 1, and the gas phase below the line. The density of the gas phase is much smaller than the liquid phase, however, when the temperature of the system approaches a certain temperature (647°K for water) the density difference between two phases vanishes. This temperature is called critical temperature, Tc. If we write density as function of temperature, the density of liquid is larger than gas below Tc and the density difference between these two phases is zero above Tc. Another well known example is magnetism.

In the study of critical phenomena, critical exponents are the quantities we can measure in experiments. What are the important properties of critical exponents, then? First of all, they are universal. No matter what kind of materials or processes they are, critical exponents are independent of them. I shall give you examples of

Special Issue of Annual Report of the Institute of Physics, Academia Sinica, Vol. 16, 1986
In Honor of Prof. Ta-You Wu on the Occasion of his 80th Birthday

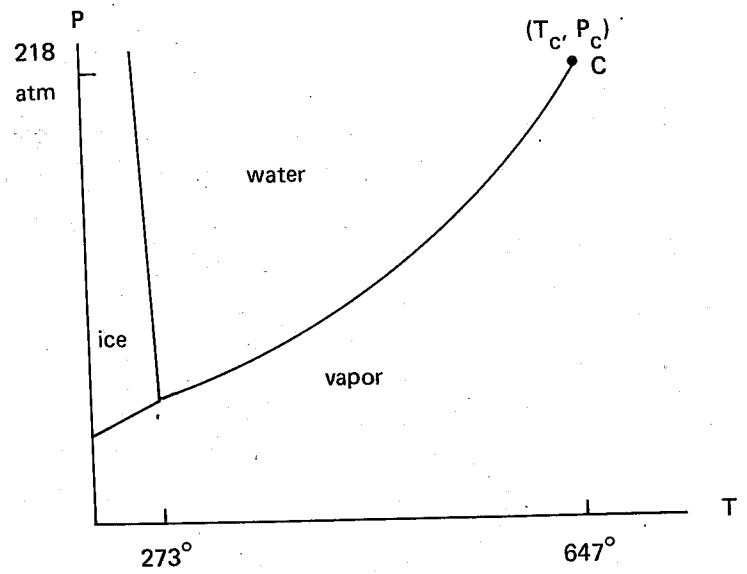

Figure 1

universality of critical exponents (see Table 1). This table is quoted from S.K.Ma's book. As you can tell from the table that all the critical exponents, whatever materials they are, are very similar to each other. They may have different critical temperatures, but they have similar exponents. It seems that universality existed. Secondly, there are scaling relations between various critical exponents. We may derive some inequalities among critical exponents from theory of thermodynamics.

Table 1 Exponents of ferromagnetic critical points

Material	Symmetry	T_c(°K)	α,α'	β	γ,γ'	δ	η
Fe	Isotropic	1044.0	$\alpha=\alpha'=-0.120$ ±0.01	0.34 ±0.02	$\gamma=1.333$ ±0.015		0.07 ±0.07
Ni	Isotropic	631.58	$\alpha=\alpha'=-0.10$ ±0.03	0.33 ±0.03	$\gamma=1.32$ ±0.02	4.2 ±0.1	
EuO	Isotropic	69.33	$\alpha=\alpha'=-0.09$ ±0.01				
$YFeO_3$	Uniaxial	643		0.354 ±0.005	$\gamma=1.33$ ±0.04 $\gamma'=0.7$ ±0.1		
Gd	Anisotropic	292.5			$\gamma=1.33$	4.0 ±0.1	

However, they also hold as equalities experimentally. These equalities are called scaling relations. How to understand scaling relations of critical exponents is one of the problems in critical phenomena. Thirdly, critical exponents are not integers, instead, they are irrational numbers such as

$$\begin{aligned} \alpha &\sim -0.1 \\ \beta &\sim 0.33 \\ \gamma &\sim 1.3 \quad . \end{aligned} \tag{1}$$

Since these exponents appear as exponents of (T – Tc), therefore, the physical quantities measured by the critical exponents must be nonanalytic (branch cut exists) functions of (T – Tc). It has been extremely difficult to understand and calculate these exponents in critical phenomena. The reason for the intrinsic difficulty is deeply rooted in statistical mechanics. We now turn to a one minute lesson of statistical mechanics.

The most important object in statistical mechanics is Boltzmann factor. It gives a relative probability for a particular configuration which is described by the momenta and coordinates of a system,

$$e^{-E/kT} \quad \rightarrow \quad e^{-\beta H} \tag{2}$$

where H is the Hamiltonian and it is nothing but the energy of the system. The Hamiltonian determines the partition function Z which is, in turn, related to the free energy per volume, F. Their relation is given as,

$$Z \equiv e^{-\frac{F}{kT}V} = \sum_{\text{configurations}} e^{-\beta H} \tag{3}$$

where V is the volume and $\beta = 1/kT$. In the above definition, partition function Z is the sum of the Boltzmann factor over all configurations at different positions and velocities. What is the usage of partition function then? If one can find the partition function of a system, free energy can be derived consequently and various physical quantities appear as derivatives of free energy.

Before sixties, the main effort of solving critical phenomena lies on the exact solution approach. This is to find the exact solutions of certain models such as Ising

model. Ising made the first attempt to solve his model, however, he only managed to solve the now called one dimensional Ising model. It was Onsager in 1944, who solved the two dimensional Ising model. Onsager's work was so difficult that only very few physicists could understand his paper. C. N. Yang was one of those people who strove to understand Onsager's theory, and managed to make many important contributions on the exact solvable models. What's so special about exact solutions? In fact, only some special types of models are known to be exactly solvable by very sophisticated mathematics. Although exact solutions are important since their results can be compared with other approximation schemes, there are snags related to the use of mathematics. The disadvantages of employing sophisticated mathematics are that exact solution approach is extremely model dependent and very little physical insight or picture could be acquired from these mathematics. Of course, there is another way to solve critical phenomena, that is, by approximate methods. These approximations are usually large scale calculations and are carried out on big mainframes or even supercomputers. However, again, we cannot obtain physical understanding from the approximate methods.

Now, let me introduce theories of critical phenomena in the modern era to you. The first important theory was Widom's scaling hypothesis in 1965. Widom assumed that thermodynamical functions, such as free energy F, are homogeneous functions of their arguments.

$$F[\lambda^a(T - T_c), \lambda^b H] = \lambda F[T - T_c, H] . \tag{4}$$

By this hypothesis with respect to various thermodynamical functions, one can derive all the following scaling relations.

$$\begin{aligned} \nu &= \nu' = \frac{\gamma}{2-\eta} \\ \alpha &= \alpha' = 2 - \nu d \\ \beta &= \frac{1}{2}\nu\,(d - 2 + \eta) \\ \delta &= \frac{d + 2 - \eta}{d - 2 + \eta} \end{aligned} \tag{5}$$

where d is the spatial dimension of the system. In order to justify Widom's hypoth-

esis, Kadanoff invented the block spin picture in 1967. Since this new idea of block spin is so important especially to renormalisation group, we shall spend some time on this topic. In a magnetic system where spins σ sit on the lattice sites, near the critical point, the whole system would be composed of block spins which, in turn, are made of original spins pointing in the same direction (See Fig. 2). The new block spins are related to the original constituent spins by, for example,

$$\sigma'_{\underset{\sim}{n'}} = \frac{1}{L^d} \sum_{\text{BLOCK}\,\underset{\sim}{n}} \sigma_{\underset{\sim}{n}} \tag{6}$$

Physical quantities calculated from the original spin variables should be possible to be expressed in terms of the new block spin variables.

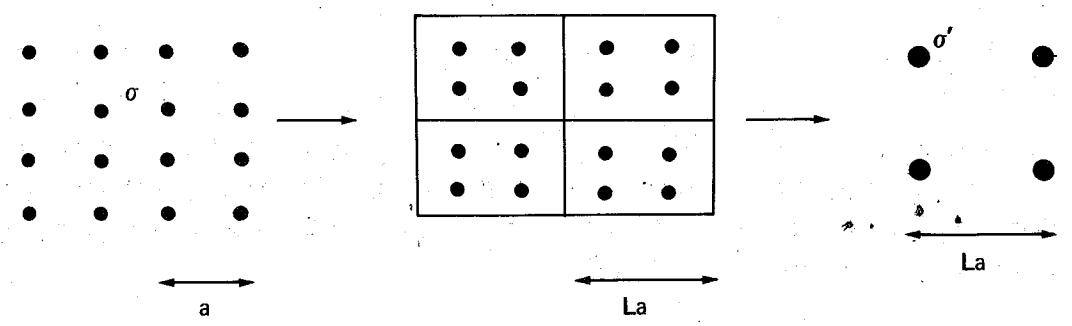

Figure 2

In 1971, Wilson generalised Kadanoff's idea by continuum approximation. He allowed the spins to take values

$$\sigma'_{\underset{\sim}{n'}} \neq \pm 1 \Rightarrow -\infty < \sigma'_{\underset{\sim}{n'}} < \infty \tag{7}$$

The magnitude of $\sigma'_{\underset{\sim}{n'}}$ can be controlled by addition of $U(\sigma)$ to H

$$e^{-\beta H} : \beta H = -\frac{J}{kT} \sum \sigma_{\underset{\sim}{n}} \sigma_{\underset{\sim}{n+\hat{i}}} + \sum U[\sigma_n] . \tag{8}$$

The advantage of working on continuum approximation is that the original summation becomes integration,

$$Z = \sum_{\sigma_n} e^{-\beta H} \rightarrow \int \prod_n d\sigma_n \, e^{-\beta H} \tag{9}$$

In his approximation, Wilson argued that as $\xi \longrightarrow$ infinity, lattice details become irrelevant and a new continuous spin variable $\sigma_L(x)$ can be defined at all points. L for the block spin is not necessary an integer any longer in Wilson's approximation. This is due to the substitution of the discrete blocking process in terms of the continuous one. When $L >> 1$, then one can find that Hamiltonian is given by

$$\beta H = \int d^d x \left[\frac{1}{2} (\nabla \sigma)^2 + U(\sigma) \right], \tag{10}$$

where $U(\sigma)$ is written

$$U(\sigma) = H\sigma + \frac{1}{2} r\sigma^2 + g\sigma^4 + \ldots\ldots, \tag{11}$$

with H the external field. Note that the block spin σ'_L cannot resolve details smaller than the size of the block L. Recall that Kadanoff's argument that physics is invariant under blocking procedure, the relation of block spin variables and original variables would be expressed as

$$e^{-\beta H[\sigma']} = \int \prod_x d\sigma(x) \, \delta \left\{ \sigma'(x) - \frac{\lambda}{L^d} \sum_{\text{BLOCK}} \sigma(x_i) \right\} e^{-\beta H[\sigma]} \tag{12}$$

By functional integration on both sides, we write

$$\int \prod_x d\sigma'(x) \, e^{-\beta H[\sigma']} = \int \prod_x d\sigma(x) \, e^{-\beta H[\sigma]} \tag{13}$$

Finally, we obtain

$$Z[\sigma'] = Z[\sigma]. \tag{14}$$

This is a simple proof that partition function remains the same after blocking. Therefore, all the physical quantities derived from partition function should be the same as well.

Let me now explain the meaning of renormalisation group. Method of renormalisation group is, in fact, a very general method of solving problems with many degrees of freedom. We may apply Kadanoff's blocking procedure to obtain new spin variables and Hamiltonian by iteration,

$$\begin{cases} 1 \rightarrow L_1 \rightarrow L_2 \rightarrow \ldots\ldots \\ \sigma_0 \rightarrow \sigma_1 \rightarrow \sigma_2 \rightarrow \ldots\ldots \\ H_0 \rightarrow H_1 \rightarrow H_2 \rightarrow \ldots\ldots \end{cases} \tag{15}$$

The two successive Hamiltonian are related by a transformation

$$H_N = \tau(H_{N-1}) \tag{16}$$

with

$$\beta H_N = \int d^d x \left[\frac{1}{2} (\nabla \sigma_N)^2 + \frac{1}{2} r_N \sigma_N^2 + g_N \sigma_N^4 + \ldots\ldots \right].$$

Parameters are analytically related for finite steps of iterations,

$$\begin{aligned} r_N &= f_1(r_{N-1}, g_{N-1}) \\ g_N &= f_2(r_{N-1}, g_{N-1}) \end{aligned}. \tag{17}$$

Nonanalytic results may appear only when N approaches infinity. The transformation (16) is the renormalisation group transformation. It is called a group since it satisfies the following condition,

$$H_N = \tau(H_{N-1}) = \tau(\tau(H_{N-2})) = \tau^2(H_{N-2}). \tag{18}$$

The transformation τ involves only neighbouring sites, that is to say, it is short ranged. This way of solving problems means that one breaks a single "$\xi \longrightarrow \infty$" problem into many steps, each is then short ranged and manageable. This is of invaluable application to practical calculation in computer. When $N >> 1$, it may happen that

$$\tau(H^*) = H^*, \tag{19}$$

where H^* is called a fixed point. This H^* is independent of the starting Hamiltonian H_0, therefore, parameters of the fixed point are virtually unrelated to the original parameters. This explains the universality and the scaling will follow.

We shall summarise the problem of critical phenomena. The problem is to calculate the partition function

$$Z = \int \prod_x d\sigma(x)\ e^{-\beta H} \tag{20}$$

where

$$\beta H[\sigma] = \int d^d x [\ \frac{1}{2}\ (\nabla \sigma)^2 + h\sigma + \frac{1}{2}\ r\sigma^2 + g\sigma^4 + \ldots\ldots] \tag{21}$$

and

$$\sigma_L(x) = \int_{k<\frac{\Lambda}{L}} \frac{d^d k}{(2\pi)^d}\ e^{ik\cdot x}\ \sigma_L(k) \tag{22}$$

represents the averaging or blocking process. This is equivalent to integrate out the higher momentum components of the system. There is no ultraviolet divergences since $\Lambda < 1/a$ where "a" is always a finite number on the lattice. When $T \to Tc$, we have infinite correlation length and physics should be independent of Λ or a. We are actually interested in the infrared behaviour of the system. The remaining problem is that how to do σ integrations by renormalisation group methods. Let me quote a comment on renormalisation group by K. G. Wilson to finish this section. He often stress that there is no definite recipe just general ideas about renormalisation group. Nevertheless, I shall still give you a specific formulation in the next sections.

III. Relativistic Quantum Field Theory

This is a totally different subject from the previous sections. It is well known that the marriage of quantum mechanics and relativity lead to the compulsory

relativistic quantum field theory. This is because that there is no satisfactory relativistic quantum mechanics. It is demonstrated by negative probability in Klein-Gordon euqation, negative energy states of Dirac equation and problem of particle creation. Principle of relativistic invariance and locality would determine the action of a field theory

$$S = \int d^4x\ \mathcal{L} \tag{23}$$

where $\mathcal{L}$ is the Lagrangian density and must be a Lorentz scalar. The simplest field theory is given by

$$\mathcal{L} = \frac{1}{2}\ \partial_\mu\phi\ \partial^\mu\phi - U(\phi)$$
$$= -\frac{1}{2}\ [(\nabla\phi)^2 - (\frac{\partial}{\partial t}\phi)^2] - U(\phi), \tag{24}$$

where the Lorentz scalar ϕ describes a scalar field theory. This Lagrangian is, in fact, analogous to the Hamiltonian in statistical mechanics. The main object of calculation in quantum field theory is the probability amplitude. Feynman invented a path integral formalism to calculate the probability amplitude of a quantum mechanical system. We know that a classical path is determined by

$$\delta S = \int_i^f dt\ \delta L = 0. \tag{25}$$

In quantum mechanics, all paths are possible. One must sum over all possible paths. Each path contributes to probability amplitude

$$e^{\frac{i}{\hbar}\int_i^f dt\ L(q_a, \dot{q}_a)}\ . \tag{26}$$

The probability amplitude from initial time t_i to final time t_f would be written as

$$<f|\ e^{-\frac{i}{\hbar}H(t_f - t_i)}\ |i>$$
$$= \sum_{SUM} e^{\frac{i}{\hbar}\int_i^f dt\ L} = \int \prod_{t,a} dq_a(t)\ e^{\frac{i}{\hbar}\int_i^f dt\ L(q_a, \dot{q}_a)} \tag{27}$$

If we translate from particle to field theory as,

Particle	Fheld Theory
$q_a(t)$	$\phi(\underset{\sim}{x}, t)$
q	ϕ
a	$\underset{\sim}{x}$
t	t

We may write down probability amplitude for field theory, accordingly,

$$\int \prod_{x,t} d\phi(\underset{\sim}{x}, t)\ e^{\frac{i}{\hbar}\int d^4x\ \mathcal{L}[\phi,\ \partial_\mu \phi]} \tag{28}$$

By Wick's rotation

$$\begin{cases} t = -ix_4 \\ d^4x = -id^4x_E \end{cases} \tag{29}$$

where E represents Euclidean, we obtain the Euclidean field theory

$$e^{\frac{i}{\hbar}S} \Rightarrow e^{-\frac{1}{\hbar}\int d^4x_E \mathcal{L}_E} \quad (\sim e^{-\beta H}) \tag{30}$$

where

$$(\nabla \phi)^2 - (\frac{\partial}{\partial t}\phi)^2 \Rightarrow (\nabla \phi)^2 + (\frac{\partial}{\partial x_4}\phi)^4 \equiv (\nabla_\mu \phi)^2 \tag{31}$$

and

$$\int d^4x_E\ \mathcal{L}_E = \int d^4x_E [\frac{1}{2}(\nabla_\mu \phi)^2 + U(\phi)] > 0\,. \tag{32}$$

In the Euclidean field theory, vacuum to vacuum amplitude is given by

$$\int \prod_x d\phi(x)\ e^{-\frac{1}{\hbar}\int d^4x_E \mathcal{L}_E} \tag{33}$$

This is completely analogous to the partition function in statistical mechanics,

$$Z = \int \prod_x d\sigma(x)\ e^{-\beta H[\sigma]} \tag{34}$$

where

$$\beta H = \int d^d x\ [\frac{1}{2}(\nabla \sigma)^2 + h\sigma + \frac{1}{2} r\sigma^2 + g\sigma^4 + \ldots\ldots]\,. \tag{35}$$

We are, therefore, dealing with the same problem both in Euclidean field theory and classical statistical mechanics provided that we make the substitution from $\sigma(x) \longleftrightarrow \phi(x)$.

We shall discuss the application of field theory to the critical phenomena now. We shall work in $(d \sim 4)$ and the calculations are based on power counting of loop integrals. In critical phenomena, one is concerned with long range or small momentum behaviour of the system. For small momenta, terms like $(\nabla \sigma)^4$, $(\nabla \sigma)^6$, σ^6, σ^8, . . . , etc. are not important, that is to say, they are irrelevant operators. (They are of technical importance in RG's treatment.) the only relevant operators are

$$\beta H = \int d^d x\ [\frac{1}{2}(\nabla \sigma)^2 + \frac{1}{2} r\sigma^2 + g\sigma^4]\,. \tag{36}$$

Therefore, if $d > 4$, loop results are not important only the mean field theory is sufficient. But when $d < 4$ mean field theory is not correct. All these are based on the power counting techniques of field theory. When $d \sim 4$, one will find that all the loop integrals would diverge logarithmically,

$$\int_q^\Lambda \frac{dk}{k} = \ln \frac{\Lambda}{q} \tag{37}$$

where Λ is the high momentum cutoff and q is the external momentum. Here Λ and q are connected and the ultraviolet (UV) and infrared (IR) divergences occur simultaneously. Renormalisation group methods were first developed to deal with the UV problem in field theory. Since critical theory is equivalent to a massless field theory, there is no intrinsic scale in critical phenomena. The only possible physical scales (UV and IR cutoffs) are connected as we discussed in the above. Therefore, RG techniques of field theory can be elegantly applied to a statistical

mechanical system at criticality.

Renormalisation in field theory is a systematic procedure to remove cutoff dependence, which has been developed for almost forty years. We are using an example to demonstrate the effective use of renormalisation techniques. Recall the two-point correlation function

$$\Gamma^{(2)}(p) = \int d^d x \; e^{ip\cdot x} < \sigma(x)\,\sigma(o) >, \tag{38}$$

where $d = 4 - \epsilon$. At $T = Tc$, it is equivalent to a massless field theory and we write,

bare coupling: X $g_o \Lambda^\epsilon$

renormalised coupling: ○ $g_R \mu^\epsilon$

where $\Lambda \sim 1/a$ with a = lattice spacing, and reference momentum $\mu \sim 1/L$ with L = block size. This reminds us that renormalisation is equivalent to the blocking procedure and the two coupling constants are related by

$$g_R = Z_g^{-1} \; g_o \,. \tag{39}$$

The two-point function is renormalised accordingly,

$$\Gamma^{(2)}(p, g_o, \Lambda) = Z \; \Gamma_R^{(2)}(p, g_R, \mu)\,,$$
$$Z = Z(g_o, \Lambda, \mu), \tag{40}$$

where $\Gamma_R^{(2)}$ is the renormalised correlation function which is independent of Λ, guaranteed by the renormalisation theory. To second order of our previous calculation, one find

$$\Gamma^{(2)}(p) = \frac{1}{p^2} \left(1 + C g_R^2 \ln \frac{\Lambda^2}{p^2}\right)$$
$$= \frac{1}{p^2} \left(1 + C g_R^2 \ln \frac{\Lambda^2}{\mu^2} + C g_R^2 \ln \frac{\mu^2}{p^2}\right)$$

$$= \left(1 + C g_R^2 \ln \frac{\Lambda^2}{\mu^2}\right) \frac{1}{p^2} \left(1 + C g_R^2 \ln \frac{\mu^2}{p^2}\right) + O(g^4)$$

$$= Z \; \Gamma_R^{(2)} + O(g^4)$$

where $Z = 1 + c\, g_R^2 \ln \frac{\Lambda^2}{\mu^2}$. (41)

IV. Callan-Symanzik Equation

Renormalisation group was first studied by Gell-Mann and Low at 1954. The simplest treatment of perturbation and renormalisation in field theory is the Callan-Symanzik (C-S) equation. The essence of C-S equation is that the correlation function of the original spin variables is independent of blocking (we use reference momentum to represent blocking),

$$\mu \frac{d}{d\mu} \Gamma^{(2)} = 0\,, \tag{42}$$

where two-point correlation function is used for the sake of simplicity. It seems to be only a very trivial fact. If one would like to know the physics of longer correlation length, one should use the renormalised correlation function to investigate. We write bare correlation function in terms of renormalised one,

$$\Gamma^{(2)}(p, g_o, \Lambda) = Z \, \Gamma_R^{(2)}(p, g_R, \mu)\,. \tag{43}$$

Substitute (43) into (42) and use

$$\mu \frac{d}{d\mu} \Gamma_R^{(2)} = \mu \frac{\partial}{\partial \mu} \Gamma_R^{(2)} + \left(\mu \frac{d}{d\mu} g_R\right) \frac{\partial}{\partial g_R} \Gamma_R^{(2)} \tag{44}$$

we finally arrive at

$$\left[\mu \frac{\partial}{\partial \mu} + \beta(g_R) \frac{\partial}{\partial g_R} + \eta(g_R)\right] \Gamma_R^{(2)}(p, g_R, \mu) = 0 \tag{45}$$

where

$$\eta \equiv \frac{1}{Z} \cdot \mu \frac{d}{d\mu} Z\Big|_{g_0, \Lambda} \tag{46}$$

and

$$\beta(g_R) = \mu \frac{d}{d\mu} g_R \,. \tag{47}$$

Equation (45) is the well known *Callan-Symanzik Equation.*

Let's discuss the running coupling constant g(t) which is introduced as a measure of dependence on momentum $t \equiv \ln (p/\mu)$, and is defined via the following equation,

$$\frac{d}{dt} g(t) = \beta(g), \qquad t \equiv \ln \frac{p}{\mu} \,. \tag{48}$$

If $\beta(g)$ has the form,

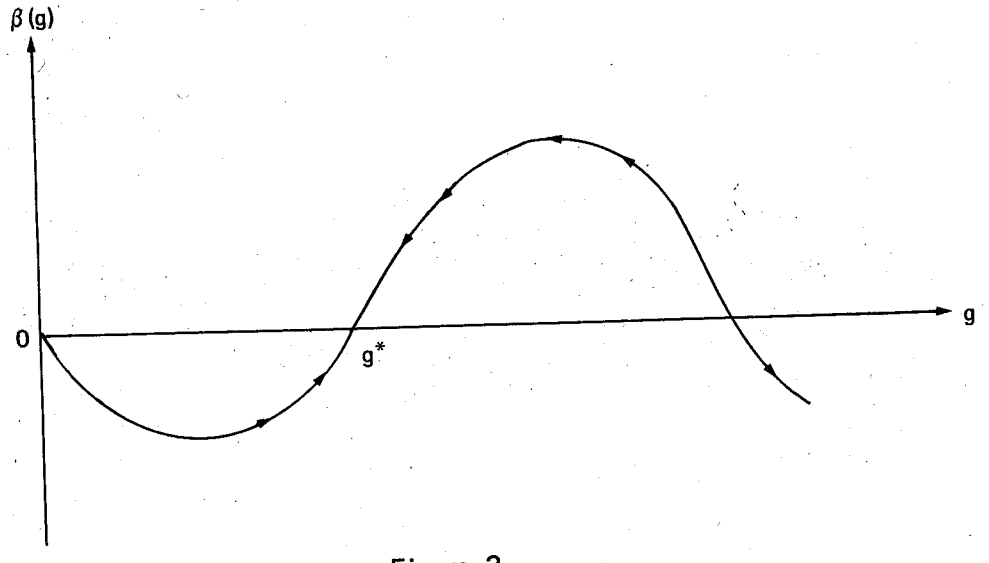

Figure 3

(A). Initial condition, $0 < g < g^*$.
Since $\beta(g) < 0$ in this region, so $(dg/dt) < 0$. As t decreases (momentum $p \to 0$), g will increase until
$g \to g^*$ as $p \to 0$.

(B). Initial condition, $g^* < g$.
$\beta(g) > 0$ in this region, so $(dg/dt) > 0$. As t decreases, g will decrease to g^* as well,
$g \to g^*$ as $p \to 0$.

This g^* is a fixed point since $\beta(g^*) = 0$, and it is an infrared stable fixed point as $p \to 0$. This g^* is a particular domain in the theory where all the neighbouring coupling constants will flow into this fixed value g^*. Of course, there may have several fixed point domains. However, within any one of the domains, the flow of coupling constants is independent of their initial conditions and the concept of universality holds.

With the help of running coupling constant, we can solve Callan-Symanzik equation quite easily now. For the two-point function

$$\Gamma^{(2)}(p) = \int d^d x \; e^{ip \cdot x} < \sigma(x) \, \sigma(0) > , \tag{49}$$

the solution of C-S equation in terms of $\beta(g)$ and g(t) reads

$$\Gamma_R^{(2)}(\lambda p, g_R, \mu) = \lambda^{-2} e^{\int_1^\lambda \frac{dx}{x} \eta[g(x)]} \Gamma_R^{(2)}(p, g(\lambda), \mu). \tag{50}$$

What we wanted to know is the behaviour of the two-point function when momentum is small. The correlation function is thus given by

$$\Gamma_R^{(2)}(\lambda p, g_R, \mu) \xrightarrow[\lambda \to 0]{} \lambda^{-2+\eta^*} \Gamma_R^{(2)}(p, g^*, \mu). \tag{51}$$

Going back to the coordinate space, it becomes

$$\Gamma_R^{(2)}(x) \xrightarrow[x \to \infty]{} \frac{1}{x^{d-2+\eta(g^*)}} \tag{52}$$

where η is called anomalous dimensions since naive dimensional analysis gives no "η" contribution. This is also one of the critical exponents in critical phenomena, and the connection of anomalous dimensions and critical exponents seems extremely intriguing. (51) is, in fact, the simplest scaling relation, one can write down much more complicated scaling relation such as

$$\Gamma_R(\lambda p_1, \ldots, \lambda p_n, g_R, \mu) = \lambda^{D+\eta_\Gamma(g^*)} \Gamma(p_1, \ldots, p_n, g^*, \mu). \tag{53}$$

In the treatment of renormalisation group, scaling relations are just natural consequences of RG. Widom's scaling hypothesis of 1965 can now be justified by the treatment of renormalisation group.

V. Conclusion

I have two comments and one question to make for the conclusion. As we have stressed again and again that statistical mechanics and field theory are the same problem. Field theorists and statistical physicists must talk to each other and they can benefit from learning others' trade. From the RG approach, one can acquire general qualitative understanding of a physical system. We have already learned the relationships between concepts of universality and fixed point, scaling and independence of blocking, critical exponents and anomalous dimensions. Apart from qualitative value, RG approach has made very important contribution in practical calculation. Systematic procedures of epsilon expansion and numerical computation from RG have already become the standard tools of solving problems in critical phenomena. Finally, I put forward to you a question which I have no answer right now. We all know that scalar field corresponds to spin variable in critical phenomena. However, there are other objects in field theory, such as fermi or gauge field. What do they correspond to in critical phenomena?

References

1. S. K. Ma, Modern Theory of Critical Phenomena. Benjamin.
2. H. E. Stanley, Introduction to Phase Transitions and Critical Phenomena. Oxford Press.
3. K. G. Wilson and J. Kogut, Physics Reports, C12, 75.
4. E. Brezin, in Methods in Field Theory, North-Holland. This 1975 Les Houches summer school lectures contains several excellent review articles on renormalisation group and its application to particle physics.
5. K. Wilson, The Renormalisation Group and Critical Phenomena, Rev. Mod. Phys. 55, 583 (1983). Nobel Lecture. It contains references to the original papers and more recent development.

TWO-BOSON SPECTRA IN ATOMIC NUCLEI

His-Tseng Chen
Department of Physics, National Taiwan University
Taipei, Taiwan, Republic of China
and
Pelletron Laboratory, Instituto de Fisica
Universidade de Sao Paulo, Sao Paulo, Brasil

L. L. Kiang
Department of Physics, National Tsing-hua University
Hsin-chu, Taiwan, Republic of Phina

G. C. Kiang *P. K. Teng*
C. W. Wang *E. K. Lin*
Institute of Physics, Academia Sinica
Nan-kang, Taipei, Taiwan 11529
Republic of China

Abstract

Within the framework of the Interacting Boson Model (IBM), the two-boson spectra in medium and heavy weight nuclei ($44 \leqslant A \leqslant 212$) are studiqd in the light of boson system where all bosons interact through a surface delta interaction which spans several single boson states. Low-lying energy levels are found to be reproduced well for the thirty-nine two-boson nuclei of interest.

In a most recent short communication[1], two of the present authors (H.T.C. and L.L.K) have proposed an extension of the interacting bosom model (IBM)[2] to include the degrees of freedom other than the sd-bosons', such as that of g-bosons or any other sort, by introducing a boson surface delta interaction (BSDI) which, in general, spans several single boson states. The model was tested with some of the medium or heavy weight two-boson nuclei and the results seem to indicate the

usefulness of the BSDI in reaching a good result with only a small number of free parameters and at the same time in preserving the elegance of the IBM.

In this report, a systematic study with BSDI is extended to A > 40 two-boson nuclei throughout the periodic table. Attempt is made to investigate the level schemes for a series of nuclei with $44 \leqslant A \leqslant 212$.

The surface delta interaction between nucleons has been proposed for use in the nuclear shell theory to calculate the spectra of a large number of nuclei, and, as a result, has indeed provided a surprisingly good first approximation to some nuclear spectra[3]. One of its interesting features is that it reproduces most often the effects of both pairing and quadrupole-quadrupple (QQ) correlations between nucleons which are responsible for both the individual-particle and collective aspects of nuclei. If we apply this type of interaction between sd-bosons, we should expect similar effects reproduced to embrace both the 0(6) and SU(3) aspects of boson symmetry. The coexistence of these two aspects has been demonstrated in the applications of the IBM to the well-deformed nucleus ^{168}Er and to the Pt and Os isotopes[4]. Furthermore, the other feature of the SDI, namely, the fact that generalized seniority being a good quantum number for degenerate single-particle states, suggests the use of the boson surface delta interaction to go beyond the limiting case of $0(6) \supset 0(5)$ and to naturally perform the mixing between different τ, or 0(5) states.

For a two-boson system where all bosons interact through a BSDI which spans several single-boson states of angular momenta, the particle-particle matrix elements are defined, in the following, as the product of two Clebsch-Gordan coefficients:

$$\langle \ell_1\ \ell_2\ \ L \,||\, \mathrm{BSDI} \,||\, \ell_3\ \ell_4\ \ L \rangle$$

$$= G_L(-1)^{\ell_3+\ell_4+L}\sqrt{(2\ell_1+1)(2\ell_2+1)(2L+1)(2\ell_3+1)(2\ell_4+1)}\,(\ell_1 0\ell_2 0|L0)(\ell_3 0\ell_4 0|L0) \tag{1}$$

where G_L, the interaction strengths, usually taken to have the same value, G, for all total angular momenta L in the case of BSDI. The secular equation is given by the dispersion relation

$$\frac{1}{G_L} + \frac{1}{2L+1}\sum_{\ell_1\ell_2}\frac{(2\ell_1+1)(2\ell_2+1)(\ell_1 0\ell_2 0|L0)^2}{\epsilon_{\ell_1}+\epsilon_{\ell_2}-E} = 0 \tag{2}$$

while the corresponding wavefunctions are shown as

$$\psi_L = \sum_{\ell_1\ell_2}\frac{\sqrt{(1+\delta_{\ell_1\ell_2})(2\ell_1+1)(2\ell_2+1)}\,(\ell_1 0\ell_2 0|L0)}{\epsilon_{\ell_1}+\epsilon_{\ell_2}-E}\,|\,\ell_1\ell_2 L\rangle \tag{3}$$

where ϵ_ℓ is the single boson energy and E the total energy.

For a system of two sd-bosons, both the energies and the wavefunction amplitudes can be written down, in terms of the ratio $G/(\epsilon_d-\epsilon_s)$, in a closed analytical form. In Fig. 1, the energies are plotted against $G/(\epsilon_d-\epsilon_s)$ in any unit. We see that the energies of the first 2^+ states increase sharply with the growing negative values of $G/(\epsilon_d-\epsilon_s)$ and remain flat as the positive values of $G/(\epsilon_d-\epsilon_s)$ increase. For $G/(\epsilon_d-\epsilon_s) > 0$, one finds the level scheme always in the sequence of $0^+ - 2^+ - 4^+ - 2^+ - 0^+$ and the corresponding wavefunctions notably with a SU(3)-like symmetry at strong coupling limit. The first 0^+ and 2^+ states are found to be very close to |(02)S> and |(02)D>, while the other states can be roughly identified with |(40)G>, |(40)D> and |(40)S>, respectively. This interesting behavior persists even when the coupling becomes weaker. A careful symmetry consideration shows that the overlap of the ground state wavefunction with |(02)S> increases from 2/3 or 0.67 to $\sqrt{5/6}$ or 0.91 as the coupling varies from the very weak to the very strong, and the overlap of the first 2^+ state with |(02)D> from $\sqrt{2}/3$ or 0.47 to $\sqrt{3}\,(7+\sqrt{10})/18$ or 0.98. In the case of negative values of $G/(\epsilon_d-\epsilon_s)$, where we find the levels either in the sequence of $0^+ - 2^+ - 0^+ - 4^+ - 2^+$ near $G/(\epsilon_d-\epsilon_s) \sim 0.6$ or of $0^+ - 2^+ - 4^+ - 0^+ - 2^+$ at the strong coupling limit, the overlap of the ground state wavefunction with |(40)S> increases from $\sqrt{5}/3$ or 0.74 at zero strength to the maximum, almost 1, and then drops slightly to the value of $\sqrt{5/6}$ or 0.91 at the strong coupling limit. The maximum overlap is found to be near $G/(\epsilon_d-\epsilon_s) \sim -0.5$. The same treng is also true for the overlap of the first 2^+ state with |(40)D> which shows the variation from $\sqrt{7}/3$ or 0.88 to the maximum and then at last $\sqrt{3}\,(7+\sqrt{10})/16$ or 0.98.

This study with BSDI has been extended to the medium and heavy weight two-boson nuclei ($44 \leqslant A \leqslant 212$) throughout the periodic table. It is found that, among the 39 two-boson nuclei under investigation, the mere sd-boson degree of freedom already explains well the energy level sequence for the first few states.

The results of the calculations, according to eq. (2), with the χ^2 fitting to the empirical data[5] are shown in Tables I-III. In general, the energies of the first five levels are fitted very well. Among the 27 nuclei shown in these Tables, there are 8 $G > 0$ nuclei, 12 $G < 0$ nuclei with the sequence $0^+ - 2^+ - 0^+ - 4^+ - 2^+$ and 7 $G < 0$ nuclei with $0^+ - 2^+ - 4^+ - 0^+ - 2^+$. As to the other nuclei which do not follow these energy level sequencies, we simply add one term α L(L+1), because of R(3) symmetry, to the total energy calculated in eq. (2). The best fit results so obtained are presented in Table IV.

In order to take into consideration the degree of freedom other than that of the sd-boson, we have carried out s-d-g-boson calculations for the nuclei ^{92}ZR, ^{94}MO, ^{110}CD, ^{110}SN and ^{146}SM and compare the results with the empirical ones[5]. The calculated and experimental energy spectra are shown in Figs. 2 to 5. In order to have a clear comparison, we, following Sakai[5], display different quasi-bands in different columns. The terms "quasi-ground band," "quasi-beta band," and "quasi-gamma band" are introduced in the so-called spherical regions as counter-parts of the "collective bands" in the deformed regions. These bands have the spin sequences 0, 2, 4, ... , 0, 2, 4, ... and 2, 3, 4, ... , respectively. As are shown in these figures, the calculations reproduced well the level schemes.

From the satisfactory results obtained for various two-boson spectra throughout the periodic table, we conclude that BSDI seems to be a simple and useful effective interaction between bosons to potentially embrace the degrees of freedom other than the sd-bosons' and thus to give a hopefully better or more complete description of nuclear collective motions without destroying the elegancs of the IBM. To carry more weight to the present statement, one definitely should make a complete study, according to the present model, on the electromagnetic transitions as well for all these two-boson nuclei. The work in this direction is already in its last phase and soon will be reported elsewhere.

One of us (H.T.C) wishes to thank the Department of Physics of the National Taiwan University, Taiwan, R.O.C. for kind hospitality and gratefully acknowledges financial support from the National Science Council, Republic of China.

References

1. Hsi-Tseng Chen, L.L. Kiang, C.C. Yang, L.M. Chen, T.L. Chen and C.W. Jiang, to be published in the LETTER TO THE EDITOR, J. Phys. G.: Nucl. Phys. (1986).
2. A. Arima and F. Iachello, Phys. Rev. Lett. 35 (1975) 1069;
   A. Arima and F. Iachello, Adv. Nucl. Phys. 13 (1984) 139-200.
3. P.J. Brussard and P.W.M. Glaudemans, Shell Model Applications in Nuclear Spectroscopy (North-Holland, Amsterdam, 1977).
4. D.D. Warner, R.F. Casten, and W.F. Davidson, Phys. Rev. C 24 (1981) 1713;
   R.F. Casten and J.A. Cizewski, Nucl. Phys. A309 (1978) 477.
5. M. Sakai, Atomic Data and Nuclear Data Tables 31 (1984) 399-432.

Table I. Energy spectra for two sd-bosons best fitted to real nuclei.
(Level sequence: $0^+ - 2^+ - 4^+ - 2^+ - 0^+$)
Experimental data taken from ref. 5.

Nucleus	Parameters		Energies (MeV)					
	G (MeV)	$\epsilon_d - \epsilon_s$ (MeV)		0^+	2^+	4^+	2^+	0^+
$^{52}_{26}$Fe	0.469	0.865	Exp.	0.0	0.850	2.385	2.762	4.142
			Th.	0.0	1.068	2.214	2.764	4.175
$^{90}_{38}$Sr	0.242	0.724	Exp.	0.0	0.832	1.656	1.892	2.674
			Th.	0.0	0.872	1.668	1.879	2.649
$^{94}_{44}$Ru	0.176	1.106	Exp.	0.0	1.431	2.187	2.51	2.995
			Th.	0.0	1.253	2.340	2.422	3.021
$^{104}_{42}$Mo	0.096	0.236	Exp.	0.0	0.192	0.561	0.812	0.866
			Th.	0.0	0.288	0.565	0.661	0.960
$^{106}_{42}$Mo	0.118	0.186	Exp.	0.0	0.172	0.522	0.711	0.957
			Th.	0.0	0.231	0.499	0.647	0.996
$^{108}_{44}$Ru	0.116	0.246	Exp.	0.0	0.242	0.665	0.708	1.092
			Th.	0.0	0.302	0.608	0.734	1.090
$^{204}_{82}$Pb	0.061	0.662	Exp.	0.0	0.988	1.274	1.354	1.583
			Th.	0.0	0.718	1.362	1.378	1.592
$^{212}_{84}$Po	0.145	0.570	Exp.	0.0	0.728	1.135	1.513	1.801
			Th.	0.0	0.672	1.261	1.364	1.839

Table II. Energy spectra for two sd-bosons best fitted to real nuclei.
(Level sequence: $0^+ - 2^+ - 0^+ - 4^+ - 2^+$)
Experimental data taken from ref. 5.

Nucleus	Parameters		Energies (MeV)					
	G (MeV)	$\epsilon_d - \epsilon_s$ (MeV)		0^+	2^+	0^+	4^+	2^+
$^{44}_{20}$Ca	–0.191	1.219	Exp.	0.0	1.157	1.884	2.283	2.657
			Th.	0.0	1.056	1.879	2.459	2.533
$^{44}_{22}$Ti	–0.179	1.219	Exp.	0.0	1.083	1.904	2.454	2.531
			Th.	0.0	1.063	1.900	2.451	2.517
$^{64}_{28}$Ni	–0.138	1.377	Exp.	0.0	1.346	2.277	2.608	2.865
			Th.	0.0	1.244	2.286	2.736	2.773
$^{76}_{36}$Kr	–0.170	0.412	Exp.	0.0	0.424	0.770	1.035	1.222
			Th.	0.0	0.428	0.775	1.067	1.197
$^{78}_{36}$Kr	–0.203	0.217	Exp.	0.0	0.455	1.017	1.119	1.148
			Th.	0.0	0.479	0.983	1.028	1.243
$^{92}_{40}$Zr	–0.086	0.850	Exp.	0.0	0.934	1.382	1.495	1.846
			Th.	0.0	0.768	1.409	1.690	1.713
$^{94}_{40}$Zr	–0.071	0.799	Exp.	0.0	0.918	1.300	1.469	1.671
			Th.	0.0	0.730	1.353	1.586	1.603
$^{98}_{38}$Sr	–0.086	0.222	Exp.	0.0	0.145	0.216	0.434	0.871
			Th.	0.0	0.221	0.396	0.555	0.617
$^{100}_{40}$Zr	–0.098	0.257	Exp.	0.0	0.213	0.331	0.565	0.879
			Th.	0.0	0.255	0.457	0.641	0.713
$^{144}_{62}$Sm	–0.321	0.555	Exp.	0.0	0.768	1.450	1.791	2.056
			Th.	0.0	0.757	1.445	1.782	2.069
$^{150}_{64}$Gd	–0.046	0.684	Exp.	0.0	0.638	1.207	1.288	1.431
			Th.	0.0	0.638	1.200	1.355	1.365
$^{208}_{84}$Po	–0.033	0.701	Exp.	0.0	0.69	1.273	1.351	1.428
			Th.	0.0	0.667	1.277	1.391	1.395

Special Issue of Annual Report of the Institute of Physics, Academia Sinica, Vol. 16, 1986
In Honor of Prof. Ta-You Wu on the Occasion of his 80th Birthday

Table III. Energy spectra for two sd-bosons best fitted to real nuclei. (Level sequence: $0^+ - 2^+ - 4^+ - 0^+ - 2^+$) Experimental data taken from ref. 5.

	Parameters		Energies (MeV)					
	G (MeV)	$\in d - \in s$ (MeV)		0^+	2^+	4^+	0^+	2^+
$^{52}_{24}$Cr	2.5×10^{-3}	1.336	Exp.	0.0	1.434	2.369	2.647	2.965
			Th.	0.0	1.339	2.673	2.682	2.673
$^{56}_{26}$Fe	−0.469	0.059	Exp.	0.0	0.847	2.085	2.942	2.960
			Th.	0.0	1.220	2.124	2.892	2.819
$^{80}_{38}$Sr	−0.192	0.157	Exp.	0.0	0.386	0.981	1.0	1.140
			Th.	0.0	0.461	0.945	0.972	1.163
$^{92}_{42}$Mo	−0.061	1.383	Exp.	0.0	1.509	2.283	2.519	3.091
			Th.	0.0	1.322	2.538	2.747	2.755
$^{96}_{42}$Mo	−0.013	0.862	Exp.	0.0	0.871	1.574	1.74	1.864
			Th.	0.0	0.849	1.718	1.737	1.737
$^{118}_{54}$Xe	−0.158	0.121	Exp.	0.0	0.337	0.810	0.830	0.928
			Th.	0.0	0.381	0.774	0.810	0.957
$^{142}_{60}$Nd	4.4×10^{-3}	1.148	Exp.	0.0	1.576	2.100	2.217	2.385
			Th.	0.0	1.153	2.298	2.314	2.298

Table IV. Energy spectra for two sd-bosons with the term α L(L+1) best fitted to real nuclei. (Level sequence: $0^+ - 2^+ - 0^+ - 2^+ - 4^+$) Experimental data taken from ref. 5.

Nucleus	Parameters			Energies (MeV)					
	G (MeV)	$\in d - \in s$ (MeV)	α (MeV)		0^+	2^+	0^+	2^+	4^+
$^{62}_{28}$Ni	−0.062	1.136	5.2×10^{-3}	Exp.	0.0	1.173	2.025	2.302	2.336
				Th.	0.0	1.105	2.043	2.295	2.358
$^{68}_{30}$Zn	2.5×10^{-3}	0.825	0.039	Exp.	0.0	1.077	1.656	1.883	2.417
				Th.	0.0	1.059	1.660	1.883	2.423
$^{70}_{30}$Zn	−0.165	0.743	0.014	Exp.	0.0	0.885	1.051	1.759	1.786
				Th.	0.0	0.721	1.107	1.727	1.844
$^{70}_{32}$Ge	−0.059	0.733	0.037	Exp.	0.0	1.039	1.214	1.709	2.153
				Th.	0.0	0.898	1.250	1.691	2.200
$^{72}_{34}$Se	−0.038	0.562	0.029	Exp.	0.0	0.862	0.937	1.317	1.637
				Th.	0.0	0.697	0.987	1.295	1.691
$^{74}_{34}$Se	−0.090	0.570	0.012	Exp.	0.0	0.635	0.854	1.269	1.363
				Th.	0.0	0.565	0.877	1.256	1.388
$^{84}_{34}$Se	−0.271	0.217	0.018	Exp.	0.0	0.654	1.410	1.731	1.734
				Th.	0.0	0.760	1.375	1.748	1.697
$^{86}_{38}$Sr	0.123	0.768	0.030	Exp.	0.0	1.077	2.102	1.854	2.229
				Th.	0.0	1.053	2.100	1.865	2.234
$^{88}_{40}$Zr	−0.032	0.831	0.026	Exp.	0.0	1.057	1.52	1.818	2.140
				Th.	0.0	0.957	1.542	1.813	2.177
$^{90}_{42}$Mo	0.034	0.915	7.1×10^{-3}	Exp.	0.0	0.948	1.979	1.896	2.002
				Th.	0.0	0.991	1.972	1.894	1.990
$^{118}_{50}$Sn	−0.026	0.952	0.022	Exp.	0.0	1.229	1.758	2.062	2.280
				Th.	0.0	1.058	1.803	2.029	2.336
$^{118}_{52}$Te	−0.043	0.552	6.5×10^{-3}	Exp.	0.0	0.606	0.934	1.151	1.206
				Th.	0.0	0.549	0.951	1.143	1.226

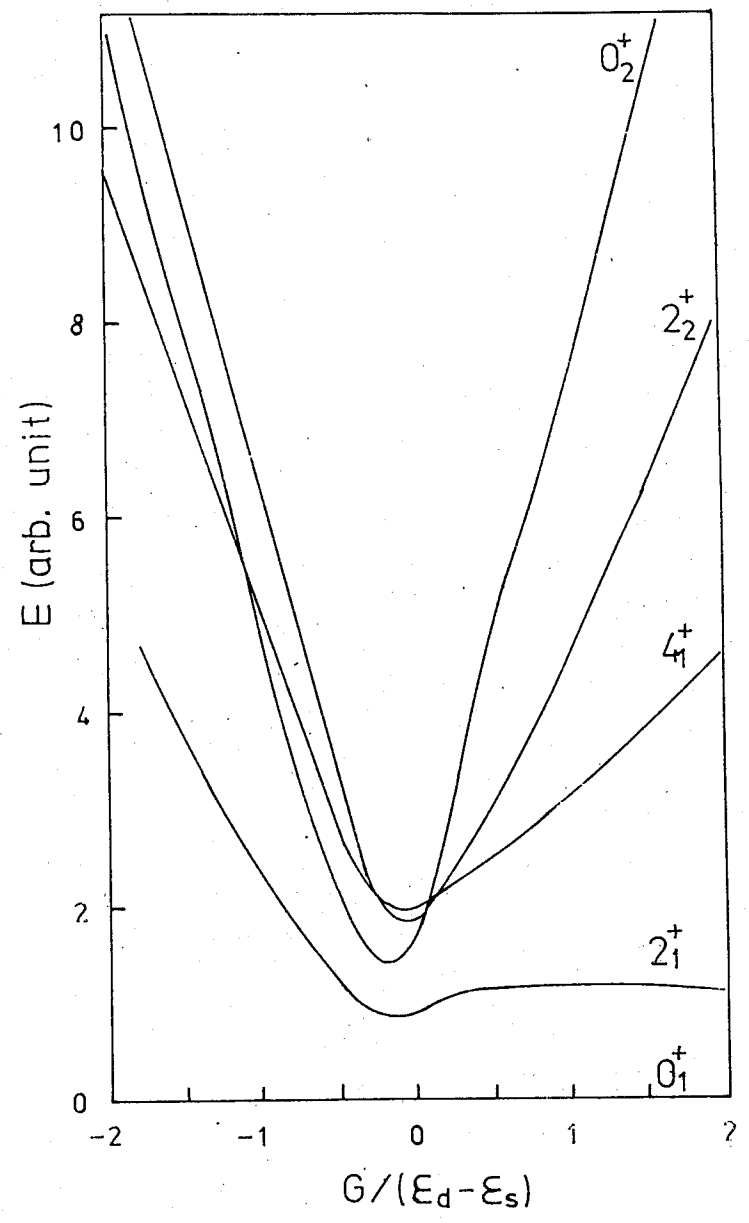

Fig. 1 BSDI energy level for two sd-bosons

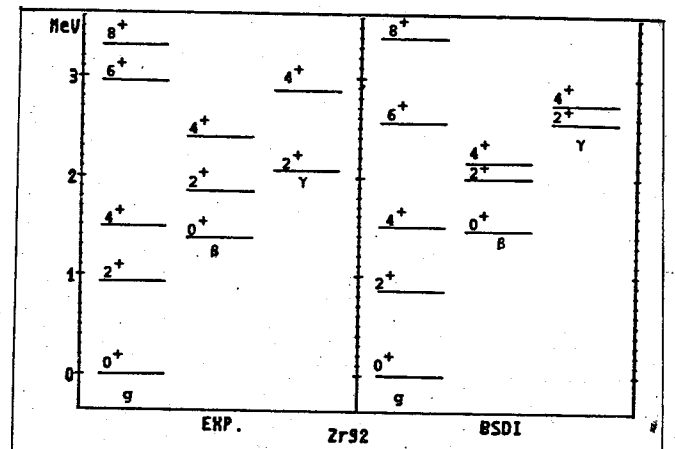

Fig. 2 Calculated and experimental energy spectra for ^{92}Zr.
Experimental data are taken from ref. 5. Parameters used in the BSDI calculation are: $\epsilon_d - \epsilon_s$ = 1.032 MeV; $\epsilon_g - \epsilon_s$ = 1.691 MeV; G = − 0.0653.

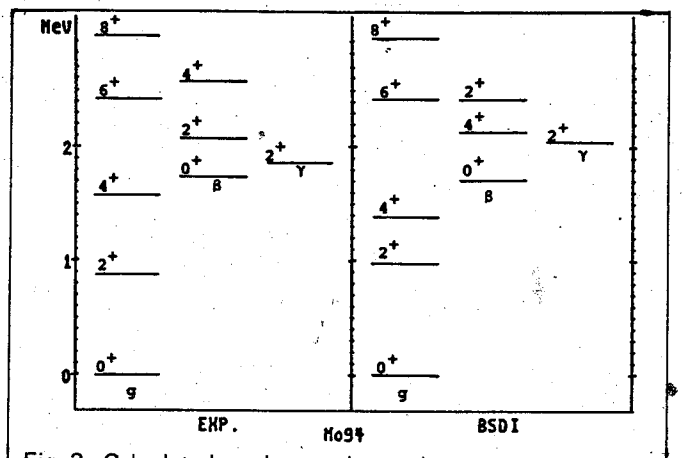

Fig. 3 Calculated and experimental energy spectra for ^{94}Mo.
Experimental data are taken from ref. 5. Parameters used in the BSDI calculation are: $\epsilon_d - \epsilon s$ = 1.076 MeV; $\epsilon_g - \epsilon_s$ = 1.4 MeV; G = − 0.0653.

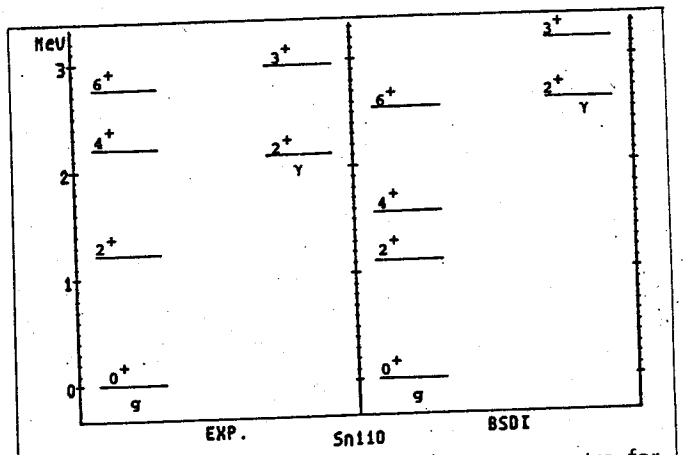

Fig. 4 Calculated and experimental energy spectra for ^{110}Sn.
Experimental data are taken from ref. 5. Parameters used in the BSDI calculation are: $\epsilon_g - \epsilon_s$ = 2.445 MeV; G = – 0.2349.

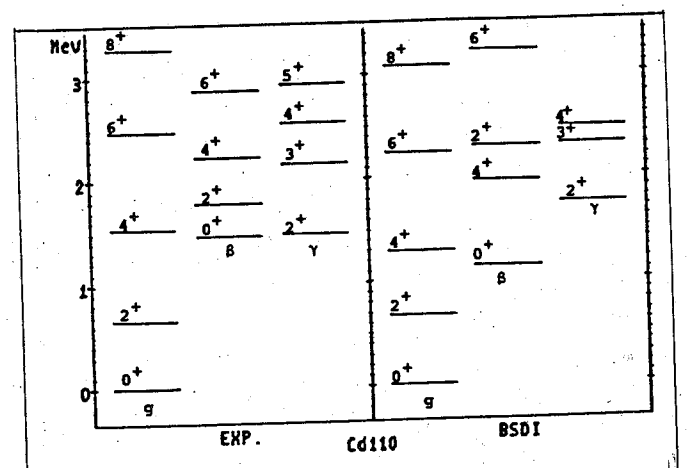

Fig. 5 Calculated and experimental energy spectra for ^{110}Cd.
Experimental data are taken from ref. 5. Parameters used in the BSDI calculation are: $\epsilon_d - \epsilon_s$ = 0.866 MeV; $\epsilon_g - \epsilon_s$ = 1.496 MeV; G = – 0.1189.

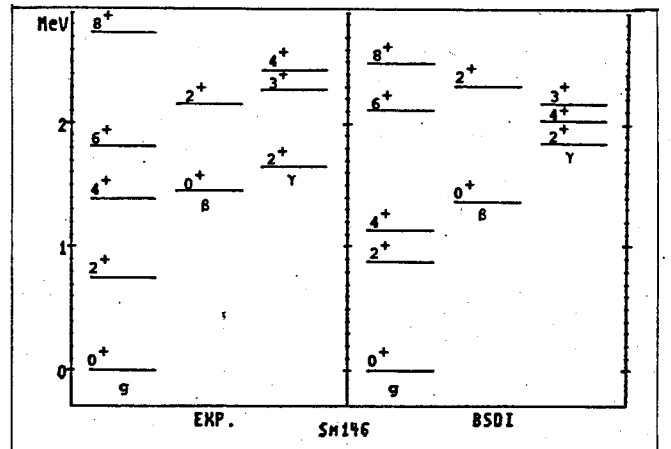

Fig. 6 Calculated and experimental energy spectra for ^{146}Sm.
Experimental data are taken from ref. 5. Parameters used in the BSDI calculation are: $\epsilon_d - \epsilon_s$ = 1.048 MeV; $\epsilon_g - \epsilon_s$ = 1.240 MeV; G = – 0.0856.

SU(3) AND THE COLOR PARTS OF THE BARYON-BARYON MULTIPLE SCATTERING MATRIX ELEMENTS

YIHARN TZENG

Institute of Physics
Academia Sinica
Nankang, Taipei, Taiwan 11529,
R.O.C.

Abstract

In quark models, the baryon-baryon scattering problems are usually treated via 3 quark–3 quark interactions. Taking the Glauber approximation as the framework, we calculate the color parts of the baryon-baryon multiple scattering matrix elements. In preparation for doing so, we first look into the SU(3) group and derive some useful identities for its generators. The color parts of matrix elements are then calculated up to triple scattering terms. Implications of these results are also discussed.

I. Introduction

It is worldwide accepted that a baryon is composed of 3 valence quarks. In order to assure the antisymmetrization of any baryon wave function in the quark degree of freedom, the wave function is written into three parts, namely, spatial, spin-flavor, and color parts. Several experimental and theoretical evidences[1] show that 3 color states are needed to form any color singlet baryon. Expressing these 3 color states as

$$a = \begin{pmatrix} 1 \\ 0 \\ 0 \end{pmatrix}, \qquad b = \begin{pmatrix} 0 \\ 1 \\ 0 \end{pmatrix}, \qquad c = \begin{pmatrix} 0 \\ 0 \\ 1 \end{pmatrix}, \tag{1}$$

(c)

one can then have any baryon color wave function as

$$\chi_c = \frac{1}{\sqrt{6}} \Sigma \in_{ijk} a_i b_j c_k , \tag{2}$$

with $\in_{ijk}$ being the Levi-Civita symbol and i, j, k being quark indices.

The interaction between quarks can be set to be

$$V_{ij} = \vec{\lambda}_i \cdot \vec{\lambda}_j \ \vec{\sigma}_i \cdot \vec{\sigma}_j \ V(r). \tag{3}$$

This form of interaction was used in the MIT bag model[2] to precit hardon mass spectrum rather successfully. Here $\vec{\sigma}$ is the Panli spinor to describe the spin part of interaction, and $\vec{\lambda}$ is the 8-component SU(3) generator to describe the color part of interaction.

Since for short-ranged baryon-baryon interaction, the interacting baryons overlap to some extent, their constituent quarks may thus play important roles on the interaction. There have been considerable amount of models[3] describing baryon-baryon interaction as 3 quark–3 quark interaction. This concept has also been applied to high energy baryon-baryon elastic scattering[4], with still a long way to success. The Glauber multiple scattering approximation[5], which has been successfully used to explain medium and high energy nucleus-nucleus scattering problems, can be a possible candidate to treat 3q-3q scattering.

The Glauber formula for 3q-3q elastic scattering amplitude reads.

$$F_{b_1 b_2}(q) = \frac{ik}{2\pi} \int d^2b \, e^{i\vec{q}\cdot\vec{b}} \left[- \sum_{n=1}^{9} \frac{f^{(n)}(b)}{n!} \right] \tag{4}$$

with

$$f^{(n)}(b) = (-)^n \sum_{i_1,\ldots,i_n=1}^{3} \sum_{j_1,\ldots,j_n=1}^{3} \tag{5}$$

$$\langle \Psi_i \Psi_j \mid \prod_{m=1}^{n} \Gamma_{i_m j_m} (\vec{b} - \vec{S}_{i_m} + \vec{S}_{j_m}) \mid \Psi_i \Psi_j \rangle$$

The physical meaning of $f^{(n)}(b)$ will be discussed later. Here $\vec{k}$ and $\vec{q}$ are, respectively, incident momentum and momentum transfer, $\vec{b}$ the impact parameter, and $\vec{S}_i$ the transverse component of quark position vector. Γ_{ij} is called to profile function, and is directly related to the q-q interaction.

To discuss the whole scattering problem is, however, a very complicated and lengthy task which is far beyond the scope of this paper. Let us concentrate only on the color part of the interaction which, unlike the sensitively model wave function-dependent spatial part, has the same matrix elements for all baryons once the interaction type is set. Hence it is worth-while to have the matrix elements calculated for the uses of all the baryon-baryon scattering problems. This is the motivation of writing this paper.

This paper is organized as follows. In Sec. II, we derive some useful identities for the SU(3) generators and the structure constants as a preparation for the calculations of color part scattering matrix elements. In Sec. III, the baryon-baryon multiple scattering amplitudes are discussed with the evaluations of color part scattering matrix elements up to triple scattering terms. Finally a brief discussion about our results is given in Sec. IV.

II. Useful Facts on the SU(3) Generators

To calculate color parts of baryon-baryon interaction matrix elements, it is necessary to look into the characteristics of SU(3) generators which, for convenience, can be chosen[6] as,

$$\lambda_1 = \begin{pmatrix} 0 & 1 & 0 \\ 1 & 0 & 0 \\ 0 & 0 & 0 \end{pmatrix}, \quad \lambda_2 = \begin{pmatrix} 0 & -i & 0 \\ i & 0 & 0 \\ 0 & 0 & 0 \end{pmatrix}, \quad \lambda_3 = \begin{pmatrix} 1 & 0 & 0 \\ 0 & -1 & 0 \\ 0 & 0 & 0 \end{pmatrix},$$

$$\lambda_4 = \begin{pmatrix} 0 & 0 & 1 \\ 0 & 0 & 0 \\ 1 & 0 & 0 \end{pmatrix}, \quad \lambda_5 = \begin{pmatrix} 0 & 0 & -i \\ 0 & 0 & 0 \\ i & 0 & 0 \end{pmatrix}, \quad \lambda_6 = \begin{pmatrix} 0 & 0 & 0 \\ 0 & 0 & 1 \\ 0 & 1 & 0 \end{pmatrix},$$

$$\lambda_7 = \begin{pmatrix} 0 & 0 & 0 \\ 0 & 0 & -i \\ 0 & i & 0 \end{pmatrix}, \quad \lambda_8 = -\frac{1}{\sqrt{3}} \begin{pmatrix} 1 & 0 & 0 \\ 0 & 1 & 0 \\ 0 & 0 & -2 \end{pmatrix} \tag{6}$$

It is well known that these generators satisfy

$$\lambda_\ell \lambda_m = \frac{2}{3}\delta_{\ell m} + \Sigma\,(d_{\ell m} + i f_{\ell mn})\,\lambda_n\,, \tag{7}$$

with the structure constant $d_{\ell mn}$ being symmetric under interchange of any pair of indices, while $f_{\ell mn}$ being antisymmetric in indices. Apart from the permutation symmetries, the non-zero elements of $d_{\ell mn}$ are

$$d_{146} = d_{157} = d_{256} = d_{344} = d_{355} = -d_{247} = -d_{366} = -d_{377} = \frac{1}{2}\,,$$

$$d_{118} = d_{228} = d_{338} = -d_{888} = 1/\sqrt{3}\,,$$

$$d_{448} = d_{558} = d_{668} = d_{778} = -1/2\sqrt{3}\,;$$

and

$$\frac{1}{2} f_{123} = f_{147} = f_{165} = f_{246} = f_{257} = f_{376} = \frac{1}{2}\,,$$

$$f_{458} = f_{678} = \sqrt{3}/2. \tag{8}$$

When calculating multiple scattering matrix elements, one can expect to encounter some complicated combinations of λ_i or $d_{\ell mn}$ and $f_{\ell mn}$. It is thus desirable to derive some identities for them so that scattering problem calculations can be made more comfortable. This is the main purpose of this section.

On the first sight, Eq. (7) looks quite similar to that for Pauli spinors, namely,

$$\sigma_\ell\,\sigma_m = \delta_{\ell m} + \sum_n i \in_{\ell mn} \sigma_n\,, \tag{9}$$

where the Levi-Civita antisymmetric symbol $\in_{\ell mn}$ satisfies the well-known identity that

$$\sum_\ell \in_{\ell mn} \in_{\ell st} = \delta_{ms}\delta_{nt} - \delta_{mt}\delta_{ns}\,. \tag{10}$$

However, due to much more complicatedly defined $d_{\ell mn}$ and $f_{\ell mn}$, they are obvious much less easy to be handled than $\in_{\ell mn}$. There are apparently no simple expressions for $\Sigma\, d_{\ell mn}\, d_{\ell st}$ and $\Sigma\, f_{\ell mn}\, f_{\ell st}$. Nevergheless, the results of setting m=s and then summing it up are still useful. Expanding the summation and leaving

out all zero elements, we have

$$\sum_{\ell,m} f_{\ell mn} f_{\ell mt} = 2\Big(\sum_{m=2}^{7} f_{1mn}f_{1mt} + \sum_{m=3}^{7} f_{2mn}f_{2mt} + \sum_{m=4}^{7} f_{3mn}f_{3mt} + \sum_{m=5}^{8} f_{4mn}f_{4mt} + \sum_{m=6}^{8} f_{5mn}f_{5mt} + \sum_{m=7}^{8} f_{6mn}f_{6mt} + f_{78n}f_{78t}\Big) \tag{11}$$

Inserting all possible n and t and using the explicit magnitudes of (8), we then obtain

$$\sum_{\ell,m} f_{\ell mn} f_{\ell mt} = 3\,\delta_{nt}\,. \tag{12}$$

Similarly,

$$\sum_{\ell,m} d_{\ell mn} d_{\ell mt} = 5/3\,\delta_{nt}\,. \tag{13}$$

Eqs. (12) and (13), though not having seen in literature, can come as a great help in calculations. They look as neat and nice as $\in_{\ell mn}$ in Eq. (9). As for the product of $d_{\ell mn}$ $f_{\ell mn}$, due to properties of symmetry and antisymmetry, is, of course,

$$\sum_{\ell,m} d_{\ell mn}\, f_{\ell mt} = 0. \tag{14}$$

Now let us turn to the generator λ. It is trivial to have

$$\sum_{i,k} d_{iik}\,\lambda_k = 0 \tag{15}$$

By using Eq. (7), (12)—(15), we then easily obtain

$$(\vec{\lambda}_\alpha \cdot \vec{\lambda}_\beta)^2 = \frac{32}{9} - \frac{4}{3}\vec{\lambda}_\alpha \cdot \vec{\lambda}_\beta. \tag{16}$$

From now on, the subscripts in Greek are used as particle indicies. Hence $\vec{\lambda}_\alpha$, with all 8 components, can act on quark α only .

Eqs. (16) can be extended to any power k, and reads,

$$(\vec{\lambda}_\alpha \cdot \vec{\lambda}_\beta)^k = C_k + d_k \vec{\lambda}_\alpha \cdot \vec{\lambda}_\beta , \tag{17}$$

with

$$C_k = \frac{32}{9} d_{k-1} , \quad d_k = \frac{32}{9} d_{k-2} - \frac{4}{3} d_{k-1} , \text{ for } k \geqslant 2. \tag{18}$$

Eqs. (17) and (18) can be verified by mathematical induction. Apparently, we have $C_o = 1$, $d_o = 0$, and $C_1 = 0$, $d_1 = 1$. Thus, for any $k \geqslant 2$, C_k and d_k can be determined via Eq. (18).

With these useful equations being derived, we are now ready to proceed color scattering matrix element calculations. This will be done in the next section.

III. Color Part of the Multiple Scattering Matrix Elements

As mentioned earlier, the baryon wave function can be expressed as a product of spatial, spin-flavor, and color parts. The quark-quark interaction of Eq. (3) thus enables us to calculate the multiple scattering amplitude $f^{(n)}(b)$ of Eq. (5) as a product of matrix elements evaluated in these three parts.

Physically, $f^{(n)}(b)$ is the scattering amplitude which contains n interactions between quarks in different baryons. The diagrammatic expressions up to n=3 are given in Figures 1 and 2. There, the vertical lines are the valuence quarks to form two baryons, and the horizontal wavy lines indicate interactions between quarks. The interactions are mediated by gluon exchanges between quarks.

Since all natural baryons are color singlet, their color parts of wave functions can all be expressed as that in Eq. (2). We now proceed to evaluate the matrix elements of

$$\Lambda_N = \langle \chi_{c_i} \chi'_{c_i} | \prod_{m=1}^{N} (\vec{\lambda}_{i_m} \cdot \vec{\lambda}_{i_m}) | \chi_{c_i} \chi'_{c_i} \rangle , \tag{19}$$

where λ_{im} acts on quark in baryon i only.

The first order term, Λ_1, which corresponds to the single scattering as shown in Figure 1(a), is

$$\Lambda_1 = \langle \chi_{c_i} \chi'_{c_i} | \vec{\lambda}_\alpha \cdot \vec{\lambda}_{\alpha'} | \chi_{c_i} \chi'_{c_i} \rangle$$

$$= \sum_{k=1}^{8} \langle \chi_{c_i} | \lambda_{\alpha k} | \chi_{c_i} \rangle \langle \chi_{c_{i'}} | \lambda_{\alpha' k} | \chi_{c_{i'}} \rangle . \tag{20}$$

Explicit calculation gives $\Lambda_1 = 0$. This is because that the vector $\vec{\lambda}$ brings a color singlet state to a color octet, which is of course orthogonal to the natural color singlet state.

Interactions in Figures 1 and 2 involve only gluon exchanges. When treating short-ranged forces, some models[3] consider both quark and gluon exchanges between baryons, as those shown in Figure 3. The expectation values $\langle \vec{\lambda}_i \cdot \vec{\lambda}_{i'} \rangle$ for these diagrams were listed by Suzuki and Hecht[3] and, in contrary to the vanighing Λ_1 of (20), are −8/9, −8/9, −8/9, 4/9, and 16/9, respectively.

Diagrams (b) and (c) in Figure 1 are double scattering terms. By using equations derived in the previous section, it is straight forward to evaluate the matrix elements of Eq. (19), though a little bit time consuming. The results are

$$\begin{aligned} &\langle \chi_{c_i} \chi_{c_i'} | \vec{\lambda}_\alpha \cdot \vec{\lambda}_{\alpha'} \vec{\lambda}_\beta \cdot \vec{\lambda}_{\beta'} | \chi_{c_i} \chi_{c_i} \rangle = 8/9, \\ &\langle \chi_{c_i} \chi_{c_i'} | \vec{\lambda}_\alpha \cdot \vec{\lambda}_{\alpha'} \vec{\lambda}_\alpha \cdot \vec{\lambda}_{\beta'} | \chi_{c_i} \chi \rangle = -16/9 \end{aligned} \tag{21}$$

There are five different types of interactions for the triple scattering, as shown in Figure 2 the matrix elements are evaluated in order as in Figure 2 as

$$\begin{aligned} &\langle \chi_{c_i} \chi'_{c_i} | \vec{\lambda}_\alpha \cdot \vec{\lambda}_{\alpha'} \vec{\lambda}_\beta \cdot \vec{\lambda}_{\beta'} \vec{\lambda}_\gamma \cdot \vec{\lambda}_{\gamma'} | \chi_{c_i} \chi_{c_{i'}} \rangle = 160/27, \\ &\langle \chi_{c_i} \chi'_{c_i} | \vec{\lambda}_\alpha \cdot \vec{\lambda}_{\alpha'} \vec{\lambda}_\alpha \cdot \vec{\lambda}_{\beta'} \vec{\lambda}_\beta \cdot \vec{\lambda}_{\gamma'} | \chi_{c_i} \chi_{c_{i'}} \rangle = -80/27, \\ &\langle \chi_{c_i} \chi'_{c_i} | \vec{\lambda}_\alpha \cdot \vec{\lambda}_{\alpha'} \vec{\lambda}_\alpha \cdot \vec{\lambda}_{\beta'} \vec{\lambda}_\beta \cdot \vec{\lambda}_{\alpha'} | \chi_{c_i} \chi_{c_{i'}} \rangle = 112/27, \\ &\langle \chi_{c_i} \chi'_{c_i} | \vec{\lambda}_\alpha \cdot \vec{\lambda}_{\alpha'} \vec{\lambda}_\alpha \cdot \vec{\lambda}_{\beta'} \vec{\lambda}_\beta \cdot \vec{\lambda}_{\beta'} | \chi_{c_i} \chi_{c_{i'}} \rangle = -32/27, \\ &\langle \chi_{c_i} \chi'_{c_i} | \vec{\lambda}_\alpha \cdot \vec{\lambda}_{\alpha'} \vec{\lambda}_\alpha \cdot \vec{\lambda}_{\beta'} \vec{\lambda}_\alpha \cdot \vec{\lambda}_{\gamma'} | \chi_{c_i} \chi_{c_i} \rangle = 160/27. \end{aligned} \tag{22}$$

For N > 3, Λ_N of Eq. (19) are to be evaluated in the same way. However, the complexlty drastically increases as N gets larger. The complexity comes from two aspects: one from the evaluation of the matrix element itself, and the other from the sharply increasing number of different types of interactions being involved. To evaluate Λ_N with higher N thus requires much more patience and carefulness.

IV. Discussion

The result of $\Lambda_1 = 0$ obtained in Eq. (20) suggests the well accepted fact that there be no one gluon exchange term in the baryon-baryon elastic scattering without quark exchange between baryons.

It is interesting to find that magnitudes of matrix elements evaluated[3] for diagrams in Figure 3 are comparable to the results of Eq. (21), the double scattering terms. Although most nonrelativisic models[3] consider only one gluon and one quark exchanges in dealing with baryon-baryon short-ranged forces, much more work with putting the spatial, spin-flavor and color parts together to make sure whether the double scattering terms are really unimportant comparing to diagrams for one gluon and one quark exchanges in Figure 3 is indeed desirable.

Results of matrix elements for triple scattering terms in Eq. (22) are in magnitudes greater than those for double scattering terms in Eq. (21). Going to higher N terms, the author has also worked out terms with N=4. With more interaction types involved, results evaluated for N=4 are in general even greater. This fact might damage the powerful multiple scattering approximation's property of fast convergence. Suitable choice of the radial part of the quark-quark interaction in Eq. (3) may overcome this possible trouble. Hence if the baryon-baryon scattering problems are treated in the framework of multiple scattering approximation, extreme care has to be taken to avoid any possible convergence problem.

This work is supported in part by the National Science Council of the Republic of China under the grant NSC75–0208–M001–12.

References

1. See for example, P. Soding and G. Wolf, Ann. Rev. Nucl. Part. Sci. 31 (1981) 231.
2. K. Johnson, Acta Physica Polonica, B6 (1975) 865.
3. For examples, C. S. Warke and R. Shanker, Phys. Rev. C21 (1980) 2643; Y. Suzuki and K. T. Hecht, Nucl. Phys. A420 (1984) 525; and F. Wang and C. W. Wong, Nucl. Phys. A438 (1985) 620; etc..
4. Y. Tzeng and C. W. Wong, Prog. of Theor. Phys. 65 (1981) 1102, and Y. Tzeng, UCLA thesis, 1980 (unpublished).
5. R. J. Glauber, in "Lectures in Theoretical Physics", edited by W. E. Britten and L. G. Dunham (Interscience, N. Y. 1959), Vol. I, p. 315.
6. M. Gell-Mann, Phys. Rev. 125 (1962) 1067.

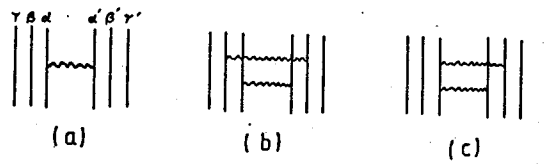

Figure 1 (a) Single scattering, and (b), (c), double scattering terms.

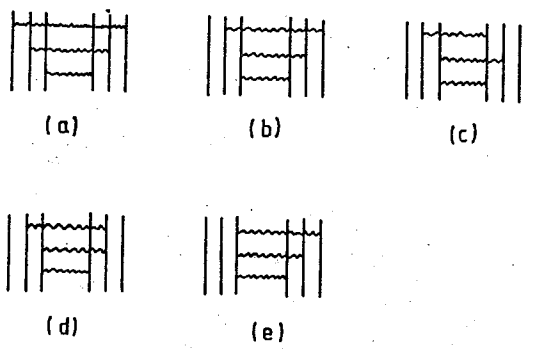

Figure 2 Triple scattering terms.

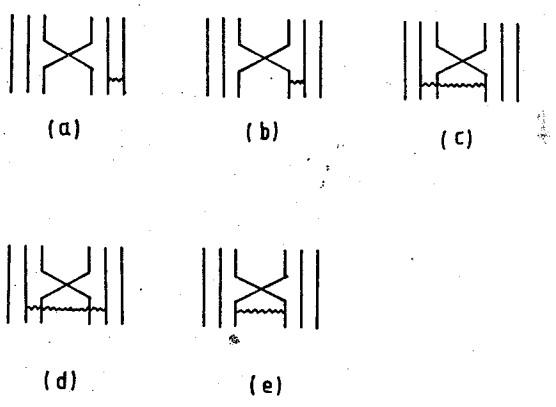

Figure 3 Single scattering with both quark and gluon exchanges.

GEOMETRICAL FACTORS, CLUSTER-SIZE DISTRIBUTIONS, AND PHASE TRANSITIONS IN SPIN MODELS: A BRIEF REVIEW*

Chin-Kun Hu

Institute of Physics, Academia Sinica
Taipei, Taiwan 11529, R.O.C.

Abstract

Whether the phase transitions in spin models, e.g. the Ising model, q-state Potts model (QPM) etc., are percolation transitions have puzzled researchers since 1974. Considering each lattice site with a spin occupied and the lattice site without a spin unoccupied, we may formally show that the partition functions of many Ising-like spin models are the generating functions of correlated percolation models. The phase transitions of the former correspond the percolation transitions of the latter. Based on such connection, we may define nonpercolating geometrical factor g_f, percolating geometrical factor g_p, and the most probable cluster-size distributions for the spin model, which depend only on the geometerical properties of the system. With certain reasonable assumptions about the behavior of g_f and g_p, we write down formula which give the free energy f, internal energy U, and the specific heat C_h of the spin model in terms of the logarithms of g_f and g_p and their first and second derivatives. Assuming that the free energy and the physical quantity, e.g. the magnetic susceptibility χ, of the spin model is determined only by the most probable cluster-size distribution, we derive an equation for the χ of the one dimensional QPM for any q. The formula for f, U, C_h and χ are confirmed by some exact transfer matrix calculations for some one-dimensional models. Such formula also provide a geometrical meaning of the finite size scaling and broadening at first-order phase transitions of the spin model. Assuming that near the critical

*This article contains the text of an invited talk given at the Second University of California Conference on Statistical Mechanics, March 26-29, 1986, at University of California, Davis. We update the references and include our recent work at the end of section III when we are invited to publish this article to celebrate Professor Wu Ta-You's eightieth birthday.

Special Issue of Annual Report of the Institute of Physics, Academia Sinica, Vol. 16, 1986
In Honor of Prof. Ta-You Wu on the Occasion of his 80th Birthday

point the cluster-size distribution for large clusters may be written in the scaling form and such large clusters contribute to the singular part of the free energy, f_{singu}, we find that f_{singu} is a general homogeneous function and therefore have the scaling law for critical exponents.

I. Introduction

The percolation transition[1-8] in the lattice percolation model and the phase transition in the Ising-like spin model[9-11] have many characteristics in common. The singular behavior in the former is clearly related to the onset of the appearance of the percolating cluster in the system. Since the work of Muller-Krumbhaar[12] in 1974, many researchers have studied whether the phase transition in the Ising model has a mechanism similar to that of the percolation transition, i.e. the onset of the appearance of the percolating cluster.[4,6,13,14] In the traditional approaches to such problem, the lattice site with an Ising spin of one sign is considered occupied in the corresponding percolation model and the lattice site with an Ising spin of an opposite sign is considered unoccupied. Such approaches have been either unsuccessful or unsatisfactory. For details, the reader is advised to consult Ref. 14 and references therein.

In this talk, we will present a new approach to such problem.[14-22] In order to establish the connection between the Ising model (and other Ising-like spin models) and the percolation problem, we propose that one should consider the sites with a spin occupied and only the sites without a spin unoccupied.[14,15] Based on such idea, in Sec. II we show that the partition function of the q-state Potts model (QPM), which becomes the simple Ising model[14] when q=2, is the generating function of a q-state bond-correlated percolation model (QBCPM) which has the same critcal properties as the QPM. Thus the phase transition in the QPM corresponds the percolation transition of the QBCPM. Based on such connection, we define nonpercolating geometrical factor g_f, and percolating geometrical factor g_p which depend only on the geometrical properties of the system.[19,22] With certain reasonable assumptions about the behavior of g_f and g_p, we write down formula which give the free energy f, internal energy U, and the specific heat C_h of the QPM in terms of the logarithms of g_f and g_p and their first and second derivatives.[22] Such formula are confirmed by an exact calculation for one-dimensional QPM and provide a geometrical meaning for the finite-size scaling[23-25] and broadening[26] at first-order phase transitions of the QPM. Based on the connection between QPM and QBCPM, in Sec. III. We define the most probable

cluster-size distribution (MPCSD) and propose that the free energy and the physical quantity of the QPM, e.g. the magnetic susceptibility, is determined by the MPCSD. This assumption[27] is confirmed by an exact calculation for the one-dimensional QPM for any q. We assume that near the critical point and for large cluster sizes the cluster-size distribution may be written in the scaling form. From such assumption we may obtain the scaling form of the singular part of the free energy and hence the scaling laws of the critical exponents.[28,29] In Sec. IV, we point out that the above result for the QPM may be extended to other interacting systems.

II. Geometrical Factors and Thermal Properties of the Potts Model

Suppose we have a lattice G of E nearest-neighbor (NN) bonds and N sites labelled by i=1, 2, ..., N. To each lattice site, we assign a q-state Potts spin s_i which has spin components j, j-1, ..., -(j-1), -j, where 2j+1=q and q is a positive integer. The partition function of the q-state Potts model (QPM) on G may be written[++] as:

$$Z_N = \sum_{s_i=-j}^{j} \prod_{\langle ij \rangle} \exp[K\delta(s_i, s_j)] \prod_i \exp(Bs_i)$$

$$= \sum_{s_i=-j}^{j} \prod_{\langle ij \rangle} [1+(e^K-1)\delta(s_i, s_j)] \prod_i \exp(Bs_i). \qquad (1)$$

Here the first product and the second product are over all NN bonds and sites of G, respectively, $K=\beta J$, $B=\beta h$; $\delta(s_i, s_j)=1$ when $s_i=s_j$ and $\delta(s_i, s_j)=0$ when $s_i \neq s_j$. Note that the coupling of B with s_i in (1) is different from that of Ref. 11. Now we expand the first product in (1) and use the subgraphs G'c G to represent the terms in the expansion. For each NN bond $\langle ij \rangle$ there occurs in (1) the two terms: 1 and $(e^K-1)\ \delta(s_i, s_j)$; subgraphs G' with no $\langle ij \rangle$ bond correspond to the former and those with an $\langle ij \rangle$ bond to the latter. There are b(G') bonds in the subgrouph G', $0 \langle b(G') \langle E$. If a particular bond $\langle ij \rangle$ is attached by the factor $(e^K-1)\ \delta(s_i, s_j)$, then $s_i=s_j$ after summing over spin states and the sites i and j are said to be in the same cluster. An example of G' is shown in Fig. 1.

++ Please do not confuse the spin component "j" with the spin index in "s_j".

Special Issue of Annual Report of the Institute of Physics, Academia Sinica, Vol. 16, 1986
In Honor of Prof. Ta-You Wu on the Occasion of his 80th Birthday

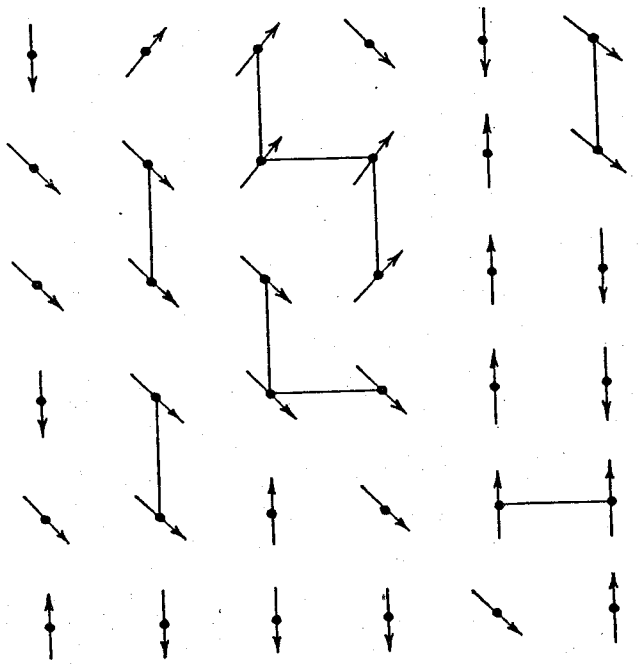

Fig. 1. A subgraph G′ of a 6x6 square lattice and a spin state on G. The solid lines represent bonds in the G′. At a given lattice site, there are four possible spin states: ↑, ↗, ↘ and ↓, i.e. q=4. Note that the spins connected by bonds must be in the same spin state.

In general, if two sites can be connected through a series of bonds, they are said to be in the same cluster. The cluster which extends from one side of G to the opposite side of G is called the percolating chuster; otherwise, it is called non-percolating or finite cluster. The percolating cluster becomes an infinite cluster in the limit $N\to\infty$. A given G′ usually contains a large number of independent clusters including isolated sites which do not connect with any other sites via bonds. For a given G′, we can sum over all spin states and in such a summation, only the terms, where all spins in the same cluster have the same spin component, have nonzero contributons. However, spins in different clusters of G′ could have different spin components. After summing over spin states, we have:

$$Z_N = \sum_{G'cG} (e^K-1)^{b(G')} \prod_c [\exp(Bn_cj)+\exp(Bn_c(j-1))+\ldots+\exp(-Bn_cj)]$$

$$= e^{KE} \sum_{G'cG} p^{b(G')} (1-p)^{E-b(G')} \prod_c [\exp(Bn_cj)+\exp(Bn_c(j-1))+\ldots+$$

$$\exp(-Bn_cj)] \,, \qquad (2)$$

where π_c extends over all clusters c in G′, $n_c=n_c(G')$ is the number of sites in the cluster c, and

$$p = 1-e^{-K} \,. \qquad (3)$$

Using (2), we may obtain expressions for the spontaneous magnetization M, internal energy U, and the specific heat C_h of the QPM in the thermodynamic limit $N\to\infty$.

$$M(G,p) = \lim_{B\to O^+} \lim_{N\to\infty} \frac{\partial}{\partial B} (\ln Z_N)/N$$

$$= \lim_{N\to\infty} W^{-1} \sum_{G'cG} \pi(G',p,q) [N^*(G')/N]\, j$$

$$\equiv j\langle N^*(G')\rangle_O \,, \qquad (4)$$

$$U(G,p) = \lim_{B\to 0^+} \lim_{N\to\infty} \frac{-\partial}{\partial\beta} (\ell n Z_N)/N$$

$$= -\frac{J}{p} \langle b(G') \rangle_0 = -\frac{zJ}{2p} \bar{p}, \tag{5}$$

$$C_h(G,p) = \frac{\partial}{\partial T} U(G,p)$$

$$= \frac{k_B K^2}{p^2} [-(1-p) \langle b(G') \rangle_0 + \langle (b(G') - [b(G')]_{av})^2 \rangle_0]$$

$$= \frac{k_B K^2}{p^2} [-\frac{z(1-p)}{2} \bar{p} + \langle (\delta b(G'))^2 \rangle_0], \tag{6}$$

where

$$\pi(G',p,q) = p^{b(G')} (1-p)^{E-b(G')} q^{n_f(G')}, \tag{7}$$

$$W = \sum_{G'cG} \pi(G',p,q), \tag{8}$$

$$\langle N^*(G') \rangle_0 = \lim_{N\to\infty} W^{-1} \sum_{G'cG} \pi(G',p,q) [N^*(G')/N], \tag{9}$$

$$\bar{p} = \lim_{N\to\infty} W^{-1} \sum_{G'cG} \pi(G',p,q) (b(G')/E), \tag{10}$$

$$[b(G')]_{av} = W^{-1} \sum_{G.cG} \pi(G',p,q) b(G'), \tag{11}$$

$$\delta b(G') = b(G') - [b(G')]_{av} \tag{12}$$

In (4) to (6), we have use $\langle Q(G') \rangle_0$ to represent the mean value of a subgraph-dependent quantity $Q(G')$ per site in the limit $N\to\infty$ (see also (9)). $N^*(G')$ of (4) is the total number of sites in the percolating clusters of G, $n_f(G')$ of (7) is the total number of nonpercolating (i.e. finite) clusters in G', and z of (5) and (6) is the coordination number of G. It is obvious that $M(G,p)/j$ is the percolation probability of the following q-state bond-correlated percolation model (QBCPM) on G:

(1) All sites of G are occupied and each bond of G is attached with the bond probability $p = 1 - \exp(-K)$.

(2) The overall probability of G'cG is enhanced by a factor q for each finite cluster in G'. Eqs. (5) and (6) relate U and C_h of the QPM to the average number of occupied bonds, $\bar{p}$, and the fluctuations of the number of occupied bonds $\langle (\delta b(G'))^2 \rangle_0$, for the QBCPM. Thus Z_N of (2) is the generating function of the QBCPM.

Now we classify all subgraphs G'cG into subgraphs with only nonpercolating cluster, G'_f, and subgraphs with at least one percolating cluster, G'_p, and consider the partial sums:

$$W_f = e^{KE} \sum_{G_f cG} \pi(G'_f, p,q) = \sum_{G'_f cG} (e^K - 1)^{b(G'_f)} q^{n_f(G'_f)}, \tag{13}$$

$$W_p = e^{KE} \sum_{G'_p cG} \pi(G'_p, p,q) = \sum_{G'_p cG} (e^K - 1)^{b(G'_p)} q^{n_f(G'_p)}. \tag{14}$$

Since only subgraphs G'_p contribute to $M(G,p)$ which is zero for $T > T_c$ and nonzero for $T < T_c$, it is reasonable to expect that for $p < p_c = 1 - e^{-Kc} = 1 - e^{-J/k_B T_c}$

$$W_f >> W_p, \tag{15}$$

for $p > p_c$,

$$W_f << W_p, \tag{16}$$

and at p_c

$$W_f = W_p. \tag{17}$$

Eq. (17) is called the geometrical condition of phase transitions.

In the following, we will consider fixed but very large E. W_f and W_p may be represented as follows:

$$W_f = \sum_{b=0}^{E} (e^K-1)^{RE} \sum'_{G'_f \subset G} q^{n_f(G'_f)}$$

$$= E \int_0^1 I(K,R)\, g_f(q,R)\, dR, \tag{18}$$

$$W_p = \sum_{b=0}^{E} (e^K-1)^{RE} \sum''_{G'_p \subset G} q^{n_f(G'_p)}$$

$$= E \int_0^1 I(K,R)\, g_p(q,R)\, dR. \tag{19}$$

Here

$$0 \leqslant R = b(G')/E \leqslant 1, \tag{20}$$

$$I(K,R) = (e^K-1)^{RE}, \tag{21}$$

$$g_f(q,R) = \sum'_{G'_f \subset G} q^{n_f(G'_f)}, \tag{22}$$

$$g_p(q,R) = \sum''_{G'_p \subset G} q^{n_f(G'_p)}. \tag{23}$$

The summations in (22) and (23) are over all G'_f and G'_p, respectively, with a fixed fraction of occupied bonds R. Since g_f and g_p are independent of K=J/kT, they will be called nonpercolating geometrical factor and percolating geometrical factor, respectively. The dependence of W_f and W_p on K comes only from I(K,R) and we will call I(K, R) the interaction factor. Examples of g_f, I(K, R) and I(K, R)g_f are shown in Figs. 2-4.

For a fixed K, I(K,R) is a monotonous function of R, but $g_f(q,R)$ and $g_p(q,R)$ are expected to peak sharply at certain values. It is reasonably to expect that the integrands in (18) and (19) also peak sharply at certain values, say R_f and R_p, respectively, which are solutions of the equations:

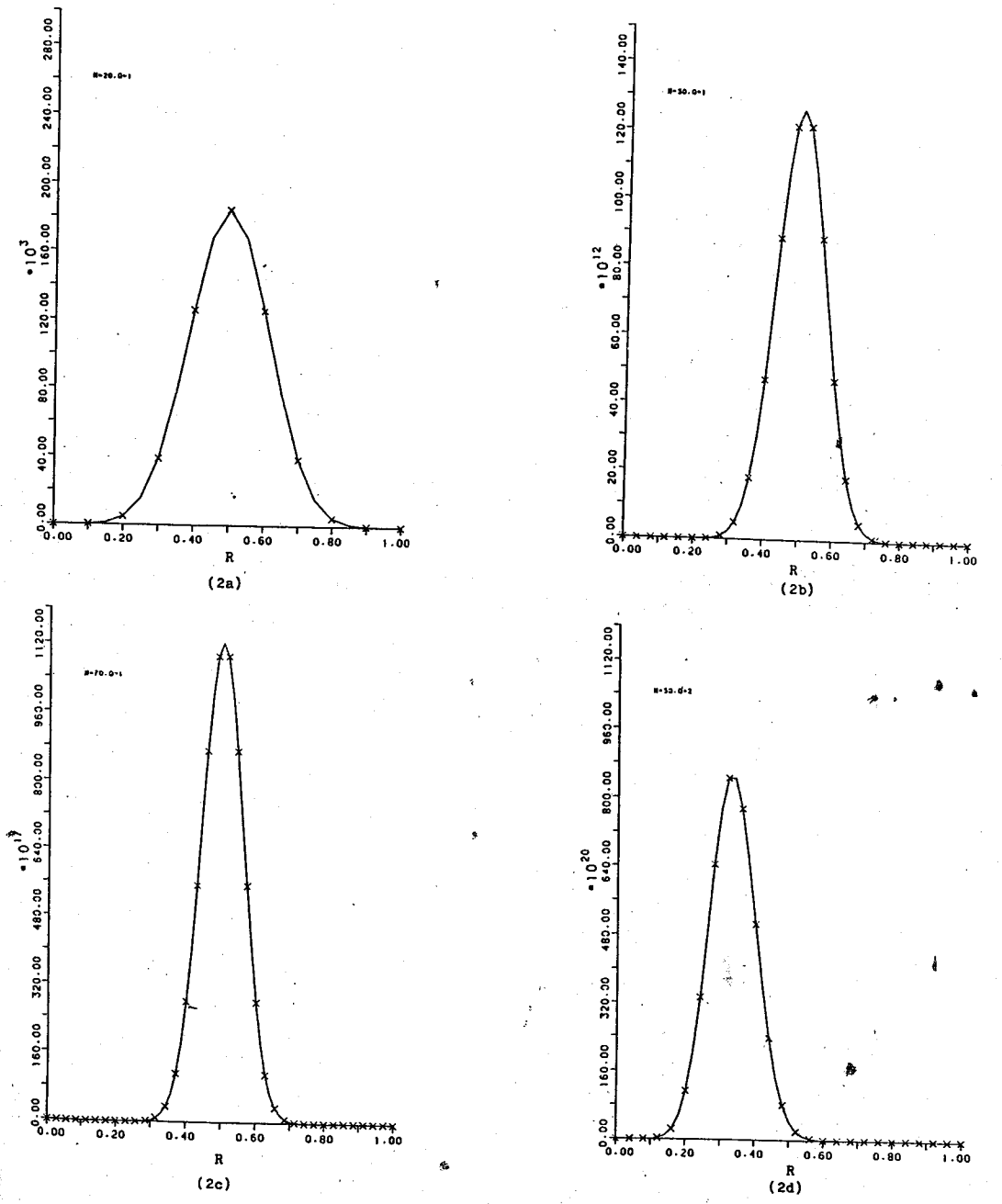

Fig. 2. Geometrical factor $g_f(q, R)$ for the one-dimensional QPM with periodic boundary condition. Here q equals 1 and N equals 20 (2a), 50 (2b), and 70 (2c). Note that when N increases the maximum of the peak of g_f increases rapidly but the width of the peak decreases. In Fig. (2d), q = 2, N = 50.

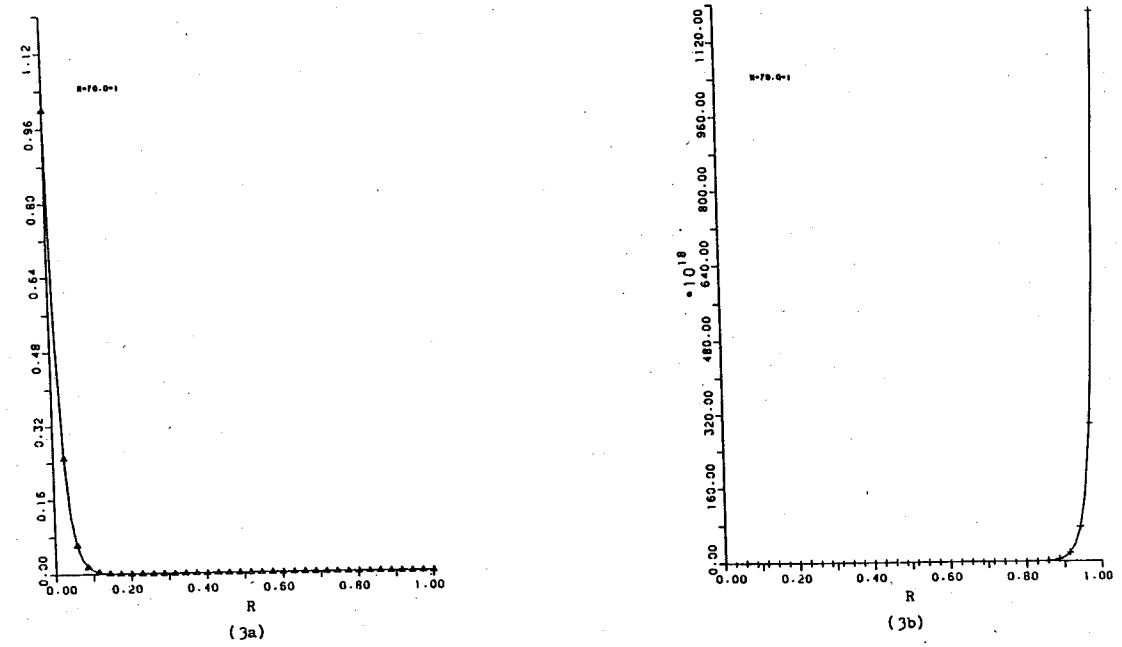

Fig. 3. Interaction factor I(K, R) for the one-dimensional QPM with periodic boundary condition. Here N equals 70 and K equal 0.5 and 2 for (3a) and (3b), respectively.

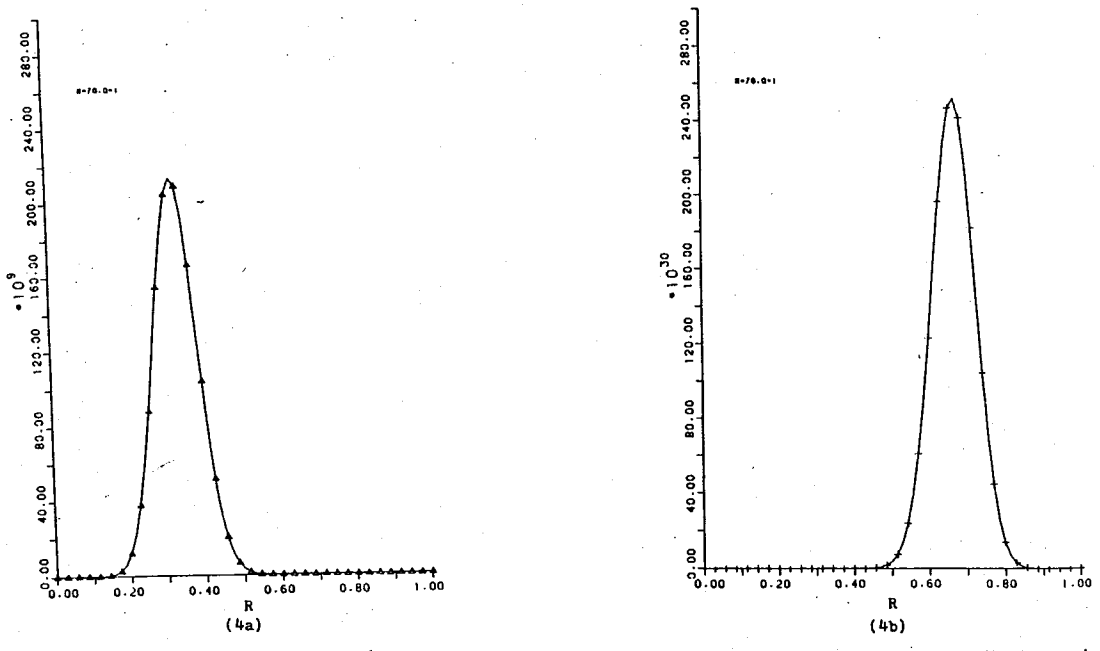

Fig. 4. The product $I(K, R)\, g_f(q, R)$ for the one-dimensional QPM with periodic boundary condition. Here N equals 70, q equals 1, and K equals 0.5 and 2 for (3a) and (3b), respectively.

$$\frac{d}{dR}\,[\ln I(K,R)g_f(q,R)]_{R_f} = E\ln(e^K-1)+\frac{d}{dR}\,[\ln g_f(q,R)]_{R_f}=0, \tag{24}$$

$$\frac{d}{dR}\,[\ln I(K,R)g_p(q,R)]_{R_p} = E\ln(e^K-1)+\frac{d}{dR}\,[\ln g_p(q,R)]_{R_p}=0. \tag{25}$$

Expanding the logarithm of the integrands in (18) and (19) at R_f and R_p, respectively, and keeping only the leading and the quadratic terms, we have:

$$W_f \cong E\, I(K,R_f)\, g_f(q,R_f)\int_0^1 \exp\,[-(R-R_f)^2/\Gamma_f{}^2]\,dR$$

$$\equiv A_f\Gamma_f\int_{-y_f}^{\bar{y}_f}\exp(-y^2)\,dy\,, \tag{26}$$

$$W_p \cong E\, I(K,R_p)\, g_p(q,R_p)\int_0^1 \exp\,[-(R-R_p)^2/\Gamma_p{}^2]\,dR$$

$$\equiv A_p\,\Gamma_p\int_{-y_p}^{\bar{y}_p}\exp(-y^2)\,dy, \tag{27}$$

where

$$\Gamma_f^{-2} = -\frac{1}{2}\,\left[\frac{d^2}{dR^2}\ln g_f(q,R)\right]_{R_f}, \tag{28}$$

$$\Gamma_p^{-2} = -\frac{1}{2}\,\left[\frac{d^2}{dR^2}\ln g_p(q,R)\right]_{R_p} \tag{29}$$

$$A_f = E\, I(K,R_f)\, g_f\,(q,R_f)\,, \tag{30}$$

$$A_p = E\, I(K,R_p)\, g_p\,(q,R_p)\,, \tag{31}$$

$$y_f = R_f/\Gamma_f\,,\ \bar{y}_f = (1-R_f)/\Gamma_f\,, \tag{32}$$

$$y_p = R_p/\Gamma_p\,,\ \bar{y}_p = (1-R_p)/\Gamma_p\,. \tag{33}$$

In the very large E limit, we expect that Γ_f and Γ_p, the half widths of the peaks at R_f and R_p respectively, tend to zero and $\bar{y}_f$, y_f, $\bar{y}_p$, and y_p tend to ∞. The integrations in (26) and (27) give simply the constant $\sqrt{\pi}$.
Thus

$$W_f \cong A_f \Gamma_f \int_{-\infty}^{\infty} \exp(-y^2)\,dy = A_f \Gamma_f \sqrt{\pi} \quad W_f^* , \tag{34}$$

$$W_p \cong A_p \Gamma_p \int_{-\infty}^{\infty} \exp(-y^2)\,dy = A_p \Gamma_p \sqrt{\pi} = W_p^* \tag{35}$$

The free energy per spin is given by:

$$f(G, q, K) = \lim_{N\to\infty} \frac{1}{N} \ln (W_f^* + W_p^*). \tag{36}$$

For a geometrical quantity Q(R) of the QBCPM which depends on R, we may use the representations of (18) and (19) to calculate the average value of Q(R):

$$[Q(R)]_{av} = \frac{\int_0^1 I(K,R)\, g_f(q,R)\, Q(R)\,dR + \int_0^1 I(K,R)\, g_p(q,R)\, Q(R)\,dR}{\int_0^1 I(K,R)\, g_f(q,R)\,dR + \int_0^1 I(K,R)\, g_p(q,R)\,dR} . \tag{37}$$

If Q(R) is a sufficiently smooth function of R, e.g. a low degree polynomial, the first and second integrands in the numerator of (37) still peak sharply at R_f and R_p, respectively. We may proceed as before to carry out the integrations.

For example, the average number of occupied bond (per bond), $\bar{p}$, is given by:

$$\bar{p} = \frac{[ER]_{av}}{E}$$

$$= \frac{A_f \int_0^1 \exp[-(R-R_f)^2/\Gamma_f^2]\, R\,dR + A_p \int_0^1 \exp[-(R-R_p)^2/\Gamma_p^2]\, R\,dR}{A_f \int_0^1 \exp[-(R-R_f)^2/\Gamma_f^2]\,dR + A_p \int_0^1 \exp[-(R-R_p)^2/\Gamma_p^2]\,dR}$$

$$= \frac{W_f^* R_f + W_p^* R_p}{W_p^* + W_p^*} \tag{38}$$

The fluctuations of the number of bonds is given by:

$$\langle (\delta b(G'))^2 \rangle_0 = \frac{[(ER - E\bar{p})^2]_{av}}{N}$$

$$= \frac{A_f E^2 \int_0^1 \exp[(R-R_f)^2/\Gamma_f^2]\,(R-\bar{p})^2 dR + A_p E^2 \int_0^1 \exp[-(R-R_p)^2/\Gamma_p^2]\,(R-\bar{p})^2 dR}{N(W_f^* + W_p^*)}$$

$$= \frac{E^2}{N(W_f^* + W_p^*)} \{ \tfrac{1}{2} W_f^* \Gamma_f^2 + \tfrac{1}{2} W_p^* \Gamma_p^2 + (R_f - \bar{p})^2 W_f^* + (R_p - \bar{p})^2 W_p^* \} \tag{39}$$

For $T \rangle T_c$, $W_f^* \rangle\rangle W_p^*$ and we have

$$\bar{p} = R_f , \tag{40}$$

$$\langle (\delta b(G'))^2 \rangle_0 = \frac{z}{4} E \Gamma_p^2 . \tag{41}$$

For $T \langle T_c$, $W_f^* \langle\langle W_p^*$ and we have

$$p = R_p , \tag{42}$$

$$\langle (\delta b(G'))^2 \rangle_0 = \frac{z}{4} E \Gamma_p^2 . \tag{43}$$

At $T = T_c$, $W_f^* = W_p^*$ and we have:

$$\bar{p} = \tfrac{1}{2} (R_f + R_p) , \tag{44}$$

$$\langle (\delta b(G'))^2 \rangle_0 = \frac{E^2}{4N} [\Gamma_f^2 + \Gamma_p^2 + (R_p - R_f)^2] . \tag{45}$$

Assuming at T_c.

$$ER_p - ER_f = b_o N^a \tag{46}$$

where a and b are constants and $0 \leqslant a \leqslant 1$, we have:

$$\langle (\delta b(G'))^2 \rangle_0 = \frac{E^2}{4N} (\Gamma_f^2 + \Gamma_p^2) + \tfrac{1}{4} b_0^2 N^{2a-1} . \tag{47}$$

The second term of (47) gives the singular part of the specific heat C_h^* which is

$$C_h^* \sim N^{\alpha/(2-\alpha)} \tag{48}$$

from the finite-size scaling of the specific heat at second order phase transitions.[25] Identifying 2a−1 with $\alpha/(2-\alpha)$, we have

$$\alpha = \frac{2a-1}{a} = 2 - \frac{1}{a} , \tag{49}$$

i.e. α increases with a.

To demonstrate that we may actually calculate the physical quantity of the QPM from the geometrical factor of the QBCPM, we now carry out an exact calculation for the one dimensional system with periodic boundary condition. In such system, E=N, z=2, $g_p(q,R)=0$ for $0 < R < 1$ and $g_f(q,1)=0$.

It follows from the Euler theorem that for any subgraph G' with $b(G')=NR<1$, the number of clusters is give by $n_f(G')=N-b(G')$. Thus for a fixed $R=b(G')/N$, $n_f(G')$ is also fixed and the summation in (22) is reduced to the problem of counting the number of independent subgraphs for a fixed number of occupied bonds. Therefore,

$$g_f(q,R) = C_{RN}^N q^{N-RN} = \frac{N!}{(N-RN)!\ RN!} q^{N(1-R)} \tag{50}$$

for $R < 1$. Using the left-hand side of (50) in (24) and (28), we find that in the large E limit

$$R_f = \frac{e^K - 1}{e^K + q - 1} , \tag{51}$$

$$\Gamma_f^2 E = 2R_f (1 - R_f) = \frac{2q(e^K - 1)}{(e^K + q - 1)^2} . \tag{52}$$

Thus Γ_f goes to zero as $1/\sqrt{E}$.

It follows from (36), (40), (41), (5), and (6) that

$$f(G,q,K) = \ln (e^K + q - 1) , \tag{53}$$

$$p = R_f = \frac{e^K - 1}{e^K + q - 1} , \tag{54}$$

$$\langle (\delta b(G'))^2 \rangle_0 = \tfrac{1}{2}\Gamma_f^2 E = \frac{q(e^K - 1)}{(e^K + q - 1)^2} , \tag{55}$$

$$U(G,p) = -\frac{J}{p} p = -\frac{Je^K}{e^K + q - 1} , \tag{56}$$

$$C_h(G,p) = \frac{k_B K^2 e^K (q-1)}{(e^K + q - 1)^2} . \tag{57}$$

The results of (53), (56), and (57) are identical with those obtained from the standard transfer matrix method where the largest eigenvalue[30] of the transfer matrix is $e^K + q - 1$.

For systems in higher dimensions, it is not easy to calculate g_f and g_p exactly and the numerical method may be used. The idea of a bias Monte-Carlo simulation

method proposed by Huang and Shih[31] may be adapted to our case to calculate g_f and g_p, even the geometrical factors of the second kind which are independent of q.[32,33]

Eq. (46) and (49) may be used to explain the change in the phase transition behavior of the QPM on dimensions $d \geqslant 2$ when q is increased.[11,22]

It follows from (7) that the subgraphs with larger number of finite clusters increase their relative probability weight when q is increased. For a given $R < 1$ we expect that the subgraphs G'_f contributing to the summation of (22) are usually more compact, hence have more closed loops and finite clusters (Euler relations), than the subgraphs contributing to the summation of (23). Usually, the smaller the value of R the larger the number $n_f(G')$ in a G'. Therefore when q is increase g_f will increase faster than g_p and that the peak of g_f will move toward smaller values of R with a speed faster than that of g_p. After increasing q to a new value, we must also increase K to a new value so that (17), (24) and (25) may still be true. At the new K, the separation between R_p and R_f is expected to increase, i.e. a of (46) will increase with q. It follows from (49) that α will increase with q. When q is larger than a critical value q_c, a of (46) will assume its largest value 1 and we have

$$E\,(R_p - R_f) = b_0\, N, \tag{58}$$

$$C_h^* = \frac{k_B K^2}{4p^2}\, b_0^2\, N = \frac{\ell^2}{4k_B T_c^2}\, N\,, \tag{59}$$

$$\ell = U^+ - U^- = \frac{J}{p}\, b_0\,, \tag{60}$$

where U^+ and U^- are internal energies at $T_c+\epsilon$ and $T_c-\epsilon$, respectively with ϵ being an infinitesimal positive number. Thus for $q > q_c$, the latent heat $\ell > 0$ and the phase transition is first-order. Eq. (59) is the finite-size scaling of specific heat at a first-order phase transition.[24-25] The finite-size rounding of the transition temperature T_c at a first-order phase transition may be estimated from the equation[26]

$$C_h^* \sim \frac{\ell}{\Delta T_c}\,, \tag{61}$$

It follow from Eq. (59) and (61) that

$$\frac{\Delta T_c}{T_c} \sim \frac{k_B T}{N\ell} = \frac{1}{N\sigma} \tag{62}$$

which is consistent with the result proposed by Imry.[26]

In conclusion, we have shown that the phase transition in the QPM corresponds the percolation transition of QBCPM and the thermal proparties of the QPM could be derived simply from g_f and g_p. Using the geometrical condition of the phase transition based on such a connection, we have given the geometrical interpretation of the increase of α with q for $q < q_c$, changeover from second-order to first-order phase transition as q increases,[11] finite size scaling of specific heat[24-25] and the rounding of transition temperature[26] at a first-order phase transition.

III. Cluster-Size Distribution and the Magnetic Property of the Potts Model

The product in Eq. (2) may be written as:

$$\prod_{m=1}^{N} \left[e^{Bmj} + e^{Bm(j-1)} + \ldots + e^{Bm(-j)}\right]^{\ell_m} \tag{63}$$

where ℓ_m, $1 < m < N$, is the number of m-site cluster in G', they satisfy the equations:

$$\sum_{m=1}^{N} \ell_m = n_f + n_p = n_t\,, \tag{64}$$

$$\sum_{m=1}^{N} \ell_m\, m = N\,, \tag{65}$$

where n_f and n_p are the number of nonpercolating clusters and the number of percolating clusters, respectively. It follows from the Euler theorem that:

$$n_f + n_p = N - b(G') + c(G')\,, \tag{66}$$

where c(G') is the number of closed loops in G'. The set of numbers $\{\ell_1, \ell_2, \ldots, \ell_N\}$ will be denoted by ρ and called a "cluster-size distribution", i.e.

$$\rho = \{\ell_1, \ell_2, \ldots, \ell_N\}. \tag{67}$$

If we add a bond to a m-site cluster in a G', m $\gg$ 1, to form a new closed loop, the cluster-size distribution of the new subgraph is the same as before. On the other hand, for a given fraction of occupied bond, R, usually there are many possible cluster-size distributions $\rho(R)$.

The cluster-size distribution ρ corresponding to a G'_f with RE occupied bonds will be denoted by $\rho_f(R)$; the cluster-size distribution corresponding to a G'_p with RE occupied bonds will be denoted by $\rho_p(R)$. The number of subgraphs with $\rho_f(R)$ and $\rho_p(R)$ as their cluster-size distribution will be denoted by $N(\rho_f(R))$ and $N(\rho_p(R))$, respectively. The subgraphs in the summation of Eq. (2) may be classified into G'_f or G'_p. Now we consider partial sums over G'_f and G'_p, respectively:

$$Z_f = \sum_{G'_f \subset G} (e^K - 1)^{b(G'_f)} \prod_c [\exp[Bn_c j] + \exp[Bn_c (j-1)] + \ldots + \exp[-Bn_c j]]$$

$$= \sum_{R=0}^{1} I(K,R) \sum_{\rho_f(R)} N(\rho_f(R)) \prod_{m=1}^{N} [e^{Bmj} + e^{Bm(j-1)} + \ldots + e^{-Bmj}]^{\ell_m}, \tag{68}$$

$$Z_p = \sum_{G' \subset G} (e^K - 1)^{b(G'_p)} \prod_c [\exp[Bn_c j] + \exp[Bn_c (j-1)] + \ldots + \exp[-Bn_c j]]$$

$$= \sum_{R=0}^{1} I(K,R) \sum_{\rho_p(R)} N(\rho_p(R)) \prod_{m=1}^{N} [e^{Bmj} + e^{Bm(j-1)} + \ldots + e^{-Bmj}]^{\ell_m}, \tag{69}$$

where I(K,R) is the interaction factor.

The sums over R in Eq. (68) and Eq. (69) run over the numbers:

$$R = 0, 1/E, 2/E, \ldots, (E-1)/E, 1. \tag{70}$$

The second sum in the second expression of Eq. (68) runs over all possible $\rho_f(R)$ for a given R; the second sum in the second expression of Eq. (69) runs over all possible $\rho_p(R)$ for a given R. For a given R, in the second summation of Eq. (68) [(69)] the particular $\rho_f(R)$ [$\rho_p(R)$] which gives the maximum contribution to the summation is called the most probable nonpercolating [percolating] cluster-size distribution for the given R and is denoted by $\bar{\rho}_f(R,B)$ [$\bar{\rho}_p(R,B)$] or simply $\bar{\rho}_f$[$\bar{\rho}_p$]. In the first summation of (68) [69)], the particular R and the corresponding $\rho_f(R,B)$ [$\rho_p(R,B)$] which give the maximum contribution to the summation are called the most probable nonpercolating [percolating] fraction of occupied bond and the most probable non-percolating [percolating] cluster-size distribution for the system, respectively. They will be denoted by R_f and $\tilde{\rho}_f$ [R_p and $\tilde{\rho}_p$], respectively. It is obvious that

$$\tilde{\rho}_f = \bar{\rho}(R_f, B), \tag{71}$$

and

$$\tilde{\rho}_p = \bar{\rho}(R_p, B). \tag{72}$$

The definition of cluster-size distributions and the most probable cluster-size distribution for other Ising-like spin models[15-23] may follow the procedure of the q-state Potts model. We proposed that in the calculation of the free energy and the physical quantities of the Ising-like spin models, we may retain only the term of the most probable cluster-size distribution.[27] This hypothesis on the most probable cluster-size distribution has been denoted as H-MPCSD.

To demonstrate that we may actually calculate the magnetic property of the QPM from its most probable cluster-size distribution (MPCSD), in this section we calculate the MPCSD for the QPM on a one-dimensional chain of lattice sites, in which E=N–1. Some typical subgraphs in the expansion of Eq. (2) for this one-dimensional system are shown in Fig. 5. Note that Fig. 5(d) is the only percolating subgraph G'_p for the system. It is obvious that in the very large N limit the contribu-

tion of the G'_p may be neglected for $T > 0$, which is the case considered in this section. It follows from Eq. (68) that the magnetic susceptibility is given by:

$$\chi = \lim_{B\to 0^+} \lim_{N\to\infty} \frac{\partial^2}{\partial B^2} (\ell N Z_f)/N$$

$$= \frac{1}{12}(q^2-1)S(K,q), \tag{73}$$

$$S(K,q) = \lim_{N\to\infty} \frac{\sum_{R=0}^{1} I(K,R) \sum_{\rho_f(R)} N(\rho_f(R)) q^{n_f} [\sum_{m=1}^{N} \ell_m m^2]/N}{\sum_{R=0}^{1} I(K,R) \sum_{\rho_f(R)} N(\rho_f(R)) q^{n_f}}, \tag{74}$$

where

$$n_f = \sum_{m=1}^{N} \ell_m . \tag{75}$$

Note that $S(K,q)$ is the mean cluster-size of the q-state bond-correlated percolation model (QBCPM) and the second summation in the denominator of Eq. (74) gives the nonpercolating geometrical factor:

$$g_f(q,R) = \sum_{\rho_f(R)} N(\rho_f(R))\, q^{n_f} . \tag{76}$$

For the linear-clain moded of the present section, there is no closed loop and we have:

$$g_f(q,R) = C^N_{RE}\, q^{n_f} = C^N_{R(N-1)}\, q^{(1-R)N+R} . \tag{77}$$

The hypothesis on the most probable cluster-size distribution (H-MPCSD) claims that it is necessary to keep only the terms of the MPCSD of the system in the denominator and numerator of Eq. (74). Thus

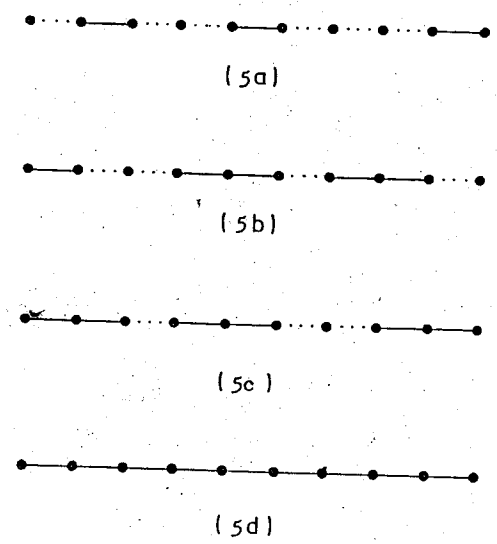

Fig. 5. Some typical subgraphs for the QPM and the corresponing QBCPM on a one-dimensional chain of lattice sites, in which E = N−1 = 9. The solid lines represent bonds in G'. Note that Fig. (5d) is the only percolating subgraph G'_p for the system.

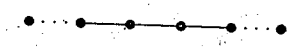

Fig. 6. A diagrammatic interpretation of Eq. (84). The (m−1) occupied bonds are separated from the rest of the subgraph by two vacant bonds. The sites connected by vacant bonds form an m-site cluster. In this example m=4.

$$S(K,q) = \lim_{N\to\infty} \frac{[\sum_{m=1}^{N} \ell_m \; m^2]\, \widetilde{\rho}_f}{N} \quad , \tag{78}$$

where the sum in the numerator is calculated for the MPCSD of the system, $\widetilde{\rho}_f$.

To calculate $\widetilde{\rho}_f$, we first calculate the MPCSD for a fixed R.

$$\bar{\rho}_f = \{ \bar{\ell}_1, \; \bar{\ell}_2, \ldots, \bar{\ell}_N \} . \tag{79}$$

Since the clusters in the present section are distributed on a one-dimensional chain of lattice sites, the clusters do not have closed loops and we may permute the clusters in a given subgraph to obtain other subgraphs. It follows from the above observation that the numbers ℓ_m, $1 \langle m \langle N$, in a given cluster-size distribution

$$\rho_f(R) = \{ \ell_1, \ell_2, \ldots, \ell_N \} . \tag{80}$$

satisfy the equation:

$$\sum_{m=1}^{N} \ell_m = n_f = N - RE = N - R(N-1) . \tag{81}$$

and the total number of subgraphs with $\rho_f(R)$ as their cluster-size distribution is

$$N(\rho_f(R)) = \frac{[(1-R)N+R]\,!}{\ell_1!\;\ell_2!\;\ell_3!\;\cdots\;\ell_N!} . \tag{82}$$

Now we should find the numbers $\bar{\ell}_m$, $1 \leq m \leq N$, which satisfy Eqs. (65) and (81) and maximize the logarithm of the number:

$$N(\rho_f(R))\; q^{n_f} = N(\rho_f(R))\; q^{(1-R)N+R} . \tag{83}$$

Using the method of Lagrange multiplier, we find that

$$\bar{\ell}_m = N(1-R)\, R^{m-1}\, (1-R) , \tag{84}$$

in the very large N limit, in which R may be neglected when compared with (1−R)N. This limit will be followed in the following. We may Eq. (84) a diagrammatic interpretation shown in Fig. 6, in which (m-1) occupied bonds are separated from the rest of the subgraph by two vacant bonds and the cluster is a m-site cluster.

With $\bar{\ell}_m$ of (84) in (79), it follows from (82), (83) and (77) that

$$\frac{1}{N} \ln [N(\bar{\rho}_f(R))\, q^{n_f}] = \frac{1}{N} \ln [g_f(q,R)]$$

$$= -(1-R) \ln(1-R) - R \ln R + (1-R) \ln q . \tag{85}$$

Note that $N(\rho_f(R))q^{n_f}$ is only one term of $g_f(q,R)$. Equation (85) shows that the term of the MPCSD dominates the contributions to the summation of Eq. (76).

It is obvious that the most probable nonpercolating fraction of occupied bond, R_f, may be determined from the equation:

$$\frac{d}{dR} \ell n \, [I(K,R)\, N(\rho_f(R))\, q^{n_f}] = 0. \tag{86}$$

It follows from Eqs. (21), (85) and (86) that

$$R_f = \frac{e^K - 1}{e^K + q - 1} \tag{87}$$

When R of Eq. (84) assumes of value of Eq. (87), we have the most probable cluster-size distribution

$$\widetilde{\rho}_f = \bar{\rho}_f (R_f, \, 0) . \tag{88}$$

Using such $\widetilde{\rho}_f$ in (78), we find that:

$$S(K,q) = \frac{2e^K + q - 2}{q} . \tag{89}$$

The magnetic susceptibility is given by:

$$\chi = \frac{1}{12} (q^2 - 1) \frac{(2e^K + q - 2)}{q} \tag{90}$$

The one-dimensional q-state bond-correlated percolation mode for q=1 corresponds one-dimensional random bond percolation model for which the mean cluster-size S has been calculated exactly[8]

$$S = \frac{1+p}{1-p} \quad . \tag{91}$$

With p of (3) in (91), we have

$$S = 2e^K - 1 \quad , \tag{92}$$

which is consistent with (89) for q=1.

To test the correctness of (90) for $q \geqslant 2$, we may calculate the exact χ using a transfer-matrix method[30] based on the subgraph expansion for the partition function and the correlation function. The calculated result[27] is the same as that of Eq. (90) for $q \geqslant 2$.

Besides the method of the transfer matrix[27], we have another simple method to obtain exact formula for the mean cluster-size S(K,q) of the one-dimensional QBCPM in which there is no closed loop in G'_f. It follows from the Euler theorem and Eq. (7) that the probability weight for a G'_f may be written as:

$$\begin{aligned} \Pi(G_f, p, q) &= p^{b(G')}(1-P)^{E-b(G')}\, q^{N-b(G')} \\ &= q(1+qe^{-K}-e^{-K})^E\, \bar{p}^{b(G'_f)}\,(1-p)^{E-b(G'_f)} , \end{aligned} \tag{93}$$

where

$$\bar{p} = R_f = \frac{e^K - 1}{e^K + q - 1} \quad . \tag{94}$$

It follows from (93) that the QBCPM on the one-dimensional lattice is equivalent to the random bond percolation problem in the same lattice with the effective bond probability $\bar{p}$ of (94). Using $\bar{p}$ to replace p of (91) we have following exact mean cluster-size for the QBCPM:

$$S(k,q) = \frac{2e^K + q - 2}{q} \tag{95}$$

which is the same as that of Eq. (89) obtained from the MPCSD. Such method may be extended to the Bethe lattice which also does not have closed loops.

It follows from the H-MPCSD, Eq. **(91) and (92) that the** free energy per spin of the QPM for $p < p_c$ (i.e. $T > T_c$), f_+, and $p > p_c$ (i.e. $T < T_c$), f_-, may be written as:

$$\begin{aligned} f_+ &= \lim_{N\to\infty} \frac{1}{N} \ln Z_f = \frac{z}{2} R_f \ln(e^K - 1) + \lim_{N\to\infty} \frac{1}{N} \ln N(\bar{\rho}_f(R_f)) \\ &\quad + \sum_{S=1}^{\infty} n_s(\epsilon, B) \ln[e^{BSj} + e^{BS(j-1)} + \ldots + e^{-BSj}] , \end{aligned} \tag{96}$$

$$\begin{aligned} f_- &= \lim_{N\to\infty} \frac{1}{N} \ln Z_p = \frac{z}{2} R_p \ln(e^K - 1) + \lim_{N\to\infty} \frac{1}{N} \ln N(\bar{\rho}_p(R_p)) \\ &\quad + \sum_{S=1}^{\infty} n_s(\epsilon, B) \ln[e^{BSj} + e^{BS(j-1)} + \ldots + e^{-BSj}] + BM_p(\epsilon, B), \end{aligned} \tag{97}$$

where

$$\epsilon = (p_c - p)/p_c \ , \tag{98}$$

$n_s(\epsilon, B)$ is the number of s-site clusters per site, and $M_p(\epsilon, B)$ is the number of sites per site in the percolating clusters. We expect that the singular parts of the free energy f_s come from the third terms of (96) and (97). We assume that near the critical point and for large s the dependent of n_s on B may be neglected and n_s may be written as

$$n_s \doteq s^{-\tau} f_c(x) , \tag{100}$$

$$x = s^{\sigma}\epsilon. \tag{101}$$

We assume further that the clusters of Eq. (100) contribute to the singular part of the free energy:

$$f_{singu}(\epsilon, B) = \sum_{s} n_s \ln [e^{BSj} + e^{BS(j-1)} + \ldots + e^{-BSj}] . \tag{102}$$

It is easy to show that

$$f_{singu}(\lambda^{y_T}\epsilon, \lambda^{y_B} B) = \lambda^d f_{singu}(\epsilon, B) , \tag{103}$$

where

$$y_T = d\sigma/\tau , \tag{104}$$

$$y_B = d/\tau . \tag{105}$$

Therefore $f_{singu}(\epsilon, B)$ is a generalized homogeneous function of ϵ and B. It is well known[28,29] that from Eq. (103) we may write $f_{singu}(\epsilon, B)$ in the scaling form and have the scaling law for the critical exponents of the spin model.

Now the most important problem is whether Eq. (100), which is similar to Eq. (1.2) of Ref. 34 for the random percolation problem, may be justified. Equation (1.2) of Ref. 34 has been confirmed by exact calculations for the one-dimensional lattice and the Bethe lattice[34] and by Monte-Carlo simulations for other lattices.[4,8,34] It is pointed out above that the q-state bond-correlated percolation model (QBCPM) on the one-dimensional lattice and the Bethe lattice, in which there are no closed loops, is equivalent to the random bond percolation problem on the same lattices with the effective bond probability $\bar{p}$ of (94). Therefore Eq. (100) is exactly true for the QBCPM on the one-dimensional lattice and the Bethe lattice as in the case random percolation. Our Monte-Carlo simulation test of Eq. (100) for the QBCPM on other lattices is in progress.

IV. Extension to Other Interacting Systems

Using the new idea[14,15] to define clusters, we have shown that a sublattice-dilute q-state Potts model (SDQPM)[35] may be mapped [15,21] into a sublattice-dilute q-state site-bond-correlated percolation model (SDQ-SBCPM), a dilute q-state Potts model (DQPM)[11] may be mapped into q-state site-bond-correlated percolation

model (QSBCPM),[36] the Ising model with multispin interactions (IMMI) may be mapped into a multisite correlated percolation model (MSCPM),[20] a lattice model for hydrogen-bonding in water molecules may be mapped into a bond-correlated percolation model.[17]

Based on the above connections, we have define the geometrical factors[20,21,36] for each lattice model and written down formula which give the free energy f, the internal energy U, and the specific heat C_h of a lattice model in terms of the logarithms of its geometrical factors, and their first and second derivatives. Such formula has been confirmed by exact[20,21] or numerical calculations[36] for the model in one dimension.

For hard-core particles on lattices, we may also define geometrical factors and relate the free energy f, the density of particle ρ, and the fluctuations of ρ to the geometrical factors and their first and second derivatives. For the one-dimensional system, the geometrical factors are known exactly. We find that the formula for f, ρ, and the fluctuations of ρ are confirmed by exact calculations for one-dimensional system.[36]

The hypothesis on the most probable cluster-size distribution (H-MPCSD) has also been confirmed by exact calculations for a one-dimensional Ising model with multispin interactions,[37] a one-dimensional ferromagnetic (antiferromagnetic) Ising model in nonzero external field, and a lattice model of hydrogen-bonding in water in external pressure.[38]

This work was supported by the National Science Council of the Republic of China (Taiwan) under contract number NSC75–0208–M001–11.

References

1. S.R. Broadbent and J.M. Hammersley, Proc. Cambridge Philos. Soc. 53, 629-641 (1957).
2. J.M. Hammersley, Proc. Cambridge Philos. Soc. 53, 642 (1957).
3. J.W. Essam, in Phase Transition and Critical Phenomena, edited by C. Domb and M.S. Green (Academic, New York, 1973), vol. 2, pp. 197-270.
4. D. Stauffer, Phys. Rep. 54, 1-74 (1979).
5. J.W. Essam, Rep. Prog. Phys. 43, 833-912 (1980).
6. D. Stauffer, A. Coniglio, and M. Adam, Adv. Polym. Sci. 44, 105 (1982).
7. Percolation Structures and Processes, edited by G. Deutscher, R. Zallen, and J. Adler (AIP, New York, 1983).

8. D. Stauffer, Introduction to Percolation Theory (Taylor and Francis, London, 1985).
9. H.N.V. Temperley, in Phase Transitions and Critical Phenomena, edited by C. Comb and M.S. Green (Academic, New York, 1973), vol. 1, pp. 227-267 (1982).
10. R.B. Potts, Proc. Cambridge Philos. Soc. 48, 106-109 (1952).
11. F.Y. Wu, Rev. Mod. Phys. 54, 235-268 (1982).
12. H. Muller-Krumbhaar, Phys. Lett. 50A, 27-28 (1974).
13. J. Kertesz, D. Stauffer, and A. Coniglio, in Percolation Structures and Processes, edited by G. Deutscher, R. Zallen, and J. Adler (AIP, New York, 1983).
14. C.-K. Hu, Phys. Rev. B29, 5103 (1984).
15. C.-K. Hu, Phys. Rev. B29, 5109 (1984).
16. C.-K. Hu, Physica 119A, 609 (1983).
17. C.-K. Hu, J. Phys. A16, L321 (1983).
18. C.-K. Hu, Annu. Rep. Inst. Phys. Acad. Sin. (Taiwan) 14, 7 (1984).
19. C.-K. Hu, Chin. J. Phys. (Taipei) 22, No. 1, 1 (1984) b. ibid 22, No. 4, 1 (1984).
20. C.-K. Hu, Chin. J. Phys. (Taipei) 23, No. 1, 47 (1985).
21. C.-K. Hu, Phys. Rev. B32, 7325 (1985).
22. C.-K. Hu, J. Phys. A19, xxx (1986).
23. C.-K. Hu and P. Kleban, Bull. Am. Phys. Soc. 26, 241 (1981); P. Kleban and C.-K. Hu, ibid., 27, 92 and 325 (1982), and Univ. of Maine preprint.
24. C.-K. Hu and P. Kleban, Ann. Rep. Inst. Phys. Acad. Sin. (Taiwan) 13, 3-22 (1983).
25. M.N. Barber, in Phase Transitions and Critical Phenomena edited by C. Domb and J.L. Labowitz (Academic, New York, 1983) Vol. 8, pp. 146-266.
26. Y. Imry, Phys. Rev. B21, 2042 (1980).
27. C.-K. Hu, Bull. Am. Phys. Soc. 31, 539 (1986); Phys. Rev. 34, xxxx (1986).
28. H.E. Stanley, Introduction to Phase Transitions and Critical Phenomena (Oxford University Press, New York, 1971).
29. A. Hankey and H.E. Stanley, Phys. Rev. B 6, 3515 (1972).
30. C.-K. Hu and H.Y. Lee, Chin. J. Phys. (Taipei) 22, No.3, 1-10 (1984).
31. H.M. Huang and Y.M. Shih, preprint.
32. C.-K. Hu, Chin. J. Phys. (Taipei), 24, xxx (1986).
33. I.N. Chern and C.-K. Hu, unpublished.
34. N. Nakanishi and H.E. Stanley, Phys. Rev. B22, 2466 (1980).
35. C.-K. Hu, Physica 116A, 265 (1982).

36. C.-K. Hu, preprints or unpublished data.
37. C.-K. Hu, Chin J. Phys. (Taipei) 24, xxx (1986).
38. C.-K. Hu and George C.S. Yang, short report given at the 1986 Summer School on Statistical Mechanics, Taipei, June 21-25, at Inst. of Phys., Academia Sinica (Taiwan).

SOLITON TRANSFORMATIONS FOR AXIALLY SYMMETRIC HIGHER DIMENSIONAL GRAVITY I. GENERALIZED NEUGEBAUER-KRAMER TRANSFORMATIONS

S. C. LEE.

Institute of Physics, Academia Somoca
Taipei, Taiwan 11529, Republic of China

Abstract

The field equations for axially symmetric gravitational fields in 4+K dimensions with K-dimensional toroidal compatification can be reduced to those of a generalized nonlinear sigma model. The dual symmetry of this model is considered first. Then we derive the soliton transformations for these equations using the method of Belinskii and Zakharov consequently generalizing their results to the higher dimensional case. From the result of one soliton transformation, a series of discrete symmetries generalizing the Nequgebauer-Kramer transformation in the four dimensional case are obtained. The basic properties of these new transformations are studied.

I. Introduction

Recently, some progress has been made toward the solutions of vacuum Einstein equations in higher dimensions under the Kaluaza-Klein [1-7]. First Sorkin [1] and Gross-Perry [2] discovered a monopole solution in five dimensions. Then we found that the field equations for spherically symmetric monopoles [3] and dyons [4] in this case can be completely integrated and explict integrations were carried out. The complete integrability was generalized to 4+K dimensions by discovering a Lax form for the field equations [5]. The explict integration in this case was accomplished later [6]. The spherically symmetric case represents solutions of vacuum Einstein equations in 4+K dimensions with 2+K commuting Killing vectors. It is natural to expect that the complete integrability might be extended to such general cases. In particular, we found [7] that the field equations for axially symmetric abelian Kaluza-Klein monopoles and dyons can be separated into two sets. The first set can be integrated by quadrature once the second set is solved

PACS 04.20. Jb, 04.50.+h

while the second set reduces to a generalized nonlinear sigma model [8], which posseses dual symmetry. When K equals zero, i.e. in four dimensions, this dual symmetry is known [9] and is related to a Lax pair proposed by Belinskii and Zakharov (B-Z) [10] as was shown by Cosgrove [11]. A Lax pair of the form of B-Z is also valid in the general case when K is nonzero. It is then possible to work out soliton transformations following the method of B-Z [10, 12]. In the five dimensional case, Belinsky and Ruffini [13] used B-Z two-soliton transformation to genreate asymptotic flat solutions from the trivial background. They found the solutions represent electric monopoles with magnetic dipole montents. Burzlaff and Maison [14] derived the linear eigenvalue problem by first constructing infinitely many conservation laws. In the series of works, we shall consider the generalization to arbitratry K. This may not be of immediate interest as a theory of higher dimensional gravity but it is quite interesting when considered as a theory generalizing the nonlinear sigma models [8]. In particular, one may ask, for example, if the rather successful formulation of Hauser and Ernst [15] for the K=0 case can be generalized to higher dimensions and used for sigma models. One key ingredient in the Hauser-Ernst formulation is the Neugebauer-Kramer (N-K) mapping [16]. Our main result in the present work is to show that this mapping admits generalizations to higher dimensions [17]. The generalized N-K transformations will play the central role in the theory of soliton transformations for axially symmetric higher dimensional gravity and for sigma models. In the following section, we shall write down the field equations and establish their relations to the genrealized non-linear sigma mdoel. The notations follow closely those of Ref. [7]. The dual symmetry transformation is then treated in detail. In section three, we derive the B-Z one soliton transformtion for all the relevant quantities so that iterations can be carried out readily. These two sections represent a straightforward generalizations of known results [10-14]. We include them for completeness and for setting up our notations for subsequent works. We then point our the fact that the B-Z one-soliton transformation can be written as successive transformations of a dual transformation followed by a certain discrete transformation and then a dual transformation again. This generalizes the known result of Cosgrove [11] for the vacuum Einstein equations in four dimensions. The discrete symmetries can then be identified as the generalized Neugebauer-Kramer (N-K) [16] transformations. Explicit formulas for them are given in section four. In section five, we derive the basic properties of the generalized N-K transformations. A brief discussion is given in section six.

II. Field Equations And Dual Symmetry

We shall consider the following metric in 4+K dimensions:

$$g = g_{\mu\nu}\, dx^{\mu} \otimes dx^{\nu} + \phi_{ab}(x)\, \theta^{a} \otimes \theta^{b}, \tag{1}$$

where

$$\theta^{a} = dy^{a} + A^{a}_{\mu}(x)\, dx^{\mu}. \tag{2}$$

y^a are coordinates of the internal space which is isomorphic to an abelian Lie group. For the four dimensional part of the metric, we asume that

$$g_{\mu\nu} dx^{\mu} dx^{\nu} = f\,(d\rho^2 + dz^2) + h_{\bar{\mu}\bar{\nu}} dx^{\bar{\mu}} dx^{\bar{\nu}}, \quad \bar{\mu} = t, \varphi \tag{3}$$

where f and $h_{\bar{\mu}\bar{\nu}}$ are functions of ρ, z only. We shall represent ρ, z by $x^{\mu'}$.

The curvature tensor of the metric can be found in Ref. [18]. The field equations are of the form of conserved currents. Explicitly, let us introduce the current [7]:

$$J = -\frac{\tau}{2} \begin{bmatrix} (\partial_{\mu'} h h^{-1})_{\bar{\mu}}{}^{\bar{\nu}} + \phi_{ab} h^{\bar{\nu}\bar{\lambda}} A^{a}_{\bar{\mu}} \partial_{\mu'} A^{b}_{\bar{\lambda}} & , & X_{\mu'\bar{\mu}}{}^{b} \\ \phi_{ab} h^{\bar{\mu}\bar{\nu}} \partial_{\mu'} A^{b}_{\bar{\mu}} & , & (\partial_{\mu'} \phi \phi^{-1})_{a}{}^{b} - \phi_{ac} h^{\bar{\mu}\bar{\nu}} A^{b}_{\bar{\nu}} \partial_{\mu'} A^{c}_{\bar{\mu}} \end{bmatrix} \tag{4}$$

where

$$X_{\mu'\bar{\mu}}{}^{b} = -(\partial_{\mu'} h h^{-1})_{\bar{\mu}}{}^{\bar{\nu}} A^{b}_{\bar{\nu}} + (\partial_{\mu'} \phi \phi^{-1})_{a}{}^{b} A^{a}_{\bar{\mu}} + \partial_{\mu'} A^{b}_{\bar{\mu}} - \phi_{ac} h^{\bar{\nu}\bar{\lambda}} A^{a}_{\bar{\mu}} A^{b}_{\bar{\nu}} \partial_{\mu'} A^{c}_{\bar{\lambda}},$$

then the field equation $\bar{R}_{a\mu} = 0$ corresponds to the conservation of the lower left block of $J_{\mu'}$, while the equations $\bar{R}_{\mu\nu} = 0$ and $\bar{R}_{ab} = 0$ correspond to the conservation of the upper and lower digonal blocks respectively. The conservation of $X_{\mu'\bar{\mu}}{}^{b}$ follows from these equations as an algebraic identity. The remaining field equations $\bar{R}_{\mu'\nu'} = 0$ can be written as

$$\partial_\xi^2 \tau - \partial_\xi \ln(-\bar{g})^{1/2} \partial_\xi \tau + \tau^{-1} \mathrm{Tr} J_\xi^2 = 0 , \tag{6}$$

$$\partial_\eta^2 \tau - \partial_\eta \ln(-\bar{g})^{1/2} \partial_\eta \tau + \tau^{-1} \mathrm{Tr} J_\eta^2 = 0 , \tag{7}$$

$$\partial_\xi \partial_\eta \ln(-\bar{g})^{1/2} = -\tau^{-2} \mathrm{Tr} J_\xi J_\eta .$$

Here we have introduced the complex coordinates

$$\xi = z - i\rho , \ \eta = z + i\rho$$

and the notations

$$(-\bar{g})^{1/2} = (-\det \bar{g})^{1/2} , \ \tau = (-\det h \cdot \det \phi)^{1/2} \tag{8}$$

The conservation of the trace of $J_{\mu'}$ implies

$$(\partial_\rho^2 + \partial_z^2)\tau = 0. \tag{9}$$

We shall introduce the conjugate harmonic function σ

$$\partial_z \tau = \partial_\rho \sigma , \ \partial_\rho \tau = -\partial_z \sigma , \tag{10}$$

and w, $\bar{w}$ such that

$$w = \tau + i\sigma , \ \bar{w} = \tau - i\sigma . \tag{11}$$

Note that w is an analytic function of η while $\bar{w}$ is an analytic function of ζ.

Once $J_{\mu'}$ is known, euation (6) can be used to get $(-\bar{g})^{1/2}$ and hence f by quadrature. Equation (7) follows from (6) and the conservation of $J_{\mu'}$. Indeed, it is the consistency condition of equation (6).

To see the relation with sigma models, let us introduce the vielbein:

$$h_{\bar{\mu}\bar{\nu}} = e_{\bar{\mu}}{}^{\bar{m}} e_{\bar{\nu}}{}^{\bar{m}} , \ (e^{-1})_{\bar{m}}{}^{\bar{\mu}} e_{\bar{\mu}}{}^{\bar{n}} = \delta_{\bar{m}}{}^{\bar{n}} ,$$

$$\phi_{ab} = e_a{}^m e_b{}^m , \ (e^{-1})_m{}^a e_a{}^n = \delta_m{}^n , \tag{12}$$

and the matrix G:

$$G = \begin{bmatrix} e_{\bar{\mu}}{}^{\bar{m}} & , & A^a{}_{\bar{\mu}} e_a{}^m \\ 0 & , & e_a{}^m \end{bmatrix} \tag{13}$$

Let σ denote the involutive automorphism on invertible matrices

$$\sigma(M) = (M^T)^{-1} , \ \sigma^2 = 1 \tag{14}$$

then

$$Q = \sigma(G) G^{-1} = (GG^T)^{-1} \tag{15}$$

depends only on the metric, indeed,

$$Q = \begin{bmatrix} h^{\bar{\mu}\bar{\nu}} & , & -h^{\bar{\mu}\bar{\nu}} A^a{}_{\bar{\nu}} \\ -h^{\bar{\mu}\bar{\nu}} A^a{}_{\bar{\mu}} & , & \phi^{ab} + h^{\bar{\mu}\bar{\nu}} A^a{}_{\bar{\mu}} A^b{}_{\bar{\nu}} \end{bmatrix} \tag{16}$$

The current $J_{\mu'}$ can be written as

$$J_{\mu'} = \frac{\tau}{2} Q^{-1} \partial_{\mu'} Q. \tag{17}$$

It follows that $J_{\mu'}$ satisfies the constraint

$$\partial_\xi J_\eta - \partial_\eta J_\xi + 2\tau^{-1} [J_\xi , J_\eta] - \tau^{-1} \partial_\xi \tau J_\eta + \tau^{-1} \partial_\eta \tau J_\xi = 0 \tag{18}$$

and the conservation equation

$$\partial_\xi J_\eta + \partial_\eta J_\xi = 0 . \tag{19}$$

Equations (18), (19) can be linearized. Following B-Z [10], we introduce the vector fields L_ζ, L_η:

$$L_\xi = \partial_\xi + 2\lambda(\tau + \lambda)^{-1} \partial_\xi \tau \partial_\lambda , \ L_\eta = \partial_\eta + 2\lambda(\tau - \lambda)^{-1} \partial_\eta \tau \partial_\lambda \tag{20}$$

it is easy to see that

$$[L_\xi , L_\eta] = 0. \tag{21}$$

The Lax pair is

$$L_\xi \psi(\cdot;\lambda) = 2(\tau+\lambda)^{-1}\psi(\cdot;\lambda)J_\xi ,$$
$$L_\eta \psi(\cdot;\lambda) = 2(\tau-\lambda)^{-1}\psi(\cdot;\lambda)J_\eta . \tag{22}$$

From equation (17), it follows that we can choose the normalization

$$\psi(\cdot;0) = Q. \tag{23}$$

We now change variables from λ to s such that $s(\cdot;\lambda)$ satisfies

$$ds(L_\xi) = 0,\ ds(L_\eta) = 0. \tag{24}$$

These equations can be integrated to give

$$s = f(\lambda + (w - \bar{w}) + \tau^2/\lambda) \tag{25}$$

where f(x) is an arbitrary smooth function. We choose $f(x) = x^{-1}$ so that

$$s = \lambda/\{\lambda^2 + (w-\bar{w})\lambda + \tau^2\} . \tag{26}$$

The Lax pair, equation (20), becomes in terms of ξ, η, s:

$$\partial_\xi U(\cdot;s) = \tau^{-1}(1+\gamma^{-1})U(\cdot;s)J_\xi ,$$
$$\partial_\eta U(\cdot;s) = \tau^{-1}(1+\gamma)U(\cdot;s)J_\eta \tag{27}$$

where

$$\psi(\cdot;\lambda) = U(\cdot;s)|_{s \text{ as in } (26)} \tag{28}$$

$$\gamma^{-1} = (1-2sw)^{1/2}(1+2s\bar{w})^{-1/2}. \tag{29}$$

Note that λ and γ are double valued functions of s so that λ, τ^2/λ correspond to the same s and so do $\gamma, -\gamma$. The value of $\psi(\cdot;\lambda)$, $U(\cdot;s)$, on the second sheet of the s surface will be denoted by $\tilde{\psi}(\cdot;\lambda)$, $\tilde{U}(\cdot;s)$ and they satisfy respectively equations (22), (27) with $\lambda \to \tau^2/\lambda$, $\gamma \to -\gamma$.

Equation (27) is the linearized quation expressing dual symmetry for the generalized nonlinear sigma models on symmetric spaces [8, 19]. Indeed, once equation (27) is solved, a new solution is given by

$$G^{(s)} = U(\cdot;s)G ,\ \tau^{(s)} = \tau/S^2 ,\ S^2 = (1-2sw)(1+2sw) \tag{30}$$

and

$$J_\xi^{(s)} = -\tau^{-1}\tau^{(s)}\gamma^{-1}U(\cdot;s)J_\xi U(\cdot;s)^{-1} = \frac{1}{2}\partial_\xi(\partial_s U U^{-1})$$
$$J_\eta^{(s)} = -\tau^{-1}\tau^{(s)}\gamma U(\cdot;s)J_\eta U(\cdot;s)^{-1} = \frac{1}{2}\partial_\eta(\partial_s U U^{-1}) \tag{31}$$

with

$$w^{(s)} = w/(1-2sw) ,\ \bar{w}^{(s)} = \bar{w}/(1+2sw) \tag{32}$$

the transformed U is given by

$$U^{(s)}(\cdot;s') \doteq \tilde{U}(\cdot;s'+s)U(\cdot;s)^{-1} \tag{33}$$

where a dot means equal up to multiplication on the left by constant matrix. The new Q follows from equations (15), (30) and also from equations (23), (33):

$$Q^{(s)} = \sigma(U(\cdot;s)QU(\cdot;s)^{-1} \doteq \tilde{U}(\cdot;s)U(\cdot;s)^{-1} \tag{34}$$

which is manifestly symmetric.

In going from equation (30) to (32), we have fixed an arbitrary additive constant. By fixing this constant, we have made the abelian character of the dual symmetry transformation manifest as is clear from equation (33) which can be used to generate successive dual transformations. In the four dimensional case (i.e. K = 0), this dual symmetry transformation corresponds to Neugebauer's I_2 transformation, or, more precisely, Cosgrove's $\tilde{Q}_{4_s}$s transformation [11, 20]. Let us also note that for successive dual transformations, we can choose either sheet of the s-surface at each

stage so that there are two variants of equation (34) and four variants of equation (33). We shall consistently use tilde to denote quantities on the second sheet.

Note that the last equality in equation (31) gives the potential for the conserved currents $J_\mu{}'^{(s)}$. If we expand $J_\phi{}'^{(s)}$ around s=0, we get infinitely many nonlocal conserved currents with the corresponding potentials given by

$$\frac{1}{2}\partial_s U U^{-1} = R_0 + 2sR_1 + 2s^2 R_2 + \cdots \tag{35}$$

$$U = (1 + 2sR_0 + 2s^2 (R_0^2 + R_1) + \ldots)\, Q \tag{36}$$

The R_i's will be called the "higher potentials". They are introduced mainly for later use.

From equations (8), (13) and (15), we find that

$$\det Q = -1/\tau^2 . \tag{37}$$

$\mathrm{Det}Q^{(s)}$ however does not satisfy the corresponding constraint. Indeed, it follows from the trace of equation (27) that

$$\det U(\cdot;s) \doteq s/\lambda \tag{38}$$

so that

$$\det Q^{(s)} \doteq -\lambda^2/s^2\tau^2 . \tag{39}$$

A solution which satisfies the proper constraint can be obtained by renormalization:

$$Q^{(s)} = (sS^2/\lambda)^{2/n} Q^{(s)}, \quad n = K + 2 \tag{40}$$

with the corresponding change

$$\hat{J}_\xi{}^{(s)} = J_\xi{}^{(s)} - \frac{1}{n}\tau^{(s)}\tau^{-1}\gamma_s{}^{-1}(1+\gamma_s{}^{-1})$$
$$\hat{J}_\eta{}^{(s)} = J_\eta{}^{(s)} - \frac{1}{n}\tau^{(s)}\tau^{-1}\gamma_s(1+\gamma_s) \tag{41}$$

where the subscript s for γ means evaluating at s. Denoting the transformed γ by

$\gamma^{(s)}$, we find from equations (29) and (32)

$$\gamma_{s'}^{(s)} = \gamma_s{}^{-1}\gamma_{s+s'} . \tag{42}$$

Similarly, we find the transformation law for S to be

$$S_s^{(s)2} = S_s^{-2} S_{s+s'}^2 \tag{43}$$

The renormalization necessary for $U^{(s)}$ is found to be

$$\hat{U}^{(s)}(\cdot;s') \doteq \{2sS(\gamma_s+\gamma_{s+s'})/(1-\gamma_s)(1-\gamma_{s+s'})\}^{2/n} U^{(s)}(\cdot;s') \tag{44}$$

Substituting equation (41) into equation (6), we find that

$$(-\bar{g}^{(s)})^{1/2} \doteq (-\bar{g})^{1/2}(\lambda^2/s^2 S)^{2/n} S^{-4} \tag{45}$$

This completes our derivation of the dual symmetry transformation. The formulas are clearly ready for iteration. Apart from the renormalization factor, the symmetry is essentially abelian. As we shall see in the following section, dual symmetry is closely related to the B-Z soliton transformation.

III. Soliton Transformations

Given Q, $J_\mu{}'$ and $\psi(\cdot;\lambda)$ satisfying equation (22), we seek a new solution $\psi'(\cdot;\lambda)$ by dressing ψ [10, 12]:

$$\psi'(\cdot;\lambda) = \psi(\cdot;\lambda)\chi(\cdot;\lambda), \quad Q' = \psi'(\cdot;0) . \tag{46}$$

It is clear that Q′ in general need not be symmetric. How can be get a symmetric Q′? Note that the symmetry requirement of Q can be expressed as

$$\sigma(Q)Q = 1. \tag{47}$$

If we normalize ψ as in equation (23) and normalize $\tilde{\psi}(\cdot;\lambda)$ by

$$\tilde{\psi}(\cdot;0) = 1 \tag{48}$$

then it is clear that to insure condition (45), we have only to require

$$\sigma(\psi(\cdot;\lambda))Q = \tilde{\psi}(\cdot;\lambda). \tag{49}$$

That this is possible can be seen from the second equality of equation (34). Requiring ψ', $\tilde{\psi}'$ to satisfy equations (48), (49) is equivalent to requiring

$$\tilde{\chi}(\cdot;0) = 1 \tag{50}$$

and

$$\sigma(\chi(\cdot;\lambda))Q' = Q\tilde{\chi}(\cdot;\lambda). \tag{51}$$

The dressing matrix $\chi(\cdot;\lambda)$ in general can be represented as a sum over discrete poles on the λ plane together with a line integral over a closed curve [12]. When only the pole terms exist, the transformation is called pure solitonic. For pure soliton transformations, we write

$$\chi(\cdot;\lambda) = 1 + \Sigma_{i=1}^{M} Q_i(\cdot)/(\lambda - \lambda_i),$$
$$\chi(\cdot;\lambda)^{-1} = 1 + \Sigma_{i=1}^{M}(\cdot)/(\lambda - \mu_i). \tag{52}$$

In general, N need not equal M, but the constraint (51) requires that they be equal and form pairs:

$$\mu_i = \tau^2/\lambda_i, \quad i = 1, \ldots, N. \tag{53}$$

Substituing equations (46) and (52) into equation (22), and requiring the residues of the double poles at $\lambda = \lambda_i$, $\lambda = \mu_i$ to vanish, we find that λ_i, μ_i have to satisfy the partial differential equation

$$\partial_\xi y = 2y(\tau + y)^{-1}\partial_\xi \tau, \quad \partial_\eta y = 2y(\tau - y)^{-1}\partial_\eta \tau, \tag{54}$$

which can be integrated so that

$$\lambda_i + (w - \bar{w}) + \tau^2/\lambda_i = 1/s_i \tag{55}$$

and μ_i satisfies the same equation with the same constant s_i, following from equation (53). It is now clear why we made the particular choice when going from equation (25) to equation (26).

In the following, we shall consider the case N = 1. The general N-soliton transformations can be obtained by iteration. Their explicit formulas will be presented in a subsequent work. The one soliton transformation that we shall consider preserves the symmetric tensor character of Q but need not preserve reality. The reality condition is easy to satisfy and we shall comment on this later.

Putting N = M = 1 in equation (52) and umltiplying the two expressions, we find the algebraic constraints:

$$R_1 = -Q_1, \quad Q_1 = Q_1^2/(\lambda_1 - \mu_1), \quad R_1 = R_1^2/(\mu_1 - \lambda_1) \tag{56}$$

which imply

$$P_1 = Q_1/(\lambda_1 - \mu_1) = R_1/(\mu_1 - \lambda_1), \quad P_1^2 = P_1 \tag{57}$$

is a projection operator. Using P_1, we can write

$$\chi(\cdot;\lambda) = 1 - P_1 + (\lambda - \mu_1)(\lambda - \lambda_1)^{-1}P_1. \tag{58}$$

Let the rank of P_1 be q_1, then we have

$$\mathrm{Tr}P_1 = q_1, \quad \det\chi(\cdot;\lambda) = (\lambda - \mu_1)^{q_1}(\lambda - \lambda_1)^{-q_1}. \tag{59}$$

The matrix P_1 can be written as

$$P_1 = X_1(F_1^+ X_1)^{-1}F_1^+, \quad X_1, F_1 = \text{complex } n \times q_1 \text{ matrices.} \tag{60}$$

Fromthe partial differential equations satisfied by $\chi(\cdot;\lambda)$, we find that P_1 satisfies

$$(1 - P_1)(\partial_\xi + 2(\tau + \lambda_1)^{-1}J_\xi)P_1 = 0,$$
$$(1 - P_1)(\partial_\eta + 2(\tau - \lambda_1)^{-1}J_\eta)P_1 = 0, \tag{61}$$

and

$$P_1 (\overleftarrow{\partial}_\xi - 2(\tau + \mu_1)^{-1} J_\xi)(1 - P_1) = 0,$$

$$P_1 (\overleftarrow{\partial}_\eta - 2(\tau - \mu_1)^{-1} J_\eta)(1 - P_1) = 0. \tag{62}$$

It follows that we may require

$$(\partial_\xi + 2(\tau + \lambda_1)^{-1} J_\xi) X_1 = 0, \ (\partial_\eta + 2(\tau - \lambda_1)^{-1} J_\eta) X_1 = 0 \tag{63}$$

so that

$$X_1 = \psi^{-1}(\cdot;\lambda_1) X_1^{(0)} \tag{64}$$

for some constant matrix $X_1^{(0)}$.

To find the remaining part of P_1, we use equation (51). Requiring Q' to have no poles on the λ plane, we find

$$P_1^T Q(1 - P_1) = 0, P_1^T Q = QP_1 \tag{65}$$

which can be solved for $(F_1^+ X_1)^{-1} F_1^+$ to give

$$P_1 = X_1 (X_1{}^T Q X_1)^{-1} X_1{}^T Q. \tag{66}$$

Using equations (34) and (64), we find

$$P_1 = \psi^{-1}(\cdot;_1) P_1^{(s_1)} \psi(\cdot;\lambda_1), \tag{67}$$

where

$$P_1^{(s_1)} = X_1^{(0)} (X_1^{(0)T} Q^{(s_1)} X_1^{(0)})^{-1} X_1^{(0)T} Q^{(s_1)} \tag{68}$$

Note that from equations (67) and (34) one can see that equation (62) is satisfied.

It follows from equations (46) and (58) that

$$\psi'(\cdot;\lambda) = \psi(\cdot;\lambda)\psi(\cdot;\lambda_1)^{-1}(1 - P_1^{(s_1)} + \frac{\lambda - \mu_1}{\lambda - \lambda_1} P_1^{(s_1)})\psi(\cdot;\lambda_1) \tag{69}$$

and

$$\hat{Q}' = (\frac{\lambda_1}{\mu_1})^{q_1/n} Q \psi(\cdot;\lambda_1)^{-1} (1 - P_1^{(s_1)} + \frac{\mu_1}{\lambda_1} P_1^{(s_1)})\psi(\cdot;\lambda_1) \tag{70}$$

where proper renormalization has been imposed on Q'. The renomalized ψ' is then

$$\psi'(\cdot;\lambda) = (\frac{\lambda - \lambda_1}{\lambda - \mu_1})^{q_1/n} \psi'(\cdot;\lambda). \tag{71}$$

The transformation law for the current J_μ, follows from the differential equations for $\chi(\cdot;\lambda)$. By examining the behavior of these equations near $\lambda = \pm\tau$, we find

$$\hat{J}'_\xi = \chi(\cdot;-\tau)^{-1} [J_\xi + \tau\partial_\xi\tau \ \frac{\mu_1 - \lambda_1}{(\tau+\lambda_1)(\tau+\mu_1)} \ (\frac{g_1}{n} - P_1)] \chi(\cdot;-\tau)$$

$$\hat{J}'_\eta = \chi(\cdot;\tau)^{-1} [J_\eta - \tau\partial_\eta\tau \ \frac{\mu_1 - \lambda_1}{(\tau-\lambda_1)(\tau-\mu_1)} \ (\frac{g_1}{n} - P_1)] \chi(\cdot;\tau). \tag{72}$$

Substituting equation (72) into equation (6) and using the relations

$$\mathrm{Tr}(X_1^T Q X_1)^{-1} \partial_\xi (X_1^T Q X_1) = \frac{2}{\tau} \ \frac{\tau - \lambda_1}{\tau + \lambda_1} \ \mathrm{Tr} J_\xi P_1,$$

$$\mathrm{Tr}(X_1^T Q X_1)^{-1} \partial_\eta (X_1^T Q X_1) = -\frac{2}{\tau} \ \frac{\tau + \lambda_1}{\tau - \lambda_1} \ \mathrm{Tr} J_\eta P_1, \tag{73}$$

which follow from equation (63), we obtain

$$(-\hat{\bar{g}}')^{1/2} = (-\bar{g})^{1/2} \det(X_1^{(0)T} \hat{Q}^{(s_1)} X_1^{(0)}) \ (\tau/S_1^2)^{q_1(n-q_1+2)/n} \tag{74}$$

where

$$S_1^2 = (1 - 2s_1 w)(1 + 2s_1 \bar{w}). \tag{75}$$

Equations (70), (71) and (74) represent the full results for one soliton transformation which can be iterated any number of times.

Now we shall say a few words about the condition for the metric to be real. From equations (22) and (27), one can see that to insure reality, we can require

$$\psi^*(\cdot;\lambda) = \psi(\cdot;-\lambda), \ U^*(\cdot;s) = U(\cdot;-s). \tag{76}$$

It follows that for $Q^{(s)}$ in equation (34) to be real, we have to chooses to be pure imaginary. For soliton transformations, insisting condition (76) for $\psi'(\cdot;\lambda)$ and hence $\chi(\cdot;\lambda)$, we see from equation (52) that if λ_i is a pole, $-\lambda_i^*$ must also be a pole. This also implies, from equation (55), that the constants s_i chosen must from $(s_i, -s_i^*)$ pairs unless s_i is pure imaginary. Moreover, for $(s_i, -s_i^*)$ pairs, the corresponding

Q_i, R_i have to form $(Q_i, -Q^*)$ and $(R_i, -R^*)$ pairs. For one soliton transformation, the only choice is to have s_1, λ_1, Q_1 pure imaginary so that P is real. This can be achieved by requiring

$$X^{(0)*} = cX^{(0)}, \tag{77}$$

where c is an arbitrary constant.

Finally, let us make the following observation. In equation (69) for B-Z one soliton transformation, we replace λ by $\mu = \tau^2/\lambda$ and notice that

$$\frac{\mu - \mu_1}{\mu - \lambda_1} = -(\gamma_{s_1} + 1)(\gamma_{s_1} - 1)^{-1}(\gamma_{s-s_1}^{(s_1)} - 1)(\gamma_{s-s_1}^{(s_1)} + 1)^{-1} \tag{78}$$

Equation (69) can then be written as

$$\tilde{\psi}'(\cdot;\lambda) = \Phi(\cdot;s-s_1)\ \Phi(\cdot;-s_1)^{-1} \tag{79}$$

where

$$\Phi(\cdot;s-s_1) = U(\cdot;s)U(\cdot;s_1)^{-1}\left(1 - P_1^{(s_1)} + \frac{\gamma_{s-s_1}^{(s_1)} - 1}{\gamma_{s-s_1}^{(s_1)} + 1} P_1^{(s_1)}\right) \tag{80}$$

and we have used the relation

$$\gamma_s^{-1} = \gamma_{-s}^{(s)} \tag{81}$$

which follows from equation (42).

Recalling the definition of $P_1^{(s_1)}$ in equation (68) and comparing equations (79), (80) with the dual symmetry transformation equation (33) and its variants, we see that the B-Z on soliton transformation consists of successive transformations of the form $I_2 I^{(q_1)} I_2$ where I_2 is a dual symmetry transformation and $I^{(q_1)}$ is a certain discrete transformation which can be read off from equation (80). Let us recall that for the four dimensional (K=0) case, Cosgrove [11] showed that the B-Z one soliton transformation can be written as $I_2 I I_2$ where I is the Neugebauer-Kramer [16] transformation. Hence we see that the Neugebauer-Kramer symmetry generalizes to a series of discrete symmetries [17]. In the following section, we derive the formulas for these symmetry transformations.

IV. Generalized Neugebauer-Kramer Mapping

The discussions at the end of the previous section suggest that we seek a new solution by writing the new generating function $U_I(\cdot;s)$ in the form

$$U_I(\cdot;s) = A(s)\,\tilde{U}(\cdot;s)\ [1 - P + (\gamma+1)(\gamma-1)^{-1}P]\ Y^{-1}(\cdot) \tag{82}$$

where $Y(\cdot)$ is a matrix function of ξ, η, undetermined from the soliton transformation. A(s) is an invertible matrix function of s only and P is a projection operator defined by

$$P = X_0 (X_0^T Q X_0)^{-1} X_0^T Q \tag{83}$$

where X_0 is a constant complex nxq matrix of rank q with $1 \leqslant q < n$.

As before, Q_I will be given by $U_I(\cdot,0)$. From equation (82), we find that in order for Q_I to exist, we must require

$$A(0)P = 0 \tag{84}$$

This is achieved by the minimum choice

$$A(s) = 1 - P_0 + 2sP_0 \tag{85}$$

where

$$P_0 = X_0 (X_0^T k_0 X_0)^{-1} X_0^T k_0 \tag{86}$$

with k_0 an arbitrary invertible matrix. This choice is minimum in the sense that any other choice can be obtained by multiplying A(s) on the left by another matrix B(s) which is analytic and invertible at s=0. Such modifications, as we shall see, affect the formulas for Q_I only trivially.

As in the case of soliton transformation, to insure that Q_I be symmetric, we shall require the validity of equations (48), (49) for $\tilde{U}_I$, U_I. This together with the fact that $\tilde{U}_I$ is the analytic continuation of U_I onto the second sheet so that it is essentially determined by U_I with the change $\tau \to -\tau$, $U_- \to U$, we obtain

$$\tilde{U}_1(\cdot;s) = \sigma(A(s))\, U(\cdot;s)\, (1 - P + \tfrac{\gamma+1}{\gamma+1} P)\, Y^{-1}(\cdot) \tag{87}$$

and

$$Q_1 = \sigma(Y)\, Q\, Y^{-1} \tag{88}$$

with $Y(\cdot)$ given by

$$\begin{aligned} Y(\cdot) &= \lim_{s\to 0} \sigma(A(s))\, U(\cdot;s)\, (1 - P + \tfrac{\gamma-1}{\gamma+1} P) \\ &= [1 - P^T + \tfrac{1}{2}\tau P^T + P^T R_0 (1 - P^T)]\, Q \end{aligned} \tag{89}$$

where R_0 is the first potential defined in equation (35). The inverse of $Y(\cdot)$ is easily found to be

$$Y^{-1}(\cdot) = Q^{-1}[1 - P_0^T + 2\tau^{-1} P^T - 2\tau^{-1} P^T R_0 (1 - P_0^T)] \tag{90}$$

One can check by straightforward computation that

$$\begin{aligned} \partial_\xi U_1(\cdot;s) &= \tau^{-1}(1+\gamma^{-1})\, U_1(\cdot;s)\, J_{1\xi} \\ \partial_\eta U_1(\cdot;s) &= \tau^{-1}(1+\gamma)\, U_1(\cdot;s)\, J_{1\eta} \end{aligned} \tag{91}$$

with

$$\begin{aligned} J_{1\xi} &= -Y[(1-P)J_\xi(1-P) + PJ_\xi P - PJ_\xi(1-P) - (1-P)J_\xi P + \partial_\xi \tau P]\, Y^{-1} \\ J_{1\eta} &= -Y(J_\eta + \partial_\eta \tau P)\, Y^{-1} \end{aligned} \tag{92}$$

From equation (6), we find the transformation formula for g:

$$(-\bar{g}_1)^{1/2} = (-\bar{g})^{1/2}\, \tau^q \det(X_0^T Q X_0) \tag{93}$$

The lack of symmetry between ξ and η in equation (92) shows the complex character of generalized N-K transformations. Indeed, if we call the above transformation $I^{(q)}$, than there exists the conjugate transformation $I_*^{(q)}$ given by

$$U_{1*}(\cdot;s) = A_*(s)\, \tilde{U}(\cdot;s)\, [1 - P - (\gamma+1)(\gamma-1)^{-1} P]\, Y_*^{-1}(\cdot) \tag{94}$$

choosing

$$A_*(s) = 1 - P_0 - 2sP_0 \tag{95}$$

we have

$$\begin{aligned} Y_*(\cdot) &= \lim_{s\to 0} \sigma(A_*(s))\, U(\cdot;s)\, (1 - P - \tfrac{\gamma-1}{\gamma+1} P) \\ &= [1 - P^T + \tfrac{1}{2}\tau P_0^T - P_0^T R_0 (1 - P^T)]\, Q \end{aligned} \tag{96}$$

The currents now transform as

$$\begin{aligned} J_{1*\xi} &= -Y_*(J_\xi + \partial_\xi \tau P)\, Y_*^{-1} \\ J_{1*\eta} &= -Y_*[(1-P)J_\eta(1-P) + PJ_\eta P - PJ_\eta(1-P) - (1-P)J_\eta P + \partial_\eta \tau P]\, Y_*^{-1} \end{aligned} \tag{97}$$

If we change A(s) by multiplying the minimum form on the left by B(s), $Y(\cdot)$ will be modified to $B(0)\, Y(\cdot)$. This amounts to applying an additional symmetry transformation, namely, the global rotation of the K+2 commuting Killing vectors by B(0).

Notice that the potential R_0 appears in the generalized N-K transformations. For completeness and for later use, we give the transformation law for R_0, which follows from equation (82) and the definition of the potential,

$$\begin{aligned} R_{10} &= P_0(P\tilde{R}_0 - i\sigma)\, P_0 + (1 - P_0)\, \tilde{R}_0 (1 - P)(1 - P_0) \\ &\quad - (1 - P_0)[i\sigma \tilde{R}_0 + \tfrac{1}{2}(\tilde{R}_0^2 - \tilde{R}_1) - \tilde{R}_0 P \tilde{R}_0]\, P_0 - P_0 P (1 - P_0) \end{aligned} \tag{98}$$

where σ is defined in equation (10) and $\tilde{R}_0$, $\tilde{R}_1$ are potentials on the second sheet. In fact, due to equation (47), we have the relations

$$\tilde{R}_i = -R_i^T \qquad \forall_i . \tag{99}$$

The generalized N-K transformations $I^{(q)}(k_0, X_0)$ depends on the matrix

parameters k_0 and X_0. One can show that the inverse transformation is

$$I^{(q)}(k_0, X_0)^{-1} = I^{(q)}(k_0^{-1}, k^T X_0) \tag{100}$$

so that $I^{(q)}$ is involutive when $K_0 = 1$. Although we have "derived" the N-K transformations from the B-Z one-soliton transformations, the exact relation between them requires more careful treatment and will be given in the next section.

V. Basic Properties Of N-K Transformations

Let us begin by introducing some obvious symmetry transformations. Let Q be a solution and $U(\cdot;s)$ the corresponding generating function. Then

$$Q \to \sigma(Q) = Q^{-1}, \quad U \to \sigma(U), \quad \tilde{U} \to \sigma(\tilde{U}) \tag{101}$$

is also a solution. We shall also use σ to denote this symmetry transformation despite possible confusions. From equations (33) and (34), we can see that

$$I_2^{(0)} = \sigma \tag{102}$$

It is convenient to define $\tilde{I}_2^{(s)}$ by

$$\tilde{I}_2^{(s)} = \sigma I_2^{(s)} \tag{103}$$

Similarly, we shall define

$$\hat{I}^{(q)}(k_0, X_0) = \sigma I^{(q)}(k_0, X_0) \tag{104}$$

Let $C \in SL(n, R)$, $n = K+2$. Then we have the symmetry transformation $R(C)$:

$$R(C)Q = \sigma(C) Q C^{-1}, \; R(C)U = \sigma(C) U C^{-1}, \; R(C)U = CUC^{-1} \tag{105}$$

Finally, let $G(s) \in GL(n, C)$ be a function of s only and $G(0) = 1$. Then we have the trivial gauge transformation $L(G)$

$$L(G)U = G(s)U(\cdot;s), \quad L(G)\tilde{U} = \sigma(G)\tilde{U} \tag{106}$$

which leaves Q unchanged.

There is another symmetry transformation which arises from projective transformations of ρ, z coordinates treating Q and U as scalar funcitons of ρ, z. This symmetry transformation is important for some purposes but will not be considered here.

The following commutation relations among these symmetry transformations can be easily derived:

$$\sigma \tilde{I}_2^{(s)} = \tilde{I}_2^{(s)} \sigma, \tag{107}$$

$$R(C)\tilde{I}_2^{(s)} = \tilde{I}_2^{(s)} R(C) \tag{108}$$

$$R(C) \cdot \sigma = \sigma \cdot R(\sigma(C)) \tag{109}$$

$$R(C)\hat{I}^{(q)}(k_0, X_0) = \hat{I}^{(q)}(\sigma(C) k_0 C^{-1}, CX_0)) R(C) \tag{110}$$

$$\sigma \hat{I}^{(q)}(k_0, X_0) = \hat{I}^{(q)}(k_0^{-1}, \sigma(k_0)^{-1} X_0)^{-1} \sigma \tag{111}$$

$$\tilde{I}_2^{(s_1)} L(G(s)) = L(G(s+s_1) G(s_1)^{-1}) R(\sigma(G(s_1))) \tilde{I}_2^{(s_1)} \tag{112}$$

$$L(G(s))\tilde{I}_2^{(s_1)} = \tilde{I}_2(s_1) L(G(s-s_1) G(-s_1)^{-1}) R(\sigma(G(s_1))) \tag{112'}$$

$$R(C) L(G(s)) = L(\sigma(C) G \sigma(C)^{-1}) R(C) \tag{113}$$

$$\sigma L(G(s)) = L(\sigma(G(s))\sigma \tag{114}$$

$$\hat{I}^{(q)} L(G(s)) = L(\sigma(A(s)) G(s) \sigma(A(s))^{-1} \sigma(C)^{-1}) R(C) \hat{I}^{(q)}, \tag{115}$$

$$\sigma(C) = \lim_{s \to 0} \sigma(A(s)) G(s) \sigma(A(s))^{-1}.$$

Now we may give the exact relations between B-Z one-soliton transformation $I_{BZ}^{(s_1)}(X_0)$ and the N-K transformations $\hat{I}^{(q)}(k_0, X_0)$:

$$\sigma I_{BZ}^{(s_1)}(X_0)\sigma =$$

$$R(\sigma(A(-s_1)^{-1}) L(A(-s_1) A(s-s_1)^{-1}) \tilde{I}_2^{(-s_1)} \hat{I}^{(q)}(k_0, X_0) \tilde{I}_2^{(s_1)} \tag{116}$$

Note that the B-Z one-soliton transformation is singular at $s_1=0$ and $s=s_1$. The SL(n, R) factor and the gauge transformation removes the singularities so that $\tilde{l}_2^{(-s_1)}\hat{l}^{(q)}\tilde{l}_2^{(s_1)}$ is regular at these points. Aside from these factors, we may think of $\hat{l}^{(q)}$ as the basic one-soliton transformation while $\tilde{l}_2^{(s_1)}$ merely translates the position of the pole in the s-plane.

Because of equation (110), we have only to consider the case $k_0=1$. We shall therefore set $k_0=1$ and omit k_0 from the arguments of $\hat{l}^{(q)}$. As we have noted in the previous section, $l^{(q)}(X_0)$ is involutive

$$l^{(q)}(X_0)^2 = 1 \tag{116'}$$

On the other hand, $\hat{l}^{(q)}(X_0)$ can be raised to any power. We shall first show that it is enough to consider the rank one case i.e. q=1. We shall omit the superscript q from $\hat{l}^{(q)}$ when the rank of X_0 is clear or is irrelevant.

Let us consider two successive rank one $\hat{l}$ transformations. Recall that $Q=\sigma(G)G^{-1}$ from equation (15). We shall chose a gauge so that G satisfies

$$(1-P_0)GP_0 = 0 \tag{117}$$

which implies

$$(1-P_0)G^{-1}P_0 = 0, \quad PG = GP_0, G^{-1}P = P_0G^{-1} \tag{118}$$

In proving these, we used the identity

$$(X_0^TX_0)^{-1}(X_0^TGX_0)(X_0^TX_0)^{-1} = (X_0^TG^{-1}X_0)^{-1} \tag{119}$$

which is valid in this gauge.

Equation (88) implies that we may choose

$$G_l = YG$$
$$= (1-P_0)\sigma(G)(1-P_0)+\frac{\tau}{2}P_0\sigma(G)P_0R_0(1-P_0)\sigma(G)(1-P_0) \tag{120}$$

which again is in the gauge of equation (117). The N-K transformation given by equation (82) can now be expressed as

$$U_{\hat{l}}G_{\hat{l}} = \sigma(A(s))(UG)(1-P_0+\frac{\gamma-1}{\gamma+1}P_0) \tag{121}$$

Now consider two $\hat{l}$ transformations denoted as $\hat{l}_1$, $\hat{l}_2$ with the corresponding projection operators P_{01}, P_{02} satisfying

$$P_{01}P_{02} = P_{02}P_{01} = 0 \tag{122}$$

so that $P_{01}+P_{02}$ is a rank two projection operator.

From equation (120), we find that

$$G_{\hat{l}_1} = (1-P_{01})G(1-P_{01})+\frac{2}{\tau}(1-P_{01})\tilde{R}_0GP_{01}+\frac{2}{\tau}P_{01}GP_{01} \tag{123}$$

In order to apply equation (121), G_{l_1} has to be chosen in the gauge

$$(1-P_{02})G_{l_1}P_{02} = (1-P_{01}-P_{02})GP_{02} = 0 \tag{124}$$

This can always be done and we find

$$\hat{l}(P_{02})\hat{l}(P_{01}) = \hat{l}(P_{01}+P_{02}) \tag{125}$$

The iterations can be continued. We have to choose G to satisfy

$$(1-\sum_{i=1}^{m}P_{0i})GP_{0m} = 0 \quad \forall\ m = 1,\ldots,n-1 \tag{126}$$

Let e_i be an orthonormal basis for R^n and $P_{0i}=e_ie_i^T$. In this basis, G satisfies equation (126) if and only if it is upper triangular. Carrying out n-1 iterations we find

$$\hat{l}(e_n)\ldots l(e_1)(UG) = (\frac{\lambda}{2s\tau})UG$$
$$\hat{l}(e_n)\ldots l(e_1)(UG) = (\frac{2s\tau}{\lambda})UG \tag{127}$$

The factor $(\lambda/2s\tau)$ can be renormalized away. It appears because we have not carried out the proper renormalization in the formulas (82) and (87), but they can always be done in the last step of successive transformations. With this in mind, we can write equations (125), (127) as

$$\hat{l}(e_i)\hat{l}(e_j) = \hat{l}(e_j)\hat{l}(e_i) = \hat{l}(e_ie_j) \qquad i\neq j \tag{128}$$

$$\hat{I}(e_n) \ \ldots \ \hat{I}(e_1) = 1 \tag{129}$$

Note that we have used e_i to represnt P_{0i} and e_ie_j to represent $P_{0i}+P_{0j}$. In general we shall use $e_{i'} \ldots e_i$ to represent the projection operator on to the subspace spanned by $e_{i'}, \ldots, e_i$. Combining equations (111), (128), (129) we find

$$\hat{I}(e_i)^{-1} = \sigma \hat{I}(e_i)\sigma = \hat{I}(*e_i) \tag{130}$$

where

$$*e_i = e_1, \ldots e_{i-1}e_{i+1} \ldots e_n \tag{131}$$

It is clear that the transformations

$$(\hat{I}(e_i))^m \qquad m \in z$$

are the basic ingredients of soliton transformations. Defining

$$I_m(e_i) = \sigma(\hat{I}(e_i))^m \qquad m \in z \tag{132}$$

we find easily that

$$I_m(e_i)^2 = 1 \qquad m \in z \tag{133}$$

The explicit formulas for $\hat{I}(e_i)^m$ and $I_m(e_i)$ are quite complicated. They are still under investigation. On the other hand, although the B-Z soliton transformations have singularities on the s-plane, their iterations for any number of times are relatively easy to write down. These formulas are derived in a subsequent work.

VI. Discussions

In this work, we first established that finding the metric tensor satisfying vacuum Einstein equations in 4+K dimensions and admitting 2+K commuting Killing vectors is equivalent to solving a generalized nonlinear sigma model. We then derived the formulas for B-Z one-soliton transformations with proper normalization and with a formula for the conformal factor f appearing in equation (3). These

formulas can be interated arbitrary number of times. The result is given in a subsequent work. From B-Z one-soliton transformations, we derived a series of involutive transformations $I^{(q)}(X_0)$ generalizing the N-K transformation in the four dimensional case. The accompanying transformations $I(e_i)$ are shown to form the basic ingredients of B-Z soliton transformations. The spectral dependence of which is generated by conjugating $\hat{I}(e_i)$ with the dual symmetry transformation $\tilde{I}_2^{(s)}$.

As we mentioned in section three, given a solution of the sigma model, new solutions can be generated by the method of dressing proposed by Zakharov and Shabat [12]. Finding the dressing matrix is equavalent to solving the matrix Riemann-Hilbert problem. The general solutions of the dressing matrix can be written in two parts. The first part arises from solving the regular Riemann-Hilbert problem which amounts to solving a singular integral equation. The second part is the pure solitonic part which arises from solving singular Riemann-Hilbert problem and can be obtained by purely algebraic method. It is known that in the four dimensional case, all solutions can be generated from the trivial solution in this way [15]. It is believed that this continues to be true in the higher dimensional case. One interesting question is whether one can solve the singular integral equation and obtain the "continuum" part of the solution also by purely algebraic method. The answer is believe to be yes but the actual construction of finite transformations is usually difficult.

The solution space decomposes into sectors labeled by soliton numbers. It is believed that an infinite dimensional Lie group acts on the vacuum sector and the corresponding Lie algebra is a Kac-Moody algebra [21]. Except in the four dimensional case, the derivation is based on infinitesimal Riemann-Hilbert transformattions which is not practically useful since we do not know how to solve matrix singular integral equations in close form except in special cases. On the other hand, elements of the group are easily written down in terms of soliton transformations. For example, $I_m(e_i)\tilde{I}_2^{(s)}I_{m_i}(e_i)$ gives infinitely many (labeled by m) one parameter (s) families of group elements. Investigation of the group structure along this direction is in progress.

I wish to thank S. -L. Lou for help in part of the calculations. This work is supported in part by a grant from the National Science Council, Taiwan, Republic of China.

References

1. R. Sorkin, Phys. Rev. Lett. 51 (1983) 87.
2. D. J. Gross and M. J. Perry, Nucl. Phys. B226 (1983) 87.
3. H. –M. Lee and S. –C. Lee, Phys. Lett. 149B (1984) 95.
4. S. –C. Lee, Phys. Lett. 149B (1984) 98.
5. S. –C. Lee and S. –L. Lou, Lett. Nuovo Cimento 44 (1985) 69.
6. S. –C. Lee, Class. and Quan. Grav. 3 (1986) 373; S. –C. Lee and S. –L. Lou, "Spherically Symmetric Dyonic Solutions For Vacuum Einstein Equations In 4 + K Dimensions", to appear in J. Math. Phys.
7. S. –C. Lee, Lett. Nuovo Cimento 44 (1985) 133.
8. S. –C. Lee, Phys. Lett. 158B (1985) 413.
9. D. Maison, J. Math. Phys. 20 (1979) 871.
10. V. A. Belinskii and V. E. Zakharov, JETP 48 (1978) 985; JETP 50 (1979) 1.
11. C. M. Cosgrove, Proceedings of the The Second Marcel Grossmann Meetings on the Recent Developments of General Relativity, Trieste, Italy, 5-11 July 1979; J. Math. Phys. 21 (1980) 2417; 23 (1982) 615.
12. V. E. Zakharov and A. B. Shabat, Funkts. Analiz 13 (1979) 13; V. E. Zakharov and A. V. Mikhailov, Sov. Phys. JETP 47 (1978) 1017; V. E. Zakharov, "The Inverse Scattering Method", in "Solitons", ed. R. K. Bullough and P. J. Caudrey, Springer-Verlag, Berlin Heideberg, 1980; S. Novikov, S. V. Manakov, L. P. Pitaevskii, and V. E. Zakharov, "Theory of Solitons", Consultants Bureau, New York, 1984.
13. V. Belinsky and R. Ruffini, Phys. Lett. 89B (1980) 195.
14. J. Burzlaff and D. Maison, J. Math. Phys. 20 (7) (1979) 1352.
15. I. Hauser and F. J. Ernst, Phys. Rev. D20 (1979) 362, 1783; J. Math. Phys. 21 (1980) 1126, 1418; 22 (1981) 1051.
16. G. Neugebauer and D. Kramer, Ann. Phys. (Leipzig) 24 (1969) 62.
17. S. –C. Lee, Phys. Lett. 164B (1985) 75.
18. C. –C. Chiang, S. –C. Lee, G. Marmo and S. –L. Lou, Phys. Rev. D32 (1985) 1364.
19. H. Eichenherr and M. Forger, Nucl. Phys. B155 (1979) 381; Nucl. Phys. B164 (1980) 52.
20. G. Neugebauer, J. Phys. A. 12 (1979) 67.
21. Y. –S. Wu, Commun. Math. Phys. 90 (1983) 461; L. Dolan, Phys. Rev. Lett. 47 (1981) 1371.

SOLITON TRANSFORMATIONS FOR AXIALLY SYMMETRIC HIGHER DIMENSIONAL GRAVITY II. BELINSKII-ZAKHAROV N-SOLITON TRANSFORMATIONS

S. -C. Lee
Institute of Physics,
Academia Sinica
Taipei, Taiwan,
R.O.C.

Abstract

We consider the solutions of vacuum Einstein equations in 4 + K dimensions with 2 + K commuting Killing vectors under the abelian Kaluza-Klein ansatz. This system admits Belinskii-Zakharov type soliton transformations. The explicit formulas for general N-soliton transformations are obtained by iterating the formulas for one-soliton transformation.

I. Introduction

In a previous work [1], which we shall refer to as paper I in the following, we showed that the vacuum Einstein equations in 4 + K dimensions under the abelian Kaluza-Klein ansatz and the assumption of axial symmetry separate into two sets. The main set is equivalent to a generalized nonlinear sigma model [2] so that the well known method of Belinskii-Zakharov (B-Z) [3, 4] can be applied to obtain the soliton transormations. The one-soliton transformation is worked out in detail in I and the results lead us to a series of new discrete symmetries [5] generalizing the Neugebauer-Kramer mapping [6]. In principle, the N-soliton transformations can be obtained by iterating the one soliton transformation. It is sometimes desirable, however, to have explicit expressions for the general N-soliton transformations. In the four dimensional case (K = 0), this had been worked out

PACS 04.20.Jb, 04.50.+h

Special Issue of Annual Report of the Institute of Physics, Academia Sinica, Vol. 16, 1986
In Honor of Prof. Ta-You Wu on the Occasion of his 80th Birthday

by Belinskii-Zakharov [4] for N rank one soliton transformations. Here, we generalize their results to 4 + K dimensions and for general N-soliton transformations of arbitrary ranks. These formulas can then be applied to flat background, to Weyl solutions [7] generalized to higher dimensions, or to other known solutions. This will be discussed in a subsequent work.

Our notations follow those of paper I. In the next section, we shall first recall the formulas for one-soliton transformation and then derive the formulas for two-soliton transformation. This is because two-soliton transformations can preserve both reality and asymptotic flatness [8] hence is particularly useful. The derivation also shows that two successive one-soliton transformations commute (permutation theorem). Moreover, it prepares us for the derivation of general N-soliton transformations which we give the results in section three and prove by induction.

II. Two-Soliton Transformations

The metric in 4 + K dimensions under the abelian Kaluza-Klein ansatz and the assumption of axial symmetry can be written as

$$d\bar{s}^2 = f(d\rho^2 + dz^2) + Q^{-1}_{\bar{a}\bar{b}} dx^{\bar{a}} dx^{\bar{b}} \qquad \bar{a} = \bar{\mu}, a \tag{1}$$

Where $Q_{\bar{a}\bar{b}}$ is a symmetric nxn matrix (n = K + 2) given in (I.16). f and Q depends on ρ and z only. Moreover,

$$\det Q^{-1} = -\tau^2 \tag{2}$$

where $\Box\tau = 0$. Instead of f, we shall often use the determinant $\bar{g}$ of the total metric tensor $\bar{g}_{AB}$ which is related to f by

$$\bar{g} = \tau^2 f^2 \tag{3}$$

Given a solution Q, $\bar{g}$ we can generate new solutions by solving the linearized equations

$$\partial_\xi U(.;s) = \tau^{-1}(1 + \gamma^{-1})\, U(.;s)\, J_\xi$$
$$\partial_\eta U(.;s) = \tau^{-1}(1 + \gamma)\, U(.;s)\, J_\eta \tag{4}$$

where ξ, η are z-iρ, z + iρ respectively and γ is a given function of ξ, η, s defined in (I.29). The new solution obtained by one soliton transformation is given by Q_1, $\bar{g}_1$, U_1 (·;s),

$$U_1(\cdot;s) = \left(\frac{\lambda - \lambda_1}{\lambda - \mu_1}\right)^{q_1/n} U(\cdot;s)\left(1 - P_1 + \frac{\lambda - \mu_1}{\lambda - \lambda_1} P_1\right) \tag{5}$$

$$Q_1 = \left(\frac{\lambda_1}{\mu_1}\right)^{q_1/n} Q\left(1 - P_1 + \frac{\mu_1}{\lambda_1} P_1\right) \tag{6}$$

$$(-\bar{g}_1)^{1/2} \doteq (-\bar{g})^{1/2} \tau^{q_1(n-q_1+2)/n} \lambda_1^{2q_1(n-q_1-1)/n}$$
$$(\tau^2 - \lambda_1^2)^{q_1(2q_1-n)/n} \det\left(\frac{1}{\tau^2 - \lambda_1^2} X_1^T Q X_1\right) \tag{7}$$

In these formulas, P_1 is a projection operator

$$P_1 = X_1 (X_1^T Q X_1)^{-1} X_1^T Q \tag{8}$$

with

$$X_1 = U(\cdot;s_1)^{-1} X_1^{(0)} \tag{9}$$

$X_1^{(0)}$ is an arbitrary constant nxq$_1$ matrix of rank q_1. s_1 is a complex parameter and is related to λ_1 in the same way s is related to λ as given in equation (I.26). Finally, $\mu_1 = \tau^2/\lambda_1$ is the value of λ_1 on the second sheet of s.

Note that P_1 can also be written as

$$P_1 = U(\cdot;s_1)^{-1} X_1^{(0)} (X_1^{(0)T} Q^{(s_1)} X_1^{(0)})^{-1} X_1^{(0)T} Q^{(S_1)} U(\cdot;s_1) \tag{10}$$

where

$$Q^{(s_1)} = \sigma(U(\cdot;s_1))\, Q U(\cdot;s_1)^{-1} \tag{11}$$

with σ being the involutive automorphism defined in (I.14).

Now we can iterate equations (5) to (7) one more time to obtain a new solution Q_2, $\bar{g}_2$ and $U_2(\cdot;s)$ depending on the parameters $X_1^{(0)}$, $X_2^{(0)}$, s_1, s_2 where

$X_2^{(0)}$ is an arbitrary nxq_2 constant matrix of rank q_2.

The first step is to construct $Q_1^{(s_2)}$ and P_2 following equations (10) and (11). We find

$$Q_1^{(s_2)} = (\frac{\lambda_1}{\mu_1})^{q_1/n} (\frac{\lambda_2 - \mu_1}{\lambda_2 - \lambda_1})^{2q_1/n} \sigma(U(\cdot;s_2))\, \tilde{Q}_1\, U(\cdot;s_2)^{-1} \tag{12}$$

where

$$\tilde{Q}_1 = Q - (\tau^2 - \lambda_2^2)\, Q(\frac{1}{\tau^2 - \lambda_1\lambda_2} X_1)(\frac{1}{\tau^2 - \lambda_1^2} X_1^T Q X_1)^{-1}$$

$$(X_1^T \frac{1}{\tau^2 - \lambda_1\lambda_2})Q \tag{13}$$

and

$$P_2 = (1 - P_1 + \frac{\lambda_2 - \lambda_1}{\lambda_2 - \mu_1} P_1)\, X_2 (X_2^T \tilde{Q}_1 X_2)^{-1} X_2^T \tilde{Q}_1 (1 - P_1 + \frac{\lambda_2 - \mu_1}{\lambda_2 - \lambda_1} P_1) \tag{14}$$

with

$$X_2 = U(\cdot;s_2)^{-1} X_2^{(0)} \tag{15}$$

Next we can construct $\tilde{g}_2$ from equations (7) and (12). This will involve the determinant

$$\det(\frac{1}{\tau^2 - \lambda_1^2} X_1^T Q X_1)\, \det(\frac{1}{\tau^2 - \lambda_2^2} X_2^T \tilde{Q}_1 X_2) \tag{16}$$

The crucial point lies in observing that $X_2^T \tilde{Q}_1 X_2$ arises naturally in the inverse of the matrix Σ_2,

$$\Sigma_2 = \begin{bmatrix} \frac{1}{\tau^2 - \lambda_1^2} X_1^T Q X_1, & \frac{1}{\tau^2 - \lambda_1\lambda_2} X_1^T Q X_2 \\ \frac{1}{\tau^2 - \lambda_2\lambda_1} X_2^T Q X_1, & \frac{1}{\tau^2 - \lambda_2^2} X_2^T Q X_2 \end{bmatrix} \tag{17}$$

This can be seen from the following lemma:

Lemma. Let S be an invertible matrix and write

$$S = \begin{bmatrix} S_{11}, S_{12} \\ S_{21}, S_{22} \end{bmatrix}$$

where S_{11} is a submatrix of dimension $n_1 x n_1$ and S_{22} is of dimension $n_2 x n_2$. Assume S_{11} is invertible. Then

$$S^{-1} = \begin{bmatrix} (S_{11})^{-1} + (S_{11})^{-1} S_{12} (\tilde{S}_{22})^{-1} S_{21} (S_{11})^{-1}, & -(S_{11})^{-1} S_{12} (\tilde{S}_{22})^{-1} \\ -(\tilde{S}_{22})^{-1} S_{21} (S_{11})^{-1} & , (\tilde{S}_{22})^{-1} \end{bmatrix} \tag{18}$$

where

$$\tilde{S}_{22} = S_{22} - S_{21} (S_{11})^{-1} S_{12} \tag{19}$$

Moreover

$$\det S = \det S_{11} \cdot \det \tilde{S}_{22} \tag{20}$$

The proof of the first part of the lemma is by straightforward computation. For the second part, we observe that S_{21} can be made to vanish by multiplying on the left with the matrix

$$\begin{bmatrix} 1_{n_1 x n_1}, & 0 \\ -S_{21} (S_{11})^{-1}, & 1_{n_2 x n_2} \end{bmatrix}$$

which does not change its determinant.

Applying this lemma to Σ_2 and recall the definition of $\tilde{Q}_1$ in equation (13), we easily see that the determinant in equation (16) is just $\det\Sigma_2$. Putting everything together, we get

$$(-\bar{g}_2)^{1/2} \doteq (-\bar{g})^{1/2} \tau^{N_2(n-N_2+2)/n} \left(\frac{\tau^2-\lambda_1\lambda_2}{\lambda_1-\lambda_2}\right)^{2q_1q_2/n}$$

$$\prod_{i=1} [\lambda_i^{2q_i(n-q_i-1)/n} (\tau^2-\lambda_i^2)^{q_i(2q_i-n)/n}] \cdot \det \Sigma_2 \tag{21}$$

where $N_2 = q_1 + q_2$.

Now we are ready to compute $U_2(\cdot;s)$. For this, we have to compute

$$(1 - P_1 + \frac{\lambda-\mu_1}{\lambda-\lambda_1} P_1)(1 - P_2 + \frac{\lambda-\mu_2}{\lambda-\lambda_2} P_2) \tag{22}$$

Since the form of P_2 suggest that Σ_2^{-1} may play a role, it is easy to guess at the answer. We shall first introduce some notations. Let $H_2(\lambda)$, $D_2(\lambda)$ be the diagonal matrices

$$H_2(\lambda) = \begin{bmatrix} (\lambda-\lambda_1)\,1_{q_1 x q_1}, & & \\ & & \\ & & (\lambda-\lambda_2)\,1_{q_2 x q_2} \end{bmatrix}$$

$$D_2(\lambda) = \begin{bmatrix} (\tau^2-\lambda\lambda_1)\,1_{q_1 x q_1}, & & \\ & & \\ & & (\tau^2-\lambda\lambda_2)\,1_{q_2 x q_2} \end{bmatrix} \tag{23}$$

We shall use $\hat{H}_2(\lambda)$ to denote the matrix obtained from $H_2(\lambda)$ by thre replacement $\lambda_1 \rightarrow \mu_1$, $\lambda_2 \rightarrow \mu_2$. This notation will be consistently used for other matrices which depend on $_i$. Similarly, we shall use $\tilde{H}_2(\lambda)$ to denote the matrix obtained from $H_2(\lambda)$ by the replacement $\lambda \rightarrow \mu = \tau^2/\lambda$. This will be consistenly used for other matrices that depend on λ and is consistent with our notation that "tilde" denotes quantities on the second sheet of s. Now we define

$$\Gamma_2(\lambda) = -H_2(0)\,\Sigma_2\,H_2(\lambda), \qquad \tilde{\Gamma}_2(\lambda) = -H_2(0)\,\Sigma_2\,\tilde{H}_2(\lambda) \tag{24}$$

and note that

$$\hat{\Gamma}_2(\lambda) = -\hat{H}_2(0)\,\Sigma_2\,\hat{H}_2(\lambda) = \Sigma_2 D_2(\lambda) \tag{25}$$

Also define the $nx(q_1+q_2)$ matrix

$$Y_2 = [X_1, X_2] \tag{26}$$

With these preparations, we can state the theorem:

Theorem. The expression in equation (22) is equal to

$$1 - Y_2\,\Gamma_2(\lambda)^{-1} Y_2^T Q \tag{27}$$

so that

$$U_2(\cdot;s) = \prod_{i=1}^{2} \left(\frac{\lambda-\lambda_i}{\lambda-\mu_i}\right)^{q_i/n} U(\cdot;s)\,(1 - Y_2\,\Gamma_2(\lambda)^{-1} Y_2^T Q) \tag{28}$$

$$Q_2 = \prod_{i=1}^{2} \left(\frac{\lambda_i}{\mu_i}\right)^{q_i/n} Q\,(1 - Y_2\,\Gamma_2(0)^{-1} Y_2^T Q). \tag{29}$$

Note that Q_2 is manifestly symmetric.

The proof of the theorem is by straightforward computation using equation (18).

Summarizing, equations (28), (29) and (21) give the formulas for two-soliton transformation. It is clear that the final result is invariant under simultaneous interchange of s_1, s_2 and $X_1^{(0)}$, $X_2^{(0)}$. This is the permutation theorem for B-Z two-soliton transformation.

Let us also remark that if we choose $s_2 = s_1$ while letting $X_1^{(0)}$, $X_2^{(0)}$ independent so that the matrix $[X_1^{(0)}, X_2^{(0)}]$ is of rank $N_2 = q_1 + q_2$, then the two-soliton transformation with ranks q_1 and q_2 reduces to a one-soliton transformation of rank N_2. This is quite obvious for equations (28) and (29), while for equation (21), a simple computation using the relation

$$\lambda_1 - \lambda_2 = \lambda_1^2 (\tau^2 - \lambda_1^2)^{-1} (s_1 - s_2) + O((s_1 - s_2)^2) \tag{30}$$

proves the assertion. This shows that for multi-soliton transformations, it is enough to consider only the rank one case. The general situation is obtained by letting some of the s_i's concide.

We have presented our results in such a way that they are ready for generaliza-

tion. Indeed, it is quite obvious how to generalize the definitions of the matrices X_2, Y_2, Σ_2, H_2, D_2, Γ_2, etc. to X_m, Y_m, . . . , etc. for any positive integer m. Using these matrices, we shall give the formulas for the general N-soliton transformations and prove them by induction in the following section.

III. N-soliton Transformations

Let us state our main result as a theorem.

Theorem. Let Q, $\bar{g}$ be a solution and let $U(\cdot;s)$ be an integral of equation (4), properly normalized. Choose m complex constants $s_1, \ldots, s_m$ and m complex constant matrices $X_1^{(0)}, \ldots, X_m^{(0)}$ of ranks $q_1, \ldots, q_m$ and dimensions $nxq_1, \ldots, nxq_m$ respectively. Let

$$X_i = U(\cdot;s_i)^{-1} X_i^{(0)}, \quad Y_m = [X_1, \ldots, X_m] \tag{31}$$

then

$$Q_m = \prod_{i=1}^{m} \left(\frac{\lambda i}{\mu i}\right)^{qi/n} Q(1 - Y_m \Gamma_m(0)^{-1} Y_m^T Q) \tag{32}$$

$$(-\bar{g}_m)^{1/2} = (-\bar{g})^{1/2} \tau^{Nm(n-Nm\ \ 2)/n} \prod_{i<j} \left(\frac{\tau^2 - \lambda i \lambda i}{\tau i - \lambda j}\right)^{2qiqi/n}$$

$$\prod_{i=1}^{m} \lambda_i^{2qi(n-qi-1)/n} (\tau^2 - \lambda_i^2)^{qi(2qi-n)/n} \cdot \det \Sigma_m \tag{33}$$

Where $N_m = q_1 + \ldots + q_m$, $\Gamma_m(\lambda)$ and Σ_m are defined as in equations (17) and (24), is also a solution. The corresponding generating function $U_m(\cdot;s)$ is given by

$$U_m(\cdot;s) = \prod_{i=1}^{m} \left(\frac{\lambda - \lambda 1}{\lambda - \mu i}\right)^{qi/n} U(\cdot;s)(1 - Y_m \Gamma_m(\lambda)^{-1} Y_m^T Q) \tag{34}$$

Before proving the theorem, let us also define the following useful quantities

$$\tilde{Q}_m = Q - (\tau^2 - \lambda_{m+1}^2) Q Y_m D_m^{-1}(\lambda_{m+1}) \Sigma_m^{-1} D^{-1}(\lambda_{m+1}) Y_m^T Q \tag{35}$$

$$P_m = (1 - Y_{m-1}\, \sigma(\hat{\Gamma}_{m-1}(\lambda_m))\, Y_{m-1}^T Q)\, X_m\, (X_m^T \tilde{Q}_{m-1} X_m)^{-1}$$

$$X_m^T \tilde{Q}_{m-1} (1 - Y_{m-1} \Gamma_{m-1}^{-1}(\lambda_m) Y_{m-1}^T Q) \tag{36}$$

$$\tilde{U}_m(\cdot;s) = \prod_{i=1}^{m} \left(\frac{\mu - \lambda_i}{\mu - \mu_i}\right)^{q_i/n} \tilde{U}(\cdot;s)(1 - Y_m \tilde{\Gamma}_m(\lambda)^{-1} Y_m^T Q) \tag{37}$$

Equations (35) and (36) are natural generalizations of equations (13) and (14) respectively.

The theorem will be proved by induction and the main steps will be presented in a series of lemmas. Assuming the theorem is true for m, we shall construct Q_{m+1}, $\bar{g}_{m+1}$ and $U_{m+1}(\cdot;s)$ by doing an one-soliton transformation. As in the two-soliton case, we first construct

$$Q_m^{(S_{m+1})} = \sigma(U_m(\cdot;s))\, Q_m\, U_m(\cdot;s_{m+1})^{-1} \tag{38}$$

This requires computation of the inverse of $(1 - Y_m \Gamma_m(\lambda)^{-1} Y_m^T Q)$. We have

Lemma 1. $(1 - Y_m \Gamma_m(\lambda)^{-1} Y_m^T Q)(1 - Y_m \sigma(\hat{\Gamma}_m(\lambda) Y_m^T Q) = 1$ (39)

The proof relies on the following identities

$$\Sigma_m^{-1} \hat{H}_m(\lambda) - H_m(\lambda) \Sigma_m^{-1} = \Sigma_m^{-1} H_m(0)^{-1} Y_m^T Q Y_m \Sigma_m^{-1} \tag{40}$$

$$H_m(0)^{-1} = \hat{H}_m(\lambda) D_m(\lambda)^{-1} \tag{41}$$

which is valid for all m. The identity (40) is easily verified by multiplying on both sides of each term with Σ_m and computing the ijth block while identity (41) follows from the definitions. A simple computation then shows that lemmal is true.

Next we show that

Lemma 2. $\tilde{U}_m(\cdot;s) = \sigma(U_m(\cdot;s))\, Q_m$ (42)

or, equivalently,

$$(1 - Y_m \hat{\Gamma}_m (\lambda)^{-1} Y_m^T Q)(1 - Y_m \Gamma_m (0)^{-1} Y_m^T Q)$$

$$= 1 - Y_m \tilde{\Gamma}_m (\lambda)^{-1} Y_m^T Q \tag{43}$$

The proof is again a simple computation using the transpose of the identity (40).

Substituting equation (42) into equation (38) and using equation (37), we can identify $\tilde{Q}_m$

Lemma 3. $\tilde{Q}_m = Q(1 - Y_m \tilde{\Gamma}_m(\lambda_{m+1})^{-1} Y_m^T Q)$

$$(1 - Y_m \sigma(\hat{\Gamma}_m (\lambda_{m+1})) Y_m^T Q) \tag{44}$$

or, equivalently

$$(1 - Y_m \tilde{\Gamma}_m (\lambda)^{-1} Y_m^T Q)(1 - Y_m \sigma(\hat{\Gamma}_m (\lambda)) Y_m^T Q)$$

$$= 1 - (\tau^2 - \lambda^2) Y_m D_m (\lambda)^{-1} \Sigma_m^{-1} D_m (\lambda)^{-1} Y_m^T Q \tag{45}$$

This is also easily verified using the identity (40).

$Q_m^{(S_{m+1})}$ can now be expressed in terms of $\tilde{Q}_m$. It is then easy to see that equation (36), when replacing m by m + 1, gives the correct formula for P_{m+1}. With P_{m+1}, we can now compute U_{m+1} (·;s). As in the two-soliton case, we first establish the relations

Lemma 4. The (m + 1), (m + 1) block of Σ_{m+1}^{-1} is

$$[\Sigma_{m+1}^{-1}]_{m+1,\,m+1} = (\tau^2 - \lambda_{m+1}^2)(X_{m+1}^T \tilde{Q}_m X_{m+1})^{-1} \tag{46}$$

and

$$\det \Sigma_{m+1} = \det \Sigma_m \cdot \det \left(\frac{1}{\tau^2 - \lambda_{m+1}^2} X_{m+1}^T \tilde{Q}_m X_{m+1} \right) \tag{47}$$

The proof follows from the definition of $\tilde{Q}_m$ in equation (35) and the lemma of the last section, i.e. equations (18) and (19).

Now we can compute $\bar{g}_{m+1}$ using the induction hypothesis equation (33),

the formula for one-soliton transformation equation (7) and the formula for $Q_m^{(S_{m+1})}$. The straiht forward computation proves the theorem for $\bar{g}_{m+1}$.

Finally to complete the construction of U_{m+1} (·;s), we have

Lemma 5. $(1 - Y_m \Gamma (\lambda)^{-1} Y_m^T Q)(1 - P_{m+1} + \frac{\lambda - \mu_{m+1}}{\lambda - \lambda_{m+1}} P_{m+1})$

$$= 1 - Y_{m+1} \Gamma_{m+1} (\lambda)^{-1} Y_{m+1}^T Q \tag{48}$$

or, equivalently,

$$1 - Y_m \Gamma_m (\lambda)^{-1} Y_m^T Q = \prod_{i=1}^{m} (1 - P_i + \frac{\lambda - \mu_i}{\lambda - \lambda_i} P_i) \quad \forall m$$

The proof of lemma 5 is quite straightforward. We expand both sides of the equation. When expanding the right hand side, we use the lemma of the last section to separate Σ_{m+1} into the (m + 1), (m + 1) block, (m + 1), i blocks, i, (m + 1) blocks and the rest. Then one collects terms and shows that the two sides are equal.

With this lemma, the theorem for U_{m+1}, Q_{m+1} is easily established.

IV. Discussion

There are other ways to obtain the formulas for general N-soliton transformations than to iterate the one-soliton transformation. For example, one may use the method of soliton correlation matrix introduced by Harnad et. al. [9]. However, in those approaches, it is usually difficult to obtain the correct normalization and to obtain the formula for $\bar{g}_m$. What we have achieved is essentially to provide a series of identities so that the different approaches can be bridged.

In this respect, it is perhaps appropriate to mention that our $\Gamma(\lambda)^{-1}$ forms the backbone of the soliton correlation matrix of Ref. [9] consequently generalizing their construction for sigma models to the present case [2].

We shoud also mention that a lot of works have been done in the four dimensional case as referred to in I. In particular, B-Z had worked out the general N successive rank one soliton transformations in four dimensions in their original works [4].

As explained in I, our interest in the soliton transformation stems partly from the possibility of using them to generate solutions in the vacuum sector. This can be achieved by letting the s-plane poles in the B-Z soliton transformations to coincide and at the same time taking suitable limits of $X_i^{(0)}$ associated with each pole. An example of this in the four dimensional case is given in [10] where a confluent double soliton transformation was carried out. The higher dimensional case is much more complicated and is currently under investigation.

This work is supported in part by a grant from the National science Council, Taiwan, Republic of China.

References

1. S. -C. Lee, "Soliton Transformations For Axially Symmetric Higher Dimensional Gravity, I", IP-ASTP-03-86.
2. S. -C. Lee, Phys. Lett. 158B(1985)413.
3. V.E. Zakharov and A.B. Shabat, Funkts. Analiz 13(1979)13; V. E. Zakharov and A. V. Mikhailov, Sov. Phys. JETP 47(1978)1017; V. E. Zakharov, "The Inverse Scattering Method", in "Solitons", ed. R. K. Bullough and P. J. Caudrey, Springer-Verlag, Berlin Heideberg, 1980; S. Novikov, S. V. Manakov, L. P. Pitaevskii, and V. E. Zakharov, "Theory of Solitons", Consultants Bureau, New York, 1984.
4. V. A. Belinskii and V. E. Zakharov, JETP 48(1978)985; JETP 50(1979)1.
5. S. -C. Lee, Phys. Lett. 164B(1985)75.
6. G. Neugebauer and D. Kramer, Ann. Phys. (Leipzig) 24(1969)62.
7. H. Weyl, Ann. Phys. (Leipzig) 54(1917)117.
8. C. M. Cosgrove, Proceedings of the The Second Marcel Grossmann Meetings on the Recent Developments of General Relativity, Trieste, Italy, 5-11 July 1979; J. Math. Phys. 21(1980)2417; 23(1982)615.
9. J. Harnad, Y. Saint-Aubin and S. Shnider, Commun. Math. Phys. 92(1984)329.
10. C.M. Cosgrove, J. Math. Phys. 21(1980)2417.

PHOTOTHERMAL IONIZATION SPECTROSCOPY OF MAGNESIUM DONORS IN SILICON*+

L T Ho
Institute of Physics
Academia Sinica
Taipei, Taiwan, Republic of China

Abstract

Photothermal ionization spectroscopy studies of magnesium donors in silicon have shown a distinct series of spectral lines corresponding to transitions from the ground state to the excited states. Experimental results indicate the existence of an optimal temperature for the photothermal ionization spectroscopy due to its being a two-step process. Because of its high sensitivity, the photothermal ionization spectrum also reveals some spectral lines of magnesium donors in a low-concentration silicon sample.

I. Introduction

Impurity states have received considerable attention since the beginning of semiconductor physics. Transitions of carriers from the ground state of the impurity to discrete excited levels were first observed by Burstein and coworkers[1] with the use of infrared absorption. Since then, the study of the optical absorption spectroscopy of impurity centers have become one of the most important methods to understand the nature and the behavior of impurity centers in semiconductors. The absorption spectroscopy and other analysis methods such as radiochemistry or mass spectrometry, however, all have a weak point as they are invalid to identify the impurities of small concentrations, especially when today's purification technology

*Work supported in part by the National Science Council. Republic of China.
+Presented at the Tenth International Conference on Infrared and Millimeter Waves, Dec. 9-13, 1985, Lake Buena Vista, Florida, U.S.A.

Special Issue of Annual Report of the Institute of Physics, Academia Sinica, Vol. 16, 1986
In Honor of Prof. Ta-You Wu on the Occasion of his 80th Birthday

of semiconductor materials has reached such a high level that, for example, single crystal germanium and silicon containing residual donor and acceptor impurities less than $10^{10}cm^{-3}$ for germanium and $10^{11}cm^{-3}$ for silicon have been grown. In order to deal with the problem of impurity identification of small concentration, a new spectroscopic technique called the photothermal ionization spectroscopy has been developed as an outcome of investigations of the extrinsic photoconductivity in semiconductors. Because of its extremely high sensitivity, a lot of work has been done related to this subject.[2]

In photothermal ionization spectroscopy an impurity center in a semiconductor is ionized in a two-step process. The electron (or hole) bound to a donor (or acceptor) impurity is first raised from the ground state to an excited state by the absorption of a photon. If there is enough thermal energy, it is subsequently thermally promoted into the conduction (or valence) band becoming a free current carrier which, then, can be detected through the change of the conductivity of the sample. This sequence is shown in Fig. 1 schematically. The photothermal ionization spectrum of a particular impurity center consists of a series of sharp photoconductivity peaks, corresponding to transitions from ground state to various excited states, on the lower energy side of the direct photoionization threshold.

As is known, the ground state energies of impurity centers in a semiconductor are dependent on the chemical species and thus the ionization energy differs for different impurities. In particular, for magnesium donors in silicon the ionization energy is 107.50meV,[3] which indicates that magnesium is a much deeper donor than group V shallow donors. Another different but interesting feature for this impurity is its being in an interstitial rather than a substitutional site in silicon. The purpose of the present paper is to report and discuss magnesium donors in silicon through the study of its photothermal ionization spectrum.

II. Experimental Procedure

Magnesium was diffused into silicon in the following manner. A thick layer of pure magnesium was first deposited by evaporation on the two surfaces of the sample. The sample, being sandwiched between two other specimens, was then heated at 1200°C in a continuously purged helium atmosphere for a period of one hour. During the heat treatment, the sample and two covers weld together and thus the magnesium does not escape into the ambient. The covers were ground off afterwards. By following this procedure an undoped high-purity silicon, initially p-type and of resistivity 3000 ohm-cm, was converted to a low-resistivity n-type specimen. From

Hall measurement, the room-temperature carrier concentration of the specimen is estimated to be of the order of $10^{15}cm^{-3}$. The magnitude of the concentration can be varied and controlled through the change of the magnesium thickness deposited on the sample surfaces as well as the length and the temperature of the heat treatment.

The spectrometer used for the measurements incorporated a single-beam, double-pass Perkin-Elmer model E-1 monochromator. A globar was used as the radiation source and a diffraction grating with 57.6 grooves/mm and blaze wavelength 13.5μ was found suitable for the spectral range of the present interest from 90 to 110 meV. The sample was connected to an electric circuit so that a bias current was provided by a dc battery via a load resistor in series with the sample. The change in voltage drop across the sample due to the chopped excitation radiation was measured using standard lock-in amplification technique.

III. Experimental Results and Discussion

The photothermal ionization spectrum of magnesium donors in silicon is shown in Fig. 2. The temperature of the specimen was approximately 20°K. As the figure shows, there is a distinct series of maxima on the curve. The positions of the maxima correspond to the peaks on the optical absorption spectrum, which is also given in Fig. 2. The excitation lines correspond to the transitions from the is ground state to the excited p states for the magnesium donors in silicon. The labeling of the excitation lines is given in Ref. 3, based on the similarity in line spacings and relative intensities as compared with the excitation spectra of group V donors in silicon and the results of a theoretical calculation by Faulkner.[4] A comparison of two spectra in Fig. 2 clearly demonstrates how the intensities of the peaks in the photothermal ionization spectrum reflect the product of the transition probability for the transition from the ground state to the excited state and the factor controlling the thermal ionization from the excited state to the conduction band. Many of the optical transitions close to the conduction band thus appear prominently in the photothermal ionization spectrum. Not only those higher lying spectral lines are better resolved, but also two new lines, $4f_{\pm}$ and $6p_{\pm}$, which are too weak to be observed in the optical absorption spectrum, now appear.

Listed in Table 1 is a tabulation of the binding energies of energy levels deduced from the experimentally observed transition energies; they are computed assuming that the theory accurately gives the binding energy of the $3p_{\pm}$ state as 3.12

meV.[4] The binding energies of energy levels observed for phosphorus donors in silicon[5] and calculated from theory are also given in Table 1 for comparison. It is clear that the magnesium data agree with both the phosphorus and the theoretical values for the higher excited states remarkably. Though magnesium is a deeper donor occupying an interstitial site, its behavior is apparently similar to the substitutional group V shallow donors.

The sample temperature for the photothermal ionization spectroscopy is a critical factor as it has to be low enough to promote substantial occupation of the ground state of the impurity centers to be investigated but high enough to ionize the optically excited impurities thermally. This is quite different as compared with a typical optical absorption experiment where lower temperature is always preferred. Fig. 3 shows such a temperature effect on the photothermal ionization spectrum of a magnesium doped silicon sample measured at different temperatures. The result clearly demonstrates that there is an optimal sample temperature in order to obtain the best spectrum. The present study is in agreement with the results of previous work on this subject that silicon samples should be cooled to 23 to 28°K while germanium to below 10°K due to its narrower band gap and usually shallower impurity centers, and diamond to above 100°K because of its much wider band gap and much deeper impurities.[2]

The excitation spectrum of magnesium donors in silicon has been reported to exhibit a time-dependent effect such that the intensity of the excitation lines decreases when the same spectrum is remeasured after a considerable lapse of time.[6] Since the most significant feature for photothermal ionization spectroscopy is its high sensitivity in dealing with low impurity concentrations, it is therefore interesting to measure the photothermal ionization spectrum of such a sample. The result is shown in Fig. 4 in which both the optical absorption spectrum and the photothermal ionization spectrum are given. While nothing can be observed in the absorption spectrum, the photothermal ionization spectrum is apparently capable of revealing some spectral line corresponding to transitions due to magnesium donor centers. This, again, shows the high-resolution advantage for the photothermal ionization spectroscopy.

In conclusion, we have shown that, besides the usual optical absorption spectroscopy, photothermal ionization spectroscopy is another important tool which can be used to study the behavior of impurities in semiconductors. Its high sensitivity is particularly useful to identify impurity centers of very low concentrations. Because of its being a two-step process, an optimal temperature condition should

be met in the measurement for different impurities and for different semiconductors.

References

1. E. Burstein, E. E. Bell, J. W. Davisson, and M. Lax, J. Phys. Chem. 57, 849 (1953).
2. A recent review has been given by Sh. M. Kogan and T. M. Lifshits, Phys. Stat. Sol. (a) 39, 11(1977).
3. L. T. Ho and A. K. Ramdas, Phys. Rav. B 5, 462(1972).
4. R. A. Faulkner, Phys. Rev. 184, 713 (1969).
5. C. Jagannath. Z. W. Grabowski, and A. K. Ramdas, Phys. Rev. B 23, 2082 (1981).
6. L. T. Ho, Phys. Stat. Sol. (a) 28, K73(1975).

Table 1. Binding energies of the energy levels of donor impurities in silicon (meV)

Energy Level	Magnesium	Phosphorus	Theory
1s	107.50	45.59	31.27
$2p_0$	11.70	11.48	11.51
$2p_\pm$	6.38	6.40	6.40
$3p_0$	5.55	5.47	5.48
$4p_0$	3.33	3.31	3.33
$3p_\pm$	3.12	3.12	3.12
$4p_\pm$	2.17	2.19	2.19
$4f_\pm$	1.87	1.90	1.89
$5p_\pm$	1.45	1.46	1.44
$6p_\pm$	1.06	1.09	1.04

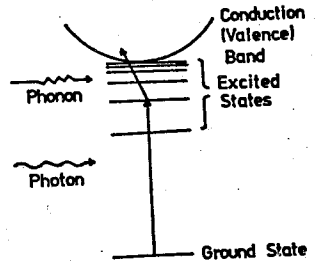

Fig. 1. Schematic representation of the photothermal ionization showing a two-step process: The bound electron (or hole) raised from the ground state to an excited state by the absorption of a photon and subsequently thermally promoted into the conduction (or valence) band.

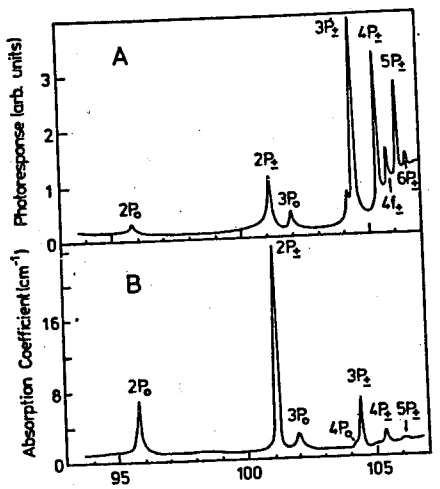

Fig. 2. Photothermal ionization spectrum (A, 30°K) and optical absorption spectrum (B, 10°K) of magnesium donors in silicon. Room-temperature carrier concentration is approximately 2×10^{15} cm^{-3}.

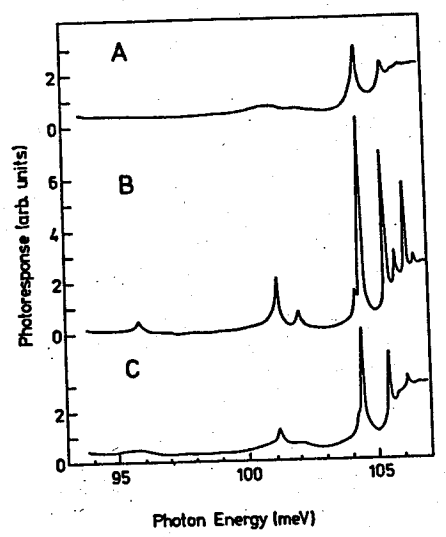

Fig. 3. Photothermal ionization spectra at (A, 50°K), (B, 30°K), and (C, 10°K) of magnesium donors in silicon. Carrier concentration at room temperature is approximately 2×10^{15} cm^{-3}.

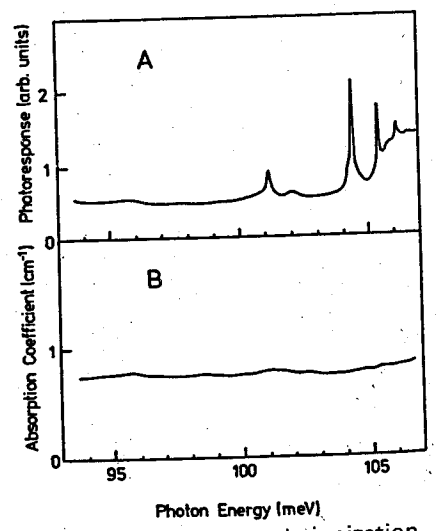

Fig. 4. Photothermal ionization spectrum (A, 30°K) and optical absorption spectrum (B, 10°K) of magnesium donors in silicon. Room-temperature carrier concentration is below 10^{13} cm^{-3}.

ELECTROLYSIS USED AS A TOOL FOR ADDING IMPURITIES INTO SEMICONDUCTORS

L. T. Ho and J. M. Liang

Institute of Physics
Academia Sinica

In a crystal, the most obvious type of imperfection is due to the presence of foreign atoms. No substance can be made perfectly pure, even the purest crystals contain many foreign atoms. Since most crystals have between 10^{22} and 10^{23} atmos per cm^3, an impurity content of 1 part in 10^9 still leaves about 10^{14} impurity atoms per cm^3 in a crystal. It is now well known that these foreign atoms, generally called impurities, play a vital part in determining the properties of semiconductors. The entire semiconductor industry, actually, also depends on the presence of these impurities.

Because of the important and the significant role played by impurities, many methods in a controlled manner have been developed throughout the years trying to add a certain amount of chemical impurity of a certain kind into a semiconductor crystal. Among them, doping is the most common process used for adding impurities. That is, when a semiconductor crystal is melted and a small amount of impurity material added, the semiconductor recrystallizes upon cooling, with the impurity atoms occupying either a substitutional or an interstitial position in the lattice.

Foreign atoms can also be added into semiconductor by diffusion. For example, lithium, a group I element, can be diffused into silicon and germanium easily as a consequence of its remarkable diffusion properties.[1] The diffusion coefficient of lithium in silicon at 800°K is about eight orders of magnitude larger than that of phosphorus in the same host.[2] When diffused into silicon and germanium, lithium has been shown to occupy an interstitial position and to behave like a shallow donor.[3]

Special Issue of Annual Report of the Institute of Physics, Academia Sinica, Vol. 16, 1986
In Honor of Prof. Ta-You Wu on the Occasion of his 80th Birthday

Sodium and potassium are two other group I elements with their position only next to lithium in the periodic table. Since lithium in silicon and germanium shows many important features which lead to quite a few industrial applications such as infrared detector, nuclear radiation detector and double-injection diode, the role of sodium and potassium as impurities in silicon and germanium should also be very interesting. Apparently due to doping difficulties, however, very few research has been done on these subjects in the past. Recently, we have made some effort trying to introduce sodium and potassium into silicon and germanium. In this report we will discuss the experimental procedure and the results we obtained.

It has been known that lithium can be introduced into silicon crystal using the diffusion technique in the following manner.[1] A silicon bar, with a small cube of lithium placed on its broad face, is heated at about 800°C for 30 seconds in a helium atmosphere. During this period, the lithium becomes alloyed with silicon and from this alloy lithium diffuses into silicon to form a himispherical n-type region. If the whole sample surface is covered with lithium and is heated at lower temperature but for longer period, then the lithium can be distributed more homogeneously. A similar diffusion process has also been found to be successful to add lithium into germanium.[3] Due to the resemblance between lithium, sodium and potassium in many features, similar diffusion technique has been attempted for sodium and potassium. Ultra pure sodium and potassium, obtained from Electronic Space Products, Inc., are used for this purpose. But unlike lithium, sodium and potassium do not seem to be able to become alloyed with silicon and germanium in this way and there is no way to start the diffusion process at all. Similarly, the sandwich method, which has been used for introducing magnesium into silicon[4] and germanium[5] successfully, does not work either.

Since the unsuccessful attempt of the conventional method as described above, direct heating of the mixture of silicon or germanium and sodium or potassium has also been tried. Because of the very low melting point of sodium and potassium, sodium or potassium is actually in its liquid phase and the sample is immersed in the sodium or potassium liquid throughout the heat treatment. After several attempts under various temperatures and periods, it has been found that no significant change of the sample characteristics can be detected. After removing a very thin layer from the surface, both the resistivity and the conduction type remain the same as before the heat treatment. Therefore, apparently sodium or potassium cannot overcome the surface barrier of the sample in this way. This result also confirms the earlier observation of McCaldin et al.[6] in an experiment

trying to determine the solubility of sodium in silicon.

The next and successful attempt is to use the electrolysis method, in which the silicon or germanium sample itself is used as the cathode and a piece of either tantalum or molybdenum as the anode. Both the sample and the anode are embedded in the sodium iodide or potassium iodide powder. Once the temperature is raised to above the melting point of sodium iodide or potassium iodide, the electrolysis process can start in the molten sodium iodide or potassium iodide if a voltage supplied by a dc battery is applied between the cathode and the anode. During the electrolysis, the sodium or potassium is able to overcome the surface barrier of the sample and diffuses into the crystal from a layer deposited on the sample surface.

By following the above procedure, all silicon samples examined are found to have converted from p-type to n-type conduction, while all germanium samples from n-type to p-type. Type conversion can be checked easily using a dc thermal probe or by Hall measurement. The resistivity of the sample, initially about 3000 ohm-cm for silicon and 40 ohm-cm for germanium, decreases to only a few ohm-cm. Specimen subjected to the same treatment remains its original high resistivity if the electrolysis does not occur by simply disconnecting the dc battery between the sample and the anode. This check is made to show that the impurity can really be diffused into the crystal and that the change of the electrical properties of the sample is indeed due to the addition of impurities.

The rate of the electrolysis can be varied by changing the voltage between the cathode and the anode. If the voltage is large enough, even the whole sample will melt in the electrolyte once the impurity concentration in the sample has been increased to such a high degree that the melting point of the sample changes to less than the temperature of the electrolyte. This also shows how powerful this electrolysis method is.

We have shown that electrolysis can be used as a tool for helping the foreign atoms to break the surface barrier and, followed by diffusion, to enter into the semiconductor crystals. For those elements which have difficulties to be doped or diffused using conventional methods, now they have a hope to be introduced into semiconductors. This also enables us to have a chance not only to study the behavior of some novel impurity centers but also to find possibilities for new applications.

Special Issue of Annual Report of the Institute of Physics, Academia Sinica, Vol. 16, 1986
In Honor of Prof. Ta-You Wu on the Occasion of his 80th Birthday

Acknowledgement

This work was partially supported by the National Science Council of the Republic of China.

References

1. H. Reiss and C. S. Fuller, Semiconductors, edited by N. B. Hannay (Reinhold, New York, 1960), p. 222.
2. H. F. Wolf, Silicon Semiconductor Data (Pergamon, 1969).
3. R. L. Aggarwal, P. Fisher, V. Mourzine and A. K. Ramdas, Phys. Rev. 138, A882 (1965).
4. L.T. Ho and A. K. Ramdas, Phys. Rev. B5, 462 (1972).
5. L. T. Ho, Appl. Phys. Lett. 35, 409 (1979).
6. J. O. McCaldin, M. J. Little and A. E. Widmer, J. Phys. Chem. Solids 26, 1119 (1965).

MAGNETORESISTANCE OF $(FeM)_{80}B_{14}Si_6$ GLASSES WITH M = Mn, Mo AND V

Y. D. Yao, B. J. Wen[a] and S. T. Lin[b]

Institute of Physics, Academia Sinica

Taipei, Taiwan, R.O.C.

Abstract

The magnetoresistance and magnetization of amorphous $Fe_{80-x}Mn_xB_{14}Si_6$ (x = 0, 2, 4, 6, 10, 12), $Fe_{80-x}Mo_xB_{14}Si_6$ (x = 2, 4, 6, 8) and $Fe_{80-x}V_xB_{14}Si_6$ (x = 2, 4, 6, 8) alloy system have been investigated at both 300K and 77K in an applied magnetic fields up to 6kG. If FAR(T) is the value of the ferromagnetic anisotropy of the electrical resistivity at absolute temperature T and $\bar{\mu}(T)$ is the averaged magnetic saturation moment per Fe atom at TK, then our experimental results suggest that in the strong-ferromagnetic region we have

$FAR(300) = A\,\bar{\mu}(0)^m$; with $A = (1.1 \pm 0.2)\times10^{-5}$
and $m = 7.9 \pm 0.1$
$FAR(77) = A\mu(0)^m$; with $A = (1.2 \pm 0.2) \times 10^{-4}$;
and $m = 5.3 \pm 0.1$
$FAR(T) = A=(T)^m$; with $A = (3.8 \pm 0.3)\times10^{-4}$,
and $m = 3.7 \pm 0.2$

Introduction

In recent years there has been an increased interest in the magnetoresistance as well as the ferromagnetic anisotropy of the electrical resistance (FAR) of amorphous ferromagnetic alloys. In an earlier publication [1] we had shown that the ferromagnetic anisotropy of the electrical resistivity of some Fe-based ferromagnetic amorphous alloys is closely related to the magnetic saturation moment ($\bar{\mu}$) per transition metal atom at OK; i.e., $FAR(T) = A\bar{\mu}(o)^m$, where A and m are temperature-dependent parameters. Extensive Fe-based amorphous alloys are also found to have quite similar results [2-4].

a. Electronic Research Laboratories, Industrial Technology Research Institute, Hsinchu, Taiwan, R. O. C.
b. Physics Department, Cheng Kung Universtiy, Tainan, Taiwan, R. O. C.

Special Issue of Annual Report of the Institute of Physics, Academia Sinica, Vol. 16, 1986
In Honor of Prof. Ta-You Wu on the Occasion of his 80th Birthday

In this investigation we present measurements on the magnetoresistance and the magnetization of amorphous $Fe_{80-x}Mn_xB_{14}Si_6$ (x = 0, 2, 4, 6, 10, 12), $Fe_{80-x}Mo_xB_{14}Si_6$ (x = 2, 4, 6, 8) and $Fe_{80-x}V_xB_{14}Si_6$ (x = 2, 4, 6, 8) alloys at both 300K and 77K in an applied magnetic field up to 6 kG, The motivation of this study is to correlate FAR(T) and $\bar{\mu}$(T) obtained experimentally at the same temperature (T) and to test whether we can get an universal relationship between them over a wide temperature region, in the strong-ferromagnetir state.

Experimental Consideration

Amorphous alloy samples were prepared by the melt spinning technique from a master alloy of predetermined concentration. They are in the form of long ribbons, typically 10 to 30 μm thick and 1 to 3 mm wide. The amorphous state was confirmed by the X-ray diffraction studies. The magnetic field was applied parallel or perpendicular to the long axis of the ribbon but always in the plane of the ribbon. A vibrating sample magnetometer was used to study the magnetization at both 300K and 77K. The electrical resistivity measurements were made using the standard four-probe method. The electrical potentiometer has 0.1μV accuracy. The electrical current was kept constant to about 1 part in 10^5.

Results and Discussion

Roughly speaking, above 2 kG the longitudinal and transverse magnetoresistances change linearly with the applied field. The typical result has been shown before [1]. The difference between both values remains constant at high magnetic fields. This phenomenon has been known quite a long time as the magnetoresistance anisotropy. The quantity FAR is defined by

$$\mathrm{FAR} = \frac{\rho_{,,} - \rho_{\perp}}{\rho_0} \tag{1}$$

where ρ_0 is the electrical resistivity in zero internal magnetic field, and $\rho_{,,}$ and $\rho_{\perp}$ are the longitudinal and transverse magnetoresistivities extrapolated to zero internal magnetic field [1]. Fig. 1 shows the FAR as a function of the Fe concentration. FAR is an inherent property of ferromagnetic materials and does not depend on the initial domain configuration in the demagnetized state. According to our experimental data, the value of the FAR decreases on replacing Fe by Mn, Mo or V. This decreasing of the FAR is quite fast at beginning (i.e. in the strong ferromagnetic

state) and then is slow down to the weak ferromagnetic state. This behavior can be explained by the two-current model [5,6]. According to this model and neglecting the higher order term, we have

$$\mathrm{FAR} = \nu(\rho_{0\downarrow}/\rho_{0\uparrow} - 1) \tag{2}$$

Where ν is a spin-orbit constant with an experimentally determined value of about 0.01 [5,6], and $\rho_{0\uparrow}$ and $\rho_{0\downarrow}$ are the residual resistivities of the spin ↓ and spin ↑ bands of the system. In strong ferromagnetic state, the holes are mostly occupied in the d ↓ band, whereas the holes in both d ↑ and d ↓ bands for the weak ferromagnetic state. Eq. (2) tell us that: first, $\rho_{0\downarrow}$ greatly exceeds $\rho_{0\uparrow}$ in the strong ferromagnetic region and the s-d scattering is allowed only for spin ↓ electrons because there are no vacant d↑ states near E_F. second, $\rho_{0\uparrow}$ and $\rho_{0\downarrow}$ are comparable in a weak ferromagnetic state, and the vacant sites near E_F are available in both d↓ and d↑ bands for s electrons to make transitions. Therefore, FAR is supposed to be quite large in the strong ferromagnetic state and very small in the weak ferromagnetic state. In this paper, we discuss the FAR only in the strong ferromagnetic state.

Figs. 2 to 7 show the magnetization study of these amorphous samples used for this study at both 300K and 77K. Evidently, the coercive field H_c of the these samples is very small and belongs to the soft magnetism. From the saturation magnetization, we can calculate the averaged magnetic moment $\bar{\mu}$ per Fe atom at both 300K and 77K. The averaged magnetic moment per Fe atom at OK can be roughly obtained by means of the extrapolation method and the $T^{3/2}$ Bloch law. Figs. 8 to 10 show the averaged magnetic moment per Fe atom of all the amorphous alloys used for this study as a function of the Fe concentration at 300K, 77K and OK, respectively. The value of $\bar{\mu}$ for all the samples decreases monotonically on replacing Fe by Mn, Mo or V.

From our experimental results, we will focus our attention on the relationship between FAR and $\bar{\mu}$. Figs. 11 and 12 show the Ln[FARx10^3] vs Ln $\bar{\mu}$(o) plots for FAR at 300K and 77K, respectively. A straight line can be plotted to pass all the experimental data by best fitting for all the amorphous alloy system. This means theat our experimental data can be fitted to the formula

$$\mathrm{FAR}(T) = A(T)\bar{\mu}(o)^{m(T)} \tag{3}$$

with the values $A = (1.1 \pm 0.2) \times 10^{-5}$ and $m = 7.9 \pm 0.1$ for FAR at 300K and $A = (1.2 \pm 0.2) \times 10^{-4}$ and $m = 5.3 \pm 0.1$ for FAR at 77K. Here, the parameters A and m are temperature dependent.

The next step is to test whether we can get a universal relationship between FAR and $\overline{\mu}$ under the constraint that A and m are temperature independent. At first we let $FAR(T) = A\overline{\mu}(T)^m$ with A and m are temperature-independent constant. The $Ln[FAR(T)\times10^3]$ vs $Ln\overline{\mu}(T)$ plots of our experimental results at 300K and 77K are presented in Figs. 13 and 14, respectively. Again, a best-fitted straight line can be obtained. From the straight lines we have $A = (3.8 \pm 0.3) \times 10^{-4}$ and $m = 3.7 \pm 0.2$ for both 300 K and 77K. This suggests that for Fe-based amorphous alloys we can get a universal relationship in the strong ferromagnetic state as

$$FAR(T) = \frac{\Delta\rho(T)}{\rho_0} = A\,\mu(T)^m \qquad (4)$$

where $A = (3.8 \pm 0.3) \times 10^{-4}$ and $m = 3.7 \pm 0.2$ over a wide temperature range. Similar concept has been tried to develope in some spin-glass systems recently [7,8]; i.e., the negative transverse magnetoresistance varies as the square of the bulk magnetization.

In conclusion, we have presented the experimental results of the magnetoresistance and magnetization measurements on $Fe_{80-x}Mo_xB_{14}Si_6$ (x = 2, 4, 6, 8) and $Fe_{80-x}V_xB_{14}Si_6$ (x = 2, 4, 6, 8) alloys at both 300K and 77K. we have suggested a universal relationship between the FAR(T) and the $\overline{\mu}(T)$ for Fe-based amorphous alloys in strong ferromagnetic state. Further experimental studies at different temperatures, especially at the liquid helium temperature, are definitely needed to confirm the universality we have suggested in this paper.

Acknowledgement

The authors are grateful to the National Science Council of R.O.C. for the financial support of this work under contract #NSC74-0208-M001-04.

References

1. Y. D. Yao, S. Arajs and S. T. Lin, J. Appl. Phys. 53, 2258(1982).
2. M. Naka, R. Kern and U. Gonser, J. Appl. Phys. 52, 1448(1981).
3. R. Kern, M. Naka and U. Gonser, Proc. 4th Int. Conf. Rapidly Quenched Metals, Vol. 2, eds. T. Masumoto and K. Suzuki (Japan Inst. Metals) p. 847 (1981).
4. R. Kern, M. Naka, U. Gonser, H. Fujimori and I. Okamoto, J. Mag. Mag. Mat. 1471(1983).

5. M. C. Cadeville and B. Loegel, J. Phys. F. 3, L115(1973).
6. O. Jaoul, I. A. Campbell and A. Fert, J. Mag. Mag. Met. 5, 23(1977).
7. A. K. Majumdar, Phys. Rev. B 28, 2750(1983).
8. A. K. Majumdar and V. Oestreich, Phys. Rev. B. 30, 5342(1984).

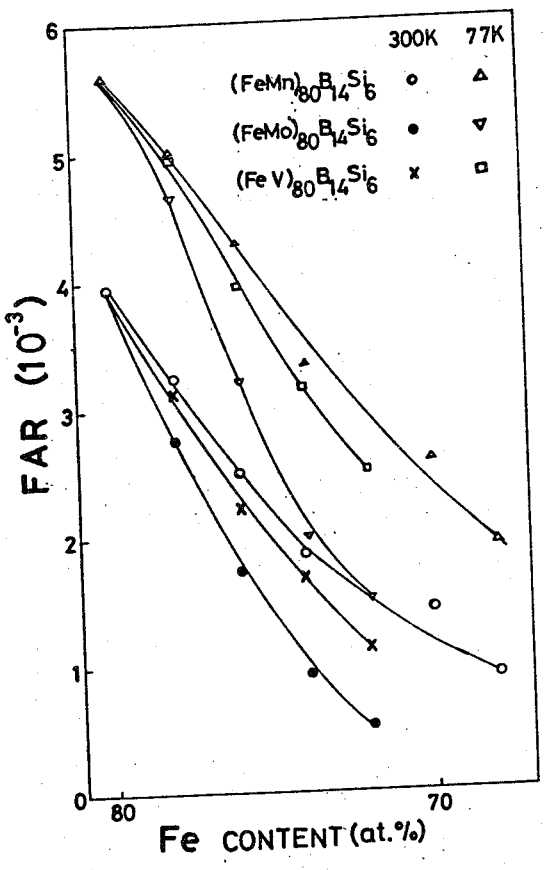

Fig. 1. The FAR of $(FeM)_{80}B_{14}Si_6$ systems with M = Mn, Mo and V as a function of Fe concentration at 77K and 300K.

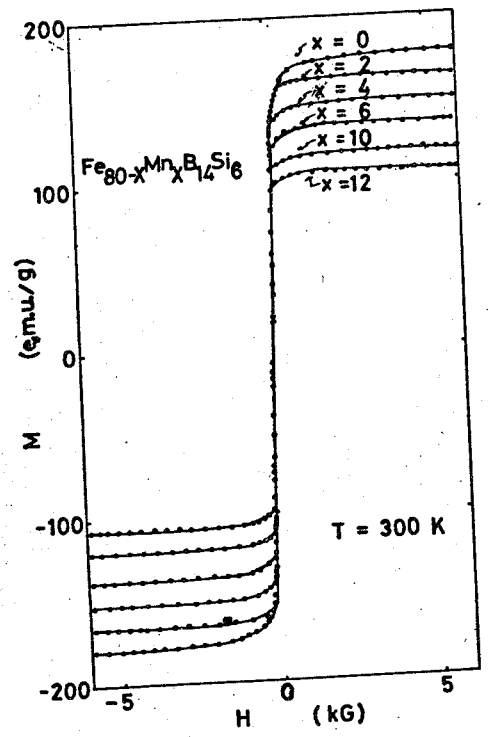

Fig. 2. The magnetization of $(FeMn)_{80}B_{14}Si_6$ alloys as a function of magnetic field at 300K.

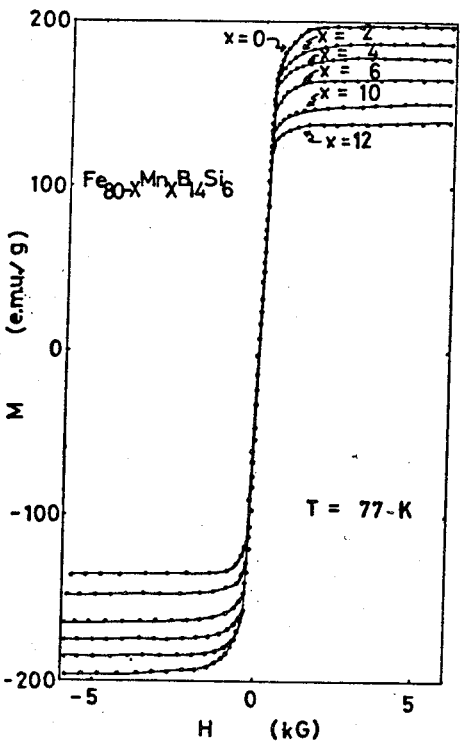

Fig. 3. The magnetization of $(FeMn)_{80}B_{14}Si_6$ alloys as a function of magnetic field at 77K.

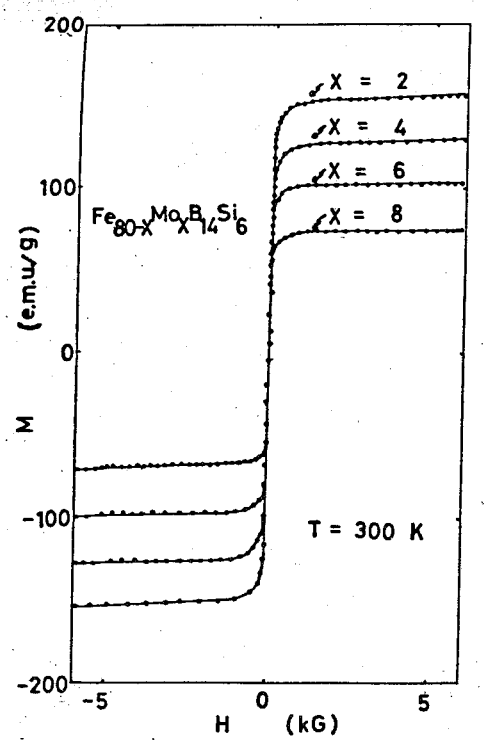

Fig. 4. The magnetization of $(FeMo)_{80}B_{14}Si_6$ alloys as a function of magnetic field at 300K.

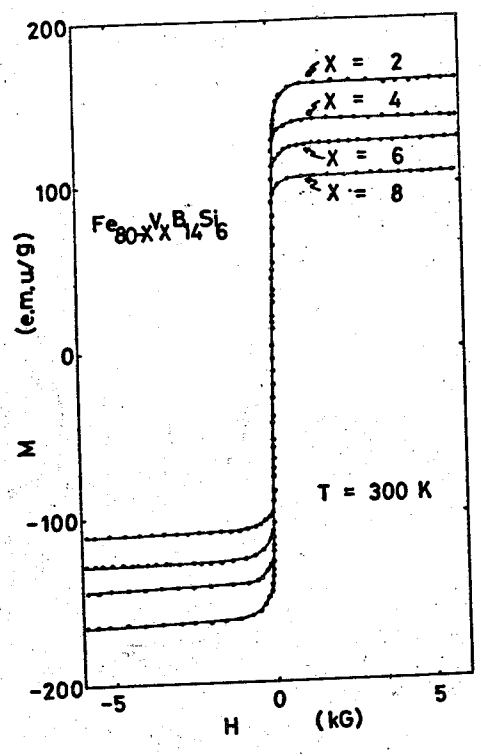

Fig. 5. The magnetization of $(FeMo)_{80}B_{14}Si_6$ alloys as a function of magnetic field at 77K.

Fig. 6. The magnetization of $(FeV)_{80}B_{14}Si_6$ alloy as a function of magnetic field at 300K.

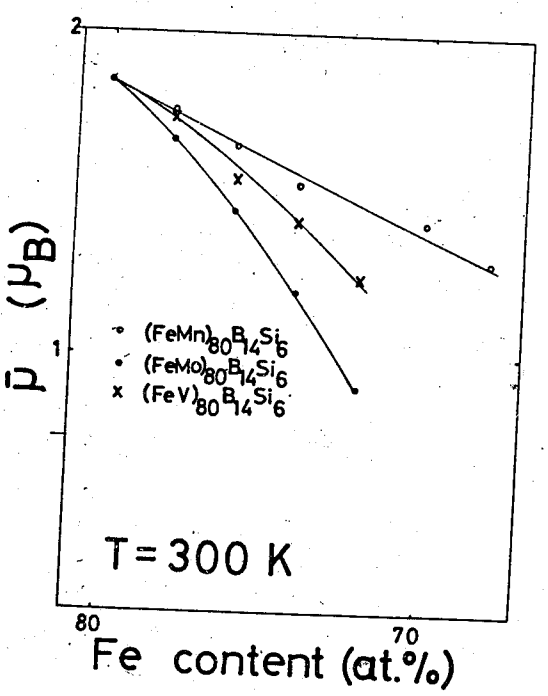

Fig. 8 The averaged magnetic moment per Fe atom as a function of Fe concentration at 300K.

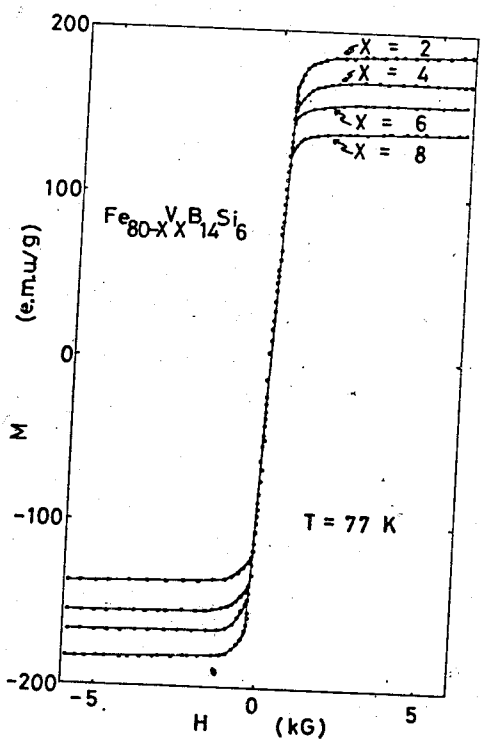

Fig. 7. The magnetization of $(FeV)_{80}B_{14}Si_6$ alloys as a function of magnetic field at 77K.

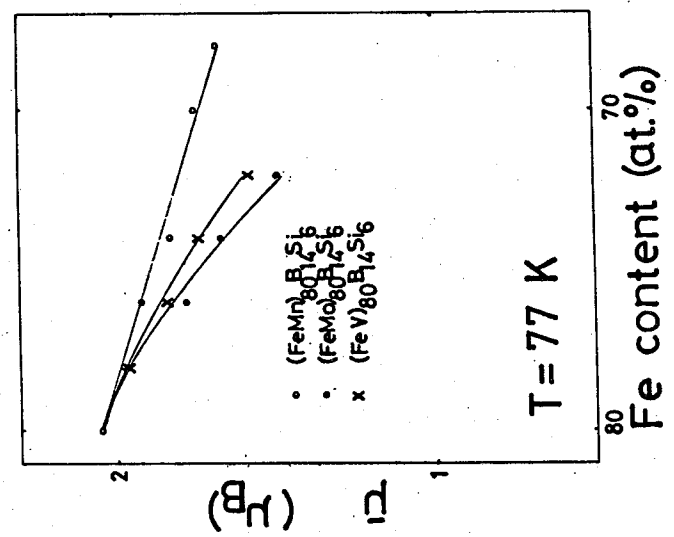

Fig. 9. The averaged magnetic moment per Fe atom as a function of Fe concentration at 77K.

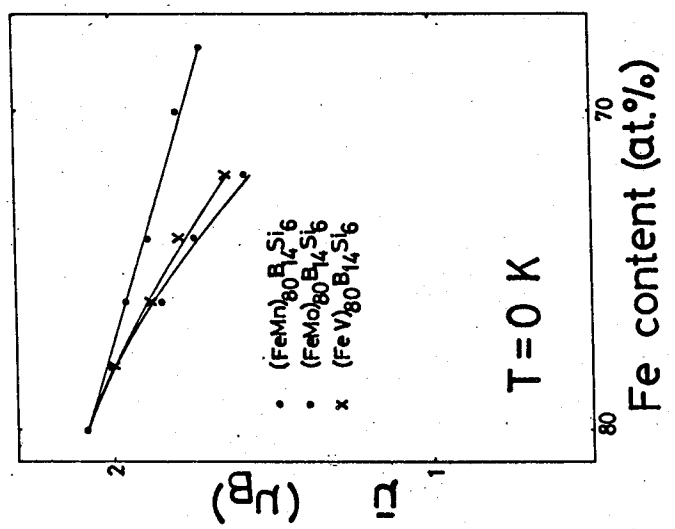

Fig. 10. The averaged magnetic moment per Fe atom as a function of Fe concentration at 0K.

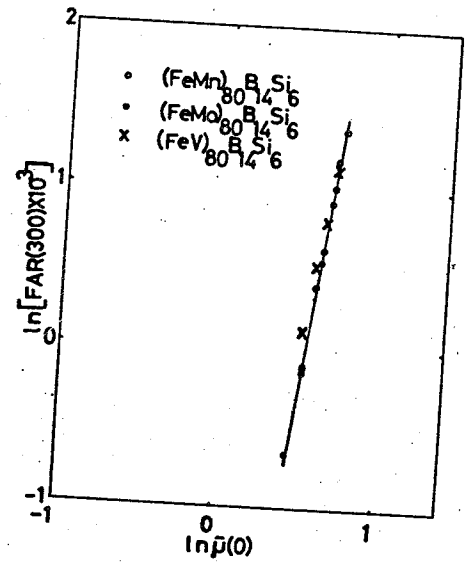

Fig. 11. Ln [FAR (300) x 10^3] versus Ln $\bar{\mu}(0)$ for $(FeM)_{80}B_{14}Si_6$ systems with M = Mn, Mo and V.

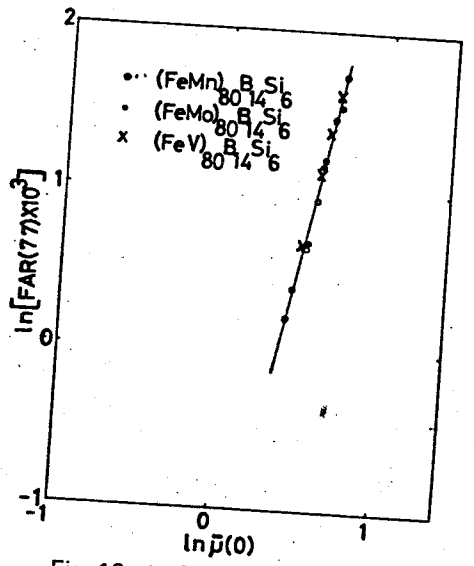

Fig. 12. Ln [FAR (77) x 10^3] versus Ln $\bar{\mu}(0)$ for $(FeM)_{80}B_{14}Si_6$ systems with M = Mn, Mo and V.

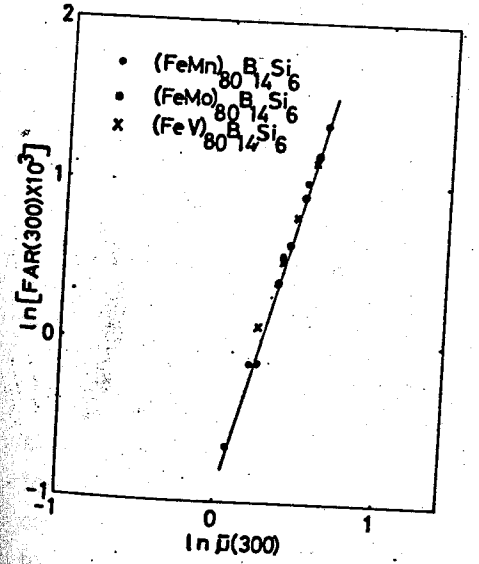

Fig. 13. Ln [FAR (300) x 10^3] versus Ln $\bar{\mu}(300)$ for $(FeM)_{80}B_{14}Si_6$ systems with M = Mn, Mo and V.

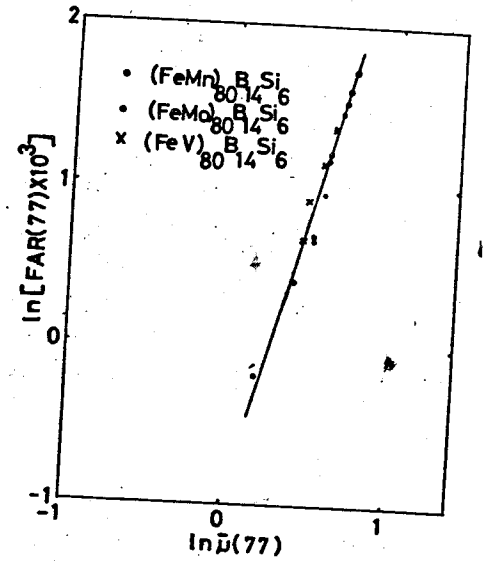

Fig. 14. Ln [FAR (77) x 10^3] versus Ln $\bar{\mu}(77)$ for $(FeM)_{80}B_{14}Si_6$ systems with M = Mn, Mo and V.

TRANSPORT PROPERTIES OF ANNEALED FEPD ALLOYS

S. U. Jen and Y. D. Yao

Institute of Physics
Academia Sinica
Taipei, Taiwan
R.O.C.

Abstract

In this paper, we review the transport and thermal expansion properties of the complete $Fe_{1-x}Pd_x$ (x=0–100 at.%) alloys system. Based on the Matthiessen's rule, the magnetoresistance $\Delta\rho/\rho_o$ of FePd alloys is found linearly proportional to $(\rho_o)_{ph}/\rho_o$. We have discussed from the two current model the basis to obtain large values of $\Delta\rho/\rho_o$. For $x \leqslant 30$ at.% Pd alloys, the electrical resistivity curves show hysteresis phenomena. Double T_c is observed for some annealed FePd. From thermal expansion measurements, the $Fe_{70}Pd_{30}$ sample exhibits a relatively low value of α near room temperature.

I. Introduction

It is interesting to study the physical and metallurgical properties of the complete FePd alloy system. In this paper, we review part of the work on magnetoresistance, electrical resistivity, and thermal expansion of FePd alloys, and present new results on the same subject. Since those published work has been shown, we will only mention them by the references in the text.

The experimental procedures in preparing the samples and the measuring techniques of magnetoresistance, electrical resistivity, and thermal expansion were all described in Refs. (1), (2), (3) and (4). Here, we only emphasize a few points as follows. First, we specify our samples with the notation $Fe_{1-x}Pd_x$, x is the atomic concentration of palladium. Secondly, all samples were homogenized at T=1200C for 24h before any thermal treatment. Thirdly, for completely quenched samples, they were quenched in water from T=1200C, and for completely annealed samples,

Special Issue of Annual Report of the Institute of Physics, Academia Sinica, Vol. 16, 1986
In Honor of Prof. Ta-You Wu on the Occasion of his 80th Birthday

they were heated in furnace at T=550C for 24h. However, for the intermediate thermal state samples, we specify them with the same notation as in Ref. (1).

In Sec. II, magnetoresistance of Fe-rich FePd alloys is discussed in view of the Matthiessen's rule. It is equivalent to the derivation of the temperature dependence of magnetoresistance. Moreover, the effect of atomic ordering and the rules for large value of magnetoresistance are also discussed. In Sec. III, the electrical resistivity of several Fe-rich samples is studied in the temperature range from 300K to 1200K. In particular, we will focus our attention on the x=15, 20, and 30 at.% Pd samples, because the interesting double T_c phenomnenon was observed. In Sec. IV, we briefly discuss the thermal expansion properties of FePd alloys, with special interest on the $Fe_{70}Pd_{30}$ sample.

II. Magnetoresistance

In the first part of following discussions, we study the temperature dependence of magnetoresistance, based on the Matthiessen's rule. Seven Fe-rich FePd alloys (x=0.9, 2.9, 6, 7.5, 10, 15, 30 at.% Pd) were used in this investigation. From Matthiessen's rule, it is known that due to impurity, or phonon scattering, ρ, ρ and ρ_o car be written as,

$$\begin{aligned} \rho &= (\rho)_{imp} + (\rho)_{ph} \\ \rho &= (\rho)_{imp} + (\rho)_{ph} \\ \rho &= (\rho_o)_{imp} + (\rho_o)_{ph} \end{aligned} \tag{1}$$

where ρ_o is the residual resistivity, ρ and ρ are the electrical resistivity measured in directions parallel and perpendicular to the saturation magnetization. Then,

$$\begin{aligned} \Delta\rho/\rho_o &= \frac{\rho_\parallel - \rho_\perp}{\rho_o} \\ &= \frac{(\rho_o)_{imp}}{\rho_o}\left[\frac{\rho_\parallel - \rho_\perp}{\rho_o}\right]_{imp} + \frac{(\rho_o)_{ph}}{\rho_o}\left[\frac{(\rho_\parallel - \rho_\perp)}{\rho_o}\right]_{ph} \\ &= \frac{(\rho_o)_{ph}}{\rho_o}\left[\left(\frac{\Delta\rho}{\rho_o}\right)_{ph} - \left(\frac{\Delta\rho}{\rho_o}\right)_{imp}\right] + \left(\frac{\Delta\rho}{\rho_o}\right)_{imp} \end{aligned} \tag{2}$$

where $(\Delta\rho/\rho_o)_{ph}$ and $(\Delta\rho/\rho_o)_{imp}$ are constants, representing $\Delta\rho/\rho_o$ when phonon, or impurity scattering is acting alone. Thus, if we plot $\Delta\rho/\rho_o$ vs $(\rho_o)_{ph}/\rho_o$, a straight line should be obtained for each sample. Fig. 1 has shown such a plot, and it is found that linear relation is generally observed for each sample. The exception of 0.9 at.% Pd sample at low value of $(\rho_o)_{ph}/\rho_o$ (or low temperature) is due to the existence of normal magnetoresistance[2].

The second part of discussion will be centered on the origin of magnetoresistance. According to Fert, Campbell, and Jaoul, they have used the two-current model of show that at low temperature in dilute nickel alloys the magnetoresistance is written as,

$$\Delta\rho/\rho_o = \gamma\left(\frac{\rho_\downarrow}{\rho_\uparrow} - 1\right) \tag{3}$$

where $\rho_\uparrow$ and $\rho_\downarrow$ are the resistivitives for spin-up and spin-down electrons. Hence, from Eq. (3), it is clear that from the theoretical point of view to obtain large $\Delta\rho/\rho_o$, $\rho_\uparrow$ must be maximized, while $\rho_\downarrow$ is minimized. Moreover, concluding both from theory and experiments, we may find that the following four conditions should be generally followed to have large $\Delta\rho/\rho_o$.

(a) Scattering by minority component of the alloy is dominant.
(b) The alloy is on the left-side or right-side part of the Slater-Pauling curve.
(c) The impurities are located to the left of iron in iron-rich alloys.
(d) The spin-down Fermi level is still located in d band of the majority component, rather than the impurity band.

Among these conditions, condition (b) minimize $\rho_\uparrow$ are conditions (c) and (d) have the effect of maximizing $\rho_\downarrow$. For a more detailed discussion in this respect, see Ref. (5). As to the atomic ordering effect on magnetoresistance, the physical origin behind the mechanism is closely related to that stated in condition (d). Experiments have shown that with increasing orderness in the $Fe_{50}Pd_{50}$ and $FePd_3$ samples (thermal treatments from (a) to (e))[1], the magnetoresistance increases accordingly, see Fig. 3 of Ref. (5). The reason is that since the Fermi level is still in the spin-down band, the atomic ordering may create a scattering resonance for $\rho_\downarrow$, and therefore increase the value of $\Delta\rho/\rho_o$. From a practical point of view, the four conditions mentioned above may serve as a guide to look for materials with large value of $\Delta\rho/\rho_o$.

Special Issue of Annual Report of the Institute of Physics, Academia Sinica, Vol. 16, 1986
In Honor of Prof. Ta-You Wu on the Occasion of his 80th Birthday

III. Electrical Resistivity

Experiments have shown that besides FePd alloys, FeNi alloys are also applicable to those conditions. At present, we are extending the search for large $\Delta\rho/\rho_0$ in the FePt alloys system.

For electrical resistivity, we summarize the results of the previous study on x=0.5, 1.0, 3.0, 7.9, 10.0 and 11.9 at.% Pd samples[3], and the results of this study on 15, 20 and 30 at.% Pd samples, Fig. 2. The resistivity measurements have been carried out between 300K and 1200K with both increasing and decreasing temperatures. Clearly, the common feature about Figs. 2 and 3 of Ref. (3) and Fig. 2 is that there exists a thermal hysteresis loop between 873K and 1073K for each curve. This signifys the α to γ and γ to α transformations. However to further determine the α to γ transition temperature $T_{\alpha\gamma}$ and γ to α transition temperature $T_{\gamma\alpha}$ from resistivity curves, the following comments are useually used. It is always observed for all the samples that during decreasing temperatures, $T_{\gamma\alpha}$ is well defined by the sharp drop in each resistivity curve. However, during increasing temperatures, the upward increase in ρ signifying $T_{\alpha\gamma}$ is only observed for samples with $x \leqslant 11.9$ at.% Pd. Table 1 has summarized all the $T_{\alpha\gamma}$ and $T_{\gamma\alpha}$ obtained from the resistivity curves. Moreover, the area enclosed by the hysteresis loop is seen to first increase with Pd concentration, Figs. 2 and 3 of Ref. (3), and then decrease, Fig. 2. This fact is also supported by the data $\Delta\rho_{\gamma\alpha}$ shown in the last column of Table 1. The definition of $\Delta\rho_{\gamma\alpha}$ is the resistivity drop measured at $T_{\gamma\alpha}$. Because $\Delta\rho_{\gamma\alpha}$ is a measure of phase changes from γ to α phase, together with the fact that $T_{\gamma\alpha}$ is less observable for $x \geqslant 11.9$ at.%, we may conclude that for $x \geqslant 15$ at.% FePd sample, it is predominantly in γ phase.

Finally, we discuss the determination of T_c from resistivity data. As usual, the T_c of each FePd alloys samples is determined from the λ type anomaly in each corresponding $d\rho/dT$ curve. Then, it is clear from Figs. 5 and 6 of Ref. (3) that there exists a sharply defined T_c transition peak for each alloy of $x \leqslant 11.9$ at.% Pd with increasing temperatures. Nevertheless, for decreasing temperatures, because T_c is higher than $T_{\alpha\gamma}$, the λ type anomaly is not observed. However, another interesting feature about T_c is that with increasing Pd, i.e. $x \geqslant 15$ at.%, there exist double T_c peaks in each resistivity curve. This is shown in Figs. 2 for 15, 20 and 30 at.% Pd samples. Further analysis with $d\rho/dT$ of these three samples is shown in Figs. 3-5. From the double peaks, we can determine the lower T_{c1} and the higher

T_{c2} for each sample, as in Table 1. This is an obvious result, since with increasing Pd concentration, more of the phase comes to coexist with the γ phase, and the lower T_{c1} which is the T_c of α phase begins to show up, while the higher T_{c2} which is the T_c of α phase still persists. Also, from Figs. 3-5, we could learn that as Pd concentration is increased from 15% to 30%, the peak altitude of T_{c1} becomes more prominent than that of T_{c2}. This indicates that more of the phase FePd exists in 30 at.% Pd sample, which is consistent with the conclusion from the previous paragraph.

IV. Thermal Expansion

Fig. 6 shows the thermal linear expansion $\Delta L/L$ vs T curves of 0.9, 6, 10, 15, 20 and 30 at.% Pd samples. The discontinuity which signifies the first-order α-γ transition is a typical phenomenon around T=800C for alloy samples with $x \leqslant 15$ at.% Pd. Besides the $\Delta L/L$ measurements with increasing temperatures, we also carried out $\Delta L/L$ measurements on 0.9, 6 and 10 at.% samples with decreasing temperatures. The result, as shown in Fig. 6, is a thermal hysleresis loop in the temperature range between 600C and 800C. This suggests that by increasing temperature, the α to γ transition temperature $T_{\alpha\gamma}$ is higher than the γ to α transition temperature $T_{\gamma\alpha}$ while cooling. This is consistent with the results from resistivity analysis and the values of $T_{\alpha\gamma}$ and $T_{\gamma\alpha}$ from thermal expansion curves are shown in Table 1. As to the discontinuous jump of $\Delta L/L$ at the transition temperature $\delta(\Delta L/L)$, we observe that for samples with $x > 15$ at.% Pd, it gradually disappears. From Table 1, it is estimated that $\delta(\Delta L/L)_{\alpha\gamma} \sim 0$ at $x \approx 17.5$ at.% Pd. Thus, this leads us to believe that the alloys samples are a mixture of the α and γ phases FePd in varying porprotions[6], the allos, with $x \geqslant 20$ at.% Pd, seem to be predominantly in γ phase. Hence, that is why the α-γ transformation in $\Delta L/L$ is not detectable in 20, 30 at.% Pd samples. This again agrees with the previous conclusions from the resistivity data.

As to the coefficient of thermal expansion α, four α vs T curves of 10, 15, 20 and 30 at.% Pd alloys are shown in Fig. 7, it is clear that for all the samples, at $T \sim 500C > \theta$ (θ: Debye temperature), approaches a constant value. This is consistent with the simple theory of Ref. (7). Since $\alpha \sim \gamma C_v$, where γ is the Gruneisen parameter and C_v is the specific heat due to the lattice vibration, and since at $T > \theta$, both γ and C_v are constants, α is a constant naturally. From Fig. 7, α is roughly equal to 3–3.5 $10^{-5}K^{-1}$ at $T > \theta$. At lower temperature ($T \sim 100C$), how-

ever, it is found that 30 at.% Pd sample shows an anomalous low value of α. This behavior is similar to that of Fe-Pd invar of quenched alloys. But, because samples phases obtained from different thermal treatments are generally different, the explanation for low α observed in the annealed sample is less clear. One possible explanation may be as follows. From the preceeding conclusions, the 30 at.% Pd sample consists mainly of γ phase at the room temperature. Hence, if the decomposition rate from γ phase to α phase FePd in the alloy is rather slow, the metastable γ phase FePd may still be the cause of low α in the annealed $Fe_{70}Pd_{30}$ [8]. The same phenomena have also been found in the annealed FeNi near 30 at.% Ni[9].

References

1. S. Jen, Y. Hsu and L. Berger, J. Appl. Phys. 50, 1907 (1979).
2. S. U. Jen and Y. D. Yao, Chin. J. Phys. 23, 310 (1985).
3. Y. D. Yao and S. Arajs, Phys. Status Solidi (A) 64, 95 (1981).
4. S. U. Jen and Y. D. Yao, Phys. Status Solidi (A) to appear.
5. S. Jen, Y. Hsu and L. Berger, J. Appl. Phys. 54, 1887 (1983).
6. M. Hansen, Constitution of Binary Alloys (New York, McGraw-Hill), 1958.
7. N. F. Mott and H. Jones, The Theory of the Properties of Metals and Alloys (New York, Dover) 1936.
8. E. I. Kondorsky and V. L. Sedov, J. Appl. Phys. 31, 3315 (1960).
9. Y. Tanji, J. Phys. Soc. Japan 31, 1366 (1971).

Table 1. $T_{\alpha\to\gamma}$, $T_{\gamma\to\alpha}$, T_c and $\delta(\Delta L/L)^*_{\alpha\to\gamma}$ of Fe-Pd alloys.

χ(nominal)	χ(analyzed)	$T_{\alpha\to\gamma}$(c)	$T_{\gamma\to\alpha}$(c)	T_C(c)	$\delta(\Delta L/L)_{\alpha\to\gamma}$(%)	$\Delta\rho(\gamma\to\alpha)$ ($\mu\Omega$cm)
0	0	912	910+	910	–	–
0.4	0.3	870	–	–	–	–
0.9	0.7	860	–	–	–	–
5.1	4.6	800	–	–	–	–
6.0	5.5	780	–	635	–	–
9.0	8.3	815	–	–	–	–
10.0	9.3	790	807	630	717	752
15.0	15.1	805	–	–	717	750
20.0	20.3	800	–	–	704	420
30.0	30.0	–	–	–	–	450
		(a)	(b)			717

(a): from thermal expansion, (b): from electrical resistivity.

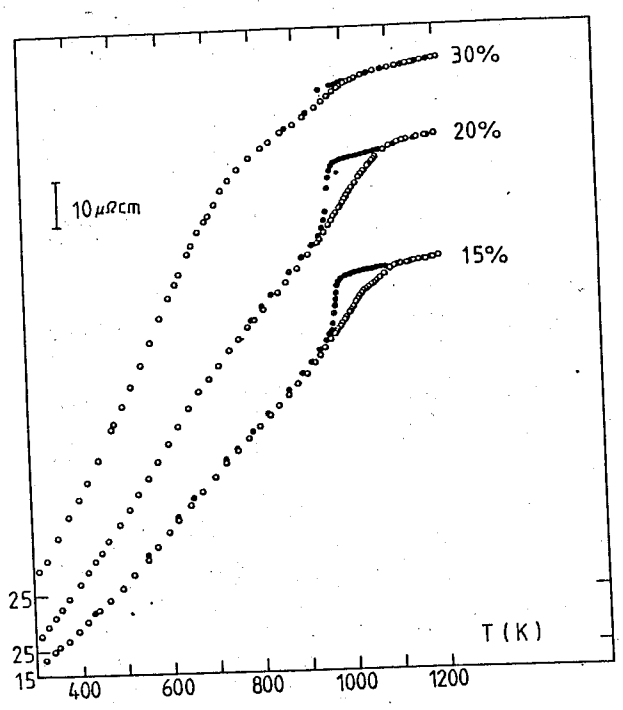

Fig. 2. The electrical resistivity of 15 at.%, 20 at.%, and 30 at.% samples versus temperature.
o: increasing temperatures and
●: decreasing temperatures.

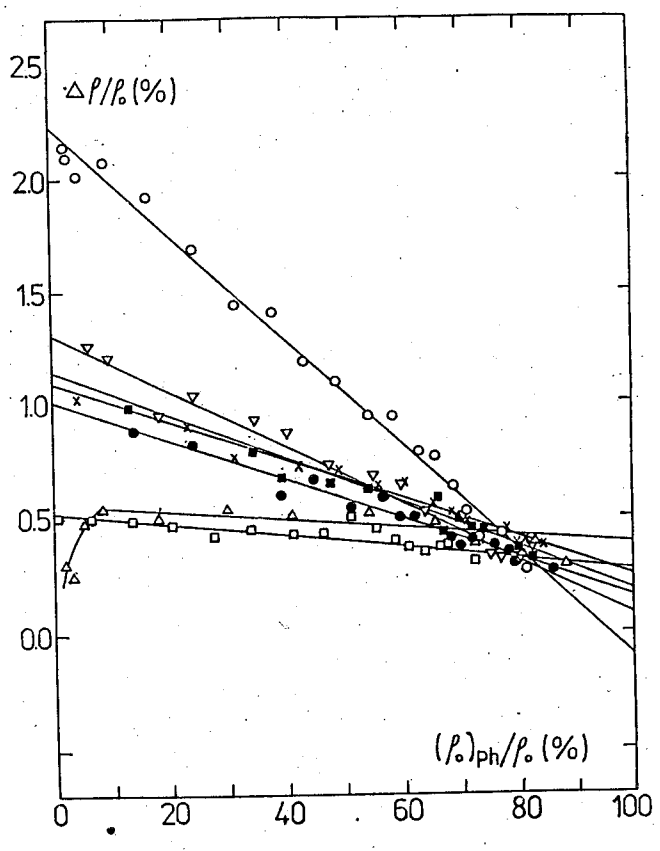

Fig. 1. The linear relation between $\Delta\rho/\rho_o$ and $(\rho_o)_{ph}/\rho_o$
o: 30 at.%, Δ: 15 at.%, x: 10 at.%, □: 6 at.%,
●: 7.5 at.%, □: 2.9 at.%, Δ: 0.9 at.%.

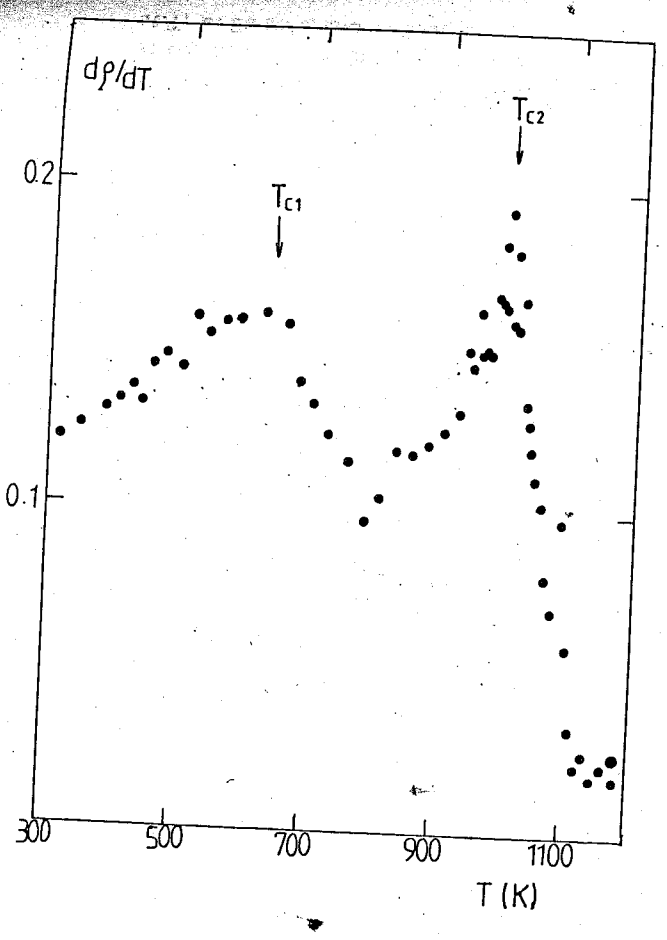

Fig. 4. $d\rho/dT$ versus temperature of $Fe_{80}Pd_{20}$.

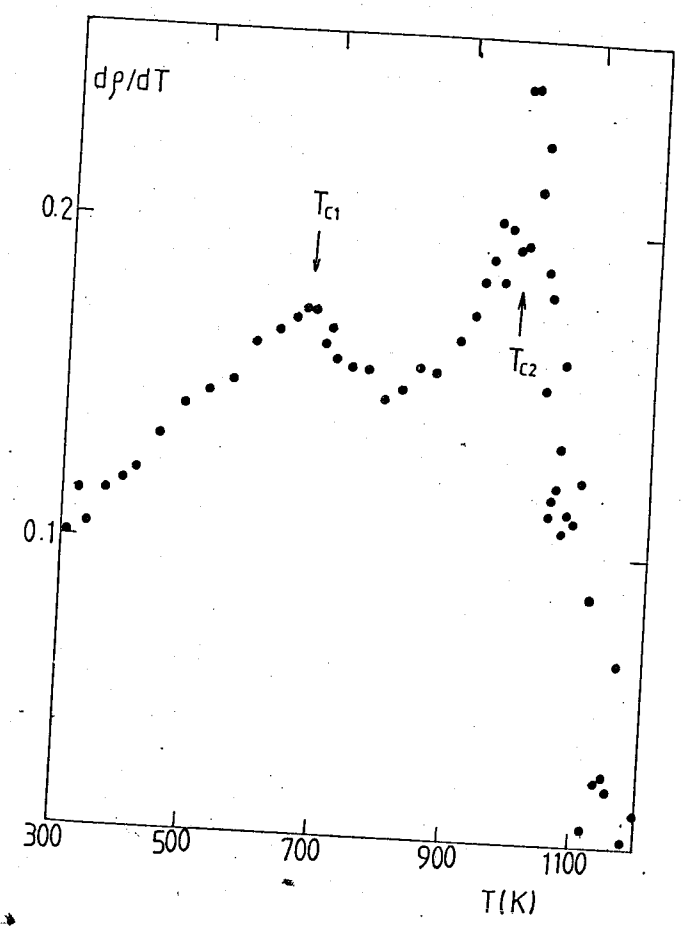

Fig. 3. $d\rho/dT$ versus temperature of $Fe_{85}Pd_{15}$

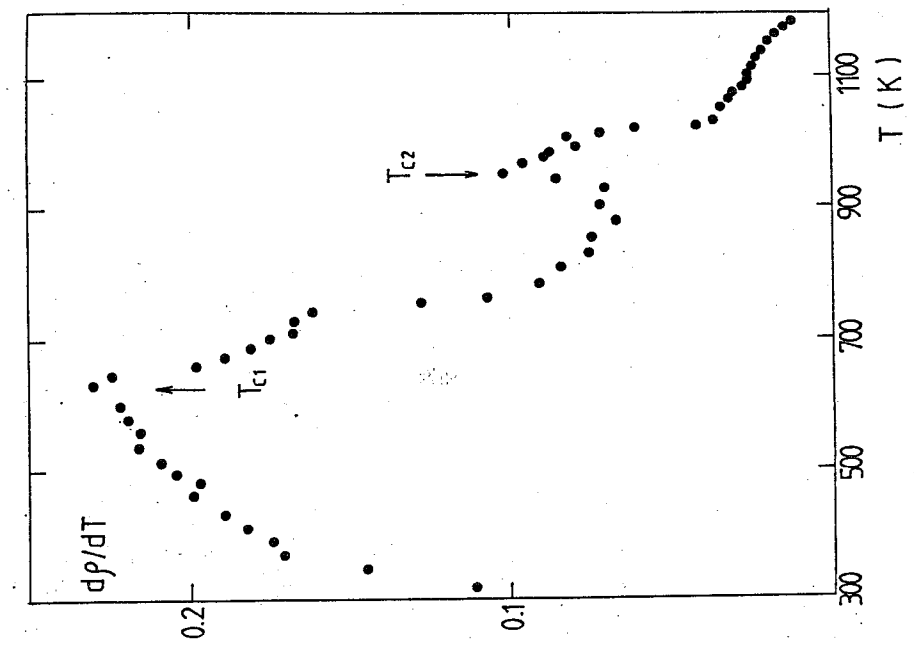

Fig. 5. dρ/dT versus temperature of $Fe_{70}Pd_{30}$.

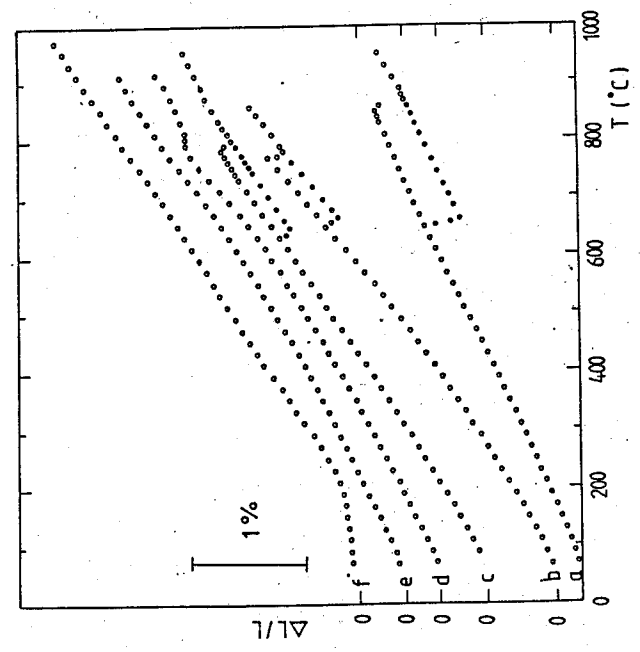

Fig. 6. Thermal expansion cuvers of ΔL/L vs T
a: 0.9 at.%, b: 6 at.%, c: 10 at.%, d: 15 at.T, e: 20 at.%, and f: 30at.%.

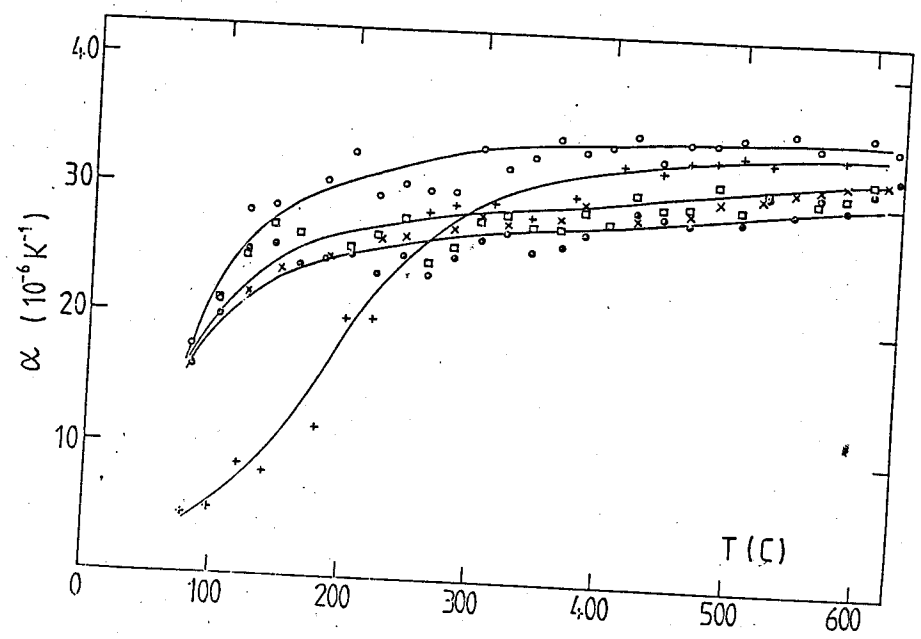

Fig. 7. The thermal expansion coefficient α of annealed FePd alloys.
o: 10 at.%, □: 15.%; ●: 20 at.%, +: 30 at.%.

ELECTRICAL RESISTIVITY AND MAGNETIZATION STUDIES OF SOME COMMERCIAL STEELS

Y. D. Yao, T. Y. Yen and J. Y. Chen

Institute of Physics
Academia Sinica
Taipei, Taiwan, R.O.C.

Abstract

The electrical resistivity ρ of rapidly solidified 304 (RS–304) stainless steel and DDQ, DQ, CQ_1, CQ_2 grade steels was measured as a function of the absolute temperature T between 4 and 1,300K. The magnetization was measured at both 77 and 300K in an applied magnetic fields up to 6 KG. From this investigation, we conclude that the Curie temperature T_c decreases slightly (small than 10K) and the α–ν transition near 1,180K is completely disturbed for Fe-based system with the Mn concentration roughly about 0.3% and the total impurity concentration roughly about 0.5%. No Kondo-like resistivity minimum anomaly is observable in these commercial steels for this study. A martensitic transformation which exhibits hysteresis in the electrical resistivity was observed for the RS–304 stainless steel near 100K.

I. Introduction

There have been considerable interest with regarding to the physical properties of Fe and Fe-based alloys [1-5]. Commercial steels are Fe-based alloys and belong to a class of technological important materials. From both fundamental and applied viewpoints, we are very interested to study their physical properties. In this investigation, we described the complete electrical resistivity behavior of commercial rapidly solidified 304 (RS–304) stainless steel and DQ, CQ_1, CQ_2 and DDQ grade steels as a function of the absolute temperature between 4K and 1,300K; and their magnetization behavior at both 77K and 300K.

Special Issue of Annual Report of the Institute of Physics, Academia Sinica, Vol. 16, 1986
In Honor of Prof. Ta-You Wu on the Occasion of his 80th Birthday

II. Experimental Consideration

RS–304 stainless steel was obtained from the Fibre Technology Limited, Germany. DQ, CQ_1, CQ_2 and DDQ grade steels were supplied by China Steel Co.. Their chemical Composition were listed in Table 1. All the samples for this study were cut in the form of rectangular parallelepipeds.

The surfaces of the samples were polished by files and sandpapers. The typical dimensions of the sample were roughly $1\times1\times20\ mm^3$ for electrical resistivity study and $1\times1\times6\ mm^3$ for magnetization study.

The electrical resistivity of these samples were measured by using the four-probe spotwelded technique. Temperature between 4K and 300K were achieved in a Displex Closed-Cycle Refrigerator, Platinum and carbon glass resistance thermometers were used to determine the temperature; temperature above 300K were obtained in a high-temperature furnance, two chromel-alumel thermocouples were taken to measure the temperature. Both furnance and refrigerator were evacuated. The DC durrent which was supplied to the samples was kept constant to about one part in 10^5. The electric potential were measured with a precision of 0.1 μv. A vibrating sample magnetometer was used to determine the magnetization.

III. Results and Discussion

Fig. 1 shows the electrical resistivity of commercial DQ, CQ_1, and CQ_2 and DDQ grade steels between 4K and 1,300K. For the comparison purpose, the electrical resistivity of pure Fe was also measured and plots in Fig. 1. The electrical resistivity of pure Fe which we obtained is consistent with that has reported before [6]. The Curie temperature, T_c, of pure Fe is determined by the maximum in the $d\rho/dT$ vs. T computer analyses (Fig. 2). The values of the T_c for pure Fe, DDQ, DQ, CQ_2 and CQ_1, are 1,041K, 1,034K, 1,036K, 1,032K and 1,037K, respectively. The α–ν structure transformation of pure Fe occurs near 1,180K by a steptype anomaly in the electrical resistivity curve.

For DQ, CQ_1, CQ_2 and DDQ grade steels, their electrical resistivity behaviors are quite similar in shape with the pure Fe; except that the electrical resistivity anomaly due to the α–ν structure transformation is not observed. The electrical resistivity anomaly near the α–ν structure transformation for Fe-Pd system has been reported before [7]. According to this study, we find that, for Fe-based

system with the Mn concentration roughly about 0.3% and the total impurity concentration roughly about 0.5%, the α–ν transition is not observable by the electrical resistivity measurement.

Fig. 3 shows the electrical resistivity of RS–304 stainless steel between 4 and 1,200K. The closed circles represent the heating run, and the open circles show the cooling run. The residual resistivity of RS–304 is quite large ($\sim 105\mu\Omega$-cm); it is almost twice the value for the slowly quenched commercial 304 and 430 stainless steels [8]. One of the possible reasons may be due to the different packing density; because the packing density of RS–304 is lower than that of the 304 and 430. The electrical resistivity data of RS–304 does not show any resistivity minimum anomaly which has been observed in commercial 304 and 430 stainless steels near 40K [8]. However, there is a small electrical resistivity hysteresis phenomenon near 100K for RS–304. This is suggested as the martensitic transformation. Similar phenomena have been observed in Li-Mg etc. system [9].

All the electrical resistivity data were fitted to the empirical formula

$$\rho(T) = \rho_o + AT^n$$

where ρ_o is the residual electrical resistivity independent of temperature and A is a constant independent of temperature. A logarithmic plot of $\rho-\rho_o$ against the absolute temperature T is shown in Fig. 4. From this plot, in the temperature range above roughly 1,050K, the index n comes out to be roughly 0.5 for all the samples. Between 100K and 1,000K, n is roughly equal to 1.8 for pure Fe, and DQ, CQ_1, CQ_2 and DDQ grade steels. However, for RS–304 stainless steels, the index n seems gradually changed from 0.5 above 1,000K to 1.9 near 100K. For pure Fe and DQ, CQ_1, CQ_2 and DDQ grade steels, it is evident that the temperature dependent part of the electrical resistivity increases faster than T in the ferromagnetic region (i.e. $T < T_c$). This is due to the spin ordering effect and the complicated combination of the interactions between electrons, phonons and magnons. Above room temperature the RS–304 stainless steel is definitely in the paramagnetic state. We believe that the gradual change of the index n from high temperatures to low temperatures could be due to the temperature-dependent scattering of the conduction electrons with the complicated impurities inside the RS–304 stainless steel.

Figs. 5 and 6 present the magnetization curves of pure Fe, DQ, CQ_1, CQ_2, DDQ and RS–304 grade steels in an applied fields up to 6 KG at 300K and 77K,

respectively. Their saturation magnetization values at both 300K and 77K are listed in Table 2. It is obvious that the saturation magnetization for DQ, CQ_1, CQ_2 and DDQ grade steels are roughly of the same order as that of pure Fe. However, the saturation magnetization value of RS–304 stainless steel is relatively quite small; and it is roughly the same order as that of the Al-Mn steels [10].

In conclusion, we have compared the electrical and magnatical properties of DQ, CQ_1, CQ_2, DDQ and RS–304 grade steels with that of the pure Fe. For Fe-based alloys, if there are roughly about 0.3% of Mn impurity and roughly about 0.5% of the total impurities, the Curie temperature of the system will decrease slightly (small than 10K); however, the α–ν structure transformation near 1,180K seems completely disturbed by these impurities. For the RS–304 stainless steel, a martensitic transformation which exhibits hysteresis in the electrical resistivity has been observed near 100K.

References

1. T. Nautiyal and S. Auluck, Phys. Rev. B32, 6424 (1985).
2. A. I. Liechtenstein, M. I. Katsnelson and V. A. Gubanov, Solid. St. Comm. 54, 327 (1985).
3. C. S. Wang, B. M. Klein and H. Krakauer, Phys. Rev. Lett. 54, 1852 (1985).
4. P. Muth and V. Christoph, Phys. St. Sol. B131, 769 (1985).
5. S. M. Bubiel and W. Zinn, Phys. Rev. B29, 2279 (1984).
6. S. Arajs and R. V. Colin, Phys. Stat. Sol. 6, 797 (1964).
7. Y. D. Yao and S. Arajs, Phys. Stat. Sol. a64, 95 (1981).
8. Y. D. Yao, Proc. Conf. Chinese Soc. Mat. Sci. p. 20 (1985).
9. G. Oomi and S. B. Woods, Solid St. Comm. 53, 223 (1985).
10. Y. D. Yao and S. U. Jen, J. Mag. Mag. Mat. 54, 949 (1986).

Table 1. Chemical Composition wt% (Fe base)

Grade	Concentration (%)									
	C	Mn	P	S	Si	Cu	Ni	Cr	V	Ti	Al
DDQ	.05	.260	.008	.009	.010	.010	.017	.019	.004		.048
DQ	.05	.250	.010	.009	.010	.010	.014	.012	.003	.003	.049
CQ_1	.08	.260	.006	.012	.010	.019	.016	.015	.009		.042
CQ_2	.06	.350	.008	.010		.006	.016	.030	.002	.003	.042
RS–304		2.68	.034	.029	5.807		19.43	25.81			

Special Issue of Annual Report of the Institute of Physics, Academia Sinica, Vol. 16, 1986
In Honor of Prof. Ta-You Wu on the Occasion of his 80th Birthday

Table 2. The saturation magnetization, M_S, at 77 and 300K

	M_S (e. m. u. / g)	
Sample	300K	77K
Fe	218.1	220.9
DQ	213.7	220.1
CQ_1	204.7	208.2
CQ_2	207.0	210.7
DDQ	206.7	210.4
RS–304	3.0	3.1

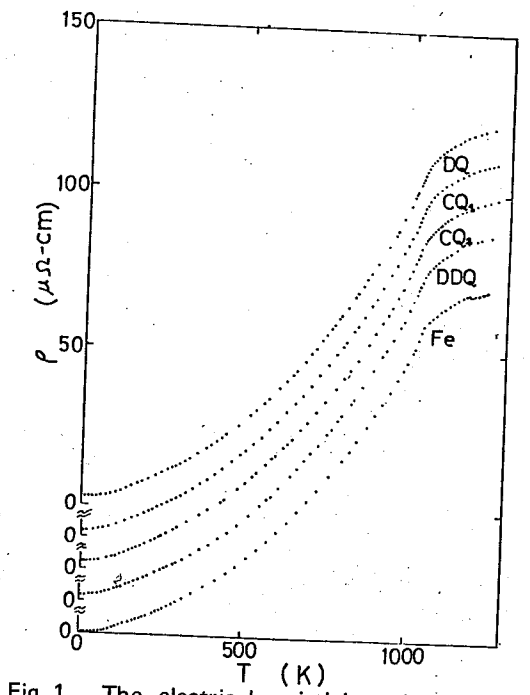

Fig. 1. The electrical resistivity of pure Fe, DDQ, CQ_2, CQ_1 and DQ grade steels as a function of temperature between 4 and 1,300 K.

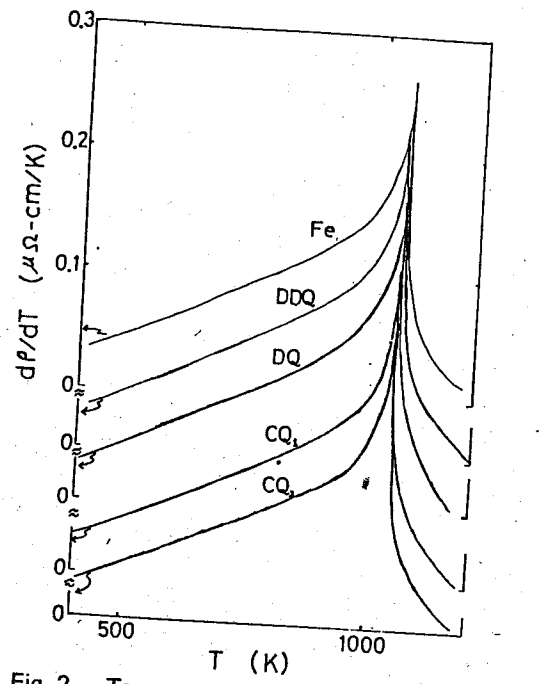

Fig. 2 Temperature derivative of the electical resistivity of Fe, DDQ, DQ, CQ_2 and CQ_1 grade steels as a function of temparture between 400 and 1,180 K.

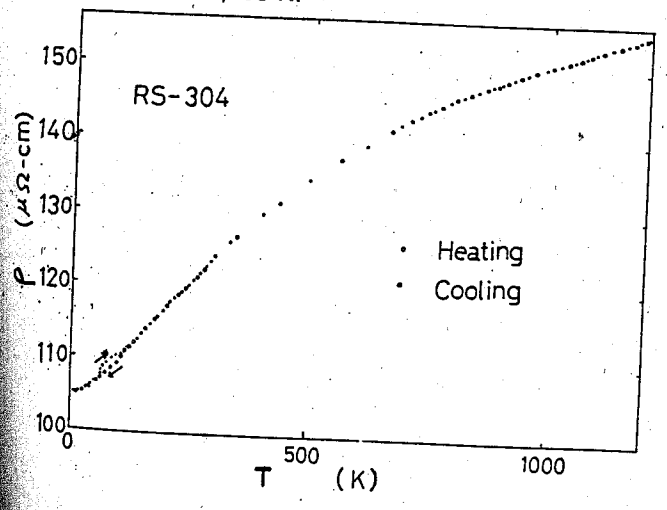

Fig. 3. The electrical resistivity of RS-304 stainless steel as a function of temperature between 4 and 1,200 K. The closed circless represent the heating run, and the open circles show the cooling run.

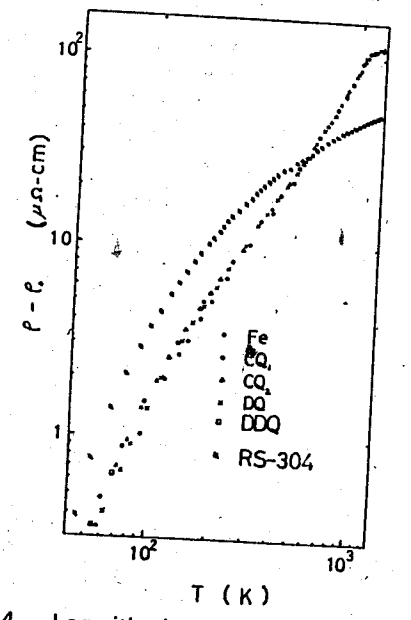

Fig. 4. Logarithmic plot of $(\rho - \rho_0)$ against T for pure Fe, CQ_1, CQ_2, DQ, DDQ and RS-304 grade steels.

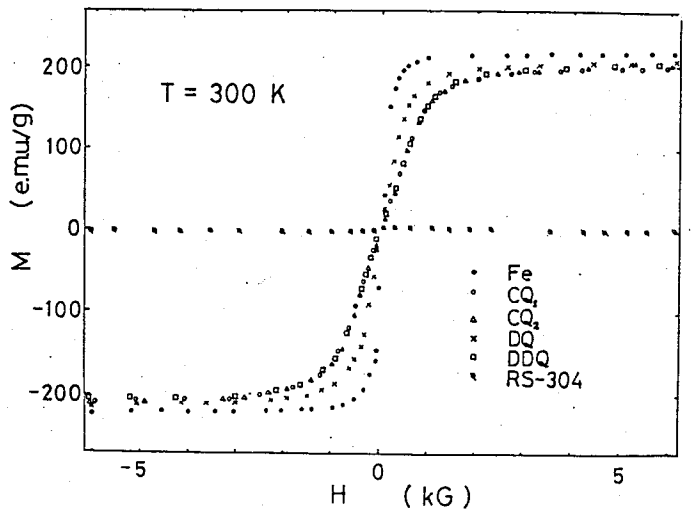

Fig. 5. Magnetization vs. Magnetic field at 300 K for pure Fe, CQ_1, CQ_2, DQ, DDQ and RS-304 grade steels.

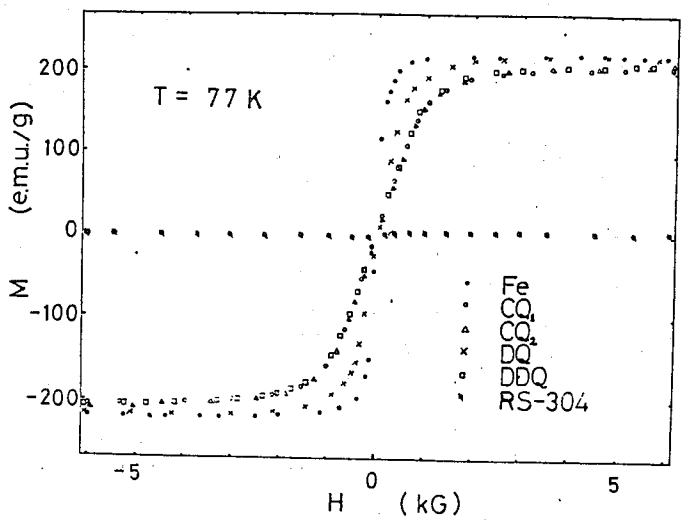

Fig. 6. Magnetization vs. magnetic field at 77K for pure Fe, CQ_1, CQ_2, DQ, DDQ and RS-304 grade steels.

TEMPERATURE DEPENDENCE OF THE ELECTRICAL RESISITIVITY AND DEVIATIONS FROM MATTHIESSEN'S RULE OF PD-ER ALLOYS

S. U. Jen and Y. D. Yao
Institute of Physic
Academia Sinica
Taipei, Taiwan
ROC

S. Arajs
Dept. of Physics
Clarkson College of Technology
Potsdam, NY
U.S.A.

Abstract

Measurements are presented of the electrical resistivity for a series of $Pd_{1-x}Er_x$ (x=0, 0.5, 1.0, 1.93, 3.97, 5.20, and 6.63 at %) alloys in the temperature range from 4K to 1200K. No Kondo like anomaly is found in each resistivity curve down to the lowest temperature. The experimental data clearly show the existence of two distinct kinds of resistivity behavior: $\rho_i \alpha AT^2$ for roughly 8K $<$ T $<$ 30K and $\rho_i \alpha$ BT for roughly 150K $<$ T $<$ 600K. Finally, the deviations from Matthiessen's rule of this alloy system is discussed in general.

I. Introduction

In the past, very few papers have dealt with the alloy system composing of transition and rare earth elements. This is partly because of the very limited solubility of rare earth elements in transition metals. However, it is known that palladium dissolves small amount of erbium [1, 2]. Due to this possibility, we

*Electrical resistivity, Pd-Er alloys, Deviations from Matthiessen's rule.

prepared several Pd-rich Pd-Er alloy samples, and studied their temperature dependence of electrical resistivity.

As to electrical resistivity, the interesting features of the Pd-Er alloys in the temperature range between 4K and 1200K include the possible Kondo like behavior [3], the s-electron-paramagnon scattering [4], the electron-phonon scattering [5], and the deviations from Matthiessen's rule [6]. In this paper, we shall give a detailed analysis of these mentioned subjects, based on the experimental results presented.

II. Experimental

A series of Pd-Er alloys containing 0.0, 0.5, 1.0, 1.93, 3.97, 5.2 and 6.63 at % Er were prepared in an arc furnace. The palladium used in forming the alloy is of 99.99% purity, and the erbium used is about 99.9% purity. The arc-melted ingots were sealed into silica capsules and homogenized at 1273K for 24 hr. After this treatment, each ingot was further swaged to a 2.5mm dia. by 15mm long rod. The final thermal treatment of the swaged rods was the anneal at 1273K for additional 1 hr.

The electrical resistivity measurements of the alloys were performed by using the four-probe method with direct current. The sensitivity of the potential meter used is as low as one part in 10^5. As to the temperature control of the samples, a 4K closed cycle refrigeration system was used to vary sample chamber's temperature between 4K and 300K, and a Varian Marshall furnace was used to vary temperature between 300K and 1200K. For low temperature measurements, a Pt- resistance thermometer was used to indicate temperature from 300K to 50K, and a silicon diode thermometer for temperature below 50K. For high temperature measurements, two type K thermocouples were placed in proximity of the sample to measure the average temperature.

III. Results and Discussion

The temperature dependence between 4K and 1200K of the electrical resistivity for all the Pd_{1-x} Er_x (x=0–6.63 at %) samples is given in Fig. 1. It is clear from this figure that each resistivity curve approaches a constant value, called residual resitivity ρ_o, at 4K. By plotting ρ_o vs Er concentration x, as in Fig. 2, a linear relationship is found. This generally insures that dilute alloys of sufficiently

good quality have been prepared. Also, from the Nordheim's rule in the limit of $x \ll 1$, $\rho_o \simeq x\,(1-x) \simeq x$.

As understood from Fig. 1, there exists no anomaly, either a minimum or a maximum, in electrical resistivity for each alloy at the lowest temperature. This indicates that Pd-Er alloy system is not a Kondo system. This is somewhat unexpected from the following viewpoints. First, from the magnetic susceptibility measurements [7], erbium's 4f electrons are localized and has a localized moment of 8.0 μ_B [8] associated with the ground state $^4I_{15/2}$ of Er^{3+} ion. Secondly, although dilute Pd-Er alloys are exchange enhanced, they are not ferromagnetic. Finally, from EPR studies [9], the s-d exchange integral $J_{s\text{-}d}$ of Pd-Er was found to be negative, in accordance with the Kondo theory. Hence, the electrical resistivity results of this study seems in contradiction with the above critera. However, if we believe that the Kondo effect is result of the interaction between the spin of s- conduction electron and the spin of the localized 4f electrons. Then, perhaps what is of interest is the s-f exchange rather than the s-d exchange as mentioned above. Thus, further experimental result of $J_{s\text{-}f}$ of Pd-Er is needed to confirm this view.

The temperature dependence of the electrical resistivity of Pd-Er alloys samples is investigated by fitting each ideal resistivity, as defined by

$$\rho_i(T) = \rho(T) - \rho_o \tag{1}$$

for the low and high temperature regions in a log ρ_i vs log T graph, as in Fig. 3. Clearly, from Fig. 3, both in the low temperature region (roughly below 40K) and in an intermediate high temperature region (roughly between 150K and 600K), the ideal resistivity data obey a T^n law. That is we may plot the linear relation of log ρ_i vs log T. In Fig. 3, each full line at low temperatures indicates the exact T^2 dependence, and at intermediate high temperatures indicates the T dependence. The dotted lines for each set of data indicates the deviations of the experimental curve from the exact T^2 or T dependence. Since the physical origin of the T^2 and T dependence happened in low and high temperature regions is different, we shall discuss them separately.

For the low temperature resistivity of exchange exchanced alloys, such as Pd-rich Pd-Ni, a theory [4], has predicated that due to the low-temperature s-electron-paramagnon scattering, the resistivity ρ_{sp} is found as

$$\rho_{sp} = A\left(\frac{T}{\theta}\right)^2 - C\left(\frac{T}{\theta}\right)^5 \qquad (T \ll \theta) \tag{2}$$

where A and C are constants, and θ is the Debye temperature. For the ideal resistivity ρ_i, besides the contribution from ρ_{sp}, there is also a mixing contribution of the phonon resistivity ρ_{ph}. As is well known, this phonon contribution gives the usual Bloch-Gruneisen T^5 resistivity results [5]. Hence, at low temperature $T \ll \theta$, there are usually two small T^5 terms in ρ_i opposing each other. This results in a strong function of T^2 dependence in the low temperature region.

For the Pd-rich Pd-Er alloys in this study, it is found that the dominance of $\rho_{sp} \propto AT^2$ at low temperature also occurs. This is because, like dilute Pd-Ni, Pd-Er is paramagnetic and the exchange enhanced alloy. To further investigate the T^2 dependence of the Pd-Er alloys, we have summarized from Fig. 3 for each alloy the temperature range of T^2 dependence in Table 1. Then, both from Fig. 3 and Table 1, it is shown that for all the Pd-Er alloys, including pure Pd, the deviations from the T^2 dependence are upward, and as the Er concentration is increased, the valid region of T^2 dependence becomes less. Hence, as in Ref. [4], it is believed that beyond the T^2 region, the upward increase in resistivity is caused by the mixing of ρ_{ph} which becomes more apparent as temperature is increased, and in the T^2 region, the shrinkage of valid region with increasing Er concentration is caused by decrease of the second T^5 term in ρ_{sp} and increase of Bloch-Gruneisen T^5 resistivity.

For the intermediate high temperatures, the T dependence of ideal resistivity of each alloy, as shown in Fig. 3, is due completely to the phonon contribution [5]. Table 1 shows the upper and the lower temperature limits of the T dependence of each alloy. From this table and Fig. 3, an interesting feature in resistivity is the deviations from the linear T dependence for temperatures higher than the upper limit. The reason for this deviation is the same as that (i.e., the narrowness of d band) given for Pd and Pt in Ref. [5], since samples under this study are all Pd-rich.

To further study the deviations of Matthiessen's rule (DMR), the electrical resistivity of the alloys is written as [6]

$$\rho_a = \rho_p + \rho_o + \Delta(C,T) \tag{3}$$

where ρ_p is the resistivity of an ideal pure host metal, and $\Delta(C,T)$ is the DMR quantity experimentally defined through Eq. (3). Suppose the value of ρ_o is replaced by the value of the electrical resistivity at 4K. Then, from Eq. (3), the deviation $\Delta(C,T)$ may be rewritten as

$$\begin{aligned}\Delta(C,T) &= [\rho(T) - \rho(4)]_a - [\rho(4)]_a - [\rho(T) - \rho(4)]_p \\ &= \Delta\rho(C,T) - \rho_c\end{aligned} \tag{4}$$

where

$$\begin{aligned}\Delta\rho(C,T) &= [\rho(T)]_a - [\rho(T)]_p \\ \rho_c &= [\rho(4)]_a - [\rho(4)]_p\end{aligned} \tag{5}$$

Sometime, $\Delta\rho(C,T)$ is called the solute resistivity.

Fig. 4 shows the temperature-dependent behavior of $\Delta\rho(C,T)$, which is the difference between electrical resistivity of Pd-Er and that of Pd. The general features of $\Delta\rho(C,T)$ are that for x=0.5 and 1.0 at % alloy, $\Delta\rho$ increases from 4K to a maximum near 750K, and then decreases, for 1.93, 3.97 and 5.20 at % alloy, $\Delta\rho$ behaves similarly, except an additional maximum exists at a lower temperature about 180K, for 6.63 at % alloy, $\Delta\rho$, with no maximum, decreases monotonically.

With Fig. 4, it is easy to calculate and plot the measured DMR, $\Delta(C,T)$, as in Fig. 5, from Eqs. (4) and (5). Since the difference between $\Delta\rho$ and Δ is just a constant term ρ_c, Figs. 4 and 5 look similar, except in Fig. 5, the hump in Δ decreases gradually with increasing Er concentration. The existence of a hump in Δ or simply monotically increasing Δ at low temperature (for $T < 300K$) can be understood from the two-band model [10]. However, the second hump and the decrease of Δ at high temperature can not be simply explained in that model. As a general rule, we can analyze $\Delta(C,T)$ at high temperature by decomposing it into two components: a component which is independent of temperature, and a component which varies approximately linearly with temperature. From Ref. [6], a temperature coefficient of resistivity, α_o, of the linear component is defined as

$$\alpha_o = \frac{1}{\rho_o}\frac{d\Delta}{dT} \tag{6}$$

For the Pd-Er alloys, α_o calculated from Fig. 5 is $-1.42\times10^{-3}K^{-1}$, $-6.45\times10^{-4}K^{-1}$, $-4.8\times10^{-4}K^{-1}$, $-2.72\times10^{-4}K^{-1}$, $-2.13\times10^{-4}K^{-1}$ and $-1.77\times10^{-4}K^{-1}$ respectively for the x=0.5, 1.0, 1.93, 3.97, 5.2 and 6.3 at % Er alloy. These values are between $10^{-3}K^{-1}$ and $10^{-4}K^{-1}$, which is in agreement in order of magnitude of α_o for transition metal impurities in noble metal alloys [6]. The same is also true for the Ni-Cr alloys [11] and Pd-Ag alloys system [12], where α_o becomes negative at high temperature.

In conclusion, we have discussed in this paper the lack of the Kondo anomaly in the electrical resistivity, the temperature dependence of ideal resistivity from the paramagnon scattering and phonon scattering mechanisms, and the deviations from Mattiessen's rule of the Pd-Er alloys system.

IV. Acknowledgement

S. U. Jen and Y. D. Yao are grateful to the National Science Council of R.O.C. for financial support of this work.

Table 1
The temperature regions of T^2 and T dependence of ideal resistivity of $Pd_{1-x}Er_x$ alloys.

Alloys (at % Er)	T^2 dependence	T dependence
0	8K < T < 30K	180K < T < 600K
0.5	8K < T < 40K	180K < T < 680K
1.0	8K < T < 30K	180K < T < 600K
1.93	12K < T < 30K	180K < T < 600K
3.97	11K < T < 28K	160K < T < 500K
5.20	12K < T < 22K	150K < T < 480K
6.63	14K< T < 20K	140K < T < 460K

Reference

1. Crangle J., Phys. Rev. Lett. 13, 569 (1964).
2. Peter M. Shaltiel D., Werrick J. H., Williams H. J., Mock, J. B. and Sherwood R. C., Phys. Rev. Lett. 9, 50 (1965).
3. Kondo J., Pogr. Theoret. Phys. 32, 37 (1964).
4. Schindler A. I., and Rice M. J., Phys. Rev. 164, 759 (1967).
5. Mott N. F. and Jones H., the Theory of the Properties of Metals and Alloys. P. 244, 268 and 273. Dover, New York (1963).
6. Bass J., Adv. Phys. 21, 431 (1972).
7. Arajs S. and Colvin R. V., Paramagnetism of Polycrystalline Rare Earth Metals, Macmillan Comp., New York (1961).
8. Cyrot M., Magnetism of Metals and Alloys, P. 275. North Holland, Amsterdam (1982).
9. Shaltiel D., Wernick, J. H., Williams J. J. and Peter M., Phys. Rev. 135 AI346 (1964).
10. Sondheimer H. E. and Wilson A. H., Proc. Roy. Soc. (London) 190, 435 (1947).
11. Yao, Y. D., Arajs S., and Anderson H. E., Phys. Status Solidi A79, 327 (1983).
12. Greign D. and Rowlands J. A., J. Phys. F. Vol. 4, 5536 (1974).

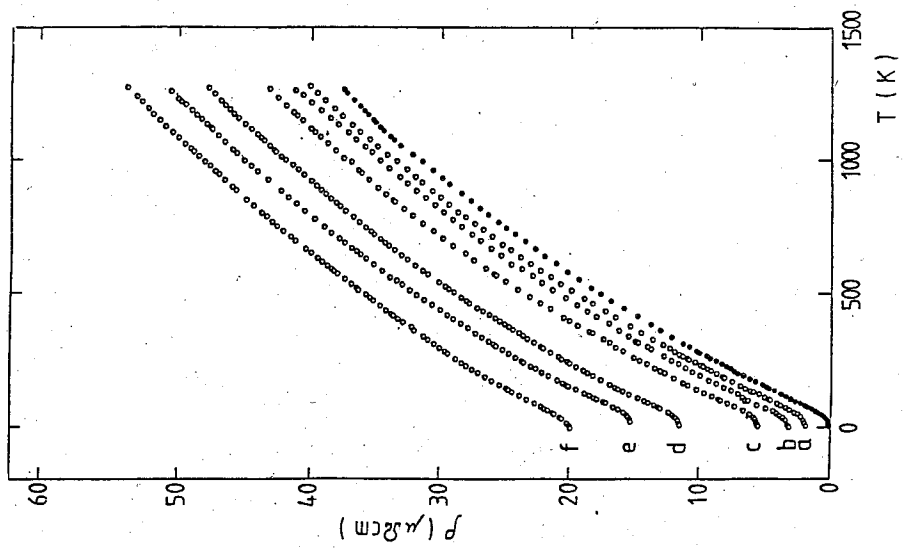

Fig. 1. Temperature dependence of electrical resistivity of Pd-Er alloys. the full circles are for pure Pd. a: 0.5, b: 1.0, c: 1.93, d: 3.97, e: 5.20, f: 6.63 at % Er.

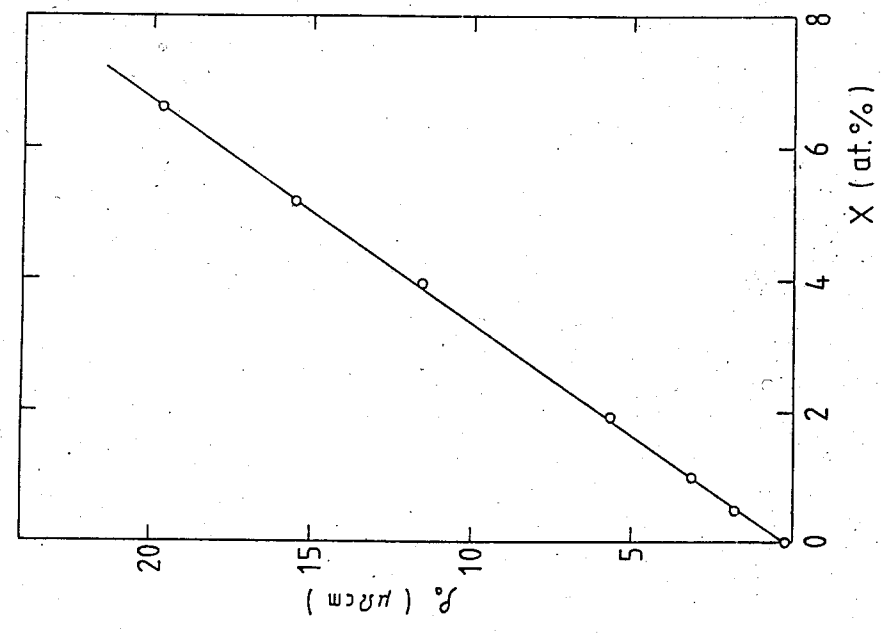

Fig. 2. Er concentration dependence of residual resistivity.

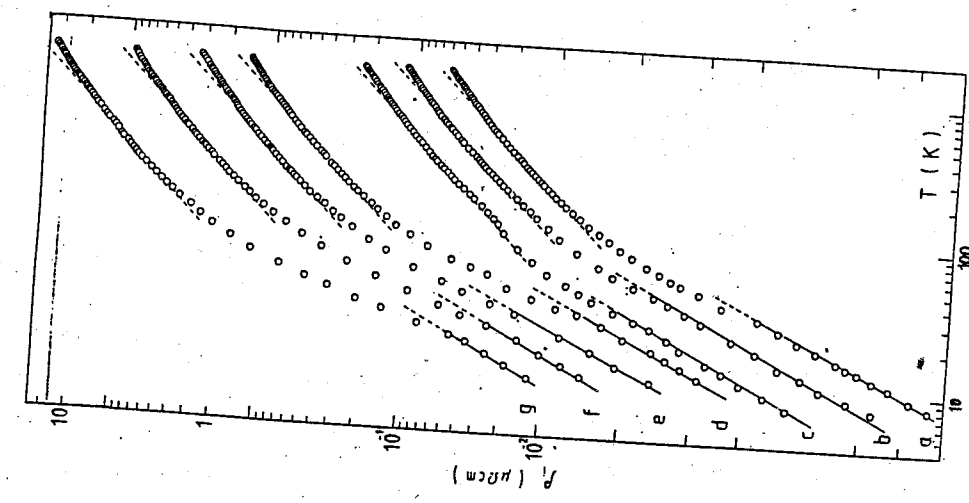

Fig. 3. The log-log plot of ideal resistivity vs temperature of Pd-Er. a: 0, b: 0.5, c: 1:0, d: 1.93, e: 3.97, f: 5.20, g: 6.63 at % Er.

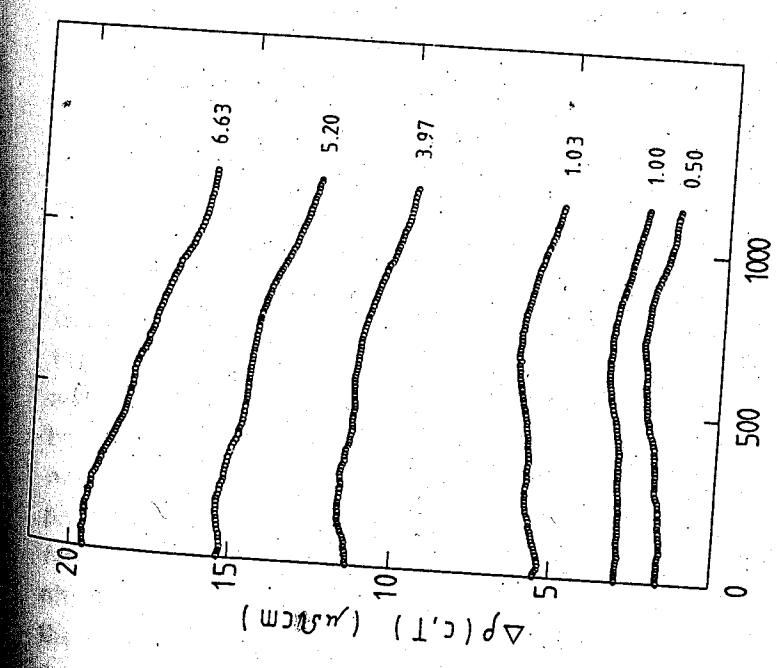

Fig. 4. Temperature dependence of $\Delta\rho$ (c, T). Parameter: Er concentration (at.%).

Special Issue of Annual Report of the Institute of Physics, Academia Sinica, Vol. 16, 1986
In Honor of Prof. Ta-You Wu on the Occasion of his 80th Birthday

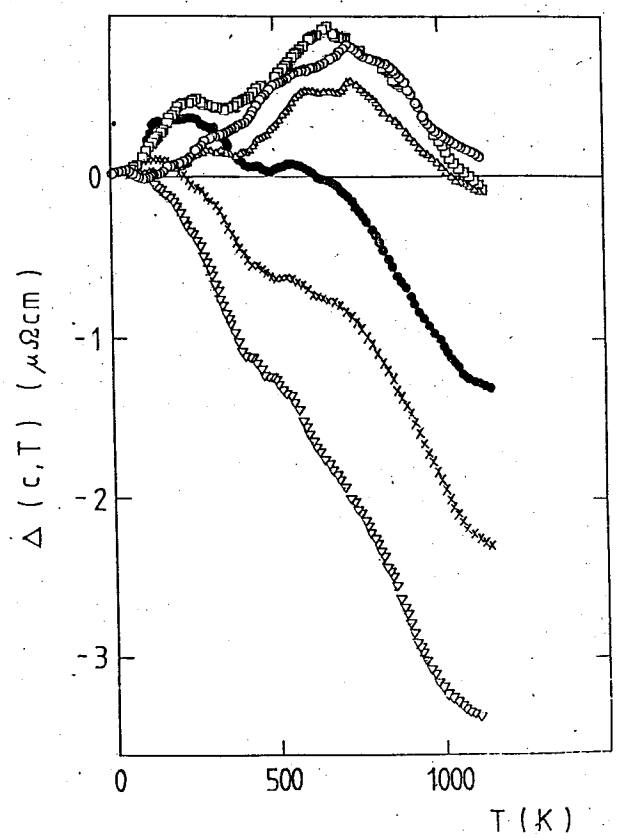

Fig. 5. Plot of measured DMR, Δ(c, T) for the Pd-Er alloys as a function of temperature. 0: 0.5, Δ: 1, □: 1.93, ●: 3.97, x: 5.2, Δ : 6.63 at% Er.

RAMAN SPECTROSCOPIC STUDIES OF CRYSTALLINE KNO_2

W. S. Tse
Institute of Physics, Academia Sinica
Taipei, Taiwan R. O. C.

K. F. Pai , W. Lih
Department of Physics, National Cheng Kung University
Tainan, Taiwan, R. O. C.

Abstract

The Raman spectrum of crystalline potassium nitrite has been studied by Raman spectroscopic techniques over the temperature range 300 k to 430 k. Above room temperature the structure of KNO_2 I and KNO_2 II is disordered. A new phase, above 380 k, has been confirmed and is thought to be an disordered variant of KNO_2 I.

I. Introduction

The complex polymorphism of the alkali nitrites affords considerable interest due to their variety of order-disorder phases related to orientation of the V-shaped anions (NO_2^-) in the ionic crystals. Several transitions have been reported in all of them, but no two salts are similiar to each other with respect to the structure of the phases in which they occur. Among them only $NaNO_2$ is most throughly studied because of its ferroelectricity at ambient conditions[1]. Crystalline potassium nitrite exists in seven polymorphic form[2] of which three (KNO_2 IV, V and VI) are existed only at elevated pressures and that all phases have been characterized by x-ray method. A calorimetric investigation of the polymorphism of potassium nitrite shows that there are at least three phases (KNO_2 I, II and III) of this compound at ordinary pressures. At high temperatures (above 312 K), the potassium nitrite form an face-centred cubic structure[3] of space group $O_h^5 - Fm3m$[4], and the nitrite ion has 32 possible orientations. In the intermediate temperature phase II, the nitrite ions are probably takes the form of 6 possible orientations to give an rhombohedral structure with space group $D^5 3d - R3m$[4]. Both two phases, I and II,

Special Issue of Annual Report of the Institute of Physics, Academia Sinica, Vol. 16, 1986
In Honor of Prof. Ta-You Wu on the Occasion of his 80th Birthday

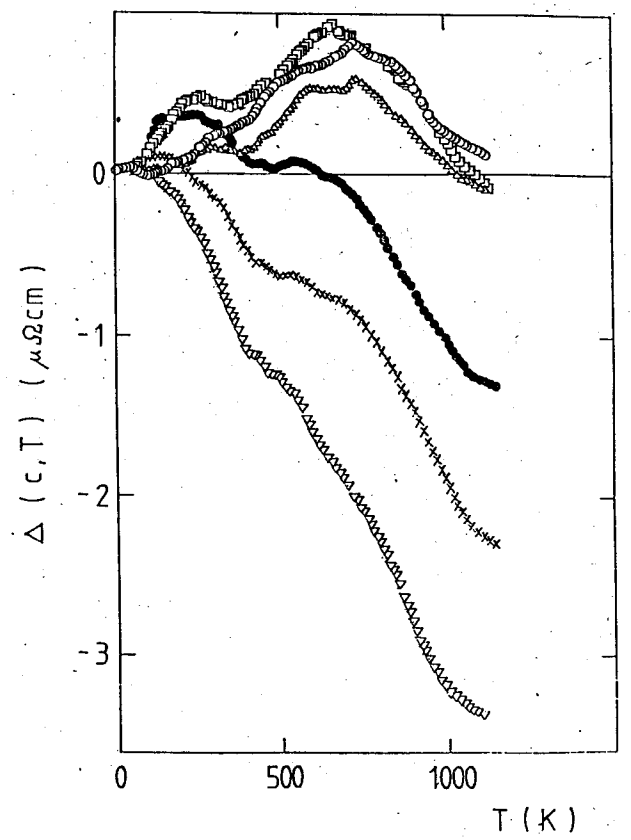

Fig. 5. Plot of measured DMR, Δ(c, T) for the Pd-Er alloys as a function of temperature. 0: 0.5, Δ: 1, □: 1.93, ●: 3.97, x: 5.2, Δ : 6.63 at% Er.

RAMAN SPECTROSCOPIC STUDIES OF CRYSTALLINE KNO_2

W. S. Tse
Institute of Physics, Academia Sinica
Taipei, Taiwan R. O. C.

K. F. Pai , W. Lih
Department of Physics, National Cheng Kung University
Tainan, Taiwan, R. O. C.

Abstract

The Raman spectrum of crystalline potassium nitrite has been studied by Raman spectroscopic techniques over the temperature range 300 k to 430 k. Above room temperature the structure of KNO_2 I and KNO_2 II is disordered. A new phase, above 380 k, has been confirmed and is thought to be an disordered variant of KNO_2 I.

I. Introduction

The complex polymorphism of the alkali nitrites affords considerable interest due to their variety of order-disorder phases related to orientation of the V-shaped anions (NO_2^-) in the ionic crystals. Several transitions have been reported in all of them, but no two salts are similiar to each other with respect to the structure of the phases in which they occur. Among them only $NaNO_2$ is most throughly studied because of its ferroelectricity at ambient conditions[1]. Crystalline potassium nitrite exists in seven polymorphic form[2] of which three (KNO_2 IV, V and VI) are existed only at elevated pressures and that all phases have been characterized by x-ray method. A calorimetric investigation of the polymorphism of potassium nitrite shows that there are at least three phases (KNO_2 I, II and III) of this compound at ordinary pressures. At high temperatures (above 312 K), the potassium nitrite form an face-centred cubic structure[3] of space group $O_h^5 - Fm3m$[4], and the nitrite ion has 32 possible orientations. In the intermediate temperature phase II, the nitrite ions are probably takes the form of 6 possible orientations to give an rhombohedral structure with space group $D^5 3d - R3m$[4]. Both two phases, I and II,

Special Issue of Annual Report of the Institute of Physics, Academia Sinica, Vol. 16, 1986
In Honor of Prof. Ta-You Wu on the Occasion of his 80th Birthday

are disordered. In the low temperature phase III, below 260K, the nitrite ions are fully ordered forming monoclinic crystal sturcture with space group $P2_1$ or $P2_{1/m}$ and four molecules per unit cell. The two transition temperatures are at $T_{c_1} = 312K$ and $T_{c2} = 260K$ respectively. In addition Tanisaki and Ishimatsu[5] reported a new phase transformation at 343K as well as an observation by Hoshino and Koyano that KNO_2 has a maximum permittivity at a transition temperature of 230K. Pistorius and Richter[6] concluded from powder x-ray method that KNO_2 III undergo a phase transition at 230 K to a new phase which labelled VII.

The room temperature Raman spectra of KNO_2 have been recorded previously by several workers[7,8,9] and also a Raman study of KNO_2 at 18K only was recorded by R. Carr et al[10]. None of these experiments extended to different temperatures other than 300 K and 18 K. It is therefore seemed worthwhile to make a detailed study of the high resolution laser-Raman spectra of crystalline KNO_2 at various temperatures between 300 K and 430 K covering KNO_2 II and KNO_2 I.

II. Experimental

Commerical KNO_2 (Merck) of high purity was used and the sample were dried and stored in an oven at 200°C for several hours. The solid powders were then loaded into the quartz cell under dry nitrogen atmosphere and placed in an Oxford Instruments DN 1714 variable temperature liquid nitrogen cryostat. The temperature sensor is a standard 100 Ω platinum resistor mounted on the inside of a heat exchanger. The heat exchanger is also fitted with a heater for temperature varying operation in conjunction with a DTC-2 temperature controller and the temperature resolution is nearly 0.1K.

Raman spectra were obtained using a standard 90° scattering configuration. The exciting source was a spectra-Physics 2000 kr^+ ion laser, operating at 0.3 - 0.4 w on the 6471Å line. Scattered light was analysed using a J. Y. Ramanor U1000 double monochromator and detected with a chilled RCA C31034A-02 photomultiplier tube and SPEX DPC-2 digital photometer. The output pulses were then fed to an IBM-PC computer for data storage, subsequent processing and also display on a X-Y plotter.

Frequencies reported here (corresponding to maximum intensities) are estimated to be accurate to $\pm 1\ cm^{-1}$ for sharp features. The spectral slit widths were set to maintain a resolution of about $1\ cm^{-1}$.

III. Results and Discussions

The Raman spectra of the crystal in the stretching mode region at various temperatures above room temperature up to 430K are shown in Figure 1. Spectra have also been recorded for the lattice mode region but are not illustrated here because they show little or no structure on a broad Rayleigh wing. Figure 2 shows the temperature dependence of the intensity of the internal mode frequencies of ν_1 and ν_2 and the temperature dependence of halfwidths of ν_2 is also shown in Figure 3.

From figure 1, it shows that the vibrational spectra in the region of the anion (NO_2^-) stretching modes is simple and has been readly assigned as refering to the C_{2v} symmetry of NO_2^- free ion as follow:

$$\nu_1(A_1) \equiv \nu\ (NO_2)\ \text{symmetric} \equiv 1323 cm^{-1}$$

$$\nu_2(A_1) \equiv \delta\ (NO_2)\ \text{bending} \equiv 806\ cm^{-1}$$

$$\nu_3(B_1) \equiv \nu\ (NO_2)\ \text{asymmetric} \equiv 1289\ cm^{-1}$$

It is noted that there are not any abrupt spectral changes in these three modes between 300 and 430K indicated that the phase transition of KNO_2 from phase I to phase II does not change the basic crystal symmetry. The absence of splitting of the ν_2 mode as compared to $LiNO_2$ may due to the absence of correlation field so that the nitrites in both phase I and II are in highly disordered state. Besides, the fact that no clearly defined lattice modes are observed in either the cubic or rhombohedral phases strongly suggests that these structures are both orientational disordered.

Curves of the peak height of ν_1 and ν_2 stretching modes versus temperatures are shown in figure 2. The resultant intensity decrease linearly as the temperature increased followed by an rapid rising as the transition temperature is approached. This may be an indication that the transition is taken from disordered phase II to more disordered phase I. A study of the linewidth (FWHM) of ν_1 mode versus temperatures shows a discontinuous change during the phase transition II → I due to the increase in reorientational freedom of the molecules from 6 possible orientations to 32 possible orientations. According to calorimetric investigations crystalline potassium nitrite exhibit only two phase transitions above room temperature. However, other workers[5] reported another higher temperature phase transition at 343K. In this work, it is shown in figures 2 and 3 that there is indeed evidence

of a further phase transition at higher temperature around 380K as reported by Tanisaki and Ishimatsu. The discontinuous change in linewidths and intensities versus temperatures during the transition I → "new phase" exhibits the increase in the reorientational freedom of the nitrite ion.

It is obvious from the above discussions that further research on crystalline KNO_2 is needed, before a fuller understand of its various crystalline phases at ambient pressure is obtained. It would be interesting to see the results by lowering the temperature to 80K so that the ordered phase I (below 260K) can be throughly studied and compared to $LiNO_2$ ordered phase. Besides, further lower temperature phase, phase VII, of KNO_2 as reported by Pistorius and Richter[6] by their thermal anomaly measurement between 173K and 238K can be investigated. There is still a considerable temperature range from 430K to 700K (melting point) of KNO_2 in which further disorder might develop. A detailed high temperature dependent Raman spectra might helpful to identify such a higher temperature transition takes place in potassium nitrite between 638 and 654K on the basis of electric conductivity measurements as reported by Frame etal[11].

IV. Acknowledgements

This research was supported by a grant from the National Science Council of the Republic of China.

References

1. S. Sawada, S. Nomura, S. Fujii and I Yoshida, phys, Rev. Lett. 1, 320 (1958).
2. C. W. F. T. Pistorius, Progr. Solid state Chem., 11, 1 (1976) and references therein.
3. J. D. Ray, J. Inorg. Nuce. Chem., 15, 290(1960).
4. J. K. Solbakk and K. O. Strømme, Acta Chim. Scand., *23*, 300 (1969).
5. S. Tanisaki and T. Ishimatsu, J. Phys. Soc. Japan. 20, 1277 (1965).
6. C. W. F. T. Pistorius and P. W. Richter, Z. Anorg. Allg. Chem. 389, 315 (1972).
7. M. H. Brooker and D. E. Irish, Can J. Chem 49, 1289(1971).
8. D. M Adams and S. K. Sharma, Solid State Commun, 23, 729(1977).
9. D. M. Adams and S. K. Sharma, Chem, Phys. Letters, 36, 407 (1975).
10. R. Carr, J. Vanos and B. H. Torrie, Chem Phys. Letter, *65,* 73 (1979).
11. J. P. Frame, E. Rhodes and A. R. Ubbelohde, Trans, Faraday Soc., 55, 2039 (1959).

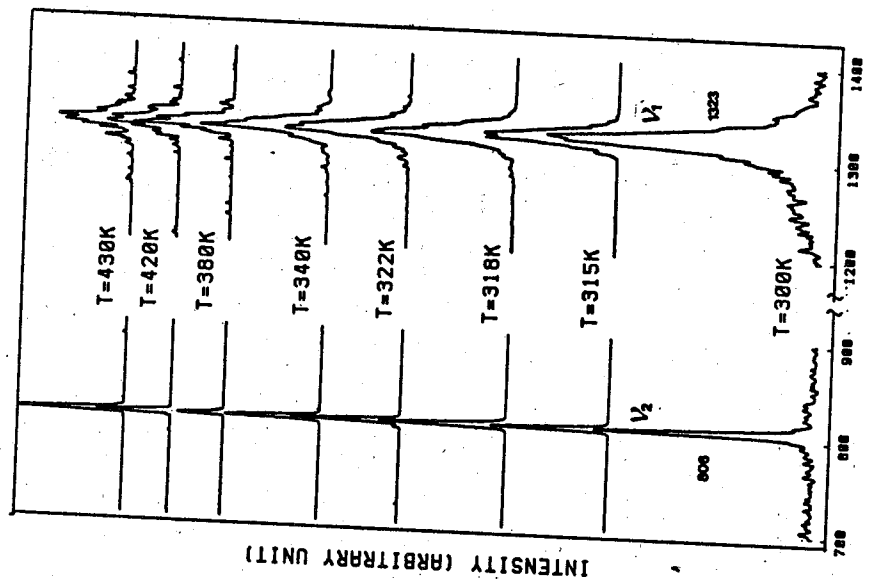

Fig. 1. The temperature dependent Raman spectra of crystalline KNO_2 in the stretching mode region.

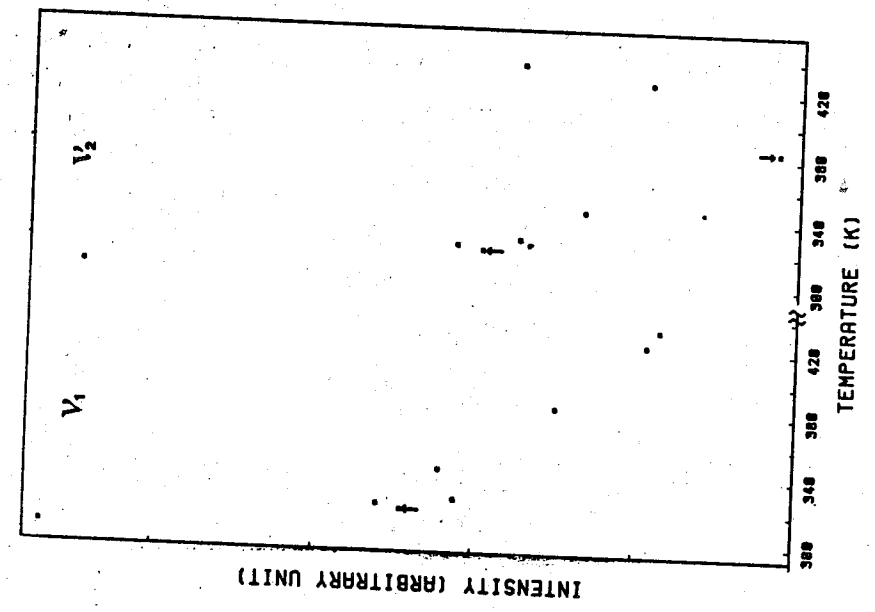

Fig. 2. The temperature dependences of the intensity of ν_1 and ν_2 internal modes.

Special Issue of Annual Report of the Institute of Physics, Academia Sinica, Vol. 16, 1986
In Honor of Prof. Ta-You Wu on the Occasion of his 80th Birthday

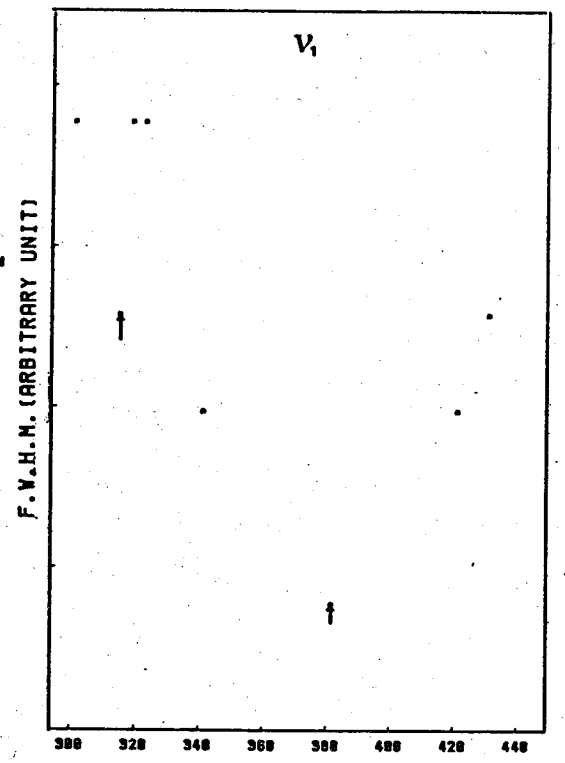

Fig. 3. The temperature dependences of the halfwidths of ν_1 internal mode.

ON BODY-FITTED COORDINATES FOR UNSTEADY INCOMPRESSIBLE VISCOUS FLOW OVER A CIRCULAR CYLINDER

Robert R. Hwang, M. T. Chiao and T. P. Chiang
Institue of Physics, Academia Sinica and
Department of Naval Architecture, Taiwan University
Taipei, Taiwan, Rep. of China

Abstract

In this study, numerical solutions of the equations governing time-dependent, viscous, incompressible fluid flow past a circular cylinder are presented for Reynolds numbers 100, 200 and 500. These solutions are based on the use of body-fitted coordinate systems having a coordinate line coincided with the body contour regardless of its shape.

The implicit solution utilizes the vorticity-stream function formulation. All field equations are approximated using central differences and are solved simultaneously at each time step by SOR iteration. Numerical computations are carried out for flows of Reynolds number 100, 200 and 500, and the results of these numerical flow simulations illustrate the phenomenon that the vortices of the flow pattern shed alternately from the two sides of the cylinder and evolve toward a periodic configuration. These solutions also reveal the oscillatory character of the drag, lift, and torque that are experienced by the cylinder.

I. Introducation

The time development of uniform flow over a circular cylinder is a classic problem in fluid mechanics. The combination of simple geometry, complicated flow phenomena, and flow interaction has led to extensive study by both experimental and theoretical investigators. At low Reynolds numbers ($Re < 40$; $Re = 2a\,U/\nu$, where a is the radius of the cylinder, U is the free stream velocity and ν is the kinematic viscosity of fluid) a steady symmetrical flow exists. On the other hand, at certain Reynolds numbers the flow in the wake of the body becomes unsteady and periodic and transforms into the so-called Karman vortex street. As a result, the forces that are imposed by the fluid upon the cylinder become oscillatory in nature.

Special Issue of Annual Report of the Institute of Physics, Academia Sinica, Vol. 16, 1986
In Honor of Prof. Ta-You Wu on the Occasion of his 80th Birthday

In the past, a number of numerical solutions for the problem of viscous flow past a circular cylinder have been reported. However, most of these solutions are for the case of steady flow or the case of unsteady symmetric flow[1-7]. Only some studies considered the problem of vortex street development [8-10]. In the computer simulation, finite difference or finite element method is usually used to formulate the numerical analysis. For flows around bluff geometries with flow seperation, conventional methods are found to be inadequate. First, the logarithmic transformation of the radial coordinate is adquate for the problem of flow over circular cylinders, but it needs a great number of grid resolutions to carry out the calculation of the entire flow field and hence consumes the computer time. Second, the use of interpolation between grid points to represent boundary conditions on a curved boundary passing through a rectangular grid may lead to poor application of the boundary conditions. Third, wall effects are obviously important and a finer element or grid size is needed to resolve large gradients accurately near the wall, it, therefore, requires larger computer storage and more computational time as compared to the steady problems.

With the above considerations, it would be highly desirable to prescribe a transformation of the physical flow field, irrespective of its shape, to a rectangular computational domain with coordinate lines coincided with all boundaries of the flow region. The method used to achieve this goal is the automatically generated body-fitted coordinate system developed by Thompson et al.,[11-12] where a coordinate line is always aligned with solid boundaries for any arbitrary two-dimensional geometry. In this study, the time development of the impulsively started unsteady viscous flow past a circular cylinder for Re = 100, 200 and 500 are thus solved on the transformed mesh. The fluid is assumed to be homogeneous, incompressible, and being governed by the Navier-Stokes equations.

II. Generation of Body-Fitted Coordinate Systems

The basic idea of the proposed body-fitted coordinate approach is to generate transformation functions such that all boundaries are coincident with coordinate lines. Following the work of Thompson et al[12], and Thames et al.,[11] the natural coordinates ξ and η are taken as solutions of an elliptic boundary value problem with one of the coordinates constant on the boundaries.

The curvilinear coordinates are generated by solving an ellipatic system of the form

$$\xi_{xx} + \xi_{yy} = P(\xi,\eta), \tag{1a}$$

$$\eta_{xx} + \eta_{yy} = Q(\xi,\eta), \tag{1b}$$

with Dirichlet boundary conditions, the ξ coordinate being specified as constant on one boundary and equal to another constant on the opposite boundary, with the η coordinate varying monotonically over the same range on both the boundaries. Subscripts indicate differentiation and will be used in the following sections.

Since it is desired to perform all numerical computations in the uniform rectangular transformed plane, the dependent and independent variables in Eq. (1) must be interchanged. This results in a coupled system of quasi-linear elliptic equations for determining the coordinate functions $x(\xi, \eta)$ and $y(\xi, \eta)$ in the transformed plane, and is given by

$$\alpha x_{\xi\xi} - 2\beta x_{\xi\eta} + \gamma x_{\eta\eta} = -J^2 [x_\xi P(\xi,\eta) + x_\eta Q(\xi,\eta)], \tag{2a}$$

$$\alpha y_{\xi\xi} - 2\beta y_{\xi\eta} + \gamma y_{\eta\eta} = -J^2 [y_\xi P(\xi,\eta) + y_\eta Q(\xi,\eta)] \tag{2b}$$

where
$$\alpha = x_\eta^2 + y_\eta^2 \qquad \gamma = x_\xi^2 + y_\xi^2 \tag{2c}$$
$$\beta = x_\xi x_\eta + y_\xi y_\eta , \qquad J = x_\xi y_\eta - x_\eta y_\xi$$

This set of equations is considerably more complex than the linear system of Eq. (1), but the boundary conditions are specified on straight boundaries, and the coordinate spacing in the transformed plane is uniform. The inhomogeneous functions $P(\xi,\eta)$ and $Q(\xi, \eta)$ are sums of decaying exponentials that allow coordinate lines to be attracted to specified lines and/or points in the domain or on the boundaries.

The solution to the finite difference approximations of Eqs. (2a) and (2b) where obtained by point SOR iteration.[13] all derinatines were approximated by second-order central difference operators. The actual values of the curvilinear coordinates ξ and η used to specify the boundary points are irrelevant to later use of the coordinate system since $\Delta\xi$ and $\Delta\eta$ simply cancel out of all difference expressions for the transformed derivatives. The application of the methodology to generate a grid system for the flow domain in this study is illustrated. Figure 1a shows the proposed boundaries of the flow domain in the transformed plane,

while Fig. 1b displays the results of the solution to Eq. (2) in the physical plane.

III. Derivation of the Basic Equations in Body-Fitted Coordinates

Consider the unsteady laminar flow of a viscous incompressible flow past a circular cylinder of radius a when the flow starts at time t = 0 with a constant velocity U in the undisturbed farther distance. The governing equation of motion in nondimensional form can be written as

$$\zeta_t + \psi_y \zeta_x - \psi_x \zeta_y = \frac{2}{Re}(\zeta_{xx} + \zeta_{yy}) \tag{3}$$

where ζ is the vorticity, Ψ is the stream function and Re = 2 Ua/ν is the Reynolds number.

The stream function ψ, the vorticity ζ and the velocity components u and v in the x and y directions are connected by the relations

$$\psi_{xx} + \psi_{yy} = -\zeta \,, \tag{4}$$

$$u = \psi_y \quad , \quad v = -\psi_x \tag{5}$$

The pressure distribution, drag, lift and torque on the circular cylinder are calculated from the vorticity and stream function fields.

The boundary conditions that are imposed upon the cylinder are the usual impermeability and no-slip conditions,

$$\psi = 0 \,, \quad \zeta = \zeta_b \qquad \text{at } r = 1 \tag{6}$$

and $$\psi_p = -(r + 1/r)\sin\theta \,, \zeta = 0 \text{ as } r \to \infty$$

Since we desire to perform all computations in the transformed plane, where the mesh system consists of simple rectangulars, Eqs. (3), (4) and (5) must be transformed such that ξ and η are the independent variables.

Using the fully conservative form of the differential operators given by

$$f_x = \frac{1}{J}[(f\, y_\eta)_\xi - (f\, y_\xi)_\eta] \tag{7a}$$

$$f_y = \frac{1}{J}[-(f x_\eta)_\xi + (f x_\xi)_\eta] \tag{7b}$$

where f denotes some arbitrary function and J is the Jacobian defined in Eq. (2c), the governing equations become

The boundary conditions under the transformation can be specified in the computational plane as

(1) On the boundary Γ^*,

$$\psi(\xi, 1, t) = 0, \zeta(\xi, 1, t,) = -\gamma\psi_{\eta\eta}/J^2$$

(2) On boundaries Γ_3, Γ_4, Γ_6 and Γ_7

$$\psi(\xi, \eta, t) = \psi_p, \ \zeta(\xi, \eta, t) \neq 0$$

(3) On the boundary Γ_5^*

$$\psi_\eta = 0, \ \zeta_\eta = 0$$

IV. Computational Procedures

The first step in the computational procedure is to solve the transformation equations (2) given a definition of the domain in terms of the x and y coordinates of boundary points along lines of constant ξ and η. Once convergence of the SOR point iteration is achieved (with convergence errors on the order of 10^{-5}), the definition of x, y locations along lines of constant ξ and η, the spatial derivatives of x_η, y_η, x_ξ and y_ξ, and J at each grid point are computed using second-order central differences for interior points and backward second-order differences along the boundaries. These derivatives, scaled to the appropriate size, are then available as input to the flow computation and consitute a complete description of the mesh geometry.

Given this definition of the mesh system, the governing equations of (8), (9) and (10) with boundary conditions were solved numerically with the fully implicit, forward-time, central-space formulation. A two-point, first-order forward difference was used to approximate the time derivative, while second-order central differences were employed for the spatial derivatives. The alternative direction implicit method of splitting the time step to obtain a multi-dimensional system equations was applied to solve Eq.(8), while point SOR iteration was employed to

$$\zeta_t + (\Psi_\eta \zeta_\xi - \Psi_\xi \zeta_\eta)/J = \frac{2}{Re}\left[\frac{2}{J^2}(\alpha\zeta_{\xi\xi} - 2\beta\zeta_{\xi\eta} + \gamma\zeta_{\eta\eta}) + (Q\zeta_\eta + P\zeta_\xi)\right] \tag{8}$$

$$(\alpha\Psi_{\xi\xi} - 2\beta\Psi_{\xi\eta} + \gamma\Psi_{\eta\eta})/J^2 + Q\Psi_\eta + P\Psi_\zeta = -\zeta \tag{9}$$

$$u = (x_\xi \Psi_\eta - x_\eta \Psi_\xi)/J, \qquad v = (y_\xi \psi_\eta - y_\eta \Psi_\xi)J \tag{10}$$

converge the elliptic space variation of Eq. (9). The basic steps of calculating algorithm involved in advancing the configuration through the cycle from time t to time t+δt are as follows:

1. At the beginning of the cycle all required quantities are available in the computer memory, either as initial data, or as results from the previous cycle.
2. Applying the ADI method, a new value of vorticity field ζ, is obtained in advancing a time step by solving of Eq. (8) subject to the appropriate boundary conditions.
3. With the new result for the vorticity field, a new value for the stream function ψ, is found from a finite-difference approximation of Eq. (9) by using the point SOR iteration.
4. From the finite-difference approximations of Eq. (10), u, v are found for the new components of the velocity.
5. Find the vorticity on the obstacle surface from Eq. (11a).
6. For selected cycles, summary inforamtion is computed and this, together with various configurations, is recorded for studying the time development of the flow field.

V. Presentation and Discussion of Results

The impulsively started unsteady viscous flows past a circular cylinder in variable Reynolds numbers were calculated using the numerical procedures outlined above. The solutions documented in the current paper utilized small time steps $O(1/R_e)$ in the initial phases to resolve the motion of the fluid under the effects of the impulsive start. Time steps were subsequently increased to values of the order of 5/Re to 10/Re without significant increases in the number of iterations required to converge each step. The spatial grid resolution in the computational domain as shown in Fig. 1 was set as $\Delta\xi = \Delta\eta = 1$ and NZ = 66, NE = 55, NZ1 = 13, NZ2 = 14, NZ3 = 52, NZ4 = 54 and NE2 = 30. In order to verify the numerical calculation of the present study, some results of the steady state solution after considerable time for Re = 100 and 200 were compared with the existing numerical and experimetal data. Figs. (2a) and (2b) give the comparisons of the time evolution of the wake length for Re = 100 and 200 respectively. The lengthe of the recirculation zone identified by L/a evolves almost linearly with time appears to be correctly agreed by comparing with other studies. Fig. 3 shows the comparisons of the time evolution of the seperation on the cylinder surface for Re = 100 and 200 respectively. They appear that good agreements are obtained with regard to the existing results of the

previous studies.

Since the solution procedure preserves symmetry approximately, the steady solution persists for long times, even for large values of Re. Thus it is desirable to introduce an artificial perturbation to excite the flow. The technique to perturbate was from Jordan's study[8] which was accomplished by impulsively twisting the circular counterclockwise, stopping, twisting clockwise and stopping. The timing and amplitude of the twists were adjusted in order to excite the Karman street as repaidly as possible without causing any long-duration effects. To twist the cylinder both clockwise and counterclockwise is related to the method of implementing the infinity conditions. It was assumed that the stream-function values on the outer edge of the computational domain are given by the free-stream values plus a correction that is independent of azimuth,

$$\psi^{b}_{fs} = \psi\ (\text{outer boundary}) = \psi^{fs} + f(r, t) \tag{12}$$

where ψ^{fs} is the stream function of the uniform free stream. Physically, this means that the effect of the cylinder at large distances is to shift all streamlines up or down slightly. The unknown perturbation f is determined seperately at each grid point on the outer edge of the computational domain from the formula

$$f_{i,j} = \psi_{i-1,j} - \psi^{fs}_{i-1,j} \tag{13}$$

where i is the index of the outer boundary. Averaging the perturbation over azimuth, the boundary values are determined,

$$\psi^{b}_{i,j} = \psi^{fs}_{i,j} + F \tag{14}$$

and $$F = N^{-1} \sum_{j=1}^{N} f_{i,j} \tag{15}$$

The function F may be interpreted as the distance, measured perpendicular to the free-stream velocity vector, that the upstream stagnation streamline has shifted. The imposed duration of the perturbation has changed for different time to check the dependence of the imposed time on the formulation of the vortex street. These computer experiments indicate that the artificial perturbation to trigger the onset of the vortex street of this approach is quite independent with respect to the selected mechanism of the perturbation. In this study, the displacement of the stagnation streamline due to the perturbation oscillates with an amplitude of about (0.01a, 0.015a and 0.02a) at (Re = 100, 200 and 500).

A typical sequence showing the streamlines, equivorticity lines and velocity vectors of the vortex shedding at Re = 100 for one appropriate cycle is given in Figs. 4, 5 and 6. The flow patterns illustrate the vortices continue to be shed alternately from the two sides of the cylinder and evolve towards a periodic configuration. As the bottom vortex behind the cylinder becomes larger and shifts slightly downstream, the top vortex continues to increase in strength, occupying paractically the entire breadth of the wake. The bottom vortex is still connected to the bottom seperation point by a feeding shear layer. When the strengthened top vortex begins to draw the bottom shear layer across the wake, it decreases in strength and shifts downstream while the bottom shear layer simultaneously forms a new bottom vortex. The new bottom vortex grows untill it occupies most of the breadth of the wake and finally draws the top shear layer across the wake cutting off further supply of vorticity to the top vortex. The top vortex is then shed and the cycle begins to repeat. The flow pattern of vortex shedding for Re = 100 gives the Strouhal number of S = 0.16 (i.e. shedding frequency x 2a/U).

The force acting on the cylinder surface arises from the surface pressure and shear forces. In terms of nondimensional local surface pressure and tangential shear forces, the drag, lift, and torque coefficients are given by

$$C_D = -\int_0^{2\pi} p \cos\theta \, d\theta - \frac{2}{Re}\int_0^{2\pi} \zeta \sin\theta \, d\theta , \tag{12a}$$

$$C_L = -\int_0^{2\pi} p \sin\theta \, d\theta - \frac{2}{Re}\int_0^{2\pi} \zeta \cos\theta \, d\theta , \tag{12b}$$

and

$$C_T = \frac{2}{Re}\int_0^{2\pi} \zeta \, d\theta . \tag{12c}$$

Using the transformations given in the previous section, the required integrations in Eqs. (12) were performed numerically along the cylinder surface (constant of η-line). Fig. 7 shows the drag, lift and torque coefficient histories for Re = 100. At early times, the drag coefficient decays repidly. Instead of settling to a small steady-state value of C_D, the wake behind the cylinder to become unsteady leads to a dramatic rise in the average drag coefficient. The fact that the average drag coefficient is larger for the oscillatory wake than the symmetric wake may be interpreted as a tendency toward an equilibrium state with maximum energy dissipation.

The effects of Re on vortex shedding phenomena are also carried out. Figs. 8-12 show the streamlines, equivorticity lines and velocity vectors of vortex shedding phenomena of flow behind the cylinder for one appropriate cycle at a higher Reynolds number of 200 and 500. We note that the vortex shape behind the cylinder at a higher Reynolds number becomes more narrow and slim compared to that for Re = 100. The shedding frequency is increased to be larger for the flow of higher Re. The Strouhal numbers for the higher Reynolds numbers of 200 and 500 are predicted to be approximately S = 0.182 and 0.2 respectively. Effects of Reynolds number on amplitude of drag, lift and torque oscillation amplitudes are also obtained and shown in Table I. Some results obtained in the present study were compared with other works and are summaried in Table II.

VI. Conclusion

With the use of body-fitted coordinate system, the study of time development of impulsively started viscous flow past a circular cylinder was performed for all numerical computation in the uniform rectangular transformation plane. In series of numerical calculations for several Reynolds numbers of flow condition, some tentative conclusions can be made as follows:

1. The use of body-fitted curvilinear coordinate system allows numerical solutions for flows of vortex shedding behind a cylinder containing a small number of grid resolution and is accurate in the results.
2. For these three cases (Re = 100, 200 and 500) of investigation, the flow pattern envolves toward a periodic configuration and an oscillatory wake associated with the so-called Karman vortex street is found.
3. The study shows that wake development is detailed from the initial formation of the two symmetric vortices to the subsequently asymetry and eventually alternate shedding.
4. These solutions show the dramatic rise of the drag coefficient during the development of the periodic vortex-shedding and reveal the oscillatory character of the drag, lift, and torque that are experienced by the cylinder.

Acknownledgment

This research is in part supported by the National Science Council of the

Republic of China.

References

1. Keller, H. B. AND Takami, H. 1966: Numerical Solutions of Non-linear Differential Equations, edited by D. Greenspan, Wiley, New York, p. 115.
2. Hamielec, A. E. and Raal, J. D. 1969: Numerical studies of viscous flow around circular cylinders, Physics of Fluids 12, 11-17.
3. Son, J. S. and Hanratty, T. J. 1969: Numerical solution of flow around a cylinder, J. Fluid Mech. 35, 369-386.
4. Underwood, R. L. 1969: Calculation of incompressible flow past a circular cylinder at moderate Reynolds numbers, J. Fluid Mech. 37, 95-114.
5. Dennis, S. C. R. and Chang, G. Z. 1970: Numerical solution for steady flow past a circular cylinder at Reynolds number up to 100, J. Fluid Mech. 42, 471-488.
6. Collin, W. M. and Dennis, S. C. R. 1973: Flow past an impulsively started circular cylinder, J. Fluid Mech. 60, 105-126.
7. Loc, T. P. 1980: Numerical analysis of unsteady secondary vortices generated by an impulsively started circulare cylinder, J. Fluid Mech. 100, 111-132.
8. Jordan, S. K. and Fromm, J. E. 1972: Oscillatory drag, lift, and torque on a circular cylinder in a uniform flow, Physics of Fluids, 15, 3, 371-376.
9. Gresho, P. M. Lee, R. L. and Sani, R. L. 1980: On the time-dependent solution of the incompressible Navier-Stokes equations, Recent Advances in Numerical Methods in Fluids, edited by C. Taylor, Pineridge Press, 27-80.
10. Deffenbaugh, F. D. and Marshall, F. J. 1976: Time development of the flow about an impulsively started cylinder, AIAA Journal, 14, 7, 908-913.
11. Thames, F. C., Thompoon, J. F. et. al. 1977: Numerical solution for viscous and potential flow about arbitary two dimensional bodies using body-fitted coordinate system, J. Comput. Phys. 24, 245-273.
12. Thompson, J. F., Thames, F. C. and Mastin, C. W. 1977: TOMCAT, J. Comput Physics 24, 274-302.
13. Roache, P. 1972: Computational Fluid Dynamics; Hermosa Publishers, 434 pp.
14. Lin, C. L., Pepper, D. W. and Lee, S. C. 1976: Numerical methods for seperated flow solutions around a circular cylinder. AIAA J. 14, 900-907.
15. Thoman, D. and Szewczyk, A. 1969: Time dependent viscous flow over a circular cylinder. Phys. Fluid, Suppl. II, 79-86.
16. Patel, V. A. 1978: Karman vortex street behind a circular cylinder by the series

truncation method, J. Comput. Physics 28, 14-42.
17. Lecointe, Y. and Piquet, J. 1984: On the use of several compact methods for the study of unsteady incompressible viscous flow round a circular cylinder. Computer & Fluids, 12, 255-280.
18. Smith, J. C. and Brebbia, C. A., 1977: Improved stability techniques for the solution of Navier-STokes equations. Appl. Math. Modeling, 1, 227-234.

Table 1. Effect of Reynolds number on amplitude of drag, lift, and torque oscillation amplitudes.

Peak-to-peak amplitude of	Re = 100	Re = i00	Re = 500
Drag oscillation (C_D)	0.012	0.082	0.18
Lift oscillation (C_L)	0.78	1.20	1.78
Torque oscillation (C_T)	0.02	0.02	0.02

Table 2. Comparison between computed values of mean drag, lift and strouhal number.

Re	C_D	C_L	S	Author(s)
100	1.28	± 0.54	0.16	Jordan and Fomm (8)
	1.29	± 0.50	0.133	Patel (16)
	1.43	± 0.50	0.166	Smith and Brebbia (18)
	1.27	± 0.6	0.161	Gresho and Lee (9)
	1.30	± 0.4	0.16	this study
200	1.17		0.18	Lin etal (14)
	1.27	± 0.7	0.154	Patel (16)
	1.17		0.15	Thoman and Szewczyk (15)
	1.46	± 0.7	0.194	Lecointe and Piquet (17)
	1.28	± 0.6	0.182	this study
500	1.25	± 0.9	0.20	this study

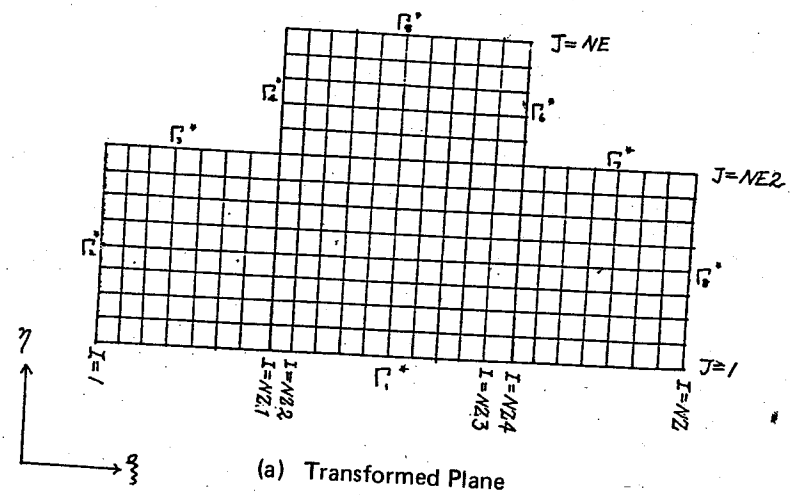

(a) Transformed Plane

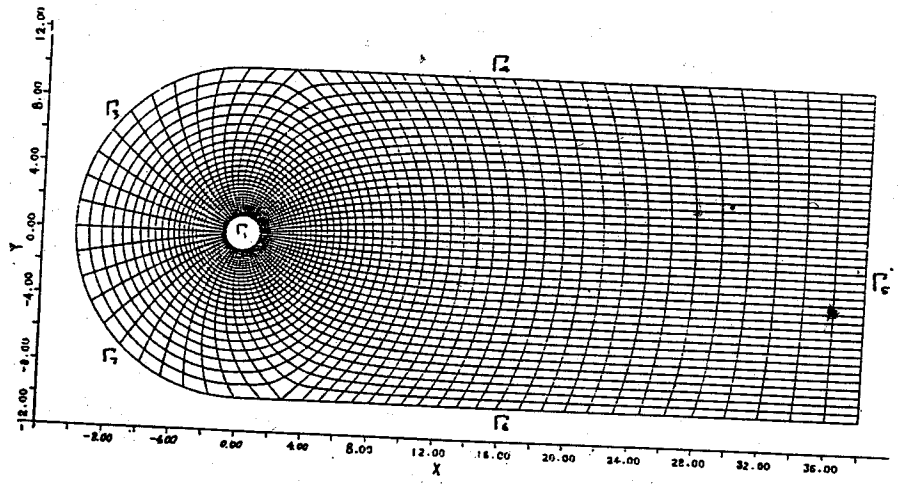

(b) Physical Plane.

Fig. 1. Transformation of the body-fitted coordinate system to the flow problem

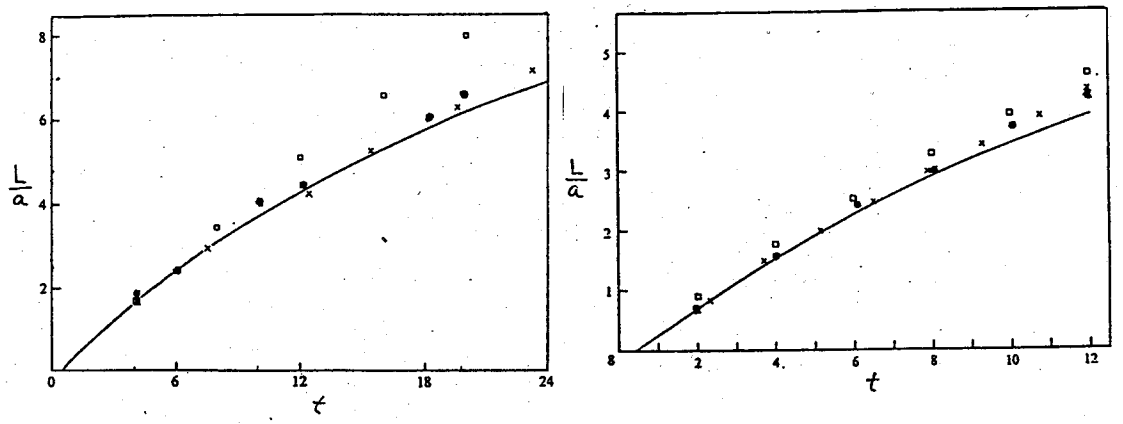

(a) Re = 100 (b) Re = 200

Fig. 2. Comparison of computational and experimental results for evolution with time of the wake length — collin & Dennis, X Honji & Taneda, □ Kawaguti & Tain, • this study.

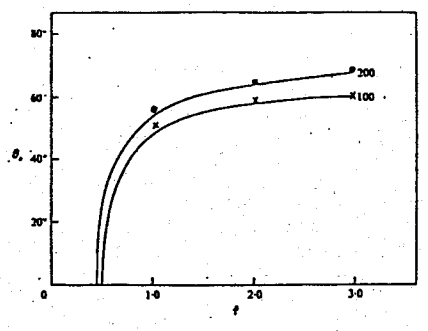

Fig. 3. Comparison between the computed values of evolution with time of the seperation angle. — Collin & Dennis, • This study (Re = 200), X this study (Re = 100).

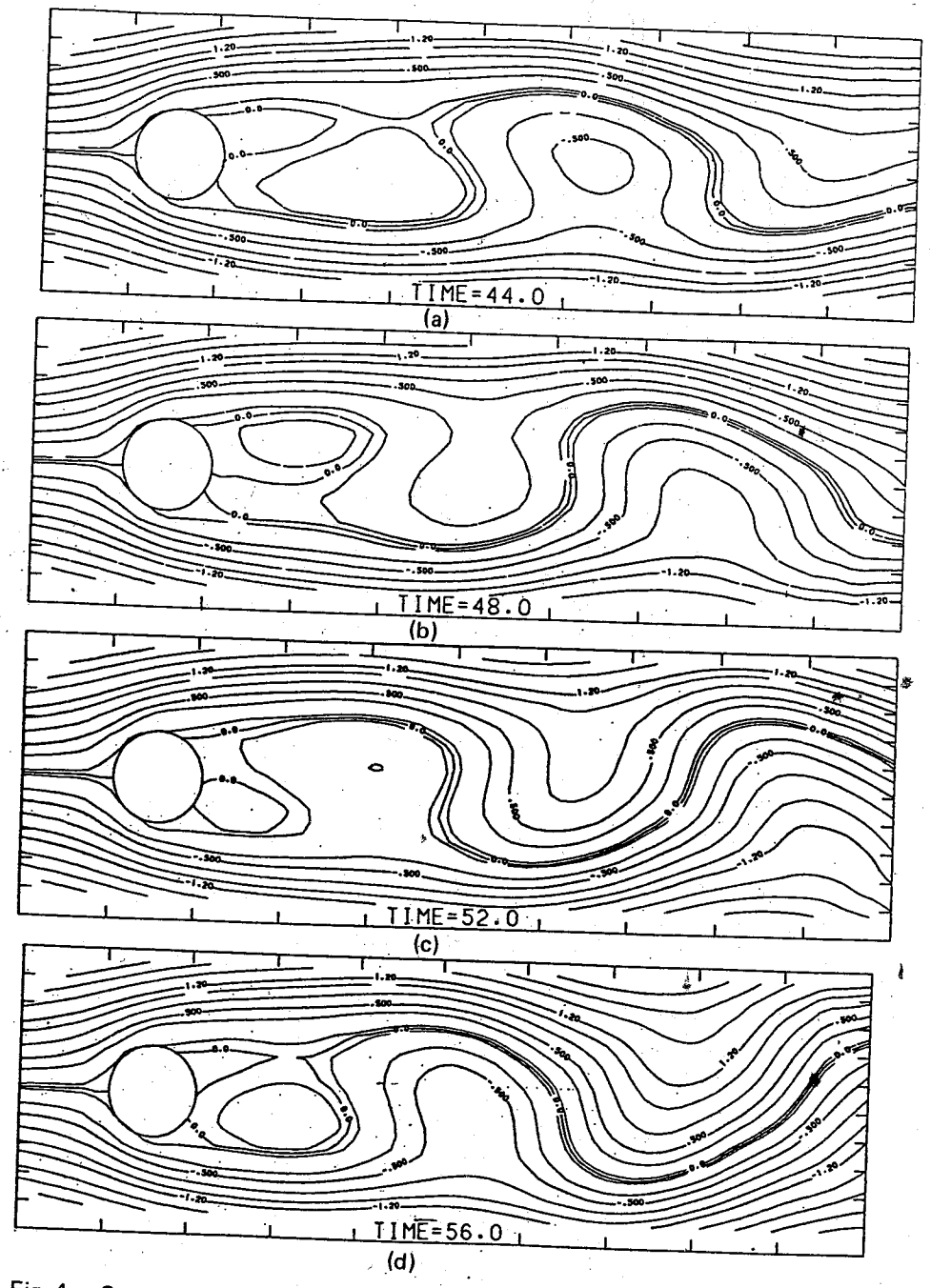

Fig. 4. Streamlines during vortex shedding for Re 100: (a) t = 44, (b) t = 48, (c) t = 52, (d) t = 56.

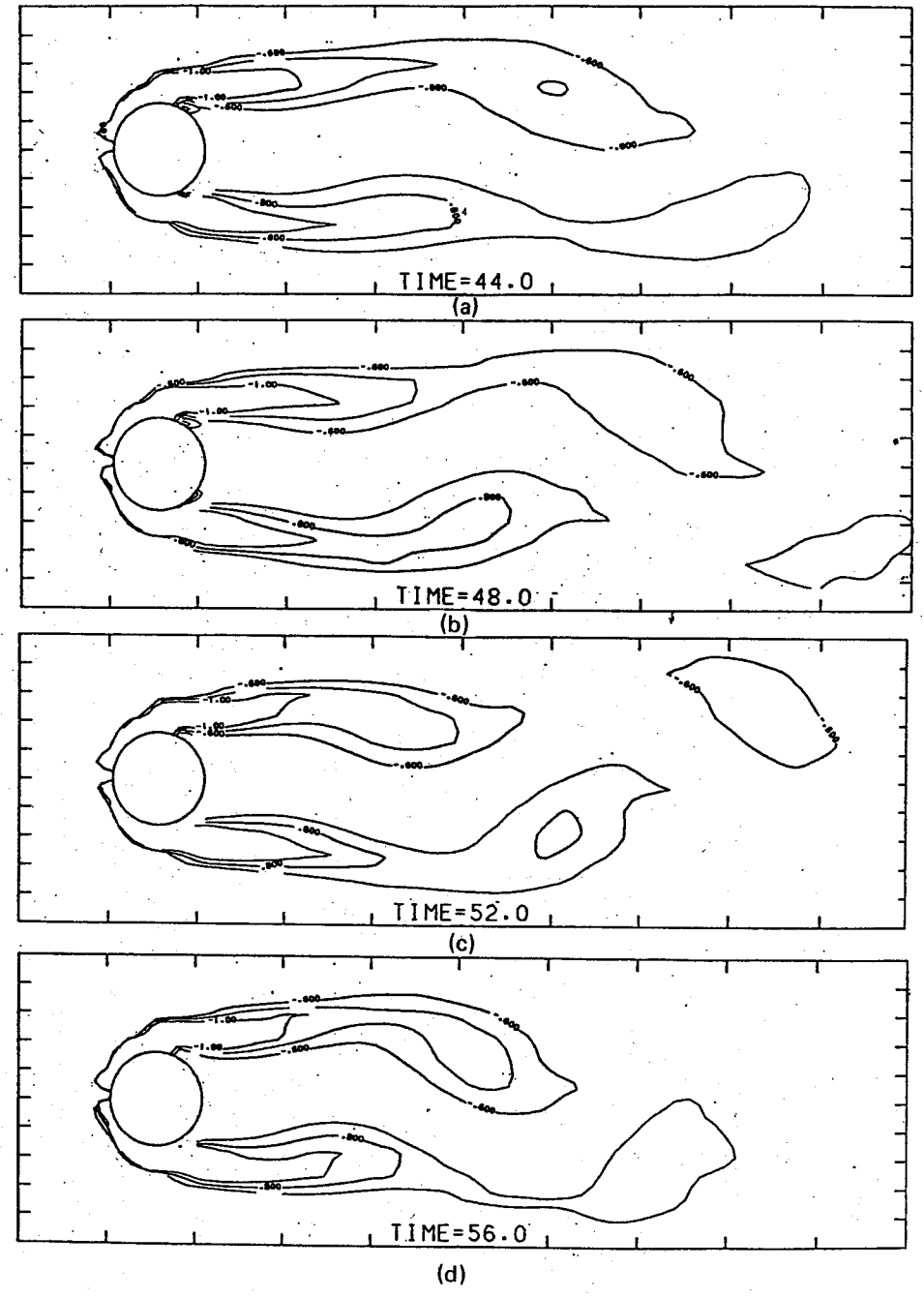

Fig. 5. Vorticity contours during the same shedding cycle as in Fig. 4.

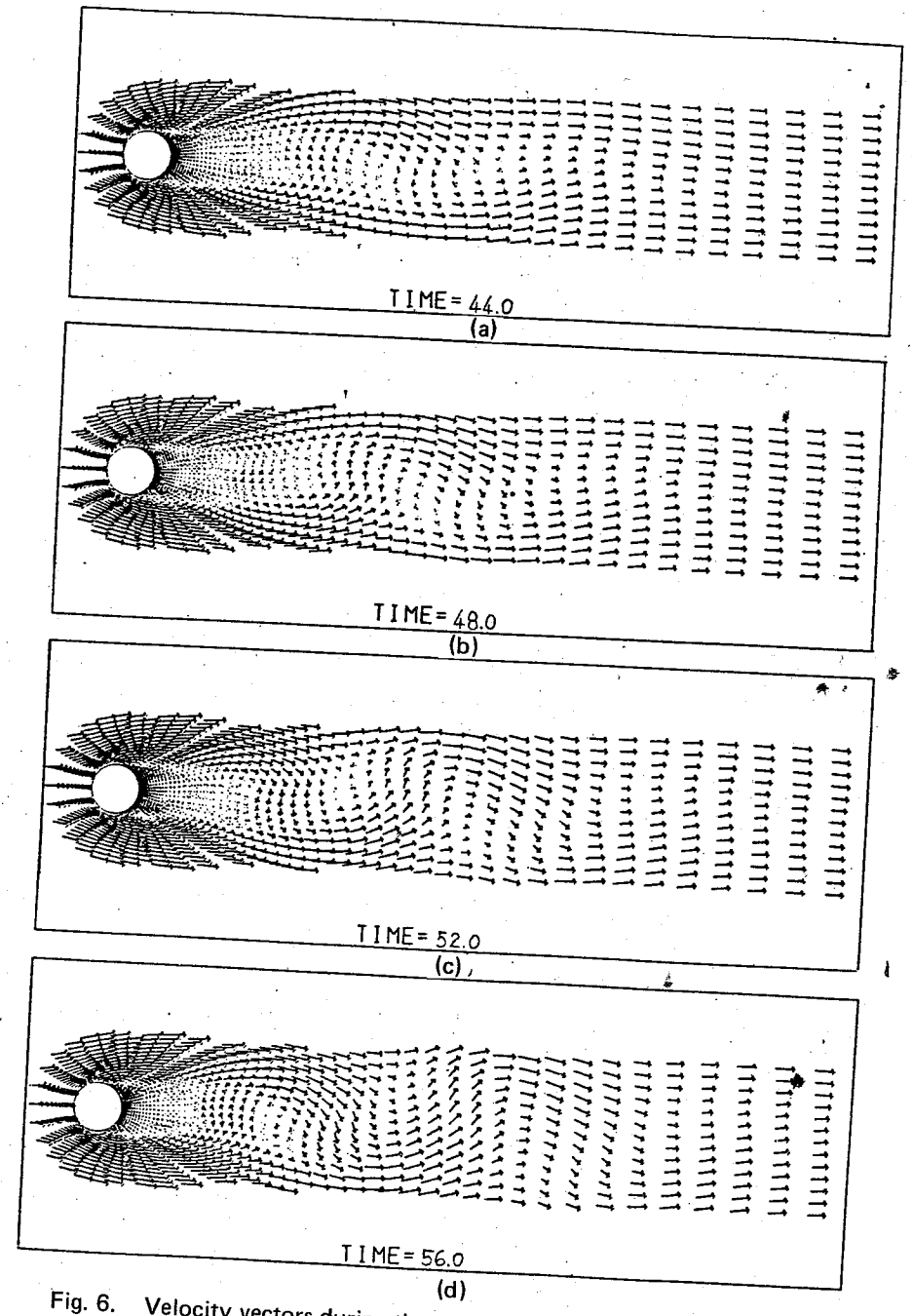

Fig. 6. Velocity vectors during the same shedding cycle as in Fig. 4.

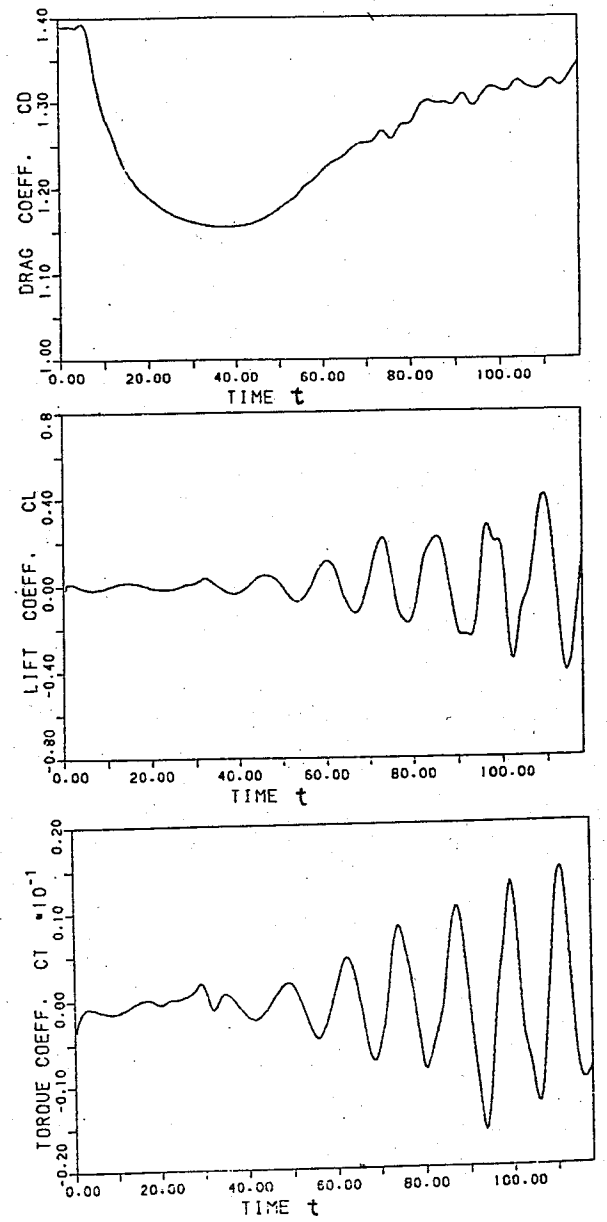

Fig. 7. Evolution with time of drag, lift, and torque coefficients for Re = 100.

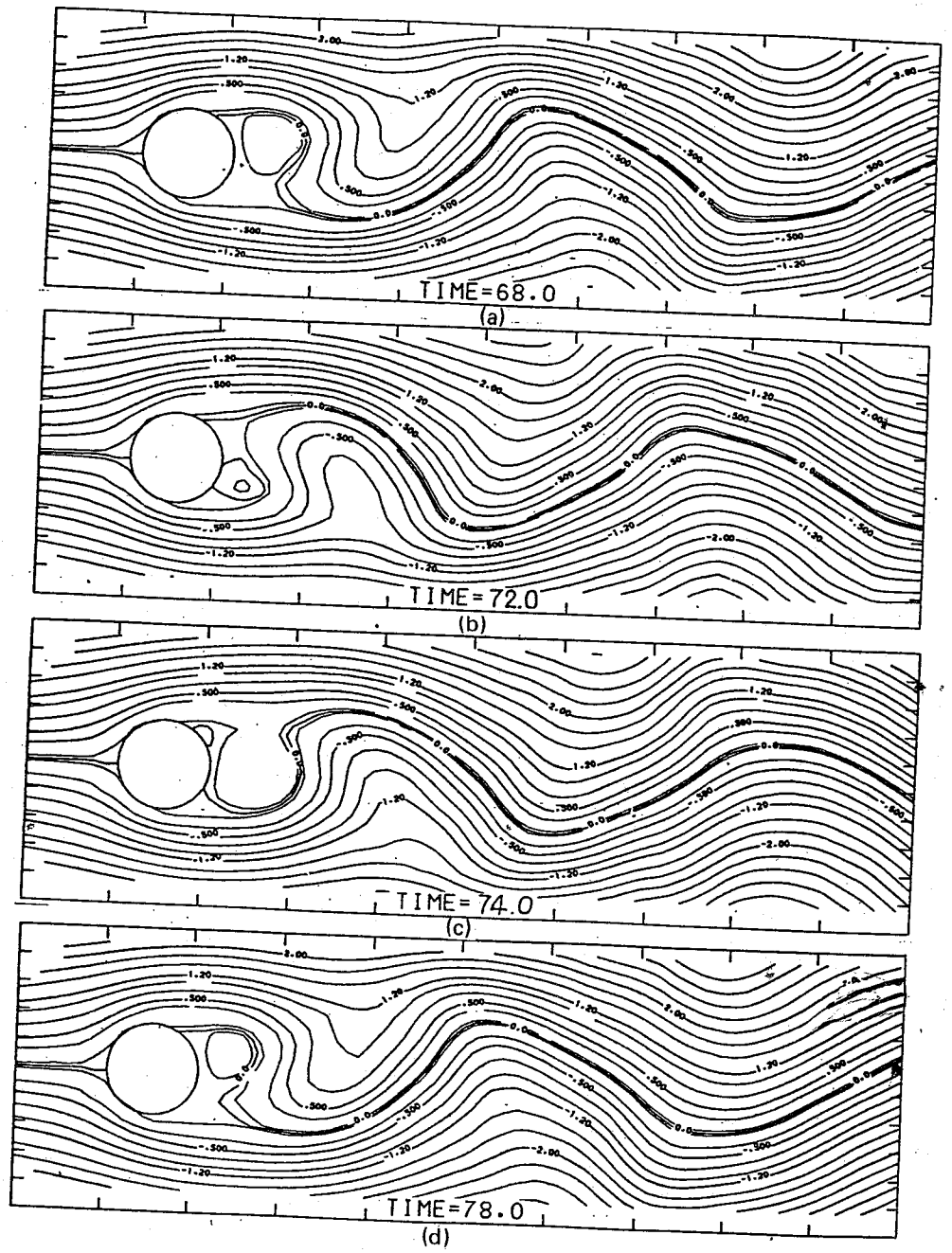

Fig. 8. Streamlines during vortex shedding for Re = 200: (a) t = 68, (b) t = 72, (c) t = 74, (d) t = 78.

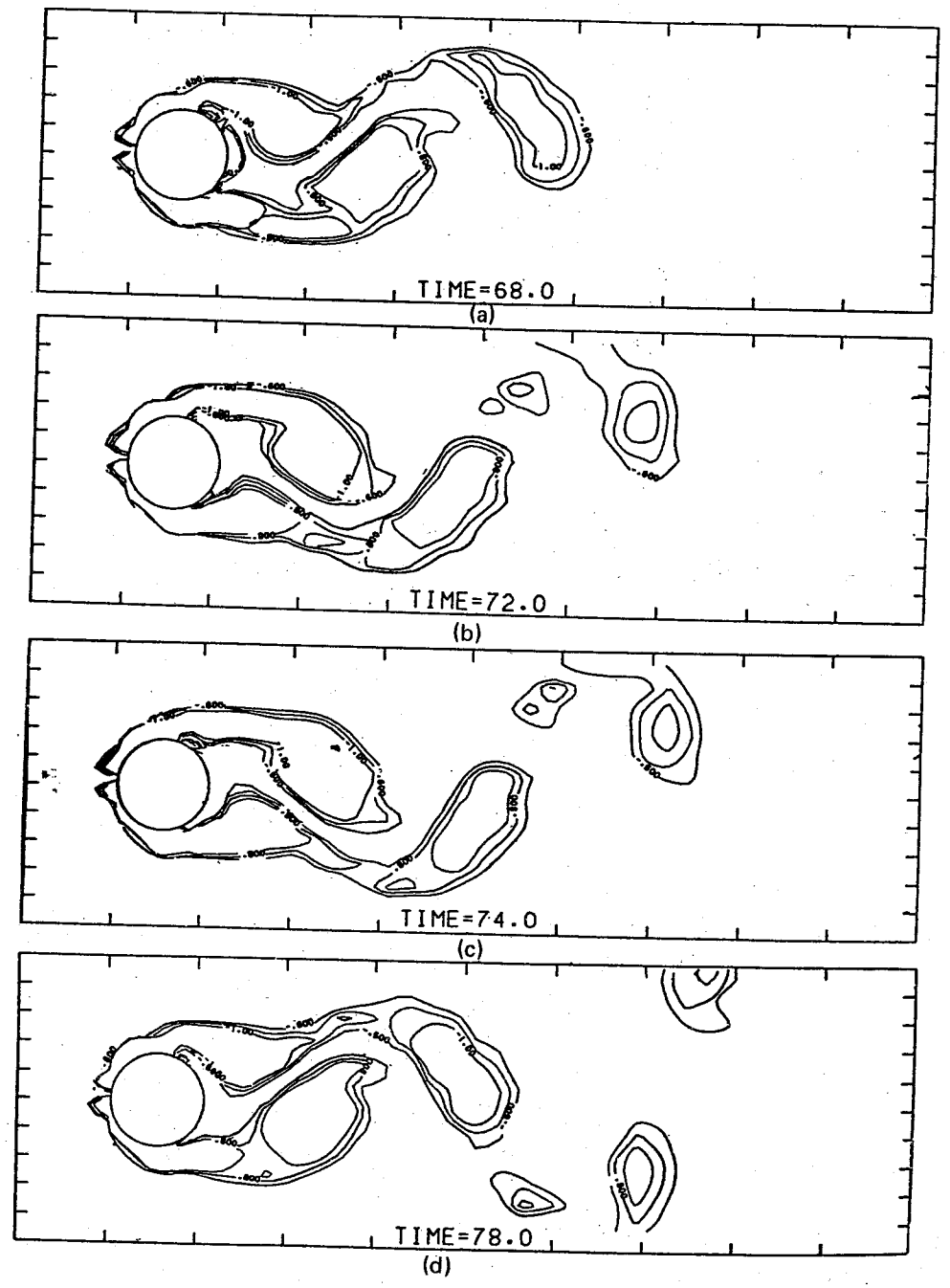

Fig. 9. Vorticity contours during the same shedding cycle as in Fig. 8.

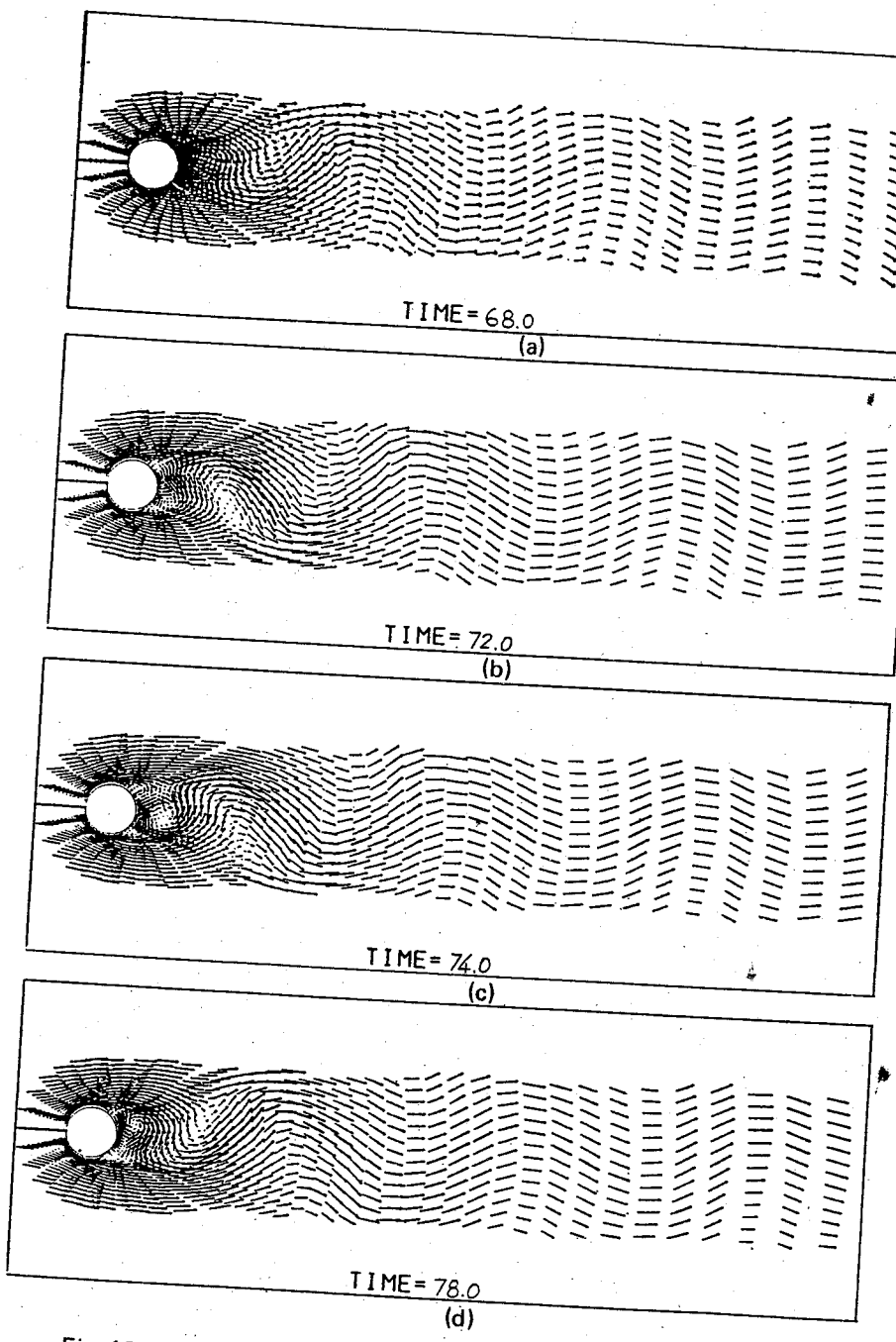

Fig. 10. Velocity vectors during the same shedding cycle as in Fig. 8.

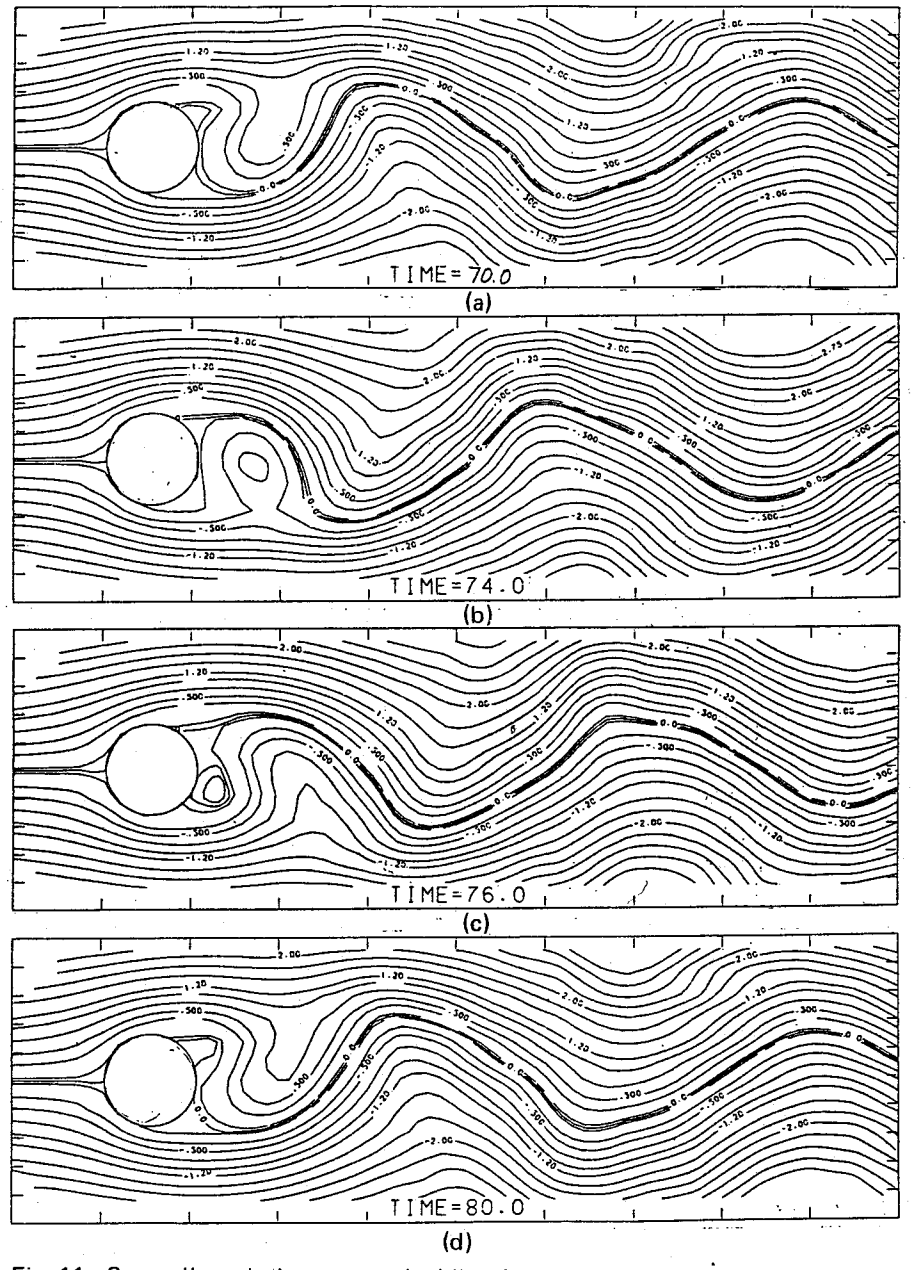

Fig. 11. Streamlines during vortex shedding for Re = 500: (a) t = 70, (b) t = 74, (c) t = 76, (d) t = 80.

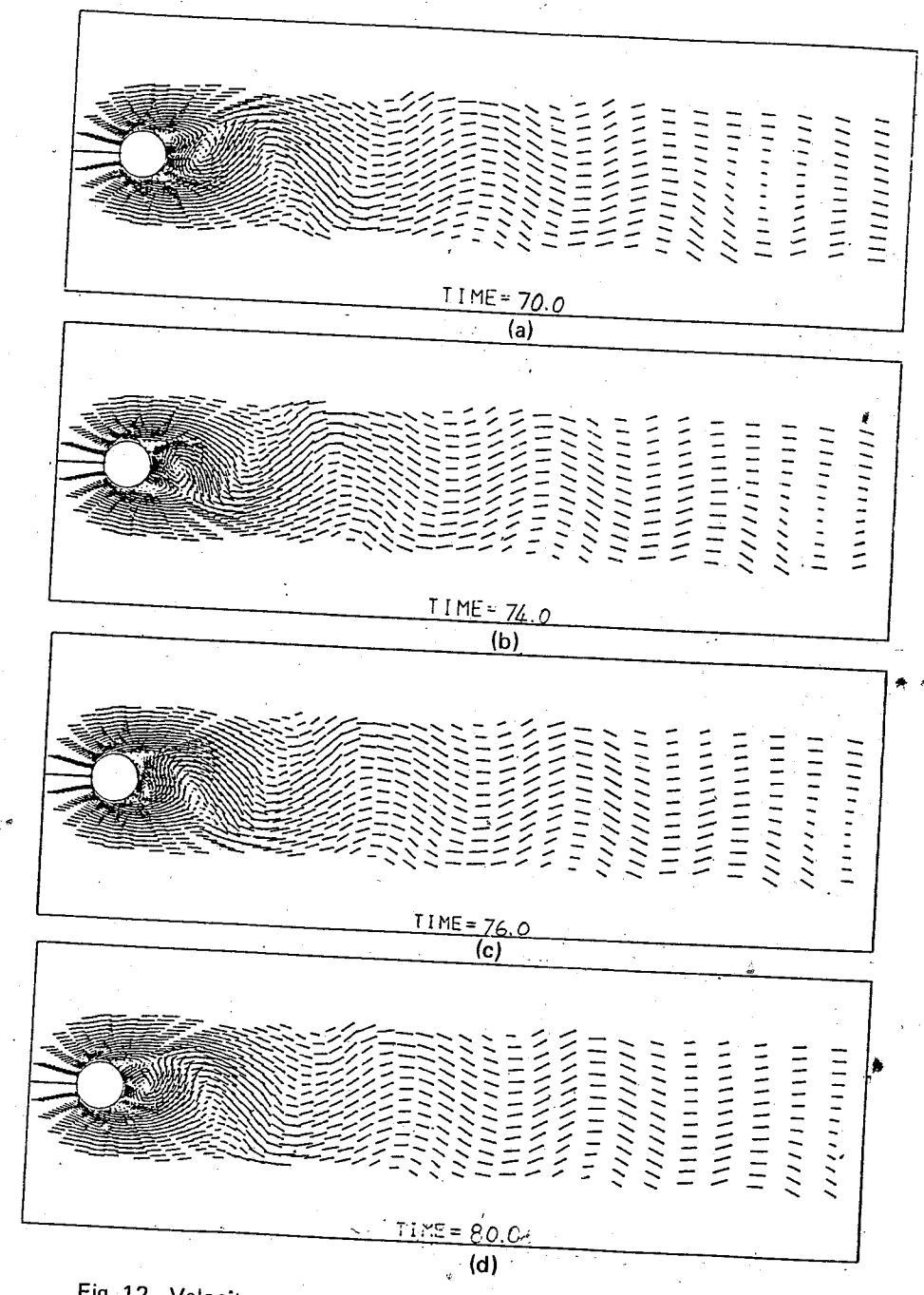

Fig. 12. Velocity vectors during the same shedding cycle as in Fig. 11.

INITIAL TEMPERATURE FIELD FOR UNSTEADY LAMINAR FORCED CONVECTION FROM AN IMPULSIVELY STARTED SPHERE

Lai-Chen Chien and Shyh-Show Lin

Institute of Physics, Academia Sinica
Taipei; Taiwan 11529
Republic of China

Abstract

Analytic solution for forced convection heat transfer from an impulsively started heated sphere is investigated. Because of the impulsive start, there is a singularity at the very beginning of the motion. The accurate analytic solution for the initial temperature field is obtained by solving the non-linear energy equation using the method of matched asymptotic expansion to the third order. The solution is in terms of exponential function and error function. The time development of the temperature field is plotted and investigated. The local Nusselt number over the sphere surface and the progress of minimum Nusselt number point with time are obtained.

I. Introduction

The problem of incompressible viscous flow over an impulsively started sphere has been studied by many investigators (Bentwich and Miloh, 1978). The extension of the problem to the heat transfer has also been the popular subject of numerous analytical and experimental investigations (Chen and Mucoglu, 1977). Several theoretical investigations have been reported centering around the classical problems of heat and mass transfer from a solid sphere into a low Reynolds number velocity field. Sano (1981), Bentwich and Miloh (1978) obtained the asymptotic solutions for Stokes-Oseen flow using the method of matched asymptotic expansions. Acrivos and Taylor (1962) used singular perturbation technique expressed the Nusselt number in terms of Peclet number, and yielded an accurate expression for the rate of tranfer of energy for small Reynolds number. Hieber and Gebhart (1969) studied

Special Issue of Annual Report of the Institute of Physics, Academia Sinica, Vol. 16, 1986
In Honor of Prof. Ta-You Wu on the Occasion of his 80th Birthday

mixed convection from a heated sphere for Stokes flow. Chen and Mucoglu (1977) solved the conservation equations of the non-similar boundary layer using finite difference method to study the combination forced and free convection about a sphere for small Reynolds number.

In this study, we try to employ the inner-outer expansion method to solve the axisymmetrical unsteady Navier-Stokes and energy equations in an attempt to extend the boundary layer theory to larger Reynolds number. The stream function for the initial flow obtained by the matched asymptotic expansion to the third order (Chien and Chen, 1984) is used to solve the energy equation. The naalytic solution to the third order for the temperature distribution corresponding to the initial flow field is treated with great care because of the complicated mathematical operation. The temperature field is thus obtained in terms of exponential and error function. The time development of the temperature field properties such as the local Nusselt number over the sphere surface, and the progress of minimum Nusselt number point with time is investigated.

II. Basic Equations

Consider a solid sphere of radius r_o which is started impulsively from rest and subsequently moves with constant velocity U. The origin of the spherical coordinate system is fixed at the center of the sphere with the axis $\theta=0$ in the direction opposite to the motion of the sphere. Assume that the fluid is an incompressible viscous continuum with constant properties, and that the effects of the heating of the fluid by viscous dissipation from sphere surface is neglected. With the foregoing assumption, the Navier-Stokes equation for the fluid motion can be expressed in the form (Chien and Chen, 1984) as

$$[\frac{\partial}{\partial t} - \frac{\epsilon}{r^2 \sin\theta}(\frac{\partial\psi}{\partial\theta}\frac{\partial}{\partial r} - \frac{\partial\psi}{\partial r}\frac{\partial}{\partial\theta} + 2\cot\theta\frac{\partial\psi}{\partial r} - \frac{2}{r}\frac{\partial\psi}{\partial\theta})]\nabla^2\psi$$
$$= \alpha\epsilon^2\nabla^4\psi \qquad (1)$$

where t is non-dimensionalized by the characteristic time t_o, radial coordinate r by the radius of the sphere r_o, stream function by r_oU. The parameters are defined by $\epsilon = Ut_o/r_o$, $\alpha = 1/(\epsilon Re)$, where Reynolds number is based on radius. For the problem of initial flow, ϵ is a small quantity much less than 1 and α is order 1. The

boundary conditions are non-slip at the surface of the sphere, and the uniform free stream conditions far from the sphere.

The flow field is divided into two regions, one is the inner region close to the sphere surface and the outer is the outer inviscid region, i.e. $\psi = \psi^o + \psi^i$. The outer solution to the third order for the stream function is obtained by Wang (1969). The inner solution to the third order by the method of inner-outer expansion is given by Chien and Chen (1984). The composition stream function is

$$\psi = \frac{1}{2}(r^2 - \frac{1}{r})\sin^2\theta + 3\frac{\tau}{\sqrt{Re}}[-\frac{1}{r\sqrt{\pi}} + \frac{3\tau}{r^2\sqrt{\pi}}(\sqrt{2} - 1 + \frac{2}{9\pi})\cos\theta$$
$$-\frac{1}{2r}\frac{\tau}{\sqrt{Re}} + (\frac{1}{\sqrt{\pi}}e^{-\eta^2} - \eta\mathrm{erfc}\eta) + \frac{\tau}{\sqrt{Re}}[(\eta^2 + \frac{1}{2})\mathrm{erfc}\eta - \frac{1}{\sqrt{\pi}}e^{-\eta^2}]$$
$$+\frac{3}{2}\tau S(\eta)\cos\theta]\sin^2\theta + 2(\frac{\tau}{Re})^{3/2}$$
$$[\int_0^\eta f_1(\eta)d\eta - (2\eta^3 - \frac{5}{\sqrt{\pi}}\eta^2 + \frac{3}{2}\eta)]\sin^2\theta + 18\frac{\tau^2}{Re}$$
$$[\int_0^\eta g_3(\eta)d\eta - \frac{2}{\sqrt{\pi}}(1 - \sqrt{2} - \frac{2}{9\pi})\eta]\sin^2\theta\cos\theta + 27\tau^2\frac{\tau}{\sqrt{Re}}$$
$$[2\int_0^\eta f_3(\eta)d\eta\sin^2\theta\cos^2\theta + \int_0^\eta F_3(\eta)d\eta\sin^4\theta], \qquad (2)$$

where η is defined by $(r-1)/2\sqrt{\alpha t}$, τ is dimensionless time and $S(\eta)$ is

$$S = \frac{3}{\sqrt{\pi}}e^{-\eta^2}\ \mathrm{erfc}\eta - \frac{2\sqrt{2}}{\sqrt{\pi}}\mathrm{erfc}\sqrt{2}\eta - \eta\mathrm{erfc}^2\eta - \frac{1}{\sqrt{\pi}}(\frac{7}{3} +$$
$$-\frac{1}{\sqrt{\pi}}(\frac{7}{3} + \frac{4}{9\pi})e^{-\eta^2} + (\frac{2}{3\pi} + 1)\eta\mathrm{erf}\eta + \frac{2}{3}(\frac{2}{3\pi} - 1)$$

$$(\eta^3 \operatorname{erf}\eta - \frac{1}{\sqrt{\pi}}\eta^2 e^{-\eta^2}) + \frac{4}{3\sqrt{\pi}}\operatorname{erfc}\eta$$

And f_1, f_3, F_3 and g_3 are polynomials of the similar forms.

In order to solve the energy equation to obtain the temperature field for the convection problem considered, the equation is written as (Chien and Kung, 1982)

$$[\frac{\partial}{\partial t} - \frac{\epsilon}{r^2 \sin\theta}(\frac{\partial \psi}{\partial \theta}\frac{\partial}{\partial r} - \frac{\partial \psi}{\partial r}\frac{\partial}{\partial \theta})]T$$

$$= \frac{\alpha \epsilon^2}{Pr}(\frac{\partial^2}{\partial r^2} - \frac{\cot\theta}{r^2}\frac{\partial}{\partial \theta} + \frac{1}{r^2}\frac{\partial^2}{\partial \theta^2})T, \tag{3}$$

where dimensionless temperature T is $(T' - T_\infty)/(T_W/T_\infty)$, T' is dimensional temperature, and T_W, T_∞ are the temperature on the sphere surface and at infinite respectively. When the sphere is impulsively started to move with a constant velocity, a constant temperature difference between the solid sphere and the fluid is suddenly imposed. The initial and boundary conditions are

$$T = 0 \qquad \text{for } t \quad 0, \tag{4a}$$

$$T = 1 \quad \text{at } r = 1 \qquad \text{for } t \quad 0, \tag{4b}$$

and

$$T \to 0 \quad \text{at } r \to \infty \qquad \text{for } t \quad 0. \tag{4c}$$

III. Analytic Solution for the Temperature Field

Similar to the problem of convective heat transfer over an impulsively started circular cylinder (Chien and Kung, 1982), we construct the solution for the temperature field by the method of additive compsotion. Sano (1978) has shown that the outer solution for the energy equation vanishes concerning the heat transfer for the flow over an impulsively started cylinder. The conclusion is also valid for the sphere problem considered in this investigation.

It can be shown that the inner solution is of the form

$$T^i = T_1(R, \theta, t) + \epsilon T_2(R, \theta, t) + \epsilon^2 T_3(R, \theta, t)$$

where R is the stretched radial coordinate and defined by $R = (R-1)/\epsilon$. Substituting the above expression into (3) and collecting the terms of the same order ϵ, we have the equations

$$T_{1t} - (\alpha/Pr)\, T_{1RR} = 0 \tag{5}$$

$$T_{2t} - (\alpha/Pr)\, T_{2RR} = (\psi^i_{1\theta} T_{1R} + \psi^i_{1R} T_{1\theta})/\sin\theta \tag{6}$$

$$T_{3t} - (\alpha/Pr)\, T_{3RR} = \alpha (T_{1\theta\theta} - \cot\theta\, T_{1\theta})/Pr +$$
$$(\psi^i_{2\theta} T_{1R} - 2R\psi^i_{1R} T_{1R} + \psi^i_{1\theta}\psi_{2R} - \psi^i_{2R} T_{1\theta} +$$
$$2R\psi^i_{1R} T_{1\theta} - \psi^i_{1R} T_{2\theta})/\sin\theta. \tag{7}$$

for the first, the second and the third order respectively.

And the boundary conditions for the above equations are

$$T_1(R, \theta, t) = 1 \qquad \text{at } R = 0, \tag{8a}$$

$$T_n(R, \theta, t) = 0 \qquad \text{at } R = 0 \qquad \text{for } n = 2, 3, \tag{8b}$$

$$T(R, \theta, t) \to 0 \qquad \text{as } R \to \infty \qquad \text{for } n = 1, 2, 3. \tag{8c}$$

The solution for the first order is similar to that obtained by Sano (1978) solving the convection of cylinder problem,

$$T_1 = \operatorname{erf}\ \mu \tag{9}$$

where μ is $\sqrt{Pr}\ \eta$ and η is the inner stretched variable $\eta = R/(2\sqrt{\alpha t})$. Substituting the first order solution (9) and the inner stream function into the right hand side of the second order equation (6), one has

$$T_{2t} - \alpha T_{2RR}/Pr = -6\sqrt{Pr}\,[(\eta - 1\sqrt{\pi})e^{-\eta^2} \operatorname{erfc}\eta$$
$$+ e^{-\xi^2}/\sqrt{\pi}]/\sqrt{\pi} \tag{10}$$

where $\zeta = \sqrt{\Pr + 1}\ \eta$. Assume the solution for T_2 be of the form $T_2 = t\, F_2\ (\eta)\cos\theta$. Then the equation (10) becomes

$$F_2''(\eta) + 2\Pr F_2' - 4\Pr F_2 = 24\,\Pr\,[(\eta - 1\sqrt{\pi})e^{-\eta^2} - \eta e^{-\mu^2}\ \mathrm{erfc}\eta + e^{-\eta^2}/\sqrt{\pi}]\ \sqrt{\Pr/\pi}\,. \tag{11}$$

The homogeneous part of equation (11) is of the form

$$f''(\eta) + 2\eta f' - 2nf = 0\,. \tag{12}$$

The solution may be in terms of error function and Hermite polynomial (Courant and Hibert, 1953, p. 90). The particular integral for (11) is obtained by the method of undetermined coefficients. Then we have the complete solution,

$$\begin{aligned} F_2(\eta) = [\,&\frac{6(2\Pr+1)\sqrt{\Pr}}{(3\Pr+1)} - 4\sqrt{\Pr} - 3C_2\pi/8 - \pi\ \sqrt{\pi}C_2\,(3\Pr+1)\,I(\infty)\,] \\ &(2\mu^2+1)\,\mathrm{erf}\mu + 2\sqrt{\Pr/\pi}\,\eta^{-\mu^2}\,]/\pi + \sqrt{\Pr}\,(4 - 3\sqrt{\pi})e^{-\mu^2}/\pi \\ &+ 3\sqrt{\Pr/\pi}\,\eta e^{-\mu^2}\ \mathrm{erfc}\eta - 6\sqrt{\Pr}\,(2\Pr+1)/ \\ &[\,\pi(3\Pr+1)e^{-\mu^2+\eta^2} + C_2\,[-\sqrt{\pi}\,(3\Pr+1)\eta e^{-\mu^2}\ \mathrm{erfc}\eta \\ &+ 3e^{-\mu^2-\eta^2} - \sqrt{\pi}\,(3\Pr+1)(2\mu^2+1)(I(\eta) - I(\infty))\,]/8 \end{aligned} \tag{13}$$

where $C_2 = 12(\Pr+1)^2\Pr/[\pi(3P+1)]$ and $I(\eta) = \int_0^{\eta} e^{-\mu^2}\ \mathrm{erfc}\eta\, d\eta$.

The right hand side of equation (7) is function of derivatives of the first and the second order expansion. Substituting (9) and (13) into the right hand side of equation (7), we have

$$\begin{aligned} T_{3t} - \alpha T_{3RR}/\Pr = {}&[M_{31}(\eta) + M_{32}(\eta)]\cos\theta + [M_{33}(\eta) + M_{34}(\eta)]\cos\theta \\ &+ [M_{34}(\eta) + M_{35}(\eta)]\sin\theta \end{aligned} \tag{14}$$

where the coefficients of the triangular functions are polynomial of error and exponential function and are presented in appendix. We assume the solution of Equation (14) to be of the form

$$\begin{aligned} T_3 = {}&3\sqrt{\alpha t\Pr/\pi}\,[8F_{31}(\eta) + F_{32}(\eta)]\,t\cos\theta + [9\sqrt{\Pr/\pi}\,F_{33}(\eta) \\ &+ 3F_{36}(\eta)]\,t^2\cos^2\theta + [-9\sqrt{\Pr/\pi}\,F_{34}(\eta) \\ &+ F_{35}(\eta)/2)]\,t^2\sin^2\theta\,. \end{aligned} \tag{15}$$

Substituting the above expression into equation (14), it gives set of six equations in of the form

$$\begin{aligned} &F''(\eta) + 2\Pr\eta F' - 2n\Pr F \\ &= GH(\mathrm{erfc}\eta,\ \exp(-\eta^2),\ \exp(-\mu^2)) \end{aligned} \tag{16}$$

The completementary solution of (16) is able to be expressed in terms of error function and Hermite polynomial. And the particular integrals are obtained by the method of undetermined coefficient. The complicated mathematical operation is repeated with great care and is shown in Appendix.

To sum up, the solution of the energy equation is

$$\begin{aligned} T = {}&\mathrm{erfc}\mu + \tau F_2(\eta)\cos\theta + \tau\,[F_{31}(\eta) + 3\tau\sqrt{\tau\Pr/(\pi\mathrm{Re})}\ F_{32}(\eta)]\cos\theta \\ &+ \tau^2\ [\,[9\sqrt{\Pr/\pi}\,F_{33}(\eta) + F_{36}(\eta)]\cos^2\theta \\ &+ \tau^2\ [-9\sqrt{\Pr/\pi}\,F_{34}(\eta) + F_{35}(\eta)/2]\sin^2\theta\,. \end{aligned} \tag{17}$$

where $F_2(\eta)$ is given by (13), F_{31} to F_{36} are presented by Equation (A—14) to (A—19) in appendix.

IV. Results

The temperature field (17) is plotted in Figure 1 for Re=100, Pr=0.7. At short time after the impulsively start, the isotherms in the front half part are almost parallel to the surface of the sphere. As time goes on, at τ=0.6, the isotherms

Special Issue of Annual Report of the Institute of Physics, Academia Sinica, Vol. 16, 1986
In Honor of Prof. Ta-You Wu on the Occasion of his 80th Birthday

displaced away from the sphere as the viscous layer thickens. Similar phenomenon is shown in Figure 2 for Re=500, Pr=0.7 at τ=0.6. The higher the Reynolds number, the thinner the thermal boundary layer because the convection becomes more effective in displacing the streamlines downstream away from the sphere.

Having computed the temperature field, we can estimate the heat transfer between the sphere and the surrounding fluid.

$$Nu = -K\,(\partial T / \partial r)_{r=1}\,.$$

The local Nusselt number distribution around the surface of the sphere for Pr=0.7 at Re=100 and 500 is shown in Figure 3. Because no existing investigation is available for comparison, we compare the trends of this solution with those obtained in studying cylinder by Sano (1978), Chien and Kung (1982). The similar results are obtained.

We differentiate the Nusselt number distribution function, set it equal to zero, and find the minimum Nusselt number point. By Newton's method, we can obtain the progress of minimum Nusselt number point at the sphere surface with respect to time, Figure 4.

V. Conclusions and Recommendations

The major objective of the present investigation has been to work out the short time solution for unsteady forced convection heat transfer from an impulsively started sphere. Because of the impulsive start, there is a singularity behavior of the flow field at the very beginning of the motion. An accurate solution is obtained by the method of asymptotic expansion to the third order. The expansion is valid for the short time only, $\tau \langle 1$. The viscous layer considered flow field (Chien and Chen, 1984) and temperature field obtained in this investigation can be used as initial conditions for numerical computation. And the solution can be continued by numerical integration to obtain the larger time solution (Schlichting, 1979, p. 149). Using the accurate stable numerical method to solve the governing equations, we can depict the time history of the flow patterns and the temperature fields.

References

1. Acrivos, A. and Taylor, T. D. (1962). Heat and Mass Transfer from Single Sphere in Stokes Flow. Phys. Fluids, Vol. 5, pp. 387-394.
2. Bentwich, M. and Miloh (1978). The Unsteady Matched Stokes-Oseen Solution for the Flow Past a Sphere. J. Fluid Mech., Vol. 98, pp. 17-32.
3. Chen, T. S. and Mutoglu (1977). Analysis of Mixed Forced and Free Convection about a Sphere. Int. J. Heat Mass Transfer, Vol. 20, pp. 867-875.
4. Chien, L. C. and Kung, I. S. (1982). Heat Transfer from an Impulsively Started Circular Cylinder. Computational and Asymptotic Methods for Boundary and Interior Layers, J.J.H. Miller ed., Boole Press, Dublin, Ireland, pp. 177-182.
5. Chien, L. C. and Chen, S. W. (1984). The Initial Flow Past an Impulsively Started Sphere. Computational and Asymptotic Methods for Boundary and Interior Layers. J.J.H. Miller ed., Boole Press, Dublin, Ireland, pp. 179-184.
6. Courant, R. and Hibert, D. (1953). Methods of Mathematical Physics, Vol. 1, Interscience Press, New York.
7. Hieber, C. A. and Gebhart, B. (1969). Mixed Convection from a Sphere at Small Reynolds and Grashof Number. J. Fluid Mech., Vol. 38, pp. 137-159.
8. Cary, J. R. (1953). The Determination of Local Forced Convection Coefficient for Sphere. Trans. Am. Soc. Mech. Eng. Vol. 75, pp. 483-487.
9. Sano, T. (1978). Short-time Solution for Unsteady Forced Convection Heat Transfer from an Impulsively Started Circular Cylinder. Int. J. Heat Mass Transfer, Vol. 21, pp. 1505-1516.
10. Sano, T. (1981). Unsteady Flow Past a Sphere at Low Reynolds Number. J. Fluid Mech., Vol. 112, pp. 433-441.
11. Schlichting, H. (1979). Boundary Layer Theory McGraw-Hill, New York.
12. Vliet, G. C. and Lepper, G. (1961). Forced Convection Heat Transfer from an Isothermal Sphere to Water. J. Heat Transfer, Vol. 83C, pp. 163-175.
13. Wang, C. Y. (1967). The Flow Past a Circular Cylinder Which is Started from Rest. J. Math. Phys., Vol. 46, pp. 195-202.

Special Issue of Annual Report of the Institute of Physics, Academia Sinica, Vol. 16, 1986
In Honor of Prof. Ta-You Wu on the Occasion of his 80th Birthday

APPENDIX
SOLUTION OF THE THIRD ORDER TEMPERATURE

As shown in equation (14), the third order equation is expressed by

$$T_{3t} - \alpha T_{3RR}/R$$
$$= [M_{31}(\eta) + M_{32}(\eta)] \cos\theta + [M_{33}(\eta) + M_{34}(\eta)] \cos^2\theta$$
$$+ [M_{35}(\eta) + M_{36}(\eta)] \sin^2\theta. \qquad (A-1)$$

The coefficients $M_{31}(\eta)$ to $M_{36}(\eta)$ of the triangular functions are polynomial of error an exponential function.

$$M_{31}(\eta) = -12R\sqrt{Pr/\pi}\,[\eta - \text{erfc}\eta + (e^{-\eta^2} - 1)\sqrt{\pi}\,]\, e^{-\mu^2} \qquad (A-2)$$

$$M_{32}(\eta) = -3\sqrt{Pr\alpha t/\pi}\,[2R(\eta) - 1]\, e^{-\mu^2} \qquad (A-3)$$

$$M_{33}(\eta) = -9t\sqrt{Pr/\pi}\,[S(\eta) - 2(1 - \sqrt{2} - 4/9\pi)/\sqrt{\pi}\,]\, e^{-\mu^2} \qquad (A-4)$$

$$M_{34}(\eta) = -9t\sqrt{Pr/\pi}\,[S(\eta) - 2(1 - \sqrt{2} - 4/9\pi)/\sqrt{\pi}\,]\, e^{-\mu^2} \qquad (A-5)$$

$$M_{35}(\eta) = 3t/2\,[A_2(1+2\mu^2)\text{erfc}\eta + \sqrt{Pr/\pi}\,(4/\sqrt{\pi} - 2A_2\eta - 3\eta)e^{-\mu^2}$$
$$+ B_2(2\mu^2+1) + [3\sqrt{Pr/\pi} - C_2\sqrt{\pi}\,(3Pr+1)/8]\,\eta e^{-\mu^2}\text{erf}\eta$$
$$+ 3[C_2/8 - 2\sqrt{\pi}\,(2Pr+1)/\pi(3Pr+1)]\, e^{-\mu^2}$$
$$- C_2\sqrt{\pi}\,(3Pr+1)(2\mu^2+1)I(\eta) - A_2(2\mu^2+1)\text{erfc}\eta\,\text{erfc}\mu$$
$$- 4\sqrt{Pr/\pi}\,(2/\sqrt{\pi} - A_2\eta - 3\eta)e^{-\mu^2}\,\text{erfc}\mu - B_2(2\mu^2+1)\text{erfc}\eta$$
$$- [3\sqrt{Pr/\pi} - C_2\sqrt{\pi}\,(3Pr+1)/8]\,\eta e^{-\mu^2}\,\text{erfc}^2\eta$$

$$- [3C_2/8 - 6\sqrt{Pr}\,(2Pr+1)/\pi(3Pr+1)]\, e^{-\mu^2}\,\text{erfc}\eta$$
$$- C_2\sqrt{\pi}\,(3Pr+1)(2\mu^2+1)/8\, I(\eta)\,\text{erfc}\eta \qquad (A-6)$$

$$M_{36}(\eta) = 3t\;A_1(\eta)(1 - \text{erfc}\eta e^{-\mu^2} + A_2(\eta)(e^{-\mu^2} - e^{-\eta^2})$$
$$+ A_3(\eta)\,[\eta^2(1 - \text{erfc}\eta) + \eta(1 - e^{-\eta^2})]\, e^{-\mu^2}$$
$$+ A_4(\eta)\,[(1 - \text{erfc}\eta) + \eta(1 - e^{-\eta^2})]\, e^{-\mu^2}$$
$$+ 4Pr(A_5\eta^2 + A_6)\text{erfc}\mu\,[\eta^2(1 - \text{erf}(\eta)$$
$$- \eta(e^{-\eta^2} - 1)/\sqrt{\pi}\,] - (3Pr-1)PrC_2\eta/2$$
$$\times [\sqrt{\pi}\,\eta\,\text{erf}\eta + (e^{-\eta^2} - 1)]\; I(\eta)\;, \qquad (A-7)$$

where $R(\eta)$, $A_1(\eta)$ to $A_6(\eta)$ are polynomials of Prandtl number.

Suppose the solution of (A–1) be of the form

$$T_3(\eta) = [tF_{31}(\eta) + 3t\sqrt{\alpha t\,Pr/\pi}\,F_{32}(\eta)]\cos\theta$$
$$+ [9t^2\sqrt{Pr/\pi}\,F_{33}(\eta) + 3t^2 F_{36}(\eta)]\cos^2\theta$$
$$+ [-9t^2\sqrt{Pr/\pi}\,F_{34}(\eta) + 3/2t^2 F_{35}(\eta)]\sin^2\theta. \qquad (A-8)$$

Substituting (A–8) into (A–1), we get the following six equations,

$$F''_{31}(\eta) + 2Pr\eta F'_{31} - 4Pr F_{31}$$
$$= 48R\sqrt{Pr^3/\pi}\,[-1/\sqrt{\pi} + \eta\,\text{erf}\eta + e^{-\eta^2}/\sqrt{\pi}\,]\, e^{-\mu^2} \qquad (A-9)$$

$$F_{32}(\eta) + 2Pr\eta F'_{32} - 6Pr F_{32}$$
$$= 4Pr\,[4\eta/\sqrt{\pi} - 2/\sqrt{\pi}e^{-\mu^2} + (1\;\;2\mu^2)\text{erfc}\eta - 1]\, e^{-\mu^2} \qquad (A-10)$$

$$F''_{33}(\eta) + 2Pr\eta F'_{33} - 8PrF_{33}$$
$$= (D_1 \operatorname{erfc}\sqrt{2}\eta + D_2 \operatorname{erfc}^2\eta)e^{-\mu^2} + (D_3 \operatorname{erfc}\eta + D_4 + D_5\eta^2)e^{-\zeta^2}$$
$$+ [(D_6 + D_7 + D_8\eta^2)\operatorname{erfc}\eta + D_9]\, e^{-\mu^2} \qquad (A-11)$$

In equation (11), D_1, D_2, ... , D_9 are constants. The differential equation for $F_{34}(\eta)$ is exactly the same form as F_{33}. For F_{35} and F_{26}, the equations are

$$F''_{35}(\eta) + 2Pr\eta F'_{35} - 8PrF_{35} = -8PrM_{35}(\eta)/(3t). \qquad (A-12)$$

$$F_{36}(\eta) + 2Pr\eta F'_{36} - 8PrF_{36} = -4PrM_{36}(\eta)/(3t). \qquad (A-13)$$

The complementary solutions for the above equations are discussed in the text section for analytic solution for the temperature field, and can be expressed in error function and Hermite polynomial. The particular solutions are obtained by undermined coefficients. The complete solutions are

$$F_{31}(\eta) = \sqrt{\pi}\,[1-(2Pr+1)(Pr+1)^2]/12Pr[2\mu^2 e^{-\mu^2}/\sqrt{\pi}$$
$$- 2(\mu^3+3\mu^2)\operatorname{erfc}\mu] - (\eta^3/3 - 2\eta/5\sqrt{\pi} + 1/12Pr)e^{-\mu^2}$$
$$- \eta e^{-\zeta^2}/3\sqrt{\pi} + (\eta^2 - 2/4Pr)e^{-\mu^2}\operatorname{erfc}\eta/3$$
$$+ (2Pr+1)(Pr+1)/12\sqrt{Pr^3}\ [\sqrt{Pr}\,(Pr+1)\zeta^2 e^{-\mu^2}\operatorname{erfc}\eta$$
$$- \sqrt{Pr^3/\pi}\eta e^{-\zeta^2}/2 - Pr(Pr+1)(2\mu^3+3\mu)[I(\infty) - I(\eta)]$$
(A-14)

$$F_{32}(\eta) = A_{32}\,[2\zeta e^{-\mu^2}/\sqrt{\pi} - 2\sqrt{Pr}\eta(2Pr^2+3)\operatorname{erfc}\mu\,]$$
$$- (8/5\ \sqrt{\pi}\eta - 1/2)e^{-\mu^2} + 2/3\sqrt{\pi}\ e^{-\mu^2}$$
$$- [2\eta^2 + (3Pr+1)/2Pr]\ e^{-\mu^2}$$
$$- [2\eta^2 + (3Pr+1)/2Pr]\ e^{-\mu^2}\operatorname{erfc}\eta/3$$
$$+ 3C_{32}\,Pr(Pr+1)/2\,[\zeta e^{-\mu^2}\operatorname{erfc}\eta + Pr\eta\zeta\,I(\eta)$$
$$- I(\infty) - Pr/\sqrt{\pi}\eta\, e^{-\zeta^2}\,] \qquad (A-15)$$

$$F_{33}(\eta) = 2A_{33}\sqrt{Pr/\pi}(5\eta + 2Pr\,\eta^3)e^{-\mu^2} + (B_{33} - A_{33}\operatorname{erf}\mu)\,,$$
$$\times (4\mu^4 + 12\mu^2 + 3) + [4\sqrt{2/\pi}/5\operatorname{erfc}\mu + \eta/3 - 2/5\,W_{33}$$
$$+ (-8/15\sqrt{\pi} + R_{33}\eta + t_{33}\eta^3)\operatorname{erfc}\ ]\, e^{-\mu^2}$$
$$+ (S_{33} + P_{33}\eta^2 - 2/3\sqrt{\pi}\operatorname{erfc}\eta)\, e^{-\zeta^2} + F_{33}(Pr), \qquad (A-16)$$

where the alphabet with subscript 33 are polynomial of Prandtl number.

$$F_{34}(\eta) = F_{33}(\eta) \qquad (A-17)$$

$$F_{35}(\eta) = 2A_{35}\sqrt{Pr/\pi}\,(5+2Pr\,\eta^3)e^{-\mu^2} + (B_{35} - A_{35})\operatorname{erfc}\mu$$
$$(4\mu^4 + 12\mu^2 + 3) + C_{35}\,e^{-\mu^2} + D_{35}\operatorname{erfc}\mu + E_{35}\operatorname{erfc}\eta$$
$$+ G_{35}\ I(\eta) + H_{35}\ \eta e^{-\eta^2} + K_{35} \qquad (A-18)$$

$$F_{36}(\eta) = A_{36}e^{-\mu^2} + B_{36}\,e^{-\mu^2}\operatorname{erfc}\ + C_{36}\,e^{-\mu^2}\operatorname{erfc}\eta$$
$$+ D_{36}\,e^{-\zeta^2}\operatorname{erfc}\eta + E_{36}\,e^{-\zeta^2} + G_{36}\operatorname{erfc}\mu$$
$$+ H_{36}\operatorname{erfc}\eta + K_{36}\,e^{-\eta^2} + L_{36}\,I(\eta) + M_{36}\,. \qquad (A-19)$$

The alphabets with subscripts correspondent to the functions are polynomials of Prandtl number. Their detailed expressions are too lengthy to be reproduced here because of the limit of pagination.

To sum up the solution of the third order temperature is expressed by equation (A–8), provided F_{31}, F_{32}, F_{33}, F_{34}, F_{35} and F_{36} given by (A–14) to (A–19).

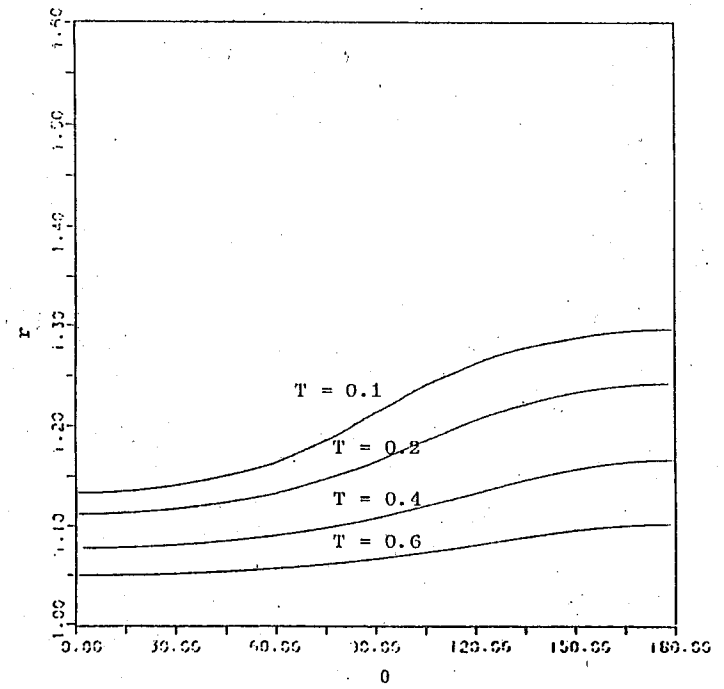

Figure 1. Isothermal for Pr = 0.7 at Re = 100, Time = 0.6.

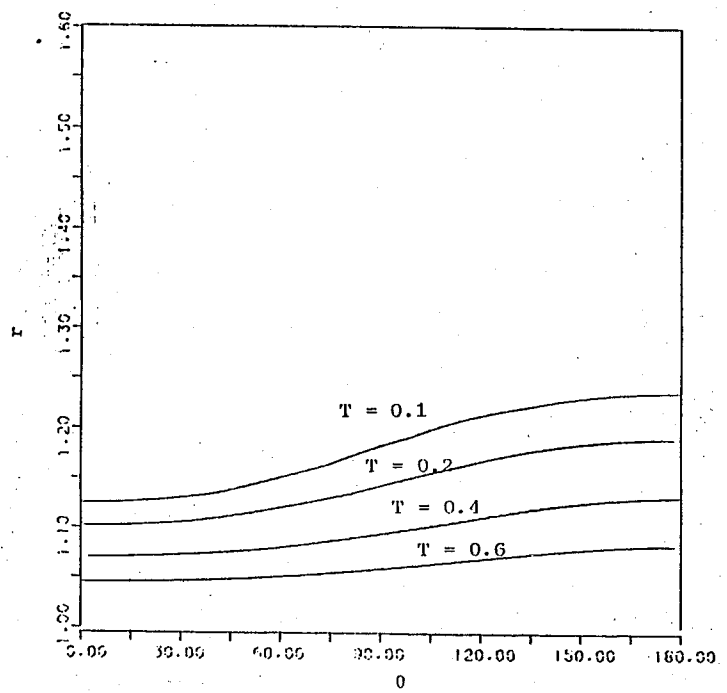

Figure 2. Isothermal for Pr = 0.7 at Re = 500, Time = 0.6.

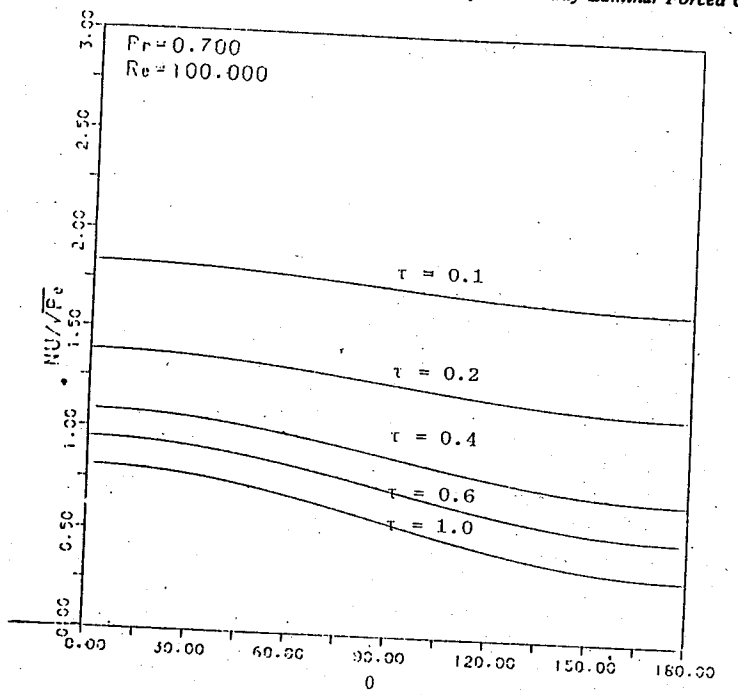

Figure 3(a). Nusselt number distribution on sphere surface for Pr = 0.7 at Re = 100.

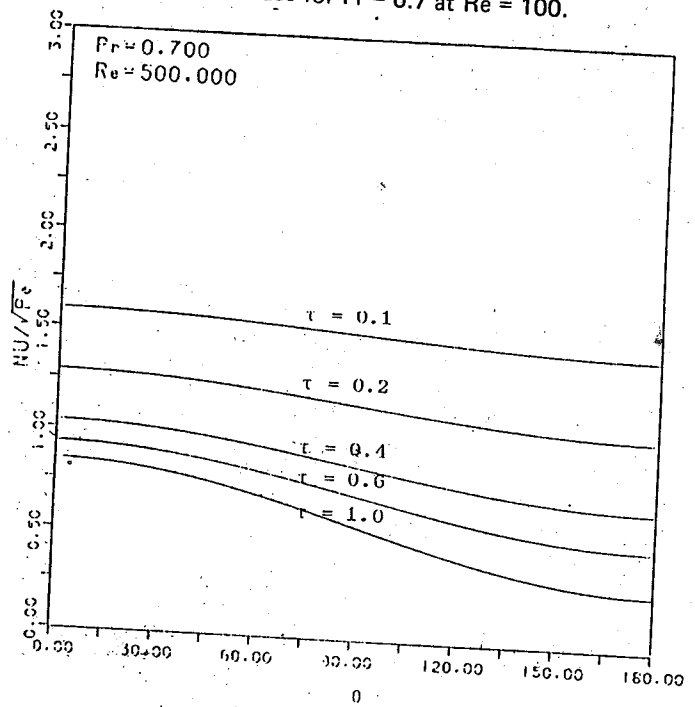

Figure 3(b). Nusselt number distribution on sphere surface for Pr = 0.7 at Re = 500.

Special Issue of Annual Report of the Institute of Physics, Academia Sinica, Vol. 16, 1986
In Honor of Prof. Ta-You Wu on the Occasion of his 80th Birthday

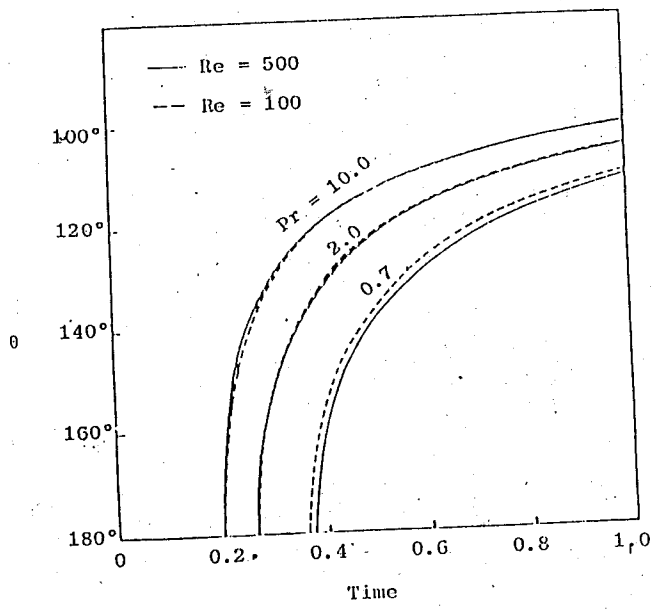

Figure 4. Progression of minimum Nusselt number point with time.

中國醫學之現代觀

中央研究院物理研究所生物物理研究室
王 唯 工

(一)前　言

一門學問是否是科學，主要看其所使用之量，是否有操作型之定義。如物理學所使用之量：質量、時間、長度，都可由實驗之操作為其定量。所以物理學是科學。

中醫所為人垢病者，為其診斷。沒有定量之方法，一些所謂火氣、寒熱的，總叫人有不知所云的感覺。其實中醫有定量之測定，那就是望聞問切（本篇之重點放在切也就是脈搏學），中醫之脈搏學與心電圖是同樣科學的，因為使用的脈搏圖，也是有操作型定義的。

我們都知道，法國酒廠僱有品酒師，他們只要喝一口，就知道是那一年份，在那裏出品的酒。同樣的，香水公司也僱有香水品管師，聞一聞就知道這種味道美國人喜歡，那種味道南美人喜歡……。可是這些工作都無法用現有的分析儀器來做。

像傳統中醫的脈搏學依靠手指的觸覺一樣，這些品酒、聞香的工作也都難免滲雜了神秘感。不過這也是在儀器的敏感度趕不上感覺器官時，所使用的一種無可奈何的操作型定義。

何況在三千年前脈搏學就已萌芽。那時沒有示波器，甚至沒有任何儀表，又怎怪祖先們以觸覺來作為操作之手段呢？只怪我們身為現代之中國人，有了各項新穎之儀器，又學了滿腦子的西洋醫學，反而責之為不科學，或反科學。這種不究事理的態度，難道就是科學的方法嗎？

(二)血液之重要

血液含有氧氣、營養成分，及抗體、白血球等生命所必需的成分，也就是中醫

Special Issue of Annual Report of the Institute of Physics, Academia Sinica, Vol. 16, 1986
In Honor of Prof. Ta-You Wu on the Occasion of his 80th Birthday

所說的宗氣、營氣、衛氣。人體可視為一群共生在一起的細胞組合，而血液就負責輸送營養及氧氣。做過細胞培養的人都知道，當細胞有足夠養分與氧氣時，長得欣欣向榮，可是一旦養分或氧氣不足，就難免奄奄一息了。所以血液流量之分配也就是養分及氧氣之分配，就決定了各器官之榮枯了。打個比方吧！如果中央政府的預算不分配給教育部，那麼全國上下的學校都要餓死了。血液之流注正像預算一樣，那裏分配得多就長得好，那裏不夠就衰弱。而人是一個整體的，五臟六腑，樣樣都要健康，才能保證一個健康的身體。

(三)脈搏學能告訴我們什麼？

中醫診斷最早之記載大約在周禮：「以五氣，五聲，五色，眡其死生，兩之以九竅之變，參之以九臟之動」，所謂「五氣，五聲，五色，眡其死生」也就是望診、聞診，再加上「九竅之變」應該是望、聞、問之綜合。而「參之以九臟之動」，古人曾解釋為「臟之動，謂脈之至與不至，謂九臟在內，其病難知，但診脈之至與不至」。可知，早在扁鵲、張仲景，或脈學大宗師王叔和之前，中國人就已知道，由脈之搏動，可測知內部臟器之疾病。

周朝是三千年前的朝代，當時所說的九臟之動，由現代生物物理來看，究竟是什麼個現象呢？

由血液的流體力學可知，每一個臟器，或組織都由動脈送入血液，而動脈在血液流入組織之前，愈分愈細成樹枝狀，這就是所謂的動脈樹。心臟之收縮為血液流入這些動脈樹之推力。心臟之搏動放鬆時為心舒壓，收緊時為心縮壓，所以血液也就有了波動流與直流兩種流動。心舒壓一方面將器官充滿起來，另一方面也可維持一個最低的血液供應。而由心縮壓所產生之脈動，才是傳送血液之主要方式，此點可由超音波血流計來證明，血液在動脈中流動時，其直流部分之流量遠在波動流量之下。

由血液流體力學之推演及實驗，Tayler 先生[1] 更指出一些器官及組織之動脈樹，對血流波動之頻率，有一定的反應。對高頻的部分其阻力幾乎都是一樣的，只

是在低頻率時之阻力有很大的不同。此不同視動脈樹之結構而定。換言之，每一種器官對不同低頻率脈動通過時所產生之阻力，並不相同。也就是每個器官或組織都容許某一種特定頻率之波動流過，因為其阻力為最小。或是以電路理論來做比方，就是每一個器官都有其特性交流電抗，具有各自的天然共振頻率，而這個頻率也就是血液最容易流入此器官或組織的頻率。這個推論也有實驗證明，Basar[2] 先生已證明心臟及腎臟都有極高之頻率選擇性，讓血液以此頻率之波動流入其間。

如果我們依此推論，認為全身所有之器官及組織，各自有一個特殊的共振頻率，則對血液在周身之流動，就有了與中醫一樣的看法了。

因此依我的看法，所謂九臟之動，就是內臟以其自己特定的頻率隨著心臟之跳動而被迫共振，同時容許此共振頻率之波動血液出入其間。共振的愈好，則流量愈大，因為阻力愈小。不同的器官，不同的組織都有其特定之頻率。但如果個個特定頻率皆不相同，則心臟豈不要做成千上萬個不同的頻率來。其實不必，大分起來，有十幾種頻率也就夠了。這種以頻率來分析血流的方法，可以把相同頻率之器官及組織歸為同一經絡，由此也就不難了解中醫十二經絡的由來了。每一經絡所接受的血流是同一頻率的，也就難怪它們的病變總是一起發生。因為一旦這種共振頻率之阻力增加了，這種頻率之血流量就會減少，因而這一整個經絡的血液分配都會減少，也就跟著衰弱，甚至逐漸產生病變了。

(四)血液之分配與脈搏

為了證明血流之分配情形可由脈搏之波形作為診斷，我們特別設計了一些實驗，我們以一個幫浦作為波動流來源以模擬心臟，以塑膠管模擬血管，而以有低頻共振特性之氣球來模擬五臟，我們發現在五臟中，血流量產生改變時，必定隨著產生脈搏上之特定改變，換言之，血流的分配與脈搏之波形變化有著密切的關係。因此由脈搏波形之改變，應可診斷出內臟器官在共振頻率上之改變，或共振頻率時阻力之改變。而此改變就與所謂的火氣、寒熱等病變相關了。有關此實驗之細節請參看 Wang[3]。

Special Issue of Annual Report of the Institute of Physics, Academia Sinica, Vol. 16, 1986
In Honor of Prof. Ta-You Wu on the Occasion of his 80th Birthday

而以相同之模型我們也曾模擬五臟之相生與相尅之現象。所謂甲乙相生，就是甲壞乙也壞，而甲丙相尅就是甲壞丙變好。一個器官的變好變壞，與流入此器官之血液流量有關，流量增大，變好，流量減少，變壞。當我們把甲之流量降低時，發現乙跟著變低，而丙之流量却特殊的變高了（其流量之增加遠大於另二器官）。因而可知相生相尅只是共振頻率間互相影響之物理關係，而陰陽五行的理論恰好滿足了其運算的規則，就像群論可以決定光譜中的一些選擇律一樣，並不是什麼神秘的原因。

(五)穴道是什麼？針灸爲什麼治病？

由上所述，我們已經了解血液流注器官及組織之法則。波動的血液流進入器官時，器官也必隨著共振。那麼有沒有辦法阻斷這種流動、或振動呢？一個振動的物體，一定有些點，壓迫後可阻止其振動。在經絡上的一些重要位置，這個位置壓下後，很容易更改此組織中動脈樹之基本頻率。當波動血液流入動脈樹時，就像敲鼓一樣整個組織必隨著血壓中的某一個頻率振動，而讓血液流入此組織。但是一旦壓著穴道時，就會阻止這種振動，或是更改其共振頻率，因此阻斷或改變了血液流注此組織之狀況。所以穴道就是經絡上的一些重要位置，這個位置壓迫後，很容易阻斷動脈樹的振動，或更改其基本頻率。所謂的穴道並不需要與血管，或組織直接有關，也就難怪多少年來，我們始終找不到穴道之解剖結構。穴道只在血液仍流動之活體上，才有意義。而一些由壓下穴道所產生之酸、麻等感覺，可能是由於血流減少而產生的。

如果外加之阻力，阻斷了動脈樹的振動，因而流入此組織之血液減少了，但是其影響還不止這一個組織而已。因為此組織之阻力增加，也增加了這一個振動頻率之阻力，所以整個經絡之血流量也都受到影響而減少。這些無法流入經絡的血液，就視相生及相尅的關係，分流進入其他的組織去了。而針灸之手法更有補與瀉之不同，簡單的說，補者加強其流動，瀉者減少其流動。所以補的手法多以一定的頻率刺激穴道，也可以加強共振，而增加血液流量。而抑制穴道使其減少共振，就是瀉

法。

由此可推論，針灸是一種改變不同頻率振動之阻力以達到調和血液分配之手法。那麼灸的目的又是什麼呢？由近代生物物理的知識，知道細胞膜的彈性與其中所含飽和脂肪酸成反比。所以膽固醇含量愈高彈性就愈壞。但是這種彈性變化亦由其熔化的程度而定。飽和脂肪酸之熔點較高，所以在體溫時就較硬（就像豬油）。而不飽和脂肪酸之熔點較低，所以在體溫時就較軟（就像沙拉油）。當由不飽和脂肪酸組成細胞膜時，彈性較好。所以灸就是以加熱來改變組織之彈性，以改變其阻力之另一種手段了。因為溫度升高後，組織總是變得較軟。由此引申，也就不難了解張仲景先生傷寒論中之基本論點了。因為手脚或體表之受寒，其間之動脈樹也就隨之因冷而硬化。因而增加了阻力，阻擋了某種共振之產生，也就造成血流之不至，進而將惡化之情形循著經路往體內傳去。這種病變又會由相生相尅的規則，由一經轉往另一經，使病情惡化。

(六)氣是什麼？

「氣行血」是中醫最常用的術語，「以心行氣」又是練氣功之不二法門。那麼氣到底是什麼呢？由上述的脈搏學及穴道之說明，我們知道血液是隨著脈動一波又一波的在血管中流入，進入動脈樹，而營養身體之各個組織及器官。而穴道就是調整這些脈動之樞紐。可以針灸之補瀉手法，加強或阻止流入穴道相關之器官，組織中之血液流量。所以氣應可視為血液波，流入各器官或組織阻力的一種描述。阻力愈小，氣愈盛。而氣不僅與血管之通順與否有密切關係，整個動脈樹，甚至整個器官之彈性，皆可表現在“氣”上。組織與器官長得愈健康，則其基本頻率愈標準，而且共振的愈乾淨俐落，因而血流就越順暢。這有點像電子學的電導，氣愈旺，電導愈大，導電愈好。所以俗話所稱打通某個穴道，就是把這個穴道相關之器官或組織強化，使其健壯，而顯示出理想之共振頻率，因而血流暢旺。同理，打通了某個經絡，就是把這個頻率相關的穴道一起都打通了，因而這個頻率的血流都能暢旺。如果身體更進步，則十二經路皆可一一打通，那麼心臟病、高血壓，甚至糖尿病等

Special Issue of Annual Report of the Institute of Physics, Academia Sinica, Vol. 16, 1986
In Honor of Prof. Ta-You Wu on the Occasion of his 80th Birthday

慢性病皆可有良好的治療效果，由此更不難了解為何推拿、拍打是打通穴道通常用之手法。

其實道家之練功，尚不止於此。如果把整個大動脈系統看成一個共振腔，那麼心臟就是加入能量之幫浦，練功時就像雷射系統一樣，不斷把能量打入此共振腔，並儲存起來，當發力時，"力由脊發"，就是由共振腔的中心——大動脈，將選定之頻率，經由經絡（相當於動脈之水壓系統）發射出來，如此就不難理解所謂爆發力，或運氣、行氣的道理了。而當血流順暢，流速很大時，因血液中含電解質是導體，流速大時與地磁之作用，難免會產生一些電壓（此即電磁式血液流量計所用之原理），如此亦可解釋有功夫的人，一旦運起氣來，手中帶有靜電的原因。

(七)耳針及手脚按摩

針灸強調耳針，而手脚按摩又說是針灸之應用，這又是什麼道理呢？人之身體如按血流頻率可分十二經絡，換言之身體各部都可按這十二種頻率來分配（其實應較十二為多，所以才有奇經八脈等額外之經絡）。所以耳朵、手、脚也一樣有隨這十二種頻率振動的組織。而耳朵特別重要，因為耳朵是動物之散熱器官，血液流量特別大，所以一旦在耳朵上改變某一特定頻率之阻力，對整個經絡之流動阻力影響也就特別大，所以別看耳朵小，耳針之效果却是特別好。手脚按摩也是同樣的道理，所以手、脚上所謂之反射點，也就是身上器官、內臟，共用同一頻率之相對應點，因此以一定之頻率（最好是共振頻率——這也就是外丹功所謂的先天氣），加以按摩，就能加強此頻率血脈之流動，而達到治療內臟疾病之效果。

(八)望診與面相

望診為中醫四診之首，而中國人更相信面相。其實這也是與手脚按摩一樣的道理，人之頭部，與手、脚及耳朵一樣有十二經絡經過。所以不同的部位由不同的頻率之血液波來灌輸。一旦肝有了病變，則肝之基本阻力將變大，因而，流入肝臟之頻率的波動就阻力大增，導至流入臉上與肝相同頻率之部位之血液流注不足，因而

此部位就因氧氣不足，營養不良而發青或發黑，或粗糙等現象來。而由面相，多少也可看出先天之內臟強弱，及形狀。因而面相多少與人之基質有關，而氣色又與你的健康有密切的關連了。

(九) 總　論

在我國的文化中，內經一直佔著重要的地位。由其引申而出的，不僅是中國醫學，其他如道家之練功，及各家各派武術之內功、氣功也或多或少與脈搏學之研究有關。神農氏嘗百草，靠的是「玻璃肚子」，換言之是靠他自己的感覺，或是脈搏。靠自己的感覺，靠自己的修練，也就成了中國人，成仙、成佛的正規途徑。這種靠自己的觀念也就是中國醫術的精要。中醫以扶正為主，也就是增強抵抗力，加強正常生理情形下身體原有的恢復能力。再由此抵抗力去抵擋疾病。因而由脈搏學以及望聞問所引伸出來之診斷，常能發現疾病於未發之前，但是對於外來的細菌感染，或者盲腸炎等，却因為經驗不足，而稍有欠缺。

作為一個現代的中國人，我們不僅要研究發揚中醫所謂的王道醫術，也要研究利用西醫的特效藥、開刀，甚至器官移植等強烈手段。扶正以去邪，或去邪正自扶，本是一體之兩面，相生相成的，又何必爭論呢？

參 考 文 獻

1. Taylor M. G.: The input impedance of an Assembly of Ramdomly Branching Elastic tubes. Bioplysics J. 6. 29, 1966.
   Taylor M. G. : Wave Transmission through an Assembly of Ramdomly-Branching Elastic tubes. Bioplysics J. 6: 697, 1966.
2. Baser, E., G. Ruedas, H. Schwarzkopf, und Ch. Weiss: Untersuchungen des zeitlichen Verhaltens druckabhängiger Anderungen des Strömunswiderstandes im Coronargefäbsystem des Rattenherzens. Pflügers Arch. 304, 189-202, 1968.
3. Wang W. K. Y. Y. Lo. Y. Chiang, T. C. Chen:
   Study on flow distribution and pulse shape — A model for pulse felling in Chinese Medicine. paper submitted for publication.

低背景屏蔽室設計報告

中央研究院物現研究所原子核物理研究組 *

江紀成

摘　要

一低背景伽瑪屏蔽室採用鐵、鉛、鐵、鋁、壓克力板之夾心設計，估計可對0.1～2.5MeV之伽瑪自然背景衰減至原強度的2～20％。屏蔽室設計之概念予以討論。

一、引　言

在我們的生活環境中，或多或少都有若干放射性的存在〔1，2〕；這些放射性，或來自宇宙射線，或由於自然界中的長生命期（long life-time）核種，或由於核爆後的輻射塵，甚或是人為因素造成的輻射污染〔2〕。這種微量的放射性對人們的生活起居或者不構成威脅〔1～3〕。可是如果存在於實驗室中，尤其是輻射量度實驗室，或原子核物理實驗室，就會對靈敏而精確的輻射量度儀器造成嚴重的干擾，影響到實驗的精確性，形成研究工作上的困擾。這種自然存在的所謂「背景放射性」（background radiation），往往會造成實驗量度上的錯覺，更麻煩的是有時會掩蓋了欲測能峰。因此，在一般的實驗室中背景輻射的認定及設法降低其對實驗室的影響，是基本的工作之一。

本所原子核研究小組，目前的研究工作之一，是利用慢中子捕獲反應，量取

---

* 本設計參與同仁包括林爾康、王建萬、江紀成、鄧炳坤、仲國慶、袁天竑、陳志遠、謝家和、陳志強＋、徐一民。

＋清華大學，物理所。

Special Issue of Annual Report of the Institute of Physics, Academia Sinica, Vol. 16, 1986
In Honor of Prof. Ta-You Wu on the Occasion of his 80th Birthday

伽瑪射線譜，分析原子核構造。在以往的測定中，發現存在的背景伽瑪輻射有21種，其能量分佈由 241 keV 至 2,614 keV 之間〔 2 〕；其來源約可分為屬於鈾系的 ^{226}Ra ，屬於釷系的 ^{212}Bi （或稱ThC ），^{208} Tℓ（或稱Th C″）及 ^{228}Ac（或稱Th D），其它還有：鉀— 40 、錳— 56 等。這些輻射，大部分來自建築用的砂石及土壤〔 2 〕。

為了防止上述的自然背景的干擾，使若干低強度的伽瑪譜線易於觀測。對用以偵測輻射的偵檢器（ detector)作適度的屏蔽（ shielding ），是必要的措施。一般小型的偵檢器屏蔽、或屏蔽室（ Shielding chamber ）亦早已商品化〔 4 〕，對輻射的單能譜量度幫助很大。我們現在使用的伽瑪量度系統，包括HpGe —NaI(Tℓ) 康普吞抑制系統，Ge(Li) — HpGe 及HpGe—NaI（Tℓ）方向角相關量度系統，體積較單一偵測器龐大甚多，於是設計了一 2.0 m（長）× 2.0 m（寬）× 1.8 m（高）的低背景屏蔽室，希望對＜ 2.5MeV之自然背景可衰減至原有的 10 % 以下。

二、低背景伽瑪屏蔽之設計概念

伽瑪能譜實驗室中對背景輻射的屏蔽，除了要求將外來背景輻射之強度衰減外，對由試料所生之伽瑪射線及貝他粒子（ Beta particle ）之多重散射，或制動輻射（ bremstralung radiation ）所造成的影響亦應列入考慮。背景輻射主要為低能量（＜ 2.5 MeV)之伽瑪射線，伽瑪射線與物質的交互作用十分複雜。其型式（ mode ）多達 10 種〔 4 〕。其中最重要的有三種，即光電效應（ photo-electric effect ）、康普吞效應（ Compton effect ）及偶生效應（ pair-production ）。因此就伽瑪射線的屏蔽，須對此三種效應妥為考慮。所謂光電效應，是指伽瑪光子在入射至靶質的原子時，靶原子的K層或L層的電子在吸收入射光子的能量後，或被擊出，或因受激而放出K X—射線或L X—射線。靶質對光子的吸收係數 τ 與靶質的原子序（ Z ）的 4 次方成正比而與入射光子能量的 2.8 次方成反比。康普吞效應則指當伽瑪光子與靶質中的靶原子碰撞後，將原子外層電子擊出，本身則於損失部分能量後再散射而出；由此康普吞效應可分為兩部分，其一是由散射後其能量

的減少，我們稱為康普吞吸收係數 σ_a ；另一則為散射後伽瑪射線方向的改變，我們稱為康普吞散射係數 σ_s 〔 5 〕。第三種效應為偶生效應，即入射的伽瑪光子，經靶原子的庫倫電場（ Coulomb field ）吸收後，形成帶有單位負電荷的電子及單位正電荷的正子（ positron ），形成此一對偶時需 1.02 MeV 的能量，即當伽瑪射線的能量小於 1.02 MeV時，偶生效應的截面積（ cross-section ）K為 0 ，K也稱為偶生吸收係數；偶生效應使伽瑪射線減弱與靶質的原子序 Z 的平方成正比〔 6 〕。

物質對入射伽瑪射線的總吸收係數可表之為：

$$\mu_T = \tau + K + \sigma_s + \sigma_a \qquad (1)$$

而基本的衰減方程式為〔 7 〕：

$$I = I_0 B \exp(-\mu_T \cdot x) \qquad (2)$$

式中 I_0 為入射伽瑪光子的強度。I 為經過厚度為 x 的吸收體後的強度。μ_T 為總吸收係數號，β 為 Fano 氏在 1953 年提出的「廣射束衰減因數」(Broad beam attenuation)〔8〕，B之值隨入射伽瑪射線的能量，吸收能量，吸收體的厚度而異〔 9 〕。

在我們的構想中，除了偵檢系統要避免外來的自然背景干擾外，另有兩項因素必須列入考慮：其一是由試料本身所放出的伽瑪射線經過屏蔽體內壁的多重散射而進入偵檢器的低能量伽瑪光子；其二是由試料放出的貝他粒子，與屏蔽體內壁造成的制動輻射（ bremstralung radiation ）。為了減少伽瑪光子的多重散射，我們加大了屏蔽體的設計，使內部淨體積為 2.0 m（長）× 2.0 m（寬）× 1.8 m（高）；不但可容下整個量度系統（見圖 2 ）亦可減少伽瑪多重散射進入偵檢器的機會。至於貝他粒子造成制動輻射的防止，我們在屏蔽體的內壁，加裝鋁板（ 3 mm厚）及壓克力板（ 5 mm厚），這類低Z低Z／A值的物質，不但可有效防止貝他粒子，同時也不易產生大量的制動輻射〔 7 ，8 〕，危害到偵檢的精確性。

綜上所述，我們知道，對背景伽瑪輻射的屏蔽，以鉛、鐵等高原子序、高密度的金屬為佳，對貝他粒子的屏蔽，則以低Z的物質，如壓克力、鋁等為有效，同時

Sp. ... Issue of Annual Report of the Institute of Physics, Academia Sinica, Vol. 16, 1986
In Honor of Prof. Ta-You Wu on the Occasion of his 80th Birthday

較大的屏蔽室，可減少試料射線源的多重散射。針對以上的考慮，我們的屏蔽體採用多層混夾式設計，如圖1所示。屏蔽室壁由內至外，依次為壓克力板（厚5 mm）、鋁板（厚3 mm）、鐵板（厚10.5 mm）、鉛板（厚15 mm）鐵板（厚10.5 mm）。以壓克力板及鋁板體內層，除可減少由射線源（試料）發射的貝他粒子所造成的制動輻射外，也可減低伽瑪射線的散（反）射。鐵板與鉛板的夾心安排一則有效減低外部背景伽瑪射線，在結構的強度及安全（不使有毒及質軟的鉛暴露在外）上也合乎要求。

三、屏蔽估算與結果

因為現存的伽瑪自然背景＜2.5 MeV，因此屏蔽能力的估算以 $E_\gamma = 1$MeV及 $E_\gamma = 2$ MeV之估算為基準。我們所採用的材料鉛、鐵及鋁，其密度分別為11.34 g／cm^3、7.86 g／cm^3及2.69 g／cm^3〔10〕；當入射伽瑪射線其能量為0.5 MeV、1 MeV及2 MeV時，其質量吸收係數列如表Ⅰ〔11〕。依式(2)分別計算的結果 I/I_0，即屏蔽後與屏蔽前的伽瑪射線強度比分別列如表II。

有關於表II的計算，我們有下列幾點的說明：

1. 壓克力板對伽瑪屏蔽的效果很差，墊襯壓克力板的目的只是防止由試料射線源中放出的貝他粒子與高Z物質作用產生的制動輻射而已。因此在表Ⅰ及表II中未把壓克力的計算列入。
2. 在式(2)中的廣射束衰累積因數B，實際上均大於1，應該在1與1.8之間。我們在計算時假設B＝1。

表Ⅰ　質量吸收係數（μ/ρ）

物　　質	質量吸收係數		
	E_r=0.5Mev	E_r=1Mev	E_r=2Mev
鉛　(pb)	0.16	0.07	0.045
鐵　(Fe)	0.085	0.061	0.045
鋁　(Ae)	0.084	0.0613	0.043

表II　自然背景經屏蔽後之計算值

物　　質	厚度	I/I*		
		0.5 Mev	1 Mev	2 Mev
鉛　(pb)	1.5	0.0657	0.304	0.465
鐵　(Fe)	2.1	0.245	0.371	0.475
鋁　(Ae)	0.3	0.934	0.951	0.966
總　　計	4.1	0.015	0.107	0.213

*：B值假設爲1

由表II可以看出，對0.5 MeV或以下的伽瑪射線，我們的屏蔽體可屏蔽98.5％，也就是僅有1.5％可通過。對1 MeV或以下的伽瑪射線僅有10.7％可通過。而對2 MeV或以下的伽瑪射線則有21.3％可通過。圖3是在屏蔽室內與屏蔽室外所測自然背景的伽瑪能譜，所用的偵檢器為62 cm^3的HpGe，其對 ^{60}Co 1.33 kev伽瑪射線的分解力為2.1 MeV，線性放大器為CABARA的Research Amp. CI 1412。紀錄能譜用的多頻分析儀為CABARNA的80型4096 MCA，量度時間為50,000 秒。由能譜圖中可看出，在低能量區之若平自然背景伽瑪射線，在屏蔽後已不復出現；經屏蔽後，整個譜域（由80 KeV至3 MeV）平均衰減約95％，可說是已達到當初之設計目的。在表Ⅲ中，我們列舉了若干較明顯的伽瑪能峰以及其在屏蔽室內外強度的比，它們的來源也列於表Ⅲ中，因所量度的時間頗短，累積的計數稍嫌過少（尤其在屏蔽室內）因此有統計誤差過大的情形。

Special Issue of Annual Report of the Institute of Physics, Academia Sinica, Vol. 16, 1986
In Honor of Prof. Ta-You Wu on the Occasion of his 80th Birthday

表Ⅲ　部分明顯之γ能峰在屏蔽室內外強度比

序號	伽瑪射線能量 (Kev)	伽瑪射線強度（計數／5×10^5秒） 屏蔽之內	屏蔽之外	I/I (100%)	來源
1.	186.18	117	1894	6.2	Ra 226
2.	238.62(241.98)	585	16529	3.5	Pb^{212}(Pb^{214})
3.	270.2	79	1232	6.4	Ac 228
4.	295.21	57	3643	1.6	Pb 214
5.	327.6	83	1456	5.7	Ac 228
6.	338.3	241	3575	6.7	Ac 228
7.	351.92	232	7776	3.0	Pb 214
8.	463.0	67	1696	4.0	Ac 228
9.	510.72	464	3961	11.7	Te 208
10.	583.6	477	7378	6.5	Te 208
11.	609.31	209	7568	2.8	Bi 214
12.	727.3	112	1748	6.4	Bi 214
13.	911.1	156	5336	2.9	Ac 228
14.	968.8	79	3675	2.2	Ac 228
15.	1120.29	13	1888	0.7	Bi 214
16.	1460.75	3243	24386	13.3	K 40
17.	1764.51	412	1952	21.1	Bi 214
18.	2614.5	1268	5338	23.8	Te 208

參考文獻

1. J. Shapiro, Radiation Protection, p56, Harvard Univensity Press, Cambridge, Mass, 1972.
2. 江紀成等，本所新竹及南港地區原子核實驗室中伽瑪背景之分析，中央研究院物理研究所集刊，第 31 頁，中華民國六十八年十二月。
3. 王志榮、張寶樹，放射性和環境污染的來源，原子能委員會彙報，第十八卷第六期，第 25 頁，中華民國七十一年十二月。
4. J. Kohl, R. D. Zentner and H. R. Lukens, Radioisotope Application Engineering, 1961 p 305, （本地翻印版）
5. 同上，頁 308 。
6. 同上，頁 309 。
7. 同上，頁 311 。
8. U. Fano, Nuclenics 11, 8, 1953 .
9. 王哲成，保健物理手册，頁 172 ，行政院原子能委員會印行，中華民國六十三年六月。
10. 理科年表，日本東京天文台編，1982 年版（物 18 頁）。
11. 同上（物 152 頁）。

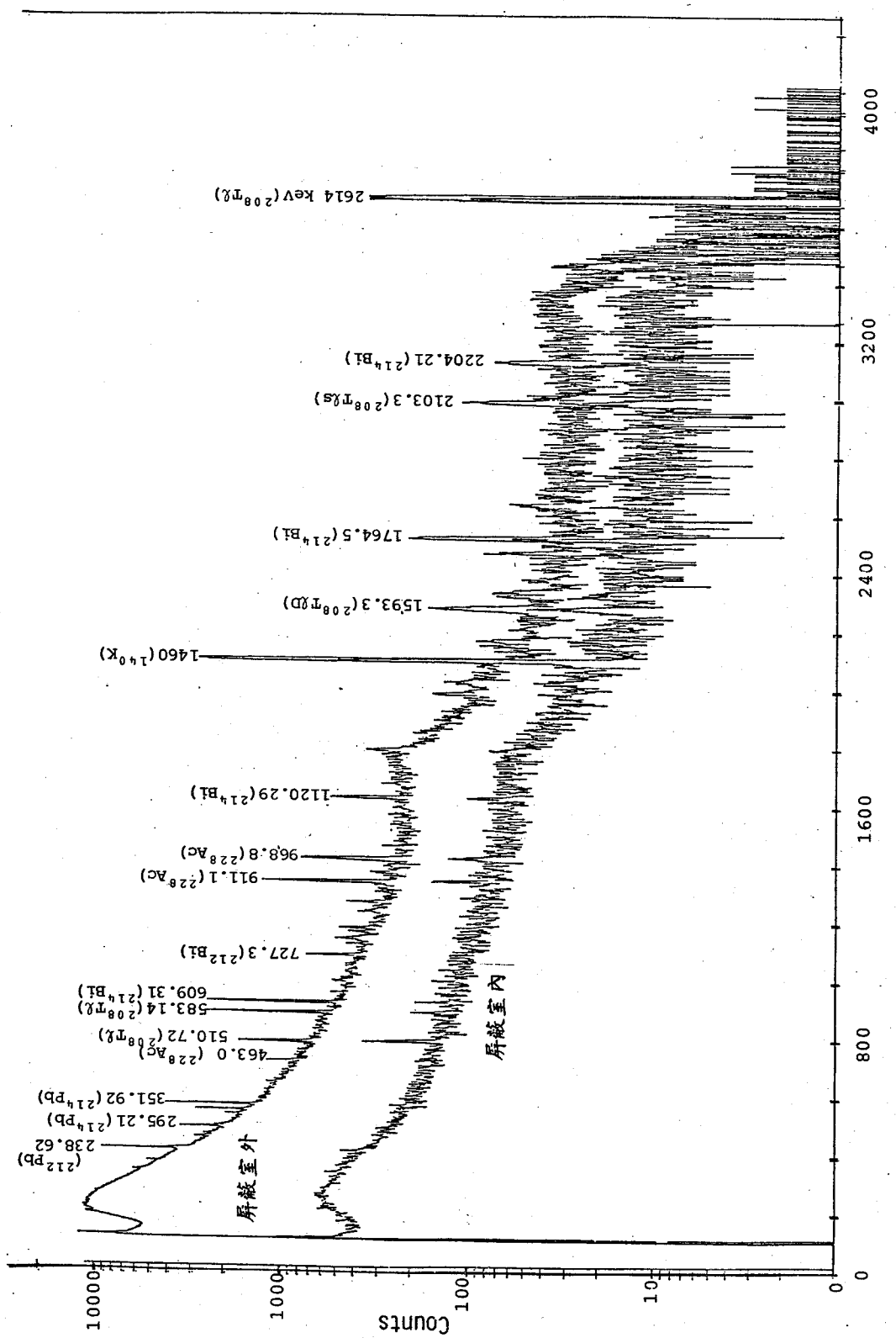

圖 3　屏蔽室內外之自然背景之比較

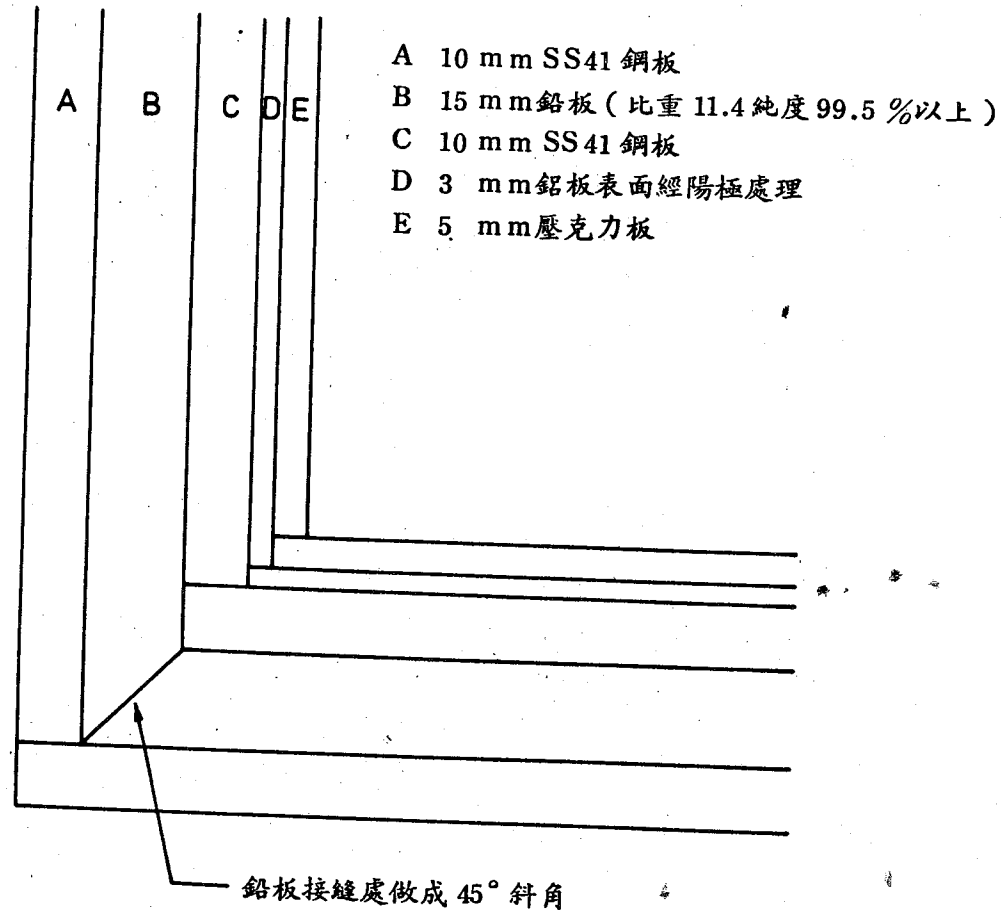

A　10 mm SS41 鋼板
B　15 mm鉛板（比重 11.4 純度 99.5 %以上）
C　10 mm SS41 鋼板
D　3 mm鋁板表面經陽極處理
E　5 mm壓克力板

圖 1　屏蔽室的平面示意圖，圖中圓盤部分為HpGe—NaI（Tl）$\gamma-\gamma$ 方向角相關量度系統

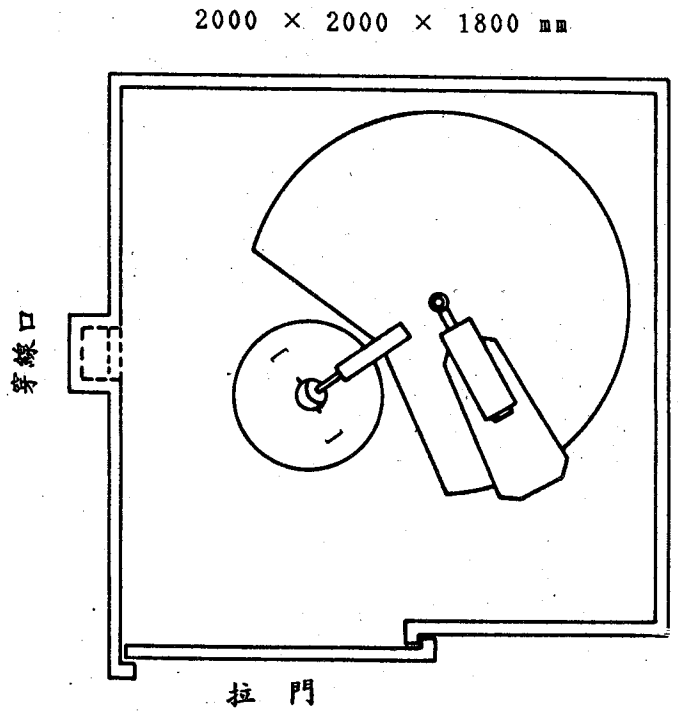

圖 2　屏蔽室壁之剖面圖

Special Issue of Annual Report of the Institute of Physics, Academia Sinica, Vol. 16, 1986
In Honor of Prof. Ta-You Wu on the Occasion of his 80th Birthday

AUTHOR INDEX

非　賣　品

中　央　研　究　院

物　理　研　究　所　集　刊

第　十　六　卷

發行人：林　　爾　　康

編輯者：中央研究院物理研究所集刊編輯委員會

出版者：中央研究院物理研究所　臺北市南港區

印刷者：萬　達　打　字　印　刷　有　限　公　司

電　話：三　九　四　〇　七　一　八

中　華　民　國　七　十　五　年　九　月　出　版